Study of the $K_L \to \pi^0 \nu\bar{\nu}$ Decay at the J-PARC KOTO Experiment

Department of Physics, Graduate School of Science, Kyoto University

Satoshi Shinohara

June 24, 2021

Abstract

In the Standard Model (SM), the rare kaon decay $K_L \to \pi^0\nu\overline{\nu}$ directly breaks CP symmetry. The branching fraction of $K_L \to \pi^0\nu\overline{\nu}$ is highly suppressed, and it can be calculated accurately in the SM. New physics beyond the SM can contribute to the process, and the branching fraction is expected to be enhanced in some theoretical models. This decay is thus sensitive to new physics beyond the SM.

This thesis describes the results of a search for the $K_L \to \pi^0\nu\overline{\nu}$ decay at the J-PARC KOTO experiment with the dataset collected in 2016–2018. Using the 2016–2018 dataset, we achieved the highest sensitivity for $K_L \to \pi^0\nu\overline{\nu}$ search of $(7.20 \pm 0.05_{\text{stat.}} \pm 0.66_{\text{syst.}}) \times 10^{-10}$, which corresponds to 1.8 times higher sensitivity than the previous KOTO analysis with the dataset collected in 2015. In this analysis, we suppressed the background caused by neutrons hitting the KOTO electromagnetic calorimeter, which was the dominant background in the previous KOTO analysis. We estimated backgrounds studied in the previous KOTO analysis to be less than 0.1 events.

We, however, examined our signal region and observed three signal candidate events. In this analysis, we found that two new types of backgrounds, one from $K^{\pm}$ decays and the other from scattered K_L decays, could be the sources of candidate events. Because we newly found such backgrounds in this analysis, we focused on the 2016–2018 data analysis and summarized those new backgrounds. With the two new background sources, we estimated the total number of background events to be 1.22 ± 0.26. We concluded that the number of observed events is statistically consistent with the number of the estimated background events. We set an upper limit of 4.9×10^{-9} for the branching fraction of the $K_L \to \pi^0\nu\overline{\nu}$ decay at the 90% confidence level (C.L.).

In this thesis, we describe methods to suppress backgrounds, especially the two new backgrounds from $K^{\pm}$ and scattered K_L decays, in future datasets. Although the upper limit given by this analysis is higher than the current best upper limit of 3.0×10^{-9} (90% C.L.) set by the previous KOTO analysis, this analysis clarified the key to suppressing the backgrounds in our measurement, and thus provided a solid potential to search for a new physics beyond the SM in KOTO with the sensitivity of $O(10^{-11})$.

Acknowledgments

This thesis was completed thanks to the great help and support from so many people. I am deeply grateful to them on this occasion.

First, I would like to express my deepest gratitude to Tsuyoshi Nakaya for giving me the opportunity for my research. I am grateful for his support and encouragement to complete this thesis. I would like to express my deep gratitude to my supervisor Hajime Nanjo for his long-time support. I learned many things about physics, as well as experimental methods. This thesis was completed thanks to his various advice. My special thank to Taku Yamanaka, the spokesperson of the KOTO experiment. In my research life at Osaka, I learned a lot from his attitudes as a researcher. I would never have completed this thesis without his heartfelt support.

I would like to express my gratitude to all the KOTO collaborators. I am grateful to Tadashi Nomura for being the chairman of the internal review committee for the KOTO 2016–2018 run paper. Thanks to tremendous support, the contents of the paper became very clear. I am grateful to Koji Shiomi for giving me thoughtful suggestions and advice on the 2016–2018 data analysis. In addition, I was given much support from him during staying at J-PARC. I would like to express my gratitude to K. Nakagiri and I. Kamiji. They helped me a lot during my research life in Kyoto. I really enjoyed researching with them.

I would like to thank M. Hutcheson and C. Lin for analyzing the 2016–2018 data together. I was inspired by the discussion with them. I am grateful to T. Komatsubara for giving me clear comments on papers. I am grateful to G. Y. Lim and H. Watanabe for the detector construction and environmental supports at J-PARC. I am grateful to T. Inagaki for being a member of the paper committee of the 2016–2018 run paper. I would like to thank M. Campbell, M. Tecchio, B. Beckford, S. Su, Y. W. Wah, M. Bogdan, J. Comfort, Y. Tajima, and Y. Sugiyama for their works for the great DAQ system. M. Tecchio gave me essential advice as a member of the paper committee of the 2016–2018 run paper. I am grateful to Y. C. Tung, Y. Luo, Q. Lin, J. C. Redeker, Y. B. Hsiung, S. H. Chen, E. J. Kim, J. L. Kim, H. M. Kim, S. K. Lee, M. Togawa, K. Sato, J. W. Lee, R. Murayama, K. Miyazaki, S. Suzuki, and T. Matsumura for working together in J-PARC and/or discussing at the meeting.

I would like to appreciate a lot of discussion with the members of the Kyoto Kaon group: N. Sasao, N. Kawasaki, D. Naito, Y. Maeda, S. Seki. I learned a lot from the discussion with them. I am grateful to KOTO colleagues and the secretaries of the Yamanaka group at Osaka University: K. Kotera, N. Shimizu, M. Ohsugi, T. Nunes, Y. Noichi, R. Shiraishi, Q. H. Vuong, K. Hanai, T. Kato, Y. Nakano, and C. Fujisaka. Especially, I am grateful to K. Kotera and N. Shimizu. Thanks to their kind supports, I enjoyed my research life at Osaka.

I would like to thank all the members of the High Energy Physics Group in Kyoto University: A. Ichikawa, M. Ishino, R. Wendell, O. Tajima, T. Sumida, A. Minamino, T. Kikawa, N. Patel, S. V. Cao, B. Quilain, K. D. Nakamura, S. Obara, S. Adachi, S. Honda, H. Kubo, K. Suzuki, K. Huang, S. Takahashi, T. Hiraki, S. Hirota, T. Tashiro, N. Kamo, K. G. Nakamura, T. Hayashino, T. Kunigo, Y. Ishiyama, K. Yoshida, M. Jiang, S. Ban, S. Yanagita, M. Yamamoto, K. Kondo, K. Haneda, R. Monden, S. Akatsuka, Y. Ashida, S. Tanaka, Y. Noguchi, A. Hiramoto, Y. Nakanishi, W. Uno, Y. Okazaki, K. Nakamura, M. Mori, M. Yoshida, K. Kuniyoshi, J. Komine, K. Yasutome, T. Abe, T. Ikemitsu, T. Odagawa, S. Kuribayashi, M. Tajima, M. Hatano, Y. Mino, I. Sanjana, E. Hayashi, H. Sekiguchi, and M. Sasaki. I really enjoyed my research life at Kyoto, thanks to exciting discussions

and pleasant conversations with them.

Finally, I would like to express my deepest appreciation to my family, especially to my parents Susumu Shinohara and Humiko Shinohara, for various supports throughout my life.

Satoshi Shinohara
Kyoto, Japan
June, 2021

Contents

Chapter 1

Introduction

The universe today is composed of matter but not anti-matter. To explain the origin of the matter-dominant universe, a CP asymmetry between particles and anti-particles (CP violation) is needed [1]. The CP violation is incorporated into the current theoretical framework of particle physics, the Standard Model (SM), and is explained to be caused by mixing between quarks in the Cabibbo-Kobayashi-Maskawa model [2, 3]. However, the size of the CP violation is known to be too small to explain the matter-dominant universe [1]. Thus a new physics beyond the SM that breaks CP symmetry is needed.

In this chapter, we first explain a key of the CP violation, and then introduce the motivation to search for the rare decay $K_L \to \pi^0 \nu\overline{\nu}$. Finally, we describe the purpose and outline of this thesis.

1.1 CP violation in the Cabibbo-Kobayashi-Maskawa Model

In this section, we explain a key to searching for new physics beyond the SM, which breaks the CP symmetry.

In the SM, the CP violation is caused by mixing between quarks. The Cabibbo-Kobayashi-Maskawa (CKM) matrix ($V_{\rm CKM}$) [2, 3] represents the mixing of the quark mass eigenstates (d, s, b) for the quark flavor eigenstates (d', s', b'):

$$\begin{pmatrix} d' \\ s' \\ b' \end{pmatrix} = V_{\rm CKM} \begin{pmatrix} d \\ s \\ b \end{pmatrix}, \tag{1.1}$$

where

$$V_{\rm CKM} = \begin{pmatrix} V_{ud} & V_{us} & V_{ub} \\ V_{cd} & V_{cs} & V_{cb} \\ V_{td} & V_{ts} & V_{tb} \end{pmatrix}. \tag{1.2}$$

The CKM matrix is parameterized by three mixing angles θ_{12}, θ_{23}, θ_{13}, and a CP-violating phase δ as

$$\begin{aligned} V_{\rm CKM} &= \begin{pmatrix} 1 & 0 & 0 \\ 0 & c_{23} & s_{23} \\ 0 & -s_{23} & c_{23} \end{pmatrix} \begin{pmatrix} c_{13} & 0 & s_{13}e^{-i\delta} \\ 0 & 1 & 0 \\ -s_{13}e^{i\delta} & 0 & c_{13} \end{pmatrix} \begin{pmatrix} c_{12} & s_{12} & 0 \\ -s_{12} & c_{12} & 0 \\ 0 & 0 & 1 \end{pmatrix} & (1.3) \\ &= \begin{pmatrix} c_{12}c_{13} & s_{12}c_{13} & s_{13}e^{-i\delta} \\ -s_{12}c_{23} - c_{12}s_{23}s_{13}e^{i\delta} & c_{12}c_{23} - s_{12}s_{23}s_{13}e^{i\delta} & s_{23}c_{13} \\ s_{12}s_{23} - c_{12}c_{23}s_{13}e^{i\delta} & -c_{12}s_{23} - s_{12}c_{23}s_{13}e^{i\delta} & c_{23}c_{13} \end{pmatrix}, & (1.4) \end{aligned}$$

where $s_{ij} = \sin\theta_{ij}$ and $c_{ij} = \cos\theta_{ij}$. The CKM matrix is also expressed with the Wolfenstein parameterization [4]:

$$V_{\rm CKM} = \begin{pmatrix} 1 - \lambda^2/2 & \lambda & A\lambda^3(\rho - i\eta) \\ -\lambda & 1 - \lambda^2/2 & A\lambda^2 \\ A\lambda^3(1 - \rho - i\eta) & -A\lambda^2 & 1 \end{pmatrix} + \mathcal{O}(\lambda^4), \tag{1.5}$$

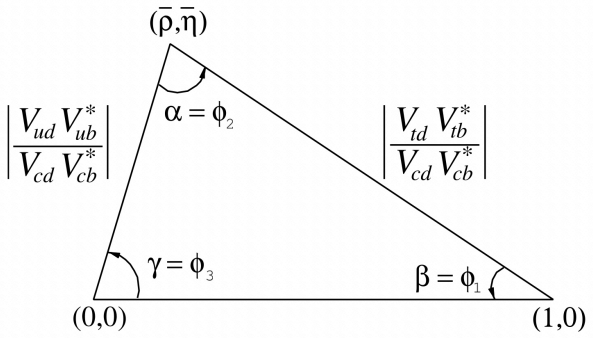

Figure 1.1: Unitarity triangle (quoted from Ref. [5]).

where

$$\lambda \equiv \frac{|V_{us}|}{\sqrt{|V_{ud}|^2 + |V_{us}|^2}}, \tag{1.6}$$

$$A \equiv \frac{1}{\lambda}\left|\frac{V_{cb}}{V_{us}}\right|, \tag{1.7}$$

$$\rho \equiv \Re\left\{\frac{V_{ub}^*}{A\lambda^3}\right\}, \tag{1.8}$$

$$\eta \equiv \Im\left\{\frac{V_{ub}^*}{A\lambda^3}\right\}. \tag{1.9}$$

The parameter η represents the imaginary part of the CKM matrix, which causes the CP violation. The unitarity of the CKM matrix gives

$$V_{ud}V_{ub}^* + V_{cd}V_{cb}^* + V_{td}V_{tb}^* = 0, \tag{1.10}$$

and thus

$$\frac{V_{ud}V_{ub}^*}{V_{cd}V_{cb}^*} + 1 + \frac{V_{td}V_{tb}^*}{V_{cd}V_{cb}^*} = 0. \tag{1.11}$$

The Eq. 1.11 shows a triangle on the complex plane. The first term of Eq. 1.11 calculated using the Wolfenstein parameterization is

$$\frac{V_{ud}V_{ub}^*}{V_{cd}V_{cb}^*} = -(1-\lambda^2/2)(\rho + i\eta), \tag{1.12}$$

$$= \overline{\rho} + i\overline{\eta}, \tag{1.13}$$

where $\overline{\rho} = \rho(1-\lambda^2/2)$ and $\overline{\eta} = \eta(1-\lambda^2/2)$. Therefore, Eq. 1.11 shows the triangle with vertexes of $(0,0)$, $(1,0)$, and $(\bar{\rho},\bar{\eta})$ on a complex plane (unitarity triangle), as shown in Fig. 1.1. The parameters of the unitarity triangle have been measured by various measurements. The global fit for the Wolfenstein parameters gives [5]

$$\lambda = 0.22650 \pm 0.00048, \tag{1.14}$$

$$A = 0.790^{+0.017}_{-0.012}, \tag{1.15}$$

$$\bar{\rho} = 0.141^{+0.016}_{-0.017}, \tag{1.16}$$

$$\bar{\eta} = 0.357 \pm 0.011. \tag{1.17}$$

Figure 1.2 shows constraints on the parameters on the $\bar{\rho}$-$\bar{\eta}$ plane.

As explained above, the parameter η causes the CP violation. A key to studying the CP violation is to study a decay whose process is sensitive to the parameter η.

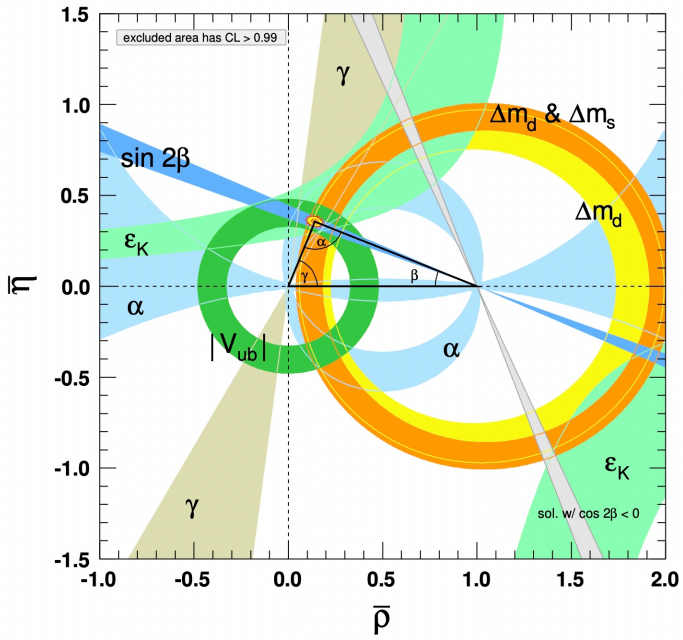

Figure 1.2: Constraints on the $\bar{\rho}$-$\bar{\eta}$ plane (quoted from Ref. [5]). The shaded areas represent the 99% C.L. allowed regions. The parameter ϵ_K was obtained from the measurement of K^0–$\bar{K}^0$, and parameters of $\sin 2\beta$, α, γ, V_{ub}, Δm_d and Δm_s were obtained from the experiment using B meson.

1.2 $K_L \to \pi^0 \nu\bar{\nu}$ Decay

1.2.1 $K_L \to \pi^0 \nu\bar{\nu}$ Decay in the Standard Model

In the SM, the rare decay $K_L \to \pi^0 \nu\bar{\nu}$ is sensitive to the parameter η. Here we describe features of $K_L \to \pi^0 \nu\bar{\nu}$ decay and the relationship between the $K_L \to \pi^0 \nu\bar{\nu}$ decay and the parameter η.

Figure 1.3 shows examples of Feynman diagrams of the $K_L \to \pi^0 \nu\bar{\nu}$ decay. In the $K_L \to \pi^0 \nu\bar{\nu}$ decay, the transition of $s \to d$ occurs. The transition by the neutral current that changes the flavor is prohibited at a tree level in the SM [6]. The lowest order processes are the loop processes with internal W boson exchanges, which causes the branching fraction to be small.

The quark level amplitude of this process $\mathcal{A}(s \to d\nu\bar{\nu})$ is described as

$$\mathcal{A}(s \to d\nu\bar{\nu}) \sim \frac{m_t^2}{M_W^2}\lambda_t + \frac{m_c^2}{M_W^2}\ln\frac{M_W}{m_c}\lambda_c + \frac{\Lambda_{\rm QCD}^2}{M_W^2}\lambda_u, \tag{1.18}$$

where λ_q is $V_{qs}^* V_{qd}$, and $\Lambda_{\rm QCD}$ ($\simeq 200$ MeV) is QCD energy scale. The M_W ($= 80.4$ GeV/c^2), m_c ($= 1.28$ GeV/c^2), and m_t ($= 173$ GeV/c^2) are the masses of W boson, charm-quark, and top-quark, respectively [7]. Due to the large mass of t quark, the t quarks have the largest contribution (68%), and u and c quarks have a small contribution (29%, and 3%, respectively) in Eq. 1.18. In the process of $s \to d\nu\bar{\nu}$, the short-distance contribution is dominant, and this makes the prediction of the $K_L \to \pi^0 \nu\bar{\nu}$ decay accurate.

For the amplitude of $K_L \to \pi^0 \nu\bar{\nu}$ decays, contributions from c and u quarks cancel out in the first order due to the following reason. First, flavor eigenstates of neutral kaons, K_0 and $\bar{K}_0$, make CP eigenstates, K_1 and K_2:

$$|K_1\rangle = \left(|K_0\rangle + |\bar{K}_0\rangle\right)/\sqrt{2}, \tag{1.19}$$
$$|K_2\rangle = \left(|K_0\rangle - |\bar{K}_0\rangle\right)/\sqrt{2}, \tag{1.20}$$

where K_1 (K_2) is a CP even (odd) eigenstate. Through the mixing of K_1 and K_2, K_L and K_S are described as

$$|K_S\rangle = \frac{1}{\sqrt{1+|\epsilon|^2}} \left(|K_1\rangle + \epsilon\,|K_2\rangle\right), \tag{1.21}$$

$$|K_L\rangle = \frac{1}{\sqrt{1+|\epsilon|^2}} \left(|K_2\rangle + \epsilon\,|K_1\rangle\right), \tag{1.22}$$

where ϵ is the mixing parameter, which indicates a size of CP-violation, and obtained as [5]

$$|\epsilon| = (2.228 \pm 0.011) \times 10^{-3}. \tag{1.23}$$

Due to the small $|\epsilon|$ in Eq. 1.22, the amplitude of $K_L \to \pi^0 \nu\bar{\nu}$ decays, $A\left(K_L \to \pi^0 \nu\bar{\nu}\right)$, is described as

$$A\left(K_L \to \pi^0 \nu\bar{\nu}\right) \sim A\left(K_2 \to \pi^0 \nu\bar{\nu}\right). \tag{1.24}$$

Finally, using Eq. 1.20, the amplitude of $K_L \to \pi^0 \nu\bar{\nu}$ is described as

$$\begin{aligned} A\left(K_L \to \pi^0 \nu\bar{\nu}\right) &\sim \frac{1}{\sqrt{2}} \left(A\left(K^0 \to \pi^0 \nu\bar{\nu}\right) - A\left(\bar{K}^0 \to \pi^0 \nu\bar{\nu}\right)\right) \\ &\propto V_{ts} V_{td}^* - V_{ts}^* V_{td} \\ &\sim -A\lambda^2 (A\lambda^3(1-\rho+i\eta) - A\lambda^3(1-\rho-i\eta)) \\ &= -i2A^2\lambda^5\eta \\ &\propto \eta. \end{aligned} \tag{1.25}$$

In the calculation of the first line in Eq. 1.25, contributions from real parts containing c and u quarks canceled out. Equation 1.25 shows that the $K_L \to \pi^0 \nu\bar{\nu}$ decay is sensitive to η which represents the size of the CP asymmetry.

The branching fraction of the $K_L \to \pi^0 \nu\bar{\nu}$ decay is calculated as

$$\mathcal{B}(K_L \to \pi^0 \nu\bar{\nu})_{\mathrm{SM}} = (3.00 \pm 0.30) \times 10^{-11}, \tag{1.26}$$

in the SM [8]. The short-distance dominant process of $s \to d\nu\bar{\nu}$ enables us to calculate the branching fraction of $K_L \to \pi^0 \nu\bar{\nu}$ accurately. In addition, the hadron matrix element can be obtained using the measurement result of $K^\pm \to \pi^0 e^\pm \nu$ decay [9], and this also makes the calculation of the branching fraction accurate. The uncertainty mostly comes from the uncertainty of the input parameters in the calculation, $|V_{ub}|$, $|V_{cb}|$, and γ (ϕ_3). Due to the small branching fraction, the signal of $K_L \to \pi^0 \nu\bar{\nu}$ have not been observed yet, and only upper limits on the branching fraction of the $K_L \to \pi^0 \nu\bar{\nu}$ decay were given by experiments, as will be described in Sec. 1.3.

1.2.2 Grossman-Nir Bound

The measurement of other decay modes gave indirect limits of the branching fraction of the $K_L \to \pi^0 \nu\bar{\nu}$ decay. Y. Grossman and Y. Nir derived a relationship of the branching fractions between $K_L \to \pi^0 \nu\bar{\nu}$ and $K^+ \to \pi^+ \nu\bar{\nu}$ from the isospin symmetry as [11]

$$\mathcal{B}(K_L \to \pi^0 \nu\bar{\nu}) < \frac{\tau_{K_L}}{\tau_{K^+}} \frac{1}{r_{is}} \mathcal{B}(K^+ \to \pi^+ \nu\bar{\nu}) \tag{1.27}$$

$$\sim 4.3\, \mathcal{B}(K^+ \to \pi^+ \nu\bar{\nu}), \tag{1.28}$$

where $\tau_{K_L}/\tau_{K^+} (= 4.13)$ [5] is the lifetime ratio of K_L and K^+, and $r_{is} = 0.954$ is the isospin breaking factor [12]. This indirect limit is called the Grossman-Nir bound. The current Grossman-Nir bound is set by the NA62 experiment [13] as

$$\mathcal{B}(K_L \to \pi^0 \nu\bar{\nu}) < 7.8 \times 10^{-10} \text{ (90\% confidence level (C.L.))}. \tag{1.29}$$

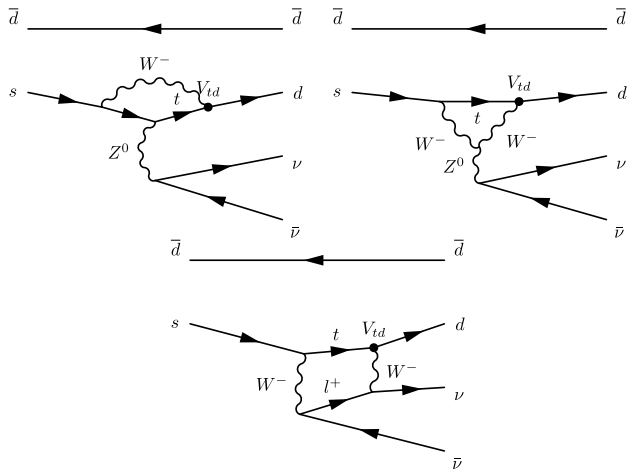

Figure 1.3: Examples of Feynman diagrams of the $K_L \to \pi^0\nu\overline{\nu}$ decay in the SM (quoted from Ref. [10]).

1.2.3 $K_L \to \pi^0\nu\overline{\nu}$ Decay Beyond the Standard Models

The $K_L \to \pi^0\nu\overline{\nu}$ decay is sensitive to new physics beyond the SM (BSM) due to the following reasons.

1. If BSM physics processes contribute the decay, the branching fraction is predicted to change (e.g. [14, 15, 16]).

2. Because the branching fraction of $K_L \to \pi^0\nu\overline{\nu}$ is predicted to be small in the SM with less theoretical uncertainty, a small deviation of the branching fraction from the SM prediction can be regarded as the result of a new physics beyond the SM.

Figure 1.4 shows the correlation between $R^0_{\nu\overline{\nu}}$ and $R^+_{\nu\overline{\nu}}$, where $R^0_{\nu\overline{\nu}} = \mathcal{B}(K_L \to \pi^0\nu\overline{\nu})/\mathcal{B}(K_L \to \pi^0\nu\overline{\nu})_{\rm SM}$ and $R^+_{\nu\overline{\nu}} = \mathcal{B}(K^+ \to \pi^+\nu\overline{\nu})/\mathcal{B}(K^+ \to \pi^+\nu\overline{\nu})_{\rm SM}$, in one of the BSM models [14]. The model [14] pointed out that if a new boson Z' directly changes a flavor with only coupling to either left-handed or right-handed particles, $R^0_{\nu\overline{\nu}}$ and $R^+_{\nu\overline{\nu}}$ change as shown in the blue and red regions, respectively, in Fig. 1.4. In this model, because the new physics process also contributes to the K_0–$\bar{K}_0$ mixing, which causes the indirect CP violation, the measured parameter of the indirect CP violation limits $R^0_{\nu\overline{\nu}}$ and $R^+_{\nu\overline{\nu}}$, and neither $R^0_{\nu\overline{\nu}}$ nor $R^+_{\nu\overline{\nu}}$ can change largely. Another model discussed in [14] pointed out that if a new boson Z' directly changes a flavor with a coupling to both left-handed and right-handed particles, $R^0_{\nu\overline{\nu}}$ and $R^+_{\nu\overline{\nu}}$ change as shown in the green region in Fig. 1.4. In this scenario, the constraint from the measured parameter of the indirect CP violation no longer works and $R^0_{\nu\overline{\nu}}$ and $R^+_{\nu\overline{\nu}}$ can change simultaneously.

Figure 1.5 shows the correlation between the branching fractions of $K_L \to \pi^0\nu\overline{\nu}$ and $K^+ \to \pi^+\nu\overline{\nu}$ in another BSM model [15, 16]. In the SM, d and s quarks give rise to isospin symmetry between $K_L \to \pi^0\nu\overline{\nu}$ and $K^+ \to \pi^+\nu\overline{\nu}$, which gives the Grossman-Nir bound. The BSM model [15, 16] pointed out that the Grossman-Nir bound no longer worked if four quarks mediated the $K \to \pi$ transition. In the scenario, the branching fractions of $K_L \to \pi^0\nu\overline{\nu}$ and $K^+ \to \pi^+\nu\overline{\nu}$ distribute as shown in the green region in Fig. 1.5.

The branching fraction of $K_L \to \pi^0\nu\overline{\nu}$ can be large in both BSM models shown above. It is essential to search for $K_L \to \pi^0\nu\overline{\nu}$ with the sensitivity of $O(10^{-10})$ to test the model [14], and $O(10^{-9})$ to test the model [15, 16] in experiments.

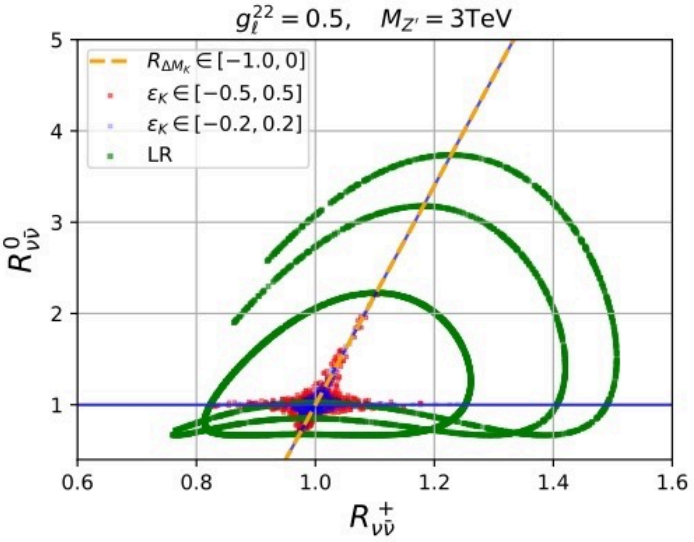

Figure 1.4: The correlation between the branching fraction of $K_L \to \pi^0 \nu\overline{\nu}$ and $K^+ \to \pi^+ \nu\overline{\nu}$ in the BSM model. The $R^0_{\nu\overline{\nu}}$ is $\mathcal{B}(K_L \to \pi^0 \nu\overline{\nu})/\mathcal{B}(K_L \to \pi^0 \nu\overline{\nu})_{\text{SM}}$ and $R^+_{\nu\overline{\nu}}$ is $\mathcal{B}(K^+ \to \pi^+ \nu\overline{\nu})/\mathcal{B}(K^+ \to \pi^+ \nu\overline{\nu})_{\text{SM}}$. The green region shows the new physics that does not have a CKM-like flavor structure and is combined with both left-handed and right-handed quarks. The red and blue regions show the case of the model of the new physics which has an interaction only to either left-handed or right-handed particles. The difference between the red and blue regions comes from the different assumption of the contribution from the new physics. In all cases, 3 TeV Z' couples to quarks. This figure is quoted from [14].

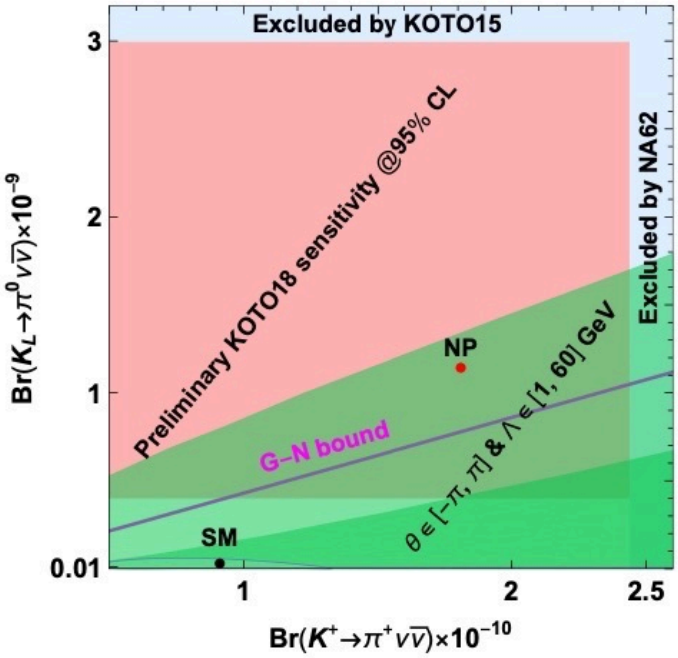

Figure 1.5: The branching fraction predictions of the model [15]. The black dot labeled SM corresponds to the branching fraction in the SM. The green region represents the region predicted by the BSM model with the BSM scale of order 1–60 GeV. The red dot labeled NP corresponds to the case of the BSM scale of 39 GeV. This figure is quoted from [15]. Note that an upper limit of $K^+ \to \pi^+ \nu\overline{\nu}$ is set to be 1.78×10^{-10} by NA62 in 2020 [13].

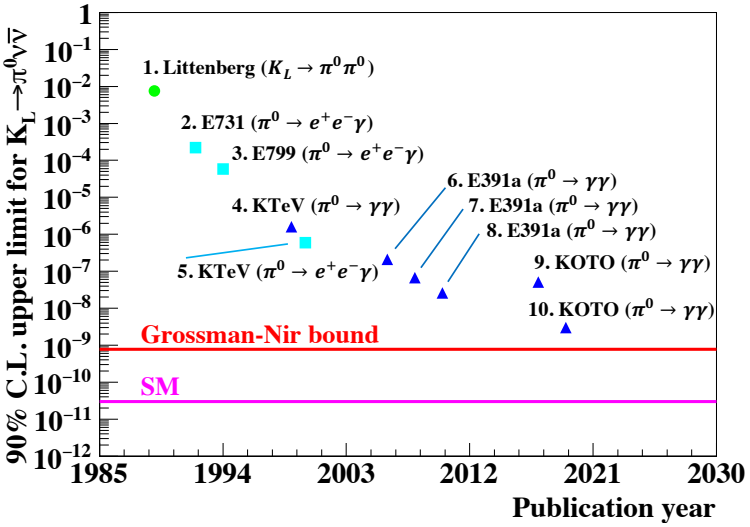

Figure 1.6: History of the upper limits on the branching fraction of the $K_L \to \pi^0\nu\overline{\nu}$ decay. The green point shows the first study by L. S. Littenberg. The cyan square (blue triangle) points represent results based on the final state of $\pi^0 \to e^+e^-\gamma$ ($\pi^0 \to 2\gamma$). The magenta line indicates the SM prediction of 3×10^{-11}. The red line indicates the Grossman-Nir bound of $< 7.8 \times 10^{-10}$ (90% C.L.).

1.3 History of the Experimental $K_L \to \pi^0\nu\overline{\nu}$ Searches

After the first study by L. S. Littenberg in 1989 [17], the rare decay $K_L \to \pi^0\nu\overline{\nu}$ has been studied by various experiments. However, due to the small branching fraction of the $K_L \to \pi^0\nu\overline{\nu}$ decay, the signal of $K_L \to \pi^0\nu\overline{\nu}$ has not been observed yet, and only upper limits were given by them. Figure 1.6 [18, 19, 20, 21, 22, 23, 24, 25, 26] shows the history of the upper limit on the branching fraction of the $K_L \to \pi^0\nu\overline{\nu}$ decay. In the following sections, we introduce experiments which were dedicated to searching for the $K_L \to \pi^0\nu\overline{\nu}$ decay.

1.3.1 KEK E391a Experiment

The KEK E391a experiment [24] was dedicated to searching for the $K_L \to \pi^0\nu\overline{\nu}$ decay at the High Energy Accelerator Research Organization (KEK) in Japan. The experiment was designed to detect two photons from a π^0 decay without any extra detectable particles. With a 12-GeV proton beam, they took data from 2004 to 2005 and set an upper limit:

$$\mathcal{B}(K_L \to \pi^0\nu\overline{\nu}) < 2.6 \times 10^{-8} \quad (90\%\ \text{C.L.}). \tag{1.30}$$

1.3.2 J-PARC KOTO Experiment

The KOTO experiment is a dedicated experiment to search for the $K_L \to \pi^0\nu\overline{\nu}$ decay at the Japan Proton Accelerator Research Complex (J-PARC) [27], in Tokai Village, Ibaraki Prefecture, Japan. The goal of the KOTO experiment is to achieve the sensitivity for $K_L \to \pi^0\nu\overline{\nu}$ of $O(10^{-11})$, which is the same order as of the SM prediction. The KOTO is a successor of the KEK E391a experiment and the experimental technique of KOTO is the same as of E391a. To improve the sensitivity by $O(10^2)$–$O(10^3)$ over the E391a limit, a high-intensity 30-GeV proton beam [28] is used, whose designed intensity is $O(10^2)$ higher than E391a. The detectors are constructed to suppress backgrounds to the level of $< O(10^{-10})$ and to have a capability for higher rates.

The KOTO experiment performed the first physics run in 2013 for 100 hours [25], and the second physics run in 2015 for four months [26]. In the 2015 data analysis, with the sensitivity of $(1.30 \pm 0.01_{\text{stat}} \pm 0.14_{\text{syst}}) \times 10^{-9}$ and the number of expected background events of 0.42 ± 0.18, no $K_L \to \pi^0\nu\overline{\nu}$

candidate was observed. From that result, KOTO set the current best upper limit on the branching fraction of $K_L \to \pi^0 \nu\overline{\nu}$ as [26]

$$\mathcal{B}(K_L \to \pi^0 \nu\overline{\nu}) < 3.0 \times 10^{-9} \quad (90\% \text{ C.L.}). \tag{1.31}$$

1.4 Purpose and Outline of This Thesis

As described so far, the study of $K_L \to \pi^0 \nu\overline{\nu}$ is a good probe to search for new physics beyond the SM. In this thesis, we describe the result of the $K_L \to \pi^0 \nu\overline{\nu}$ analysis based on the data collected in 2016–2018 at the J-PARC KOTO experiment. This analysis achieved the highest sensitivity to search for $K_L \to \pi^0 \nu\overline{\nu}$. Thus, this analysis enabled us to get new knowledge of our measurement and to discuss a potential to discover new physics beyond the SM in KOTO.

A piece of new knowledge we obtained in this analysis is a background caused by neutrons hitting the KOTO electromagnetic calorimeter. The background was the dominant background in the KOTO 2015 analysis. We found that the background had been suppressed by introducing new cuts and revising analysis methods. This thesis describes the new knowledge on the neutron background.

Another piece of new knowledge is backgrounds from $K^{\pm}$ and scattering K_L decays. Those backgrounds were not studied in the KOTO 2015 analysis. In this work, we observed three signal candidate events. We found that those backgrounds could be the sources of the candidate events. Because we newly found such background sources in this work, this thesis focuses on the analysis for the 2016–2018 dataset and summarizes those new backgrounds.

With new knowledge, this thesis gives a result of the $K_L \to \pi^0 \nu\overline{\nu}$ search for the 2016–2018 dataset. After discussing a comparison to the previous KOTO analysis and prospects, we finally give a conclusion of this work.

The outline of this thesis is as follows. The experimental method and apparatus are described in Chapter 2. The data taking conditions and triggers are described in Chapter 3. The event reconstruction is described in Chapter 4, and the method of our simulation is described in Chapter 5. The flow of the 2016–2018 analysis is described in Chapter 6. Studies to estimate the $K_L \to \pi^0 \nu\overline{\nu}$ sensitivity are described in Chapter 7. Studies to estimate the numbers of background events are described in Chapter 8. The result of the $K_L \to \pi^0 \nu\overline{\nu}$ search in 2016–2018 is described in Chapter 9. Prospects are discussed in Chapter 10. Finally, in Chapter 11, we summarize impacts of this work and conclude this thesis.

Chapter 2

The KOTO Experiment

The KOTO experiment [29, 30] is dedicated to studying the $K_L \to \pi^0\nu\overline{\nu}$ decay. In this chapter, the experimental method and apparatus of KOTO are described.

2.1 Experimental Methods

In this section, we describe experimental methods to search for $K_L \to \pi^0\nu\overline{\nu}$ in KOTO. We first describe how we identify the $K_L \to \pi^0\nu\overline{\nu}$ decay in a neutral K_L beam. To test the existence of new physics processes, it is essential to suppress backgrounds in our measurement because the branching fraction of $K_L \to \pi^0\nu\overline{\nu}$ is highly suppressed in the SM. We introduce major backgrounds in our measurement. Next, we explain the definition of the sensitivity for $K_L \to \pi^0\nu\overline{\nu}$ search in KOTO, and finally explain a mechanism of losing signal events.

2.1.1 Signal Identification

Figure 2.1 shows a schematic view of the $K_L \to \pi^0\nu\overline{\nu}$ signal detection. The K_L enters from the left in Fig. 2.1. We defined the beam-axis lying along the beam-direction. The π^0 has a short lifetime ($c\tau_{\pi^0} \sim 2.5 \times 10^{-8}$ m) and decays into two photons with a large branching fraction (98.8%) [5]. We identify the $K_L \to \pi^0\nu\overline{\nu}$ decay by detecting two photons from the π^0 decay, and by ensuring that there are no other detectable particles.

The π^0 from the decay is reconstructed from two photons detected by a KOTO electromagnetic calorimeter. Figure 2.2 shows a schematic view of two photons from the π^0 decay hitting the calorimeter. To reconstruct the π^0, we first calculated the opening angle between the two photon directions with two equations. One is derived from the conservation of 4-momentum of the $\pi^0 \to 2\gamma$ decay:

$$M_{\pi^0}^2 = (E_1 + E_2)^2 - (\boldsymbol{p}_1 + \boldsymbol{p}_2)^2, \tag{2.1}$$
$$= 2E_1E_2(1 - \cos\theta), \tag{2.2}$$

where M_{π^0} is the nominal π^0 mass[*1], E_i and $\boldsymbol{p}_i$ are the energy and momentum of the i-th photon, respectively, and θ is the opening angle between the two photon directions. We then get

$$\cos\theta = 1 - \frac{M_{\pi^0}^2}{2E_1E_2}. \tag{2.3}$$

The other is derived from a cosine theorem with each photon hit position in the calorimeter and the π^0 decay position as vertices of a triangle. By using the opening angle from Eq. 2.3 and the cosine theorem and assuming that the $\pi^0 \to 2\gamma$ decays on the beam-axis, we get the π^0 decay vertex position ($Z_{\rm vtx}$). After we get the π^0 decay position, each photon direction is calculated from the π^0 decay position and the photon hit position on the calorimeter, and then the photon momentum is calculated

[*1] The nominal mass of π^0 is 134.9768 MeV/c^2 [5].

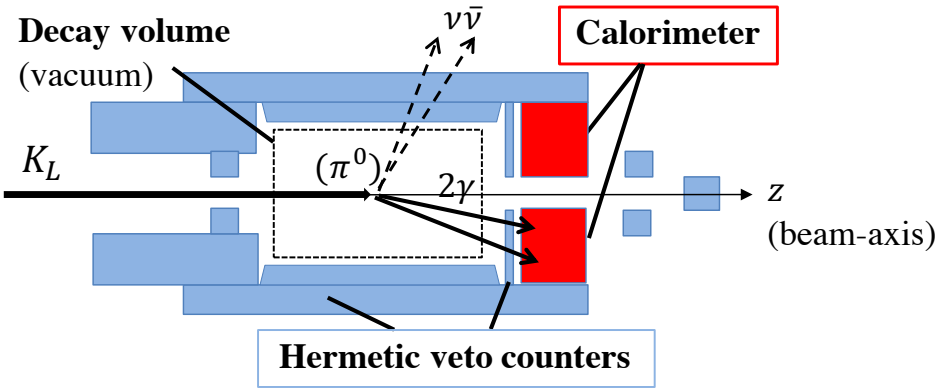

Figure 2.1: Schematic view of the signal detection in KOTO. The π^0 from the $K_L \to \pi^0\nu\bar{\nu}$ decay immediately decays into two photons. We detect the two photons from the π^0 decay with a calorimeter, and ensure that there are no other detectable particles by hermetic veto counters surrounding the decay volume.

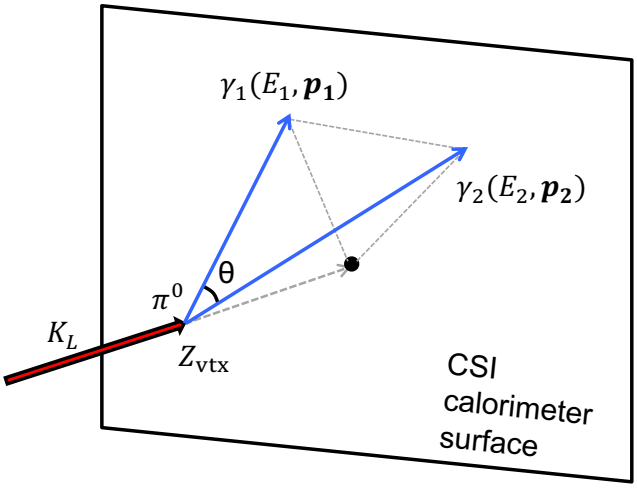

Figure 2.2: Schematic view of the opening angle between the two photons and Z_{vtx}.

using E_i. We finally get the 4-momentum of the π^0 from the 4-momentum of the two photons. Details of the π^0 reconstruction will be described in Sec. 4.2.

The π^0 from the $K_L \to \pi^0\nu\bar{\nu}$ decay is expected to have a finite transverse momentum (P_t) with respect to the beam-axis, due to the neutrinos. We defined the signal region with the P_t and Z_{vtx} of the reconstructed π^0, as shown in Fig. 2.3. To determine the selection criteria for $K_L \to \pi^0\nu\bar{\nu}$ with less human bias, we used a dataset excluding events in a region slightly larger than the signal region (blind region). After we determined the selection criteria, we examined inside the blind region.

2.1.2 Neutral Beam Containing K_L's

Figure 2.4 shows the conceptual design to make a neutral K_L beam in KOTO. The particles produced at the production target are guided through a beamline. The key to making the beam is a long beamline to eliminate short-lived particles, two collimators to make a narrow beam with sharp edges, and a sweeping magnet to remove charged particles. The length of our beamline, the distance from the target to the end of the downstream collimator (beam-exit), is 20 m. Because we assume that the π^0 decays on the beam-axis, we need a narrow beam. Details of the beamline will be explained in

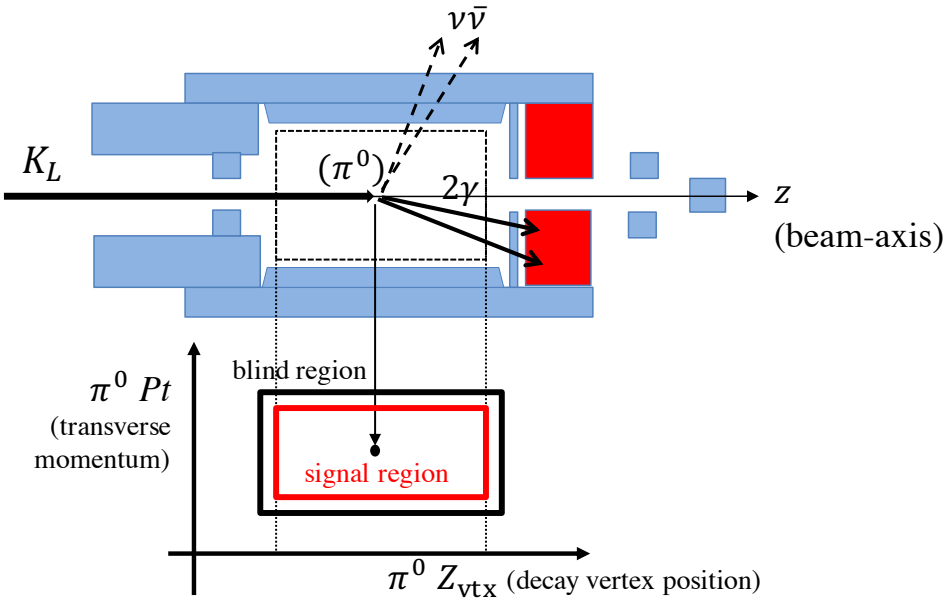

Figure 2.3: Schematic view of the opening angle between the two photons and Z_{vtx}.

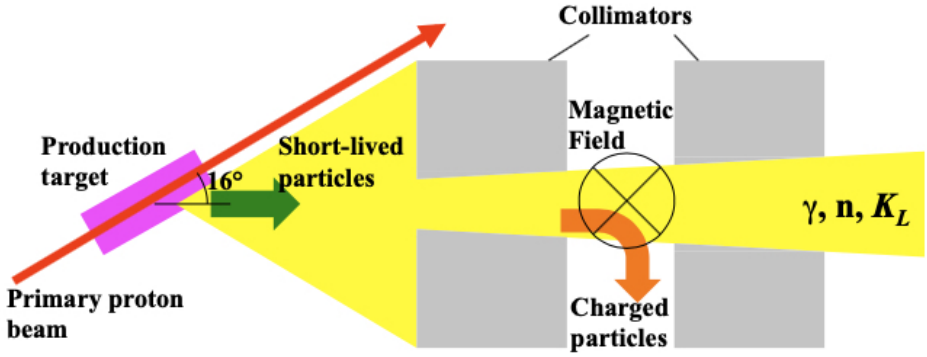

Figure 2.4: Conceptual design to make a neutral beam (quoted from [31]).

Sec. 2.3.3.

2.1.3 Backgrounds

Two types of backgrounds exist in KOTO: one is caused by K_L's, and the other is caused by particles scattered in the beamline components.

2.1.3.1 Backgrounds from K_L Decays

Because the branching fraction of the $K_L \to \pi^0\nu\bar{\nu}$ decay is predicted to be small as 3×10^{-11} in the SM, it is essential to suppress backgrounds from other K_L decays. The main K_L decay modes and their branching fractions are summarized in Table 2.1.

The events from K_L decays which have other particles in addition to two particles in the final state can be suppressed by detecting such extra particles with hermetic veto counters. Figure 2.5 shows a schematic view of the $K_L \to 2\pi^0$ decay. If two photons hit the calorimeter (CSI), and extra photons are detected with the veto counters, the background from $K_L \to 2\pi^0$ decays can be suppressed.

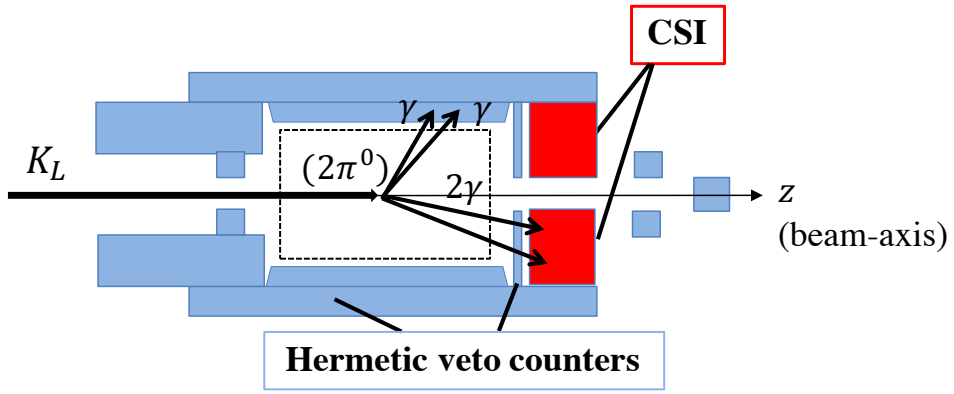

Figure 2.5: Schematic view of the $K_L \to 2\pi^0$ decay. The event can be a background if two extra photons are not detected by veto counters.

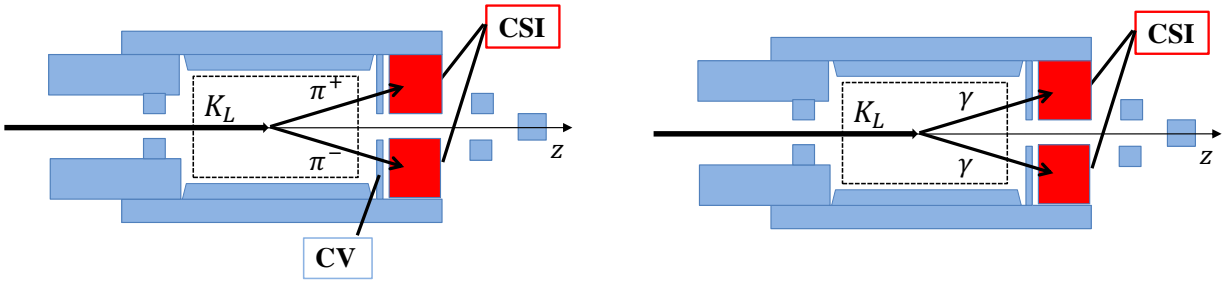

(a) $K_L \to \pi^+\pi^-$ (b) $K_L \to 2\gamma$

Figure 2.6: Schematic views of the $K_L \to \pi^+\pi^-$ (left) and the $K_L \to 2\gamma$ (right) decay.

Figure 2.6 shows a schematic view of the decays, which have no extra particles in the final state. Figure 2.6a shows a schematic view of the $K_L \to \pi^+\pi^-$ decay. The background event from $K_L \to \pi^+\pi^-$ decay can be suppressed by detecting charged-particles with a veto counter to detect charged-particles located in front of the calorimeter (CV). Figure 2.6b shows a schematic view of the $K_L \to 2\gamma$ decay. Because we use a narrow beam, the transverse momentum of K_L's is small. Therefore, the sum of the transverse momentum of two photons from $K_L \to 2\gamma$ decays is also small, and the reconstructed P_t of π^0 is also small. We thus suppress the background events from $K_L \to 2\gamma$ decays by requiring a large reconstructed P_t.

2.1.3.2 Backgrounds from Scattered Particles

Figure 2.7 shows a schematic view of beam particles entering the KOTO detectors. Particles that do not hit beamline components are referred to as "beam-core" particles (Fig. 2.7a), and particles scattered in the beamline components are referred to as "beam-halo" particles (Fig. 2.7b). Some backgrounds are caused by beam-halo particles. We describe such backgrounds below.

Figure 2.8 shows a schematic view of a so-called "hadron-cluster" background. The hadron-cluster background is caused by two hadronic showers in CSI being misidentified as electromagnetic showers originated by photons. This can occur when a beam-halo neutron hits CSI and produces a shower, and another neutron from the hadronic interaction produces an additional shower in CSI. Details of the hadron-cluster background will be described in Sec. 8.3.1.

The "CV-η" background is caused by a beam-halo neutron hitting CV and producing an η meson[*2].

[*2]The nominal mass of η is 547.862 MeV/c^2 [5].

Table 2.1: Main decay modes of K_L and their branching fractions [5].

decay mode	branching fraction
$K_L \to \pi^{\pm} e^{\mp} \nu$	$40.55 \pm 0.11\%$
$K_L \to \pi^{\pm} \mu^{\mp} \nu$	$27.04 \pm 0.07\%$
$K_L \to 3\pi^0$	$19.52 \pm 0.12\%$
$K_L \to \pi^+ \pi^- \pi^0$	$12.54 \pm 0.05\%$
$K_L \to \pi^+ \pi^-$	$(1.967 \pm 0.010) \times 10^{-3}$
$K_L \to \pi^{\pm} e^{\mp} \nu_e \gamma$	$(3.79 \pm 0.06) \times 10^{-3}$
$K_L \to 2\pi^0$	$(8.64 \pm 0.06) \times 10^{-4}$
$K_L \to 2\gamma$	$(5.47 \pm 0.04) \times 10^{-4}$
$K_L \to \pi^0 \pi^{\pm} e^{\mp} \nu_e$	$(5.20 \pm 0.11) \times 10^{-5}$
$K_L \to e^+ e^- \gamma$	$(9.4 \pm 0.4) \times 10^{-6}$

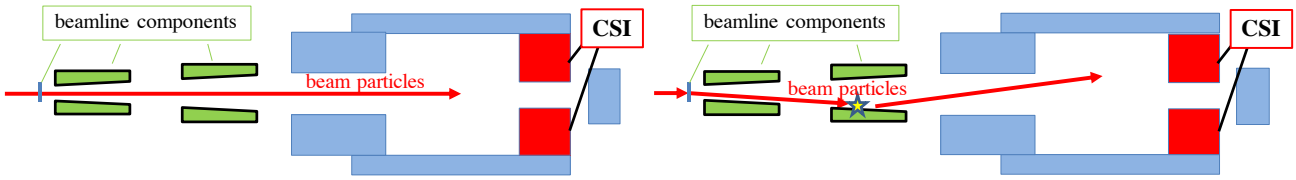

(a) Beam-core particles (b) Beam-halo particles

Figure 2.7: Schematic view of beam-core particles (left) and beam-halo particles (right).

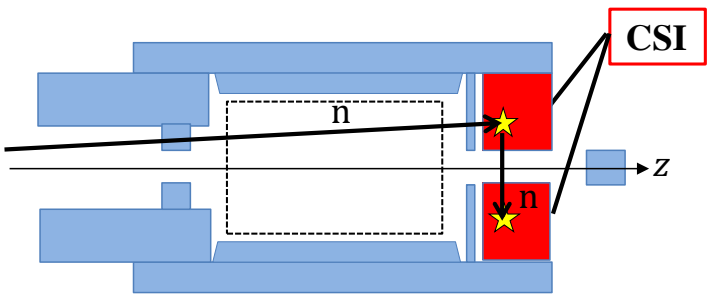

Figure 2.8: Schematic view of the hadron-cluster background.

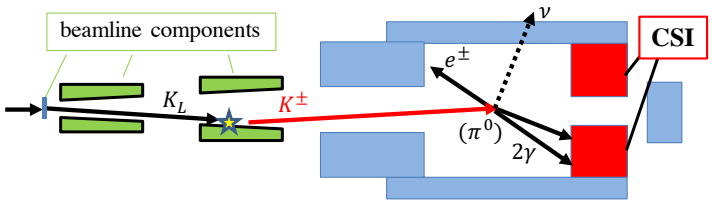

Figure 2.9: Schematic view of the $K^\pm \to \pi^0 e^\pm \nu$ decay background.

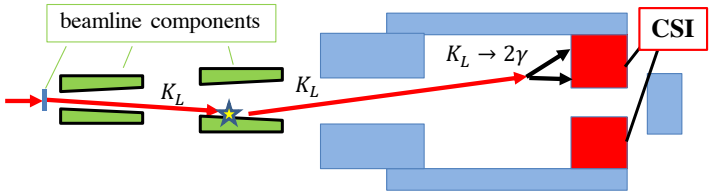

Figure 2.10: Schematic view of the beam-halo $K_L \to 2\gamma$ decay background.

If two photons from η decays[*3] hit CSI and the two photons are reconstructed as a π^0, the event can be a background. Details of the CV-η background will be described in Sec. 8.3.2.

The "upstream-π^0" background is caused by a beam-halo neutron hitting a veto counter located upstream part of the KOTO detector and producing a π^0. If two photons from the π^0 hit CSI and the energy of photon is mismeasured, the event can be a background. Details of the upstream-π^0 background will be described in Sec. 8.3.3.

The $K^\pm$ decays can be a background source in KOTO. A $K^\pm$ generated in the collision of a K_L with the downstream collimator can enter the KOTO detector. Figure 2.9 shows a schematic view of the $K^\pm \to \pi^0 e^\pm \nu$ decay. Among $K^\pm$ decays, $K^\pm \to \pi^0 e^\pm \nu$ is the most likely source of background because the kinematics of the π^0 is similar to the one from the $K_L \to \pi^0 \nu\overline{\nu}$ decay, and the low energy $e^\pm$ emitted in the backward direction has a higher probability to be missed. Details of $K^\pm$ decays background will be described in Sec. 8.4.

Figure 2.10 shows a schematic view of the beam-halo K_L decaying to two photons. The beam-halo $K_L \to 2\gamma$ can be a background source because the K_L itself has a finite P_t and the decay occurring off the beam axis makes the reconstructed P_t large. Details of the beam-halo $K_L \to 2\gamma$ background will be described in Sec. 8.5.

2.1.4 Sensitivity for $K_L \to \pi^0 \nu\overline{\nu}$

The sensitivity for the $K_L \to \pi^0 \nu\overline{\nu}$ decay search is expressed by single event sensitivity (SES), defined as

$$\mathrm{SES} = \frac{1}{\mu}\,\mathcal{B}(K_L \to \pi^0 \nu\overline{\nu}), \tag{2.4}$$

where μ is the expected number of $K_L \to \pi^0 \nu\overline{\nu}$ events, and $\mathcal{B}(K_L \to \pi^0 \nu\overline{\nu})$ is the actual branching fraction of $K_L \to \pi^0 \nu\overline{\nu}$. If the $\mathcal{B}(K_L \to \pi^0 \nu\overline{\nu})$ is equal to SES, we expect to observe one signal event. The μ is calculated as

$$\mu = A_{\mathrm{sig}}\, N_{K_L}\, \mathcal{B}(K_L \to \pi^0 \nu\overline{\nu}), \tag{2.5}$$

where A_{sig} is the product of the K_L decay probability and signal acceptance of the $K_L \to \pi^0 \nu\overline{\nu}$ decay and N_{K_L} is the number of K_L's entering the KOTO detector (K_L yield). The signal acceptance is defined as the survival probability for the $K_L \to \pi^0 \nu\overline{\nu}$ events after imposing the $K_L \to \pi^0 \nu\overline{\nu}$ selection

[*3] The branching fraction of $\eta \to 2\gamma$ is 39.41% [5]

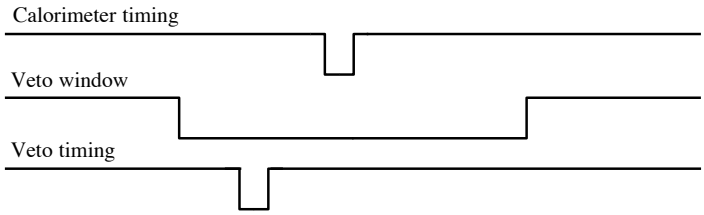

Figure 2.11: Schematic view of a veto window and timings measured with the calorimeter and veto counters.

criteria. It was evaluated using GEANT4-based [32, 33, 34] Monte Carlo (MC) simulations. The N_{K_L} was estimated using $K_L \to 2\pi^0$ decays. We reconstructed $K_L \to 2\pi^0$ decays from events containing four photons in the calorimeter. We calculated the N_{K_L} as

$$N_{K_L} = \frac{N_{\text{norm}}}{A_{\text{norm}}\ \mathcal{B}(K_L \to 2\pi^0)}, \tag{2.6}$$

where N_{norm} is the number of reconstructed $K_L \to 2\pi^0$ events, A_{norm} is the acceptance for $K_L \to 2\pi^0$, and $\mathcal{B}(K_L \to 2\pi^0)$ is the branching fraction of $K_L \to 2\pi^0$ [5]. The acceptance for $K_L \to 2\pi^0$ was also evaluated using MC simulations and defined as the survival probability for the $K_L \to 2\pi^0$ events after imposing the $K_L \to 2\pi^0$ selection criteria. Using equations 2.4, 2.5, and 2.6, SES is

$$\text{SES} = \frac{1}{A_{\text{sig}}\, N_{K_L}}, \tag{2.7}$$

$$= \frac{1}{A_{\text{sig}}} \frac{A_{\text{norm}}\ \mathcal{B}(K_L \to 2\pi^0)}{N_{\text{norm}}}. \tag{2.8}$$

2.1.5 Accidental Loss

In this section, the mechanism of losing the signal events due to veto counters is explained.

For the $K_L \to \pi^0\nu\overline{\nu}$ search in KOTO, it is essential to detect extra particles with hermetic veto counters. Figure 2.11 shows the schematic view of timings measured with the calorimeter and veto counters. Based on the timing measured with the calorimeter, we open a timing window (veto window) for each veto counter according to the characteristics of each counter. We veto the event when we observe a hit in veto counters within the veto timing window.

In this veto scheme, signal events are lost in the following mechanism. The veto counters are continuously hit by particles from K_L decays and neutral particles in the beam (accidental hit). If such a hit occurs within the veto timing window of a $K_L \to \pi^0\nu\overline{\nu}$ decay event, the $K_L \to \pi^0\nu\overline{\nu}$ event is lost (accidental loss). The probability of the accidental loss L is described as

$$L = 1 - P(k = 0; \lambda = RT) \tag{2.9}$$

$$= 1 - \exp(-RT), \tag{2.10}$$

where $P(k;\lambda)$ is the Poisson probability function for observing k events when the expected number of events is λ, R is the rate of the accidental hit, and T is the width of the veto window in veto counters. This equation means that the accidental loss is large if the accidental hit rate is high or the veto window is wide.

2.2 Lessons from Previous $K_L \to \pi^0\nu\overline{\nu}$ Search in KOTO

The current best upper limit on the branching fraction of $K_L \to \pi^0\nu\overline{\nu}$ search was set by the previous $K_L \to \pi^0\nu\overline{\nu}$ search in KOTO with the data taken in 2015, as introduced in Sec. 1.3. In the following sections, we briefly review the results of the 2015 data analysis and describe lessons from the results.

Table 2.2: Summary of background estimation in the 2015 analysis [26].

source		Number of events
K_L decay	$K_L \to \pi^+\pi^-\pi^0$	0.05 ± 0.02
	$K_L \to 2\pi^0$	0.02 ± 0.02
	other K_L decays	0.03 ± 0.01
neutron-induced	hadron-cluster	0.24 ± 0.17
	upstream-π^0	0.04 ± 0.03
	CV-η	0.04 ± 0.02
total		0.42 ± 0.18

2.2.1 Signal Acceptance

In the 2015 data analysis, we lost 75% of signal events due to the accidental hits in veto counters [35]. In the 2016–2018 data analysis, it is essential to reduce the accidental loss. This is because the primary beam intensity in 2016–2018 was higher than in 2015, as will be described in Sec. 3.1, and the detector counting rate increased, which would cause a higher probability of the accidental loss.

2.2.2 Backgrounds

In the 2015 data analysis, the total number of background events was estimated to be 0.42 ± 0.18, as shown in Table 2.2. Among the background sources in the 2015 analysis, the hadron-cluster background had the largest background contribution of 0.24 ± 0.17 events. In addition, selection criteria to suppress the hadron-cluster background reduced the signal acceptance. In the 2016–2018 analysis, it is essential to understand and reduce the hadron-cluster background events with a small signal acceptance loss.

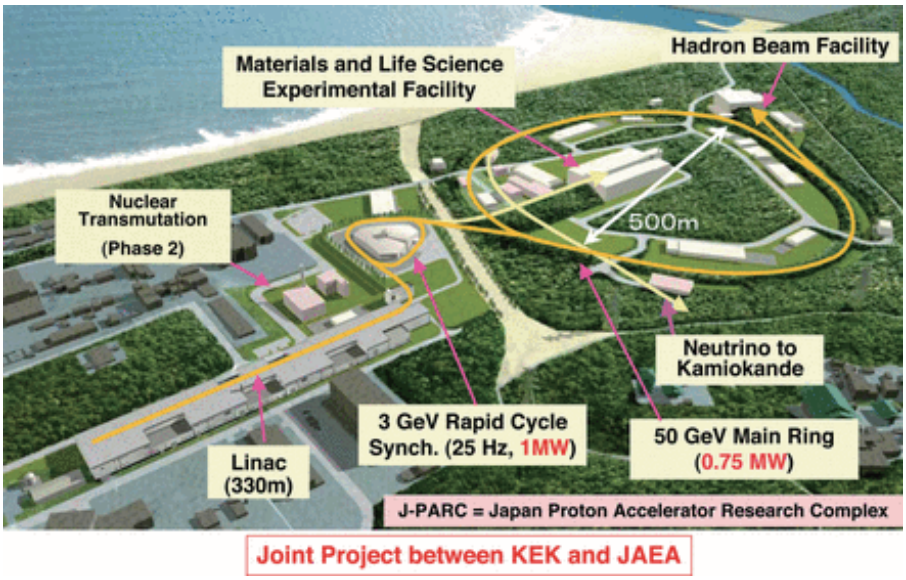

Figure 2.12: View of J-PARC (quoted from Ref. [27]).

2.3 Experimental Facility and Beamline

2.3.1 J-PARC

The KOTO experiment is conducted at the Japan Proton Accelerator Research Complex (J-PARC) [27], in Tokai Village, Ibaraki Prefecture, Japan. A 30 GeV proton beam is made with three accelerators in J-PARC: the Linac [36, 37], the 3 GeV synchrotron (a rapid-cycle synchrotron, hereafter RCS [38]), and the 30 GeV synchrotron (a main ring, hereafter MR [28]), as shown in Fig. 2.12. Negative hydrogen ions (H^-) from an ion source are accelerated up to 400 MeV in the Linac. The accelerated ions are converted into protons with a charge-exchange process, and they are injected into the RCS accelerator. In the RCS accelerator, two proton beam bunches are accelerated up to 3 GeV. The bunches are transported from RCS to MR four times, and eight bunches are accelerated up to 30 GeV as a spill. With a slow extraction system, the 30 GeV debunched proton beam is extracted to the Hadron Experimental Facility.

The beam power is calculated as

$$\text{Beam power} = E_{\text{proton}}\, F_{\text{proton}}, \tag{2.11}$$

where E_{proton} is the energy of extracted proton beam of 30 GeV, and F_{proton} is the flux of the extracted protons. The F_{proton} is calculated as

$$F_{\text{proton}} = N_{\text{spill}}^{\text{proton}} / s_{\text{spill}}, \tag{2.12}$$

where $N_{\text{spill}}^{\text{proton}}$ is the number of extracted protons in a spill, and s_{spill} is the proton beam spill cycle. In 2016–2018, $N_{\text{spill}}^{\text{proton}}$ was $(4\text{–}5)\times10^{13}$, s_{spill} was 5.2–5.5 sec, and the duration of the beam extraction was 2 sec. More detailed beam power in 2016–2018 will be described in Sec. 3.1.

The primary proton beam from the MR had a spiky time structure in spills during the beam extraction. The structure was caused by a ripple noise in the power supplies for MR. In 2016-2018, the structure made the instantaneous rate 1.5–2.0 times higher than the mean rate.

2.3.2 Hadron Experimental Facility

The KOTO experiment area is located in the Hadron Experimental Facility in J-PARC. Figure 2.13 shows the layout of the Hadron Experimental Facility. A 30-GeV proton beam transported through

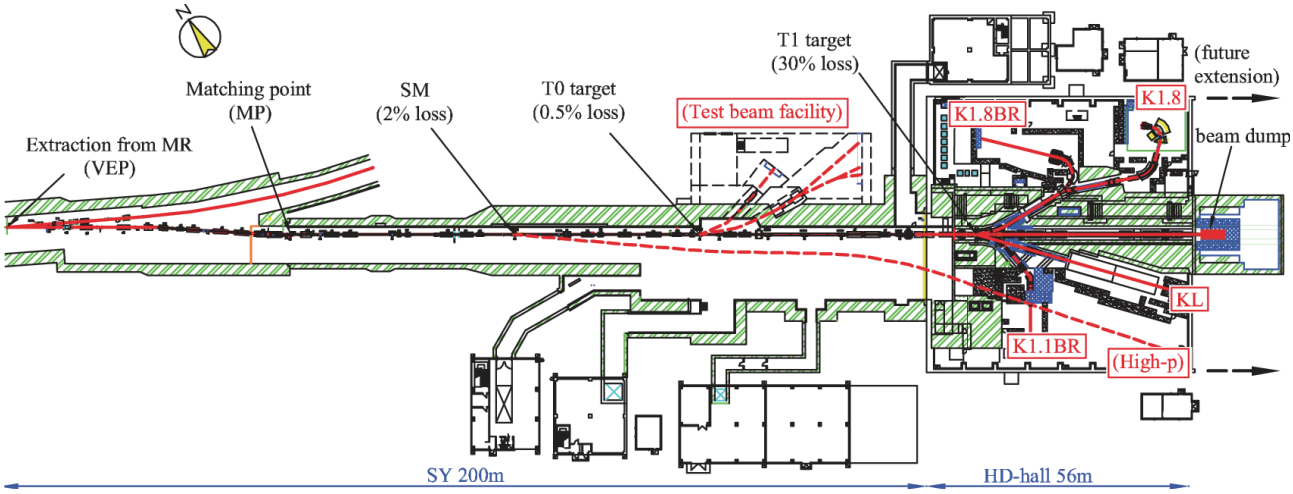

Figure 2.13: Layout of the Hadron Experimental Facility including beam switchyard region (quoted from Ref. [39]).

the beam switchyard (SY) is incident on a gold production target (see Fig. 2.14) in the Hadron Experimental Facility. Two 66-mm-long gold blocks are bonded on a water-cooled copper block. One of them is used as a production target, and the second gold block is a spare. The horizontal and vertical dimensions of the target are 15 mm and 11 mm, respectively. The secondary particles produced in the target are transported to multiple experiments in the Hadron Experimental Facility.

2.3.3 KL Beamline

Figure 2.15 shows the schematic view of the KL beamline [41]. The beamline is set 16° away from the primary proton beam direction. The 20-m-long beamline to eliminate short-lived particles consists of vacuum pipes, a 7-cm-thick lead absorber to reduce photons, two collimators to make a narrow beam with sharp edges, a beam plug to stop the beam if necessary, and a sweeping magnet to remove charged particles. To eliminate charged-particles, the magnetic field of 1.2 T is applied with the sweeping magnet which is located between the two collimators. The peak K_L momentum is 1.4 GeV/c [42]. The K_L flux was measured to be 2.1×10^{-7} K_L's per proton on target (POT) [35].

2.4 KOTO Detector

The cross-sectional view of the KOTO detector is shown in Fig. 2.16. The z-axis lies along the beam direction, and the origin of the z is the upstream edge of the KOTO detector. The x (horizontal) and y (vertical) axes are defined using the right-handed coordinate system. We measure the photon energy and timing with an electromagnetic calorimeter. To ensure that there are no other detectable particles, the decay volume is surrounded by hermetic veto counters. The decay volume should be kept in a high vacuum degree of $\mathcal{O}(10^{-5})$ Pa to suppress π^0's generated by beam neutrons interacting with residual gas. The detector regions should also be kept in a vacuum to suppress backgrounds from particles absorbing in the vacuum vessel. However, it is difficult to keep in a high vacuum degree of $\mathcal{O}(10^{-5})$ Pa in the decay volume due to the outgas from detector components flowing into the decay volume. The decay volume and the detector region are thus separated by thin films (*Membranes*). The detector region is kept in a vacuum of 0.1 Pa. In the following sections, we briefly explain detector components.

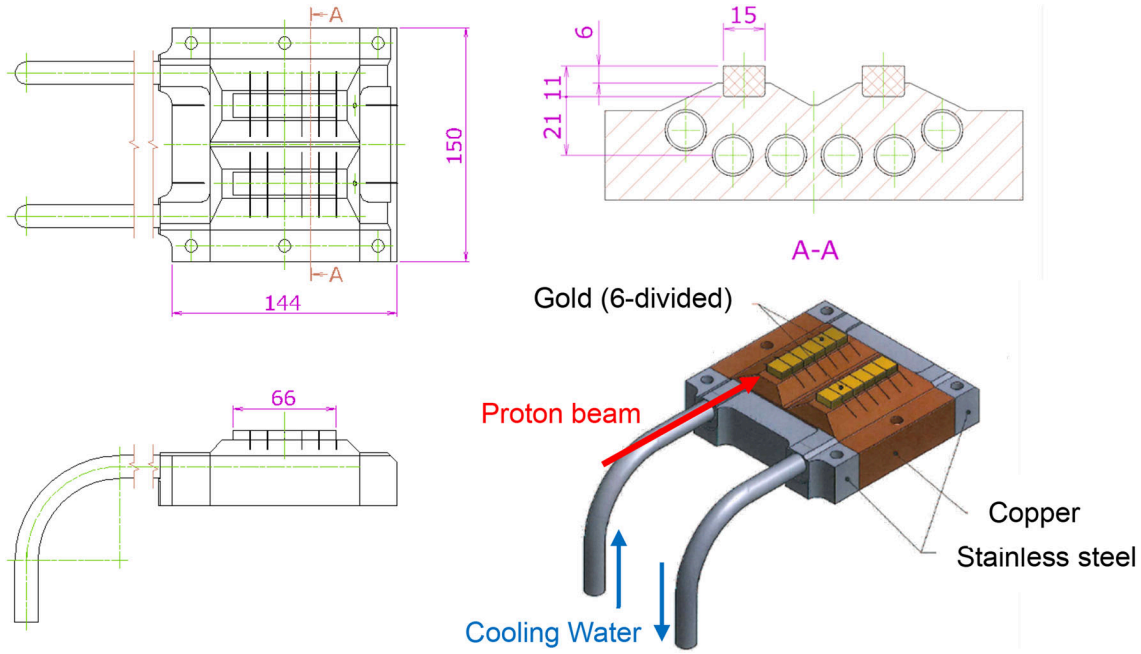

Figure 2.14: Drawings of the T1 production target (quoted from Ref. [40]). One block is used as a production target, and the other is a spare.

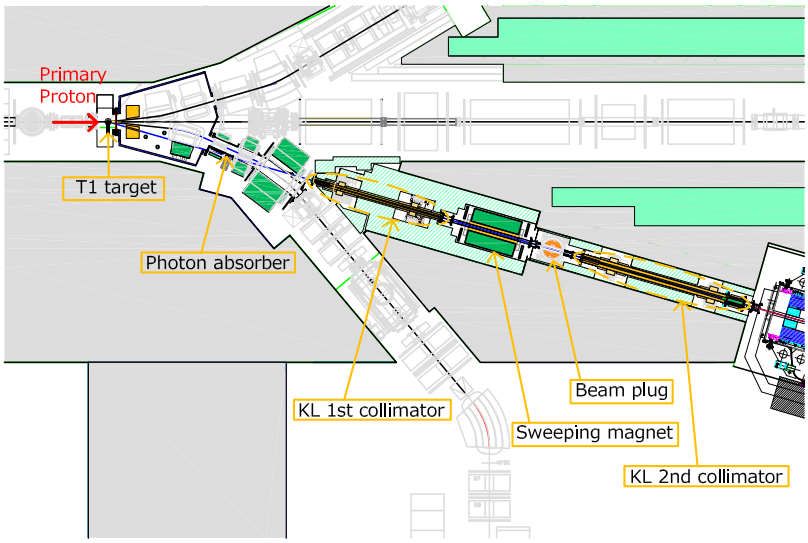

Figure 2.15: Schematic view of the KL beamline. A sweeping magnet and a beam plug are located between two collimators.

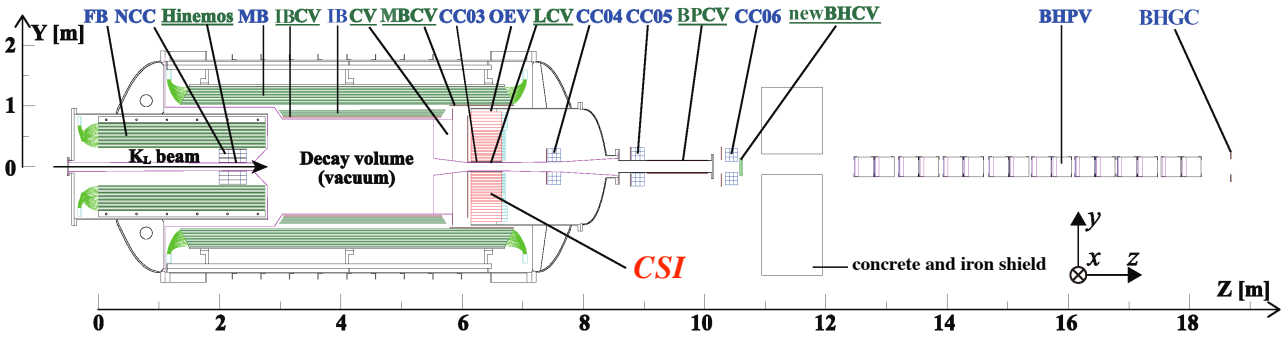

Figure 2.16: Cross-sectional view of the KOTO detector. The beam enters from the left. Detector components with their abbreviated names written in blue (in green and underlined) are photon (charged-particle) veto counters.

2.4.1 Electromagnetic Calorimeter (CSI)

The electromagnetic calorimeter (CSI) is used to measure the energy and timing of photons. Figure 2.17 shows the schematic view and picture of CSI. The CSI is a 2-m-diameter cylindrical electromagnetic calorimeter centered on the beam axis. The CSI has a 15×15 cm beam hole to let the beam-core particles pass through.

The CSI is composed of 2716 undoped-CsI crystals that have a length of 50 cm and a cross-section of 2.5×2.5 cm (5×5 cm) inside (outside) the central 1.2×1.2 m region. The 2.5 cm-square and 5 cm-square crystals are referred to as small and large crystals, respectively. There are 2240 small and 476 large crystals in CSI. The radiation length (X_0) of the CsI is 1.85 cm [5], and the crystal length corresponds to $27X_0$. The Molière radius of the CsI is 3.57 cm [5]. An electromagnetic shower spread out to multiple crystals. In the analysis, we grouped such crystals into a cluster.

The scintillation lights from each crystal are detected with a photomultiplier tube (PMT) attached on the downstream end of each crystal. To couple each crystal and PMT optically, a cured silicone elastomer disk is placed between them. The scintillation light from the CsI crystal contains two components: one is a fast component with decay times of 10 ns and 36 ns, and the maximum peak at a wavelength of 315 nm. The other is a slow component with a decay time of 1 μs and the maximum light output at 480 nm [43]. To cut the slow component of the scintillation light, a 1 mm-thick UV transmitting filter is glued on each PMT window. Details of CSI are available in [44].

2.4.2 Veto Counters in Upstream Section

Veto counters located upstream section of the KOTO detector are used to detect particles from K_L's decaying not only in the decay volume but also in the upstream of the KOTO detector.

2.4.2.1 Front Barrel (FB)

The Front Barrel (FB) is a photon veto counter located most upstream of the KOTO detector. The FB is made of a lead-scintillator sandwich. The FB is composed of 16 modules with a length of 2.75 m along the z-axis, forming a cylinder with a 1.5-m-outer-diameter. Each module consists of 27 inner and 32 outer layers. Each layer consists of 1.5-mm-thick lead and 5-mm-thick plastic scintillator sheets. The total radiation length along the radial direction is $16.5X_0$. Wavelength-shifting (WLS) fibers are embedded in the scintillator sheets to absorb scintillation lights in the WLS fibers, and the emitted light is transferred to PMT's on the upstream end of the module. The scintillation light from the inner and outer layers are read separately. The number of total channels is 32. Details of FB are available in [46].

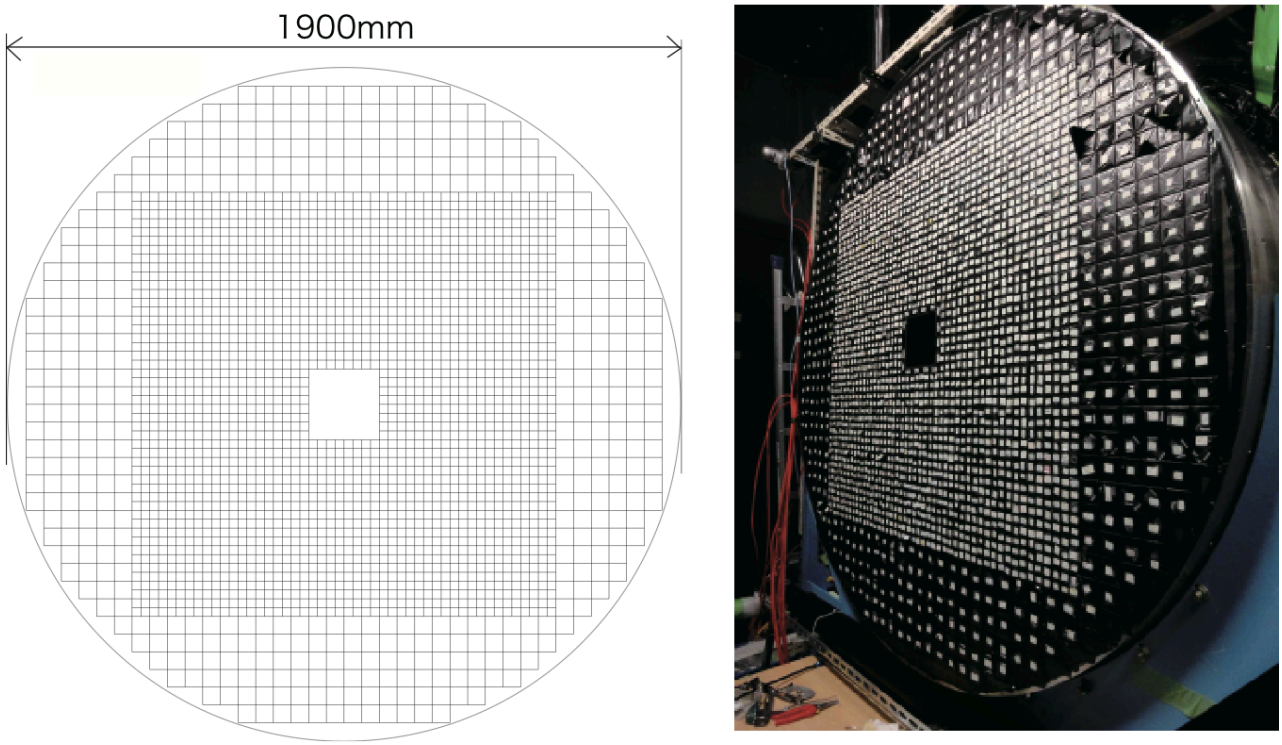

Figure 2.17: Schematic front view (left) and picture (right) of the CsI calorimeter (quoted from Ref. [45]).

2.4.2.2 Neutron Collar Counter (NCC) and HINEMOS

The Neutron Collar Counter (NCC) is a photon veto counter located inside FB. In addition to vetoing photons from the upstream and decay volume, NCC is also used to shield photons that come from the upstream hitting CSI. Figure 2.18 shows a schematic view of NCC. The NCC is composed of 48 inner modules and 8 outer modules. Each inner module consists of three individual undoped-CsI crystals, which are optically separated and named Front, Middle, and Rear. Each crystal has four dedicated WLS fibers to read out its output. In the Front, Middle, and Rear module, four fibers are optically connected to only each separated region. In addition, there are 28 fibers to read out all three crystals (referred to as Common readout). The Common readout is used for the $K_L \to \pi^0\nu\overline{\nu}$ analysis[*4]. For outer modules, the signal is detected by a PMT attached to the crystal.

The NCC has a beam-hole made with a 2-mm-thick carbon fiber reinforced plastic (CFRP) pipe. To detect charged-particles before being absorbed in the CFRP pipe, we installed a charged-particle veto counter, named HINEMOS, on the inner surface of the CFRP pipe. The HINEMOS consists of plastic scintillator sheets and WLS fibers. The events with π^0's generated in NCC or the CFRP pipe are vetoed by detecting associated particles with HINEMOS.

2.4.3 Veto Counters in Middle Section

Veto counters located in the middle section of the KOTO detector are used to detect particles from K_L's decaying in the decay volume.

[*4]The three individual readouts are used for another study on the halo-neutron flux measurement.

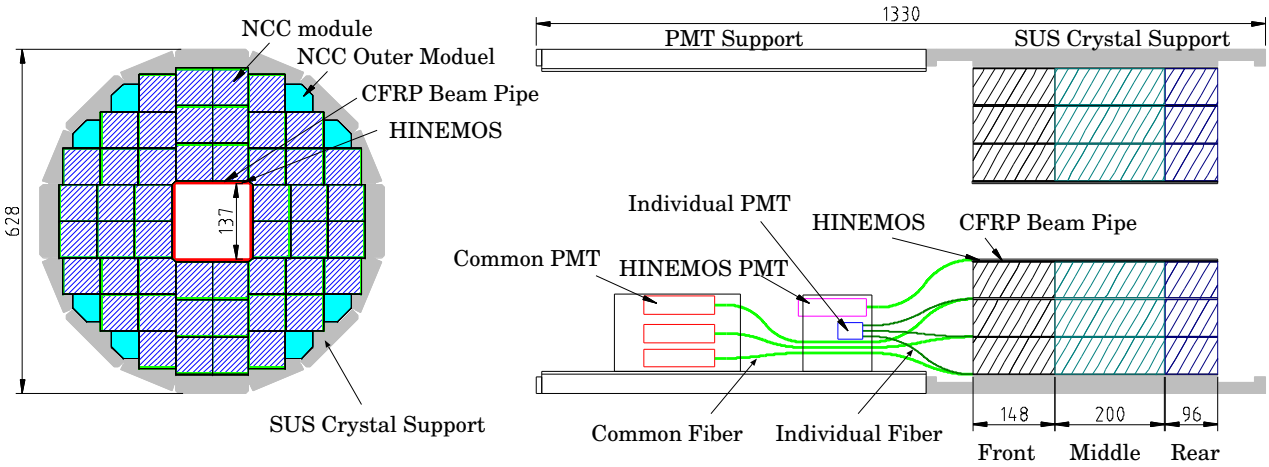

Figure 2.18: Schematic front (left) and side (right) views of NCC (quoted from Ref. [31]).

2.4.3.1 Main Barrel (MB)

The Main Barrel (MB) is a photon veto counter located in the middle section of the KOTO detector. Figure 2.19 shows the cross-sectional view of MB. The MB is composed of 32 modules with a length of 5.5 m along the z-axis, forming a 3.5-m-diameter cylinder. Each module consists of 15 inner and 30 outer layers. Each inner (outer) layer consists of a 1-mm-thick (2-mm-thick) lead and a 5-mm-thick plastic scintillator sheet. The total radiation length along the radial direction is $14.0X_0$. The emitted scintillation light is absorbed in the WLS fibers embedded in the scintillator sheets and transferred to PMT's on the upstream and downstream ends of the module. The scintillation light from the inner and outer layers are readout separately. The number of total readout channels is 128. Details of MB are available in [46].

2.4.3.2 Inner Barrel (IB)

The Inner Barrel (IB) is a photon veto counter located inside MB. This counter was installed in 2016 to suppress $K_L \to 2\pi^0$ backgrounds by a factor of three by reducing the probability of punch-through of photons and sampling effect [47]. Figure 2.20 shows the picture of IB just before installation. Figure 2.21 shows the cross-sectional view of IB. The IB is a lead-scintillator sandwich detector composed of 32 modules with a length of 2.8 m along the z-axis, forming a 1.5m-inner-diameter cylinder. Each module consists of 25 layers of 1-mm-thick lead and 5-mm-thick plastic scintillator sheets. The total radiation length along the radial direction is $5.0X_0$. The emitted scintillation light is absorbed in the WLS fibers embedded in the scintillator sheets and transferred to PMT's on the upstream and downstream end of the module. The number of total readout channels is 64. Details of IB are available in [47].

2.4.3.3 Inner Barrel Charged Veto (IBCV) and Main Barrel Charged Veto (MBCV)

The Inner Barrel Charged Veto (IBCV) and Main Barrel Charged Veto (MBCV) are charged-particle veto counters attached on the inner surfaces of IB and MB, respectively. These counters were installed in 2016. Figure 2.22 shows the side view of IB, MB, IBCV and MBCV. The IBCV covers all the inner surfaces of IB, and MBCV covers from the downstream end of IB to the downstream end of MB.

The IBCV detects charged particles from K_L's decaying inside the decay volume, and works as the first sampling layer of IB. The IBCV consists of 32 plastic scintillator sheets with a thickness of 5 mm. With WLS fibers embedded in the scintillator sheets, the emitted scintillation light is transferred to the upstream and downstream end of the module. From the end of the module, the scintillation

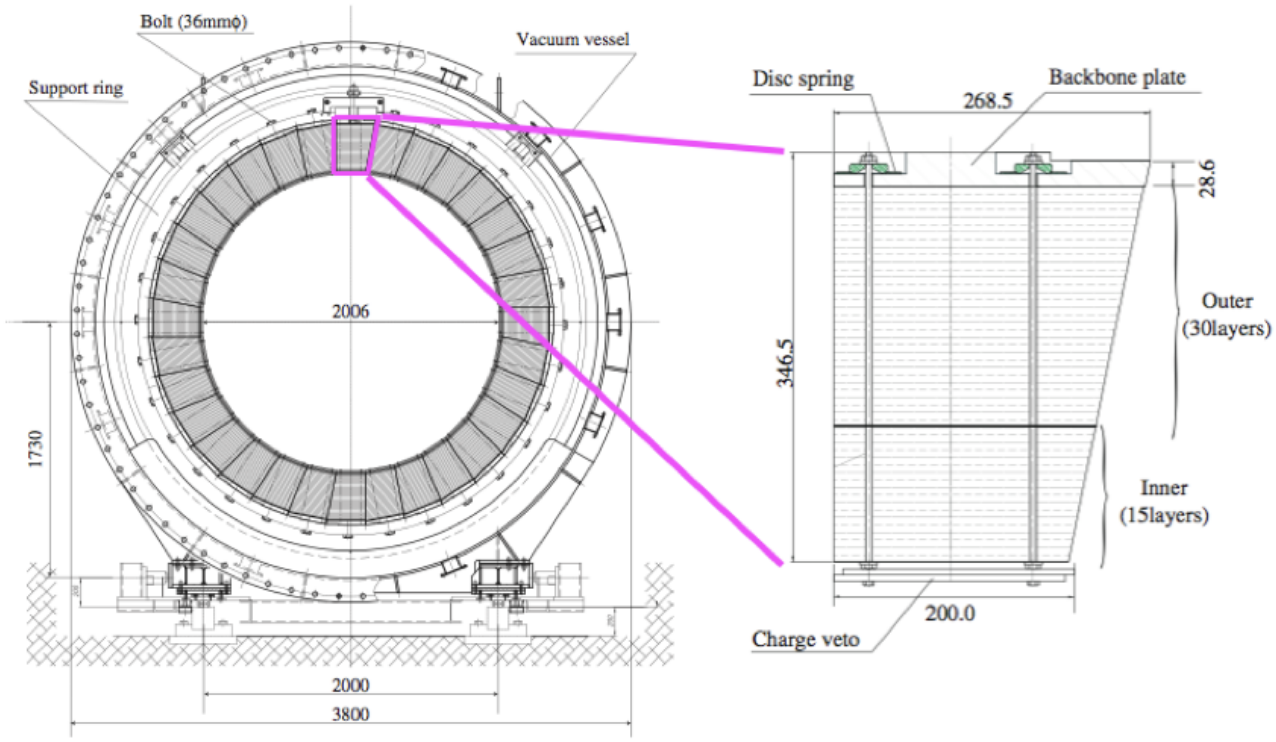

Figure 2.19: Cross-sectional views of MB and the vacuum vessel (left) and a MB module (right). The figures are quoted from Ref. [46]. Scales in the figures are in units of mm.

lights are transferred to PMT's with Polymer Light Guides (PLG's) [*5]. The number of total readout channels is 64.

The MBCV detects charged particles from K_L's decaying inside the decay volume, and works as the first sampling layer of MB. The MBCV also detects associated particles generated by photons entering the outer edge region of CSI. The MBCV has 32 modules consisting of two 5-mm-thick plastic scintillator layers. With WLS fibers embedded in the scintillator sheets, the emitted scintillation light is transferred to the downstream end of the module. From the end of the module, the scintillation light is transferred through PLG's to PMT's. We read out the scintillation light with PMT's from both two neighboring modules of MBCV. The number of total readout channels is 16.

2.4.3.4 Charged Veto (CV)

The Charged Veto (CV) is a charged-particle veto counter located in front of CSI to detect charged particles entering CSI. Figure 2.23 shows the schematic view of CV. The CV consists of two layers: Front CV (FCV) and Rear CV (RCV). The FCV (RCV) layer is located 30 cm (5 cm) upstream of the CSI surface. The CV is made of plastic scintillator strips. Each strip consists of 3-mm-thick and 69-mm-wide plastic scintillator. With WLS fibers embedded in the scintillator sheets, the scintillation light is transferred to multi-pixel photon counters (MPPC's) attached on both ends of the fibers. Details of CV are available in [48].

2.4.3.5 Outer Edge Veto (OEV)

The Outer Edge Veto (OEV) is a photon veto counter located on the outer edge of CSI. The shape of OEV varied, as shown in Fig. 2.24, to fill the gap between CSI crystals and the cylinder-shaped structure which holds CSI crystals. The OEV consists of 44 modules of lead-scintillator sandwich

[*5] Polymer Light Guide is a soft acrylic resin tube

Figure 2.20: Photograph of the IB (forward) just before its insertion to MB (backward). The figures are quoted from Ref. [47].

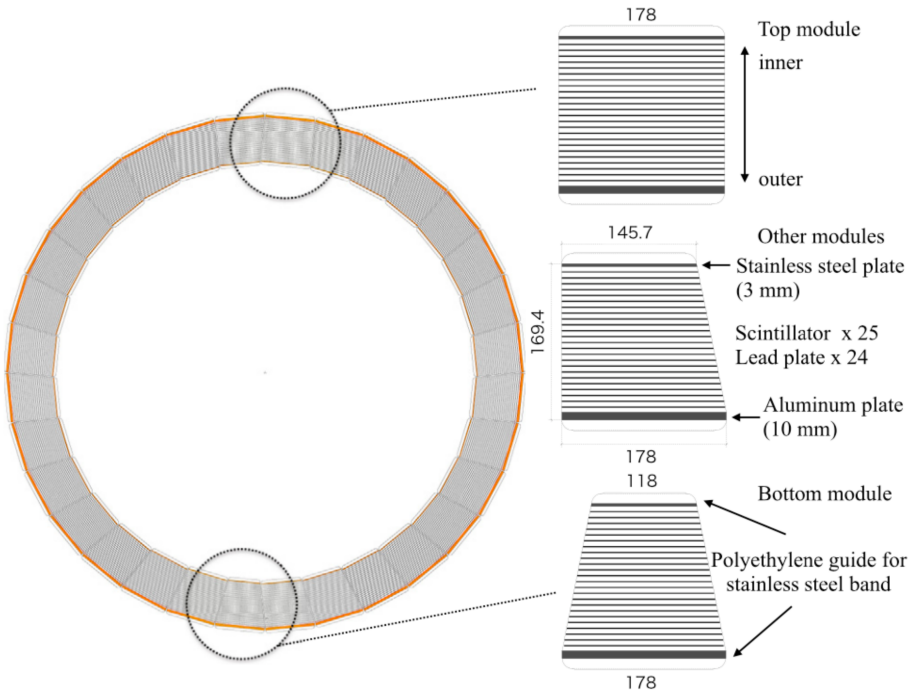

Figure 2.21: Cross-sectional views of IB (left) and a IB module (right). The figures are quoted from Ref. [47]. Scales in the figures are in units of mm.

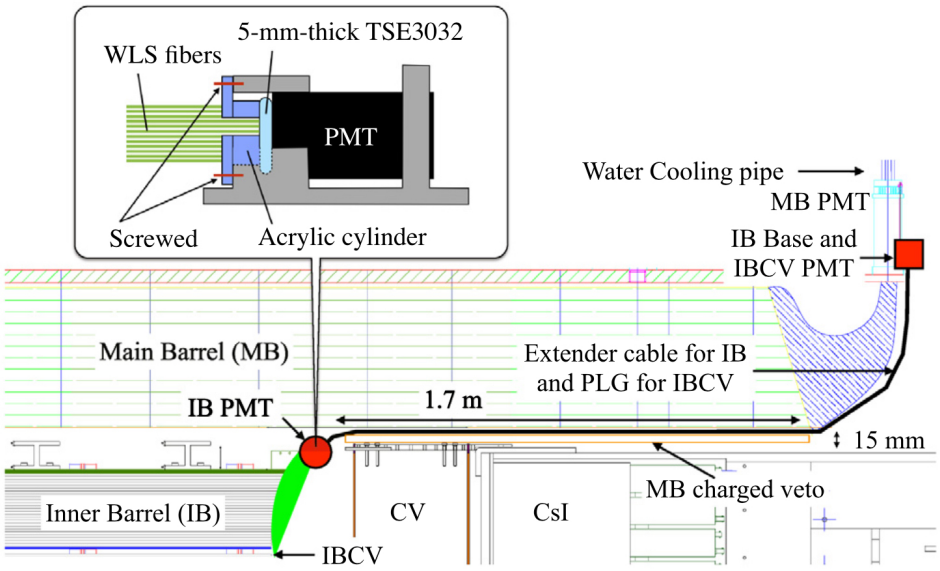

Figure 2.22: Schematic side view of IB, MB, IBCV, and MBCV. The figures are quoted from Ref. [47].

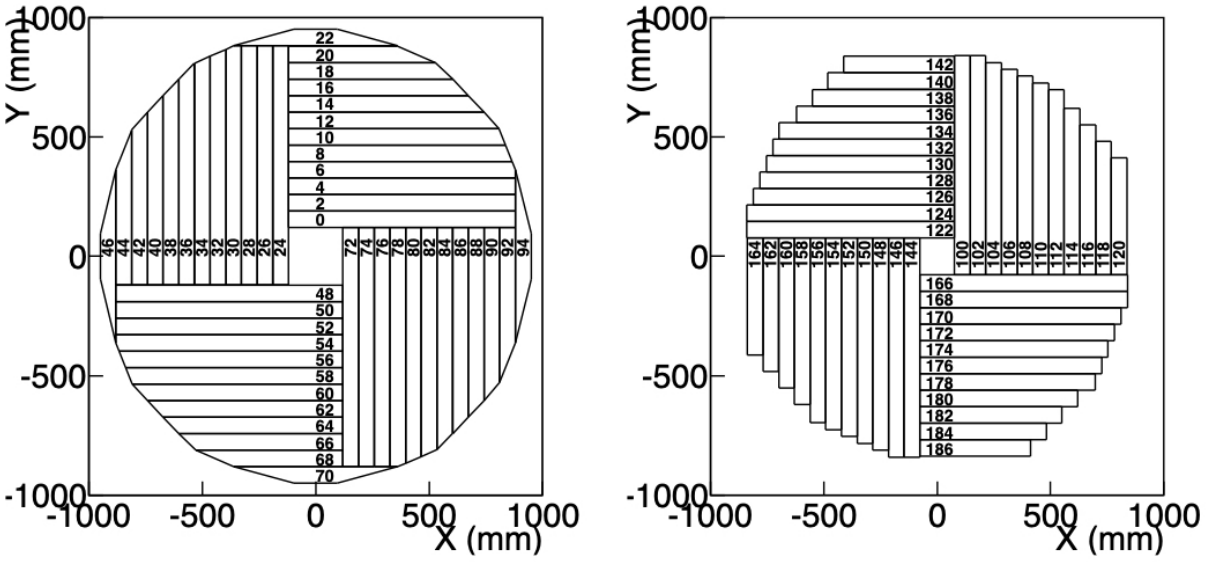

Figure 2.23: Schematic view of CV modules viewed from downstream (quoted from Ref. [49]). Left: Front CV. Right: Rear CV.

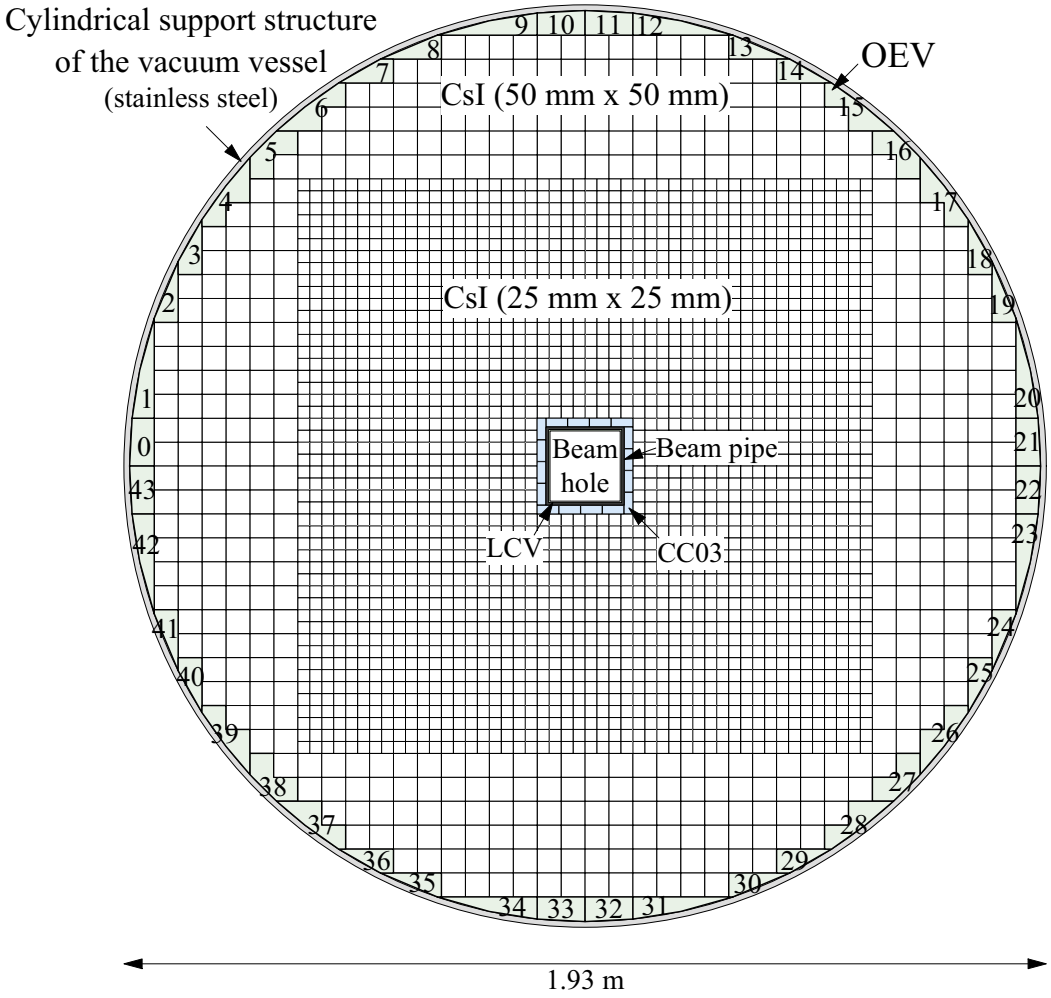

Figure 2.24: CsI calorimeter and veto counters covering inside and outside the calorimeter (quoted from Ref. [50]).

counters. With WLS fibers embedded in the scintillator sheets, the scintillation light is transferred to PMT's. Details of OEV are available in [50].

2.4.3.6 Collar Counter 3 (CC03) and Liner Charged Veto (LCV)

The Collar Counter 3 (CC03) is a photon veto counter located inside CSI. Figure 2.25 shows a closeup view of the CSI beam hole. The CC03 is used to veto events containing photons that come from K_L's decaying near CSI. The CC03 is composed of 16 undoped-CsI crystals that have a length of 500 mm and a cross-section of 45.5×18 mm^2. The scintillation light is detected by two PMT's for each module, and the total number of readout channels is 32.

To support CSI and CC03, the CSI beam-hole is made with a 4.5-mm-thick CFRP pipe. To detect charged particles before being absorbed in the CFRP pipe, we installed a charged-particle veto counter, named Liner Charged Veto (LCV), on the inner surface of the CFRP pipe. The LCV is made of four 3-mm-thick plastic scintillators. With WLS fibers embedded in the scintillator sheets, the scintillation light is transferred to PMT's.

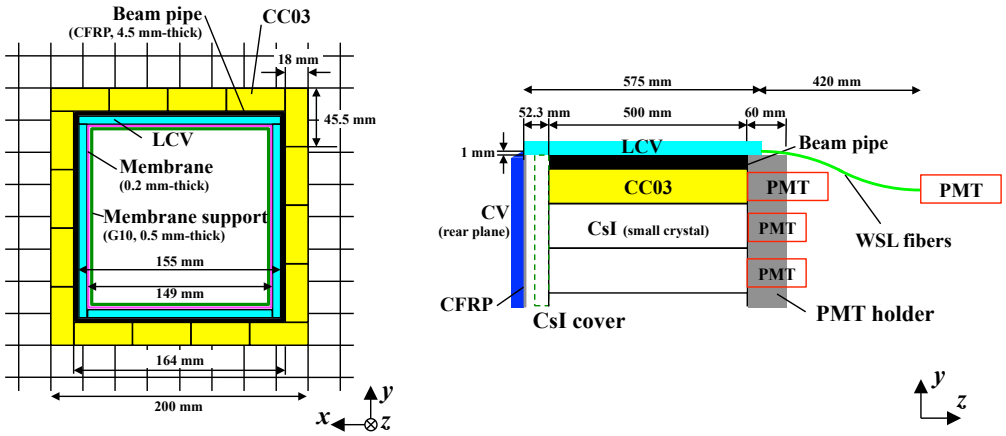

Figure 2.25: Closeup front (left) and side (right) views of the beam-hole of CSI (quoted from Ref. [31]).

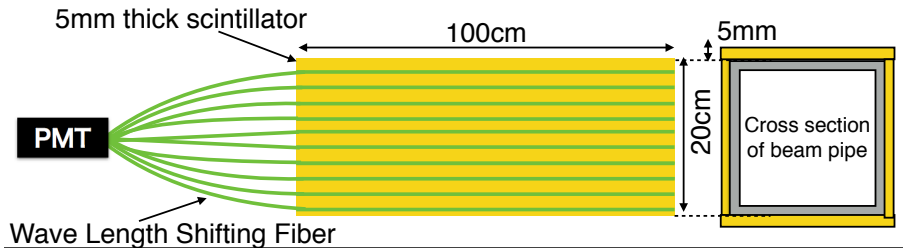

Figure 2.26: Schematic view of BPCV (quoted from Ref. [51]). The gray square in the right figure (cross-sectional view) represents the downstream beam pipe.

2.4.4 Veto Counters in Downstream Section

Veto counters located downstream of CSI are used to detect particles passing through the CSI beam hole.

2.4.4.1 Collar Counter 4, 5, and 6 (CC04, CC05, and CC06)

The Collar Counters 4 (CC04), 5 (CC05), and 6 (CC06) are photon and charged-particle veto counters located downstream of CSI. Each counter consists of undoped-CsI crystals and plastic scintillators. The plastic scintillators are located just in front of the CsI crystals. The scintillation light of each module is detected by a PMT attached on each module.

2.4.4.2 Beam Pipe Charged Veto (BPCV)

The Beam Pipe Charged Veto (BPCV) is a charged-particle veto counter located between CC05 and CC06 surrounding a 5-mm-thick aluminum vacuum pipe. This counter detects secondary-charged-particles produced by charged-particles from K_L decays interacting with the beam pipe. Figure 2.26 shows a schematic view of BPCV. The BPCV is composed of four plastic scintillator sheets of a 5-mm thickness. With WLS fibers embedded in the scintillator sheets, the scintillation light is transferred to PMT's in the upstream end of the modules.

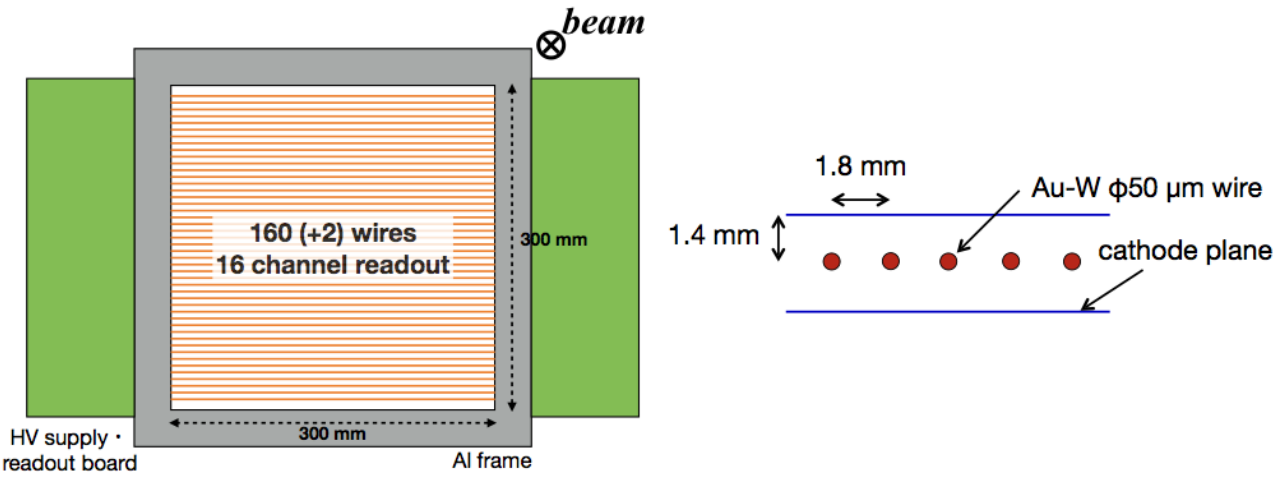

Figure 2.27: Schematic view of a newBHCV module (left) and its cell structure (quoted from Ref. [35]).

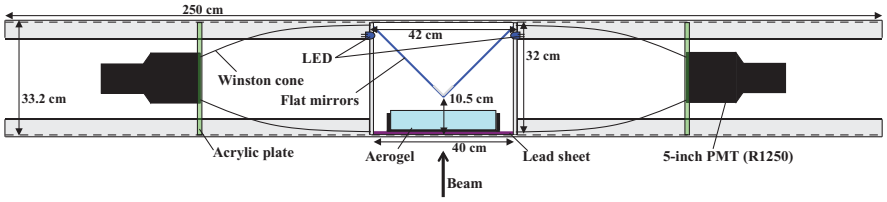

Figure 2.28: Schematic view of a BHPV module (quoted from Ref. [52]).

2.4.4.3 Beam Hole Charged Veto (newBHCV)

The Beam Hole Charged Veto (newBHCV[*6]) is a charged-particle veto counter made of wire chambers. This counter detects in-beam charged particles escaping through the CSI beam-hole. Figure 2.27 shows the structure of a newBHCV chamber. Three chambers are in beam in tandem. The anode wires consist of gold-plated 30-cm-long tungsten wires of 50-μm in diameter. The cathode planes consist of graphite-coated polyimide films with a thickness of 50 μm.

2.4.4.4 Beam Hole Photon Veto (BHPV)

The Beam Hole Photon Veto (BHPV) is a photon veto counter located downstream section of the KOTO detector. This counter detects in-beam photons escaping through the CSI beam hole. The BHPV consists of 16 modules placed along the beam axis. A schematic view of the module is shown in Fig. 2.28. Each module consists of a lead converter, an aerogel radiator, light-collecting mirrors, and PMT's. The total radiation length of BHPV is $6.2X_0$. Details of BHPV are available in [52].

2.4.4.5 Beam Hole Guard Counter (BHGC)

The Beam Hole Guard Counter (BHGC)[*7] is a photon veto counter located in the KOTO detector's most downstream part. Figure 2.29 shows a schematic view and a picture of BHGC. This counter detects photons passing through the edge region of BHPV, and secondary particles produced at the edge region of BHPV. The BHGC consists of four modules. Each module consists of a 9.6-mm-thick

[*6] In 2015, the Beam Hole Charged Veto was upgraded [35]. We thus named the upgraded one newBHCV.
[*7] This BHGC was developed by the author of this thesis (S. Shinohara).

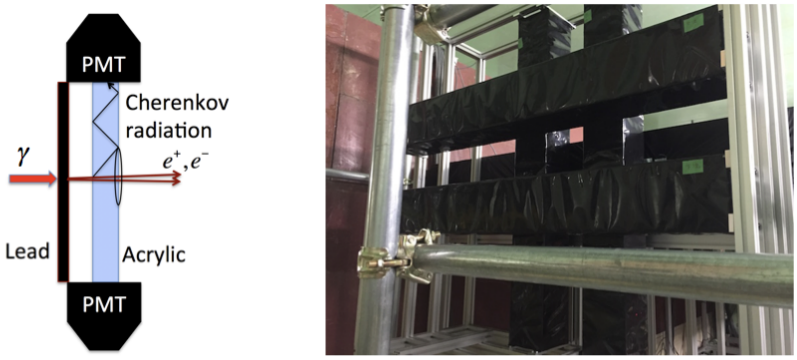

Figure 2.29: Left: Schematic view of a BHGC module. Right: a picture of BHGC viewed from downstream.

lead plate, and a 10-mm-thick acrylic plate that acts as a Cherenkov radiator, and a light guide to PMT's attached on both ends of the acrylic plate.

One feature of BHGC is insensitiveness to neutrons because of two requirements.

- To emit Cherenkov light, passing charged particles should have $\beta > 0.67$.
- The Cherenkov light should satisfy the total reflection condition to reach PMT's. In particular, charged particles passing to an acrylic plate normally should have $\beta > 0.89$.

With these two requirements, BHGC is sensitive to photons but insensitive to neutrons because the speed of charged particles generated by neutrons, such as protons and $\pi^{\pm}$'s, tends to be slow compared to that of $e^{\pm}$'s from photons. Details of BHGC are available in [53, 54].

2.5 Front-end Electronics

The KOTO data acquisition (DAQ) system uses a pipeline readout [55, 56] to shorten dead time caused by the trigger decision time. The output signals from the KOTO detectors are digitized with either 14-bit 125-MHz [57] or 12-bit 500-MHz sampling analog-to-digital converters (ADCs) [58], and are stored in pipeline buffers in Field Programmable Gate Arrays (FPGAs) on ADC's until a trigger decision is made.

Figure 2.30 shows recorded waveforms by 125-MHz and 500-MHz ADCs. The waveform is recorded for 512 ns for every triggered event, which corresponds to 64 and 256 sampling points for 125-MHz and 500-MHz sampling ADCs, respectively. Detectors IB, newBHCV, BHPV, and BHGC use 500-MHz sampling ADCs, and others use 125-MHz sampling ADCs.

The ADC modules are custom-built for the KOTO experiment. With the 125-MHz sampling ADC module, we can measure the deposited energy in each CSI crystal from $\mathcal{O}(1$ MeV) to $\mathcal{O}(1$ GeV). Figure 2.31 shows the waveform from a PMT on a CsI crystal, recorded by an oscilloscope. The original waveform from the detectors is too sharp to be recorded with a 125-MHz sampling frequency. Because of this, the 125-MHz ADC has a ten-pole Bessel filter to widen and reshape the input waveform before digitization [59].

If the counting rate of detectors is high, consecutive pulses recorded by a 125-MHz ADCs with the Bessel filter might overlap. We thus use the 500-MHz sampling ADC modules for detectors of newBHCV, BHPV, and BHGC, whose counting rates are high. To get a better timing resolution, we use the 500-MHz sampling ADC modules for IB [47].

The triggers and data flow in the KOTO DAQ system will be described in Sec. 3.2.

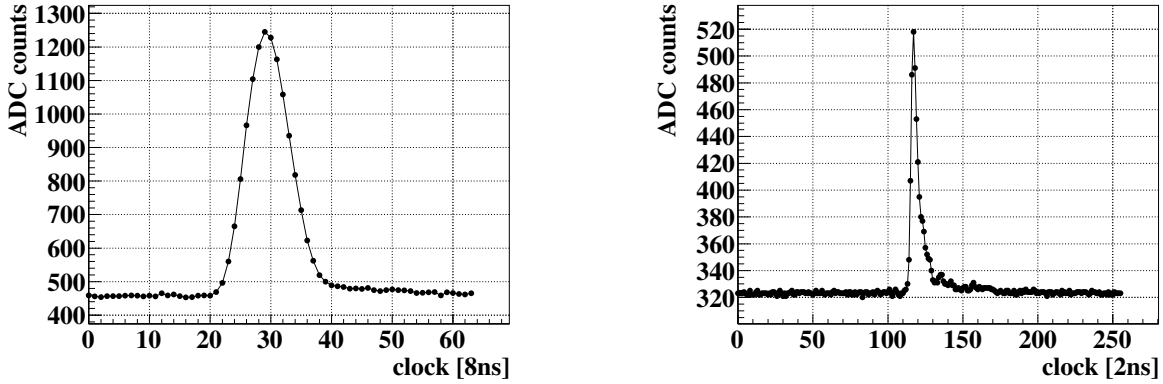

(a) 125-MHz sampling ADC (b) 500-MHz sampling ADC

Figure 2.30: Recorded waveforms by a 125-MHz in CSI (a) and a 500-MHz ADC in IB (b).

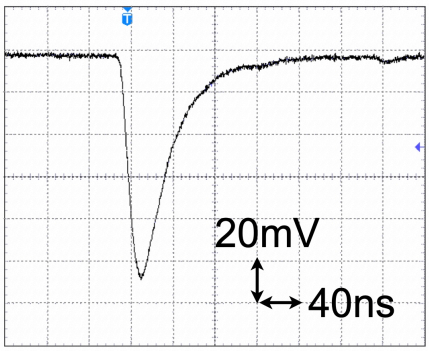

Figure 2.31: Signal from a CsI crystal with a photomultiplier tube recorded by an oscilloscope (quoted from [51]).

Chapter 3

Data Taking

In this chapter, the beam, trigger, and DAQ conditions in 2016–2018 are explained.

3.1 Beam Conditions

Beam conditions and periods in 2016–2018 are summarized in Table 3.1. In 2016–2018, the proton beam spill cycle (s_{spill}) varied between 5.2–5.5 sec. The beam power varied between 31–51 kW. The run number in periods of the table was incremented when an ion source in the accelerator was replaced. The accidental activities changed by the beam power, beam structure, and detector configuration. In the 2016–2018 data analysis, the data taking period was divided into sub-periods every time the condition of accidental activities changed in order to generate MC samples in each condition. In 2016, we divided the period into two sub-periods because the beam structure was improved, and amplifiers were installed in the FB detector readout to reduce the noise. In Apr. 2017, one of the two Electrostatic Septums (ESSs), which were used to extract the beam from MR to the Hadron Experimental Facility, broke down. Because of this trouble, the beam power in RUN75 was lower than in RUN69. The new ESS was installed during the accelerator shutdown period, and the beam power increased up to 50 kW in RUN78 and 51 kW in RUN79. In 2016–2018, the accumulated number of protons on target (POT) was 3.05×10^{19}, which corresponds to 1.4 times larger statistics than that of the 2015 dataset [26].

3.2 Triggers

To collect the $K_L \to \pi^0\nu\overline{\nu}$ signal sample, we have a first-level (Lv1) trigger and a second-level (Lv2) trigger. The diagram of the KOTO DAQ system in 2016–2018 is shown in Fig 3.1. In the following sections, the Lv1 and Lv2 triggers are explained.

Table 3.1: Summary of beam conditions and periods in 2016–2018

period	sub-period	notation	beam power	s_{spill}	POT	start–end
RUN69	0	Run69.0	42 kW	5.52 sec	1.78×10^{18}	May 27–Jun. 15, 2016
RUN69	1	Run69.1	42 kW	5.52 sec	1.34×10^{18}	Jun 16–Jun. 30, 2016
RUN75	0	Run75.0	31 kW	5.52 sec	0.27×10^{18}	May 30–Jun. 1, 2017
RUN75	1	Run75.1	35 kW	5.52 sec	0.58×10^{18}	Jun. 1–Jun. 2, 2017
RUN75	2	Run75.2	37.5 kW	5.52 sec	7.31×10^{18}	Jun. 2–Jul. 1, 2017
RUN78	0	Run78.0	33 kW	5.22 sec	0.51×10^{18}	Jan. 25–Jan. 26, 2018
RUN78	1	Run78.1	44 kW	5.22 sec	0.21×10^{18}	Jan. 26–Jan. 30, 2018
RUN78	2	Run78.2	50 kW	5.22 sec	7.36×10^{18}	Jan. 30–Feb. 26, 2018
RUN79	0	Run79.0	51 kW	5.22 sec	1.14×10^{19}	Jun. 1–Jun. 30, 2018
total					3.05×10^{19}	

3.2.1 Lv1 Trigger

As described in Sec. 2.1.1, we identify the $K_L \to \pi^0\nu\overline{\nu}$ decay by detecting two photons from the π^0 using the information from CSI, and by ensuring that there are no other detectable particles using the information from hermetic veto counters. To ensure these characteristics, the Lv1 trigger is issued when the total deposited energy in CSI (CSIEt) is larger than 550 MeV (CSIEt trigger) and there is no coincident hit in veto counters (online veto). In 2016–2018, we required no coincident hit in NCC, MB, IB, CV, and CC03. In 2018, we further required no coincident hit in CC04, CC05, and CC06 to reduce the trigger rate.

The Lv1 trigger system for the CSIEt calculation was upgraded just before Run79.0. Before the upgrade, CSIEt was calculated by summing up waveforms whose peak height exceeded a given threshold without considering the timings of those peaks. Because all such waveforms were summed up, accidental activities were included in CSIEt. Also, the gain variations between CSI channels were not considered before the upgrade. After the upgrade, we searched for a peak within a given timing window to reduce accidental activities in triggers. In addition, we calculated the deposited energy in each CSI channel from the peak height based on the energy calibration at the online stage.

3.2.2 Lv2 Trigger

The Lv1 trigger described above is not efficient enough to collect $K_L \to \pi^0\nu\overline{\nu}$ sample because other K_L decay modes of $K_L \to 3\pi^0$, $K_L \to 2\pi^0$, and $K_L \to 2\gamma$ (normalization modes) can satisfy the Lv1 trigger requirement. To reduce contributions from normalization modes, the Lv2 trigger decision was made based on the position of the center of deposited energy (COE) in CSI, defined as $\boldsymbol{R}_{\mathrm{COE}} = \sum e_i \boldsymbol{r}_i / \sum e_i$ where e_i and $\boldsymbol{r}_i$ are the deposited energy and the (x, y) position of each CSI crystal, respectively. We refer to the Lv2 trigger using the COE information as the COE trigger. The R_{COE} of events from normalization modes, which passes the online veto criterion, is smaller than that of $K_L \to \pi^0\nu\overline{\nu}$ because there are no missing particles in normalization modes. In the Lv2 trigger system, we selected events whose R_{COE} was larger than 165 mm [55]. This Lv2 trigger reduced the trigger rate by $\sim 70\%$.

To enable studying specific decay modes whose R_{COE} is small, such as $K_L \to \pi^0\gamma\gamma$, we upgraded the Lv2 trigger system during 2017. After the upgrade, the number of clusters in CSI is counted by the Lv2 trigger system and the events with the desired number of clusters can be selected [60]. We refer to the upgraded Lv2 trigger as the online clustering trigger. The condition of the online clustering trigger in each period is summarized in Table 3.2. The trigger rate reduction with the online clustering trigger will be described in Sec. 3.3.1. Note that the algorithm used in the online clustering trigger is not the same as the one used in the offline analysis for $K_L \to \pi^0\nu\overline{\nu}$. The effect of the difference of the algorithm on the analysis for $K_L \to \pi^0\nu\overline{\nu}$ will be described in Sec. 7.2.1. During the data taking, we found that noisy channels in CSI affected the number of showers counted with the online clustering trigger because it was easy to exceed a given energy threshold used in the trigger due to the baseline fluctuation. The noise fluctuation in some CSI channels was increasing during the data taking in 2016–2018. We masked noisy channels in the calculation of the trigger when the noise fluctuation exceeded a given threshold. We had 6, 13, and 14 masked channels in Run75, 78, and 79, respectively. The effect from accidental activities containing activities from the noise will also be described in Sec. 7.2.1.

3.3 Run Types

In 2016–2018, we took data to collect a $K_L \to \pi^0\nu\overline{\nu}$ sample, as well as samples to measure the K_L yield, to study backgrounds, and to calibrate detectors. In the 2016–2018 KOTO DAQ system, the maximum number of events recorded per spill was limited to 12 k due to the buffer size in the Lv2 trigger system and the data transfer speed from the local storage in J-PARC to the mass storage system in KEK. In each run type, we managed the event rate to be within this limit by changing the online

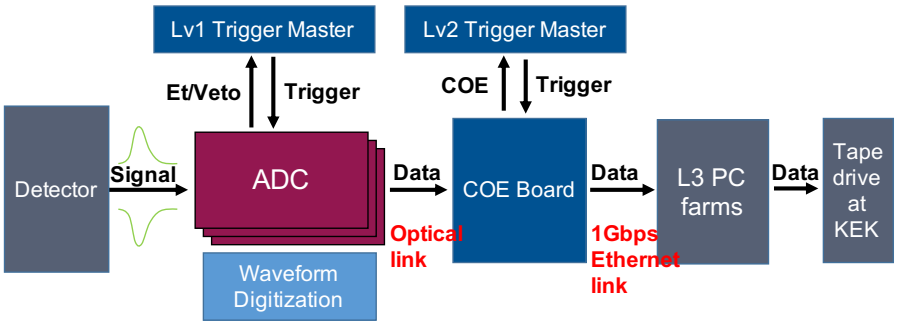

(a) Period in RUN69.

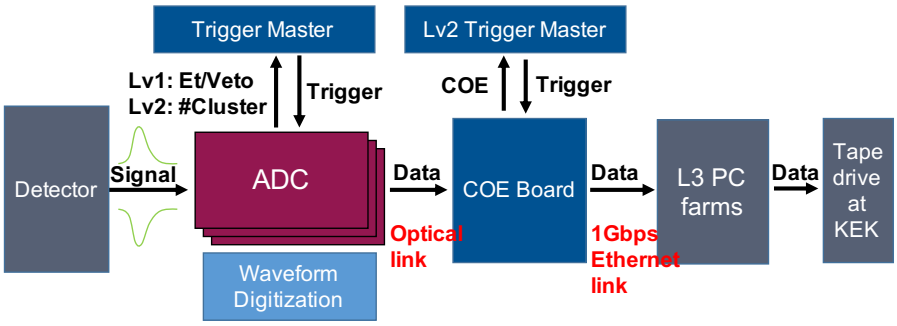

(b) Period in Run75.0–Run78.2.

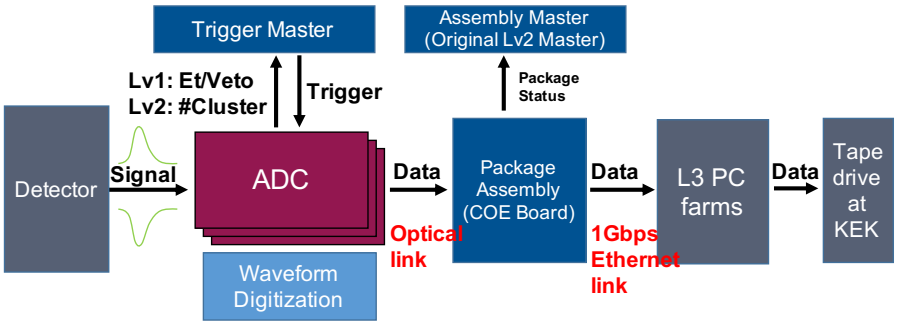

(c) Period in RUN79.

Figure 3.1: Diagrams of the KOTO data accession system. In RUN69 (a), the Lv2 trigger was made by the position of the center of deposited energy (COE) in CSI calculated in the module named "COE Board". In Run75.0–Run78.2 (b), the Lv2 trigger was made by COE or the number of clusters in CSI. In RUN79 (c), the Lv2 trigger was made by the number of clusters in CSI because we removed the COE calculation system from the COE Board and used the COE Board to assemble packages from ADCs. L3 PC farms worked just as the local temporary storage in J-PARC. The data is finally transferred to a mass storage system at KEK Computer Research Center in Tsukuba.

Table 3.2: Summary of the Lv2 trigger conditions in subdivided periods

period	beam power	COE trigger	cluster-counting trigger	accumulated POT
Run69.0	42 kW	Enabled	-	1.78×10^{18}
Run69.1	42 kW	Enabled	-	1.34×10^{18}
Run75.0	31 kW	Enabled	Disabled	0.27×10^{18}
Run75.1	35 kW	Enabled	Disabled	0.58×10^{18}
Run75.2	37.5 kW	Enabled	Disabled	1.29×10^{18}
	37.5 kW	Enabled	Enabled	2.31×10^{18}
	37.5 kW	Disabled	Enabled	3.71×10^{18}
Run78.0	33 kW	Disabled	Enabled	0.51×10^{18}
Run78.1	44 kW	Disabled	Enabled	0.21×10^{18}
Run78.2	50 kW	Disabled	Enabled	7.36×10^{18}
Run79.0	51 kW	-	Enabled	11.14×10^{18}

veto thresholds or by prescaling the triggered events. In this section, we explain the content of the runs to collect each sample of interest. The runs to calibrate detectors are explained in Appendix A.

3.3.1 Physics Run

The $K_L \to \pi^0\nu\overline{\nu}$ sample is collected in the physics run.

3.3.1.1 Triggers in Physics Run

The main trigger in the physics run is the "physics trigger" to collect a $K_L \to \pi^0\nu\overline{\nu}$ sample. Triggers in the physics run are explained below.

- physics trigger
  The physics trigger was designed to collect the $K_L \to \pi^0\nu\overline{\nu}$ sample. To manage the event rate of the data taking within the limitation without prescaling, both Lv1 and Lv2 triggers were used. As described in Sec. 3.2, the Lv2 trigger system was upgraded during 2017. Before the upgrade, we used the COE trigger. After the upgrade, we used the online clustering trigger, and we collected two-cluster samples for $K_L \to \pi^0\nu\overline{\nu}$. In addition, we collected four- and six-cluster samples without prescaling to study other K_L decays, such as $K_L \to \pi^0\gamma\gamma$ and $K_L \to 3\pi^0$.

  Figure 3.2 shows the trigger rate reduction in Run79.0. The online veto reduced the trigger rate by ∼96%. In addition, collecting only 2, 4, and 6 clusters reduced the trigger rate to half.

- normalization trigger
  The normalization trigger collected the sample of normalization modes, $K_L \to 2\pi^0$, $K_L \to 3\pi^0$, and $K_L \to 2\gamma$, using only the Lv1 trigger. Using the normalization trigger data, we also checked the performance of the Lv2 trigger. To suppress the total trigger rate, this trigger was prescaled by a factor of 30. The $K_L \to 2\pi^0$ sample was used to estimate the sensitivity for $K_L \to \pi^0\nu\overline{\nu}$, as described in Sec. 2.1.4. As will be described in Sec. 7.1, the statistical uncertainty is sufficiently small with this prescale factor. The other normalization modes were used to cross-check the sensitivity estimation, as will be described in Sec. 7.1.

- Minimum-Bias Trigger
  The minimum-bias trigger collected events to study the data without any online veto. For this purpose, only the CSIEt trigger was used to take data in this trigger. To suppress the total trigger rate, this trigger was prescaled by a factor of 300.

- TMon Trigger
  In KOTO, the accidental activities were collected with the trigger generated from the signals

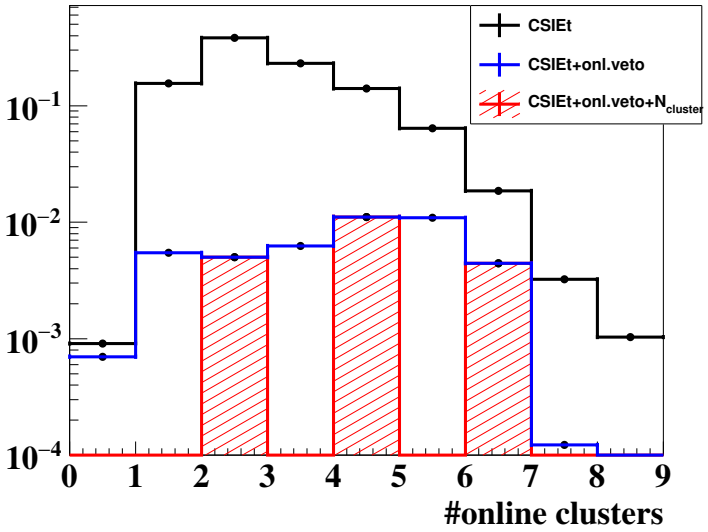

Figure 3.2: Trigger rate reduction in Run79.0. Each histogram shows the number of clusters counted by the Lv2 trigger in the physics run without any prescaling. The black histogram shows data collected by the CSIEt trigger. The area of the black histogram was normalized to be one event. The blue histogram shows data after applying the online veto to the events of the black histogram. The red histogram shows data after selecting the number of clusters to the events of the blue histogram.

Table 3.3: Prescale factors in the physics run

Trigger	2016	2017 and 2018
Physics	1	1
Normalization	-	30
Minimum-Bias	-	300

of the target monitor (TMon). The TMon consists of three plastic scintillators located in 50° direction from the primary beamline. The TMon monitors the secondary particle yield from the target. The events collected with the TMon trigger contained accidental activities which reflected the time structure in spills. In the analysis using MC simulations, we overlaid accidental activities collected with the TMon trigger on MC events, as will be described in Sec. 5.3.3. We collected a few hundred TMon trigger events per spill after prescaling.

- Clock, LED and Laser Trigger
  The clock trigger was issued at a regular interval, used to study the detectors' average counting rates in beam periods. We flashed an LED and laser at a regular interval to monitor timing responses in detectors. The signal to flash the LED and laser was also used as a trigger. The clock, LED, and laser triggers were issued every 0.1, 0.1, and 0.2 sec, respectively.

3.3.1.2 Conditions in 2016–2018

Table 3.3 summarizes the prescale factors used in the physics run. In the 2017–2018 physics run, we took the physics, normalization, and minimum-bias trigger data simultaneously. However, there were troubles in the 2016 DAQ system, and we could not take the normalization trigger data in the physics run simultaneously. In 2016, the normalization trigger data was taken in another run, named the normalization run, as will be described in the next section, Sec. 3.3.2.

Figure 3.3 shows the DAQ live ratio in the 2015–2018 physics run, which was defined by the ratio of the number of recorded events to the number of triggered events. In 2015, the limited buffer size

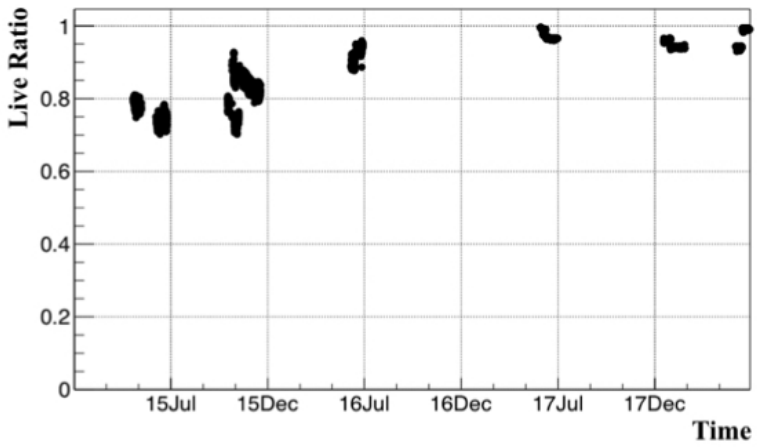

Figure 3.3: DAQ live ratio in the 2015–2018 physics run quoted from [61]

in the Lv2 trigger system caused dead time of the DAQ system [35]. Before 2016, we increased the buffer size in the Lv2 trigger system, which improved a DAQ live ratio by ∼10%. The Lv1 trigger system upgrade just before Run79.0 reduced the number of events sent to the Lv2 trigger system, which improved a DAQ live ratio by ∼5%.

3.3.2 Normalization Run

In 2016, there were troubles in the DAQ system, and we could not take the normalization trigger data in the physics run simultaneously. Due to the troubles, we took normalization runs in which we collected samples of the normalization modes, $K_L \to 2\pi^0$, $K_L \to 3\pi^0$, and $K_L \to 2\gamma$. We took the physics and normalization runs alternately.

The main trigger in the normalization run is the normalization trigger to collect a normalization decay mode sample, prescaled by a factor of 7. For other triggers, we took a minimum bias, TMon, Clock, LED and Laser trigger data.

3.3.3 Special Runs

In this section, special runs to collect control samples for background studies are explained.

3.3.3.1 Z0Al Run for Hadron-Cluster Background Study

To study the hadron-cluster background (Sec. 2.1.3.2), we collected a control sample in a special run, referred to as the "Z0Al" run.

Figure 3.4 shows the schematic view of the Z0Al run. In the Z0Al run, we inserted an $80 \times 80 \times 10$ mm^3 aluminum plate in the beam at $Z = -634$ mm and collected a sample with an enhanced number of scattered neutrons hitting CSI and producing the hadron-cluster events. Figure 3.5 shows a schematic view of the aluminum target which can be inserted remotely.

This control sample was taken with the physics trigger. Before the Lv2 trigger system upgrade, the online COE trigger reduced the event rate by 40%. We applied a prescale factor of 7–10 in the Z0Al runs because the trigger rate in the Z0Al runs was ten times higher than in physics runs. After the Lv2 trigger upgrade, we could select the number of clusters at the online stage. Figure 3.6 shows the number of clusters counted by the Lv2 trigger system with the data taken during Run79.0. The trigger requiring two clusters reduced the event rate by 70%. With the upgraded Lv2 trigger system, we took the Z0Al run data with a prescale factor of 2–5 depending on the beam power.

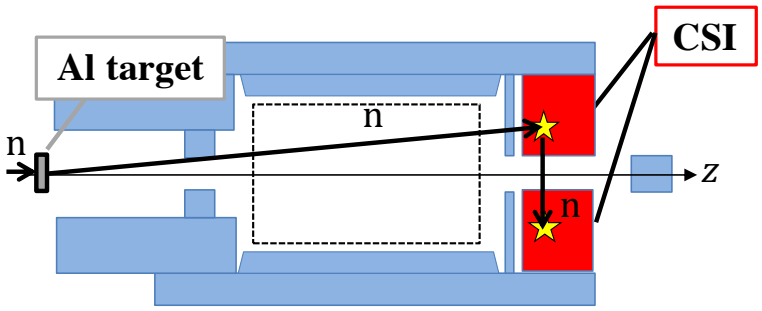

Figure 3.4: Schematic view of the Z0Al run.

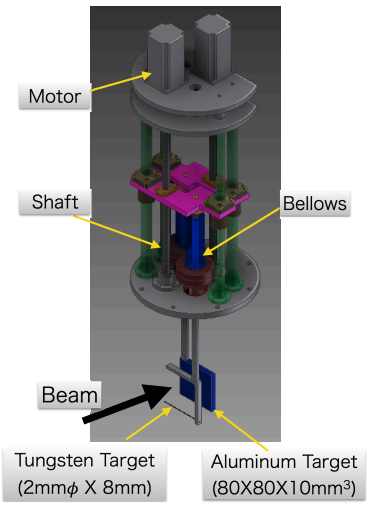

Figure 3.5: Schematic view of the aluminum target. We can insert the aluminum target remotely when we take a control sample. A tungsten target was not used in the analysis.

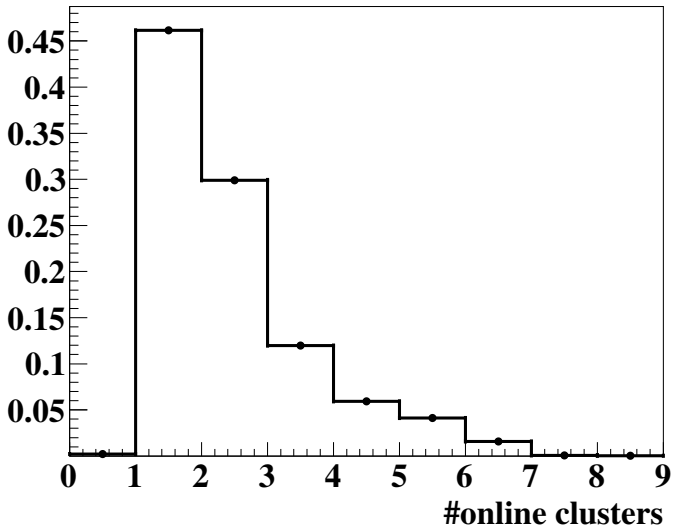

Figure 3.6: The number of clusters counted by L2 in the Z0Al run. The area of the histogram was normalized to be one event.

3.3.3.2 Runs for $K^{\pm}$ Background Study

Two sets of control samples for $K^{\pm}$ backgrounds were taken in 2020. One was a $K^{\pm} \to \pi^{\pm}\pi^0$ sample to measure the $K^{\pm}$ flux, and the other was a $K^{\pm}$ enhanced sample to study a $K^{\pm}$ decay background in the $K_L \to \pi^0\nu\overline{\nu}$ analysis.

$K^{\pm} \to \pi^{\pm}\pi^0$ Sample The $K^{\pm} \to \pi^{\pm}\pi^0$ sample was used to measure the $K^{\pm}$ flux. The final state of this decay is two photons from the π^0 decay and a $\pi^{\pm}$. With the dataset taken in 2016–2018, it was not easy to study this decay due to the limited statistics because only the minimum-bias trigger data with a prescale factor of 300 were available for the study. To evaluate the $K^{\pm}$ flux with $K^{\pm} \to \pi^{\pm}\pi^0$ decays, we collected a control sample using a dedicated trigger ($\pi^{\pm}\pi^0$ trigger) in 2020. The $\pi^{\pm}\pi^0$ trigger was used to select events with three clusters in CSI, one coincident hit in CV, and no coincident hits in other veto counters. With this trigger, 7.5 k events per spill were recorded without applying any prescale factor. The evaluation of the $K^{\pm}$ flux with the $\pi^{\pm}\pi^0$ trigger will be discussed in Sec. 8.4.

$K^{\pm}$ Sample Without Using Sweeping Magnet To validate a $K^{\pm}$ background estimation in the $K_L \to \pi^0\nu\overline{\nu}$ analysis, we collected another control sample in 2020. This control sample consisted of data taken with the physics trigger while the sweeping magnet in the beamline was turned off to enhance the $K^{\pm}$ flux at the beam-exit. We simultaneously collected data with the $\pi^{\pm}\pi^0$ trigger in this magnet-off configuration to normalize the $K^{\pm}$ yield. By turning off the magnet, the $K^{\pm}$ flux increased by a factor of 2×10^3. The study of this sample will also be discussed in Sec. 8.4.

Chapter 4

Event Reconstruction

In this chapter, the event reconstruction procedure is explained. The waveform from the detectors is recorded by either 125-MHz [57] or 500-MHz sampling ADCs [58]. We reconstructed deposited energies and hit timings from waveforms. Using the information from CSI, we reconstructed photons, π^0's, and K_L's.

4.1 Energy and Timing Reconstruction from Waveform

In this section, the procedure for reconstructing deposited energies and hit timings from waveforms is explained. We used different reconstruction procedures according to ADC types and detectors.

4.1.1 Baseline

The baseline of the waveform was calculated from the two sets of ten sampling points, one was the first ten sampling points, and the other was the last ten sampling points, for the Run69.0–Run78.2 dataset. For the Run79.0 dataset, nine sampling points were used in the calculation because the first sampling point was used for calculating a baseline for the trigger system. We calculated the standard deviations for each set and selected one with a smaller standard deviation. The mean of the selected set of ten sampling points was used as the baseline of each waveform. This baseline calculation procedure was used for both the 125-MHz and 500-MHz sampling ADCs.

4.1.2 Detectors using 125-MHz Sampling ADCs

4.1.2.1 Energy

To reconstruct deposited energies from waveforms, we calculated the sum of ADC counts of 64 sampling points after subtracting the baseline. Using energy calibration constants, the sum of ADC counts is translated into energy.

4.1.2.2 Timing for CSI

To reconstruct hit timings in CSI from waveforms, we searched for a sampling point with the largest ADC counts in the waveform and defined it as a peak sample. The pulse timing was defined as the time of the waveform that exceeded half of the peak height, referred to as "constant-fraction timing ($t^{\mathrm{CF}}_{\mathrm{pulse}}$)." Figure 4.1 shows the waveform and its constant-fraction timing. We calculated $t^{\mathrm{CF}}_{\mathrm{pulse}}$ by solving an equation of $f(t^{\mathrm{CF}}_{\mathrm{pulse}}) = h/2 + B$, where $f(t^{\mathrm{CF}}_{\mathrm{pulse}})$ is the linear interpolation between the j- and $(j+1)$-th sample in Fig. 4.1, h is the peak height, and B is the baseline. If multiple candidates before the peak existed, the one closest to the peak was chosen. The timing resolution of the constant-fraction timing is better than the timing of the peak. Because the pulse shape changed when the deposited energy

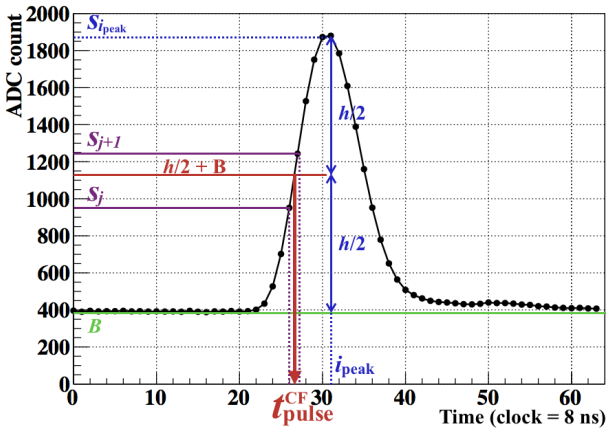

Figure 4.1: Waveform and its constant fraction time quoted from [35].

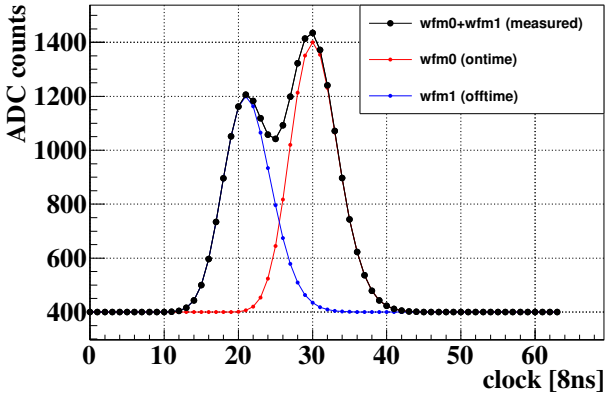

Figure 4.2: Schematic view of the off-time accidental pulse overlapping the on-time pulse which should be vetoed. The black dots represent the measured pulse. The red and blue dots represent the pulse existing on the on-time and off-time, respectively. The half of the peak height is determined by the on-time pulse ($\sim$ 900 ADC counts), but the off-time pulse determines the timing exceeding half of the peak height ($\sim$ 18 clock).

became large, the obtained pulse timing is corrected with an energy-dependent correction function [45]. Each pulse timing was finally adjusted based on the timing calibration.

4.1.2.3 Timing for Veto Counters

The constant-fraction timing is not suitable if an accidental pulse overlapped the on-time pulse which should be vetoed, as shown in Fig. 4.2. In such a case, if the constant-fraction timing shifts outside the veto window, the event will not be vetoed and it can be a background. To avoid such veto inefficiency, we used the peak timing for veto counters. First, to avoid baseline fluctuations, we searched for peak candidates in the waveform smoothed by taking a moving average of five sampling points. Figure 4.3 shows the original and smoothed waveforms. We interpolated three continuous sampling points with a parabola, and defined the timing of the parabola's peak as the peak timing. If there are multiple candidate peaks, we selected the one closest to the nominal timing. The nominal timing was determined for each detector. The obtained pulse timing was corrected with an energy-dependent correlation function due to the same reason as in Sec. 4.1.2.2.

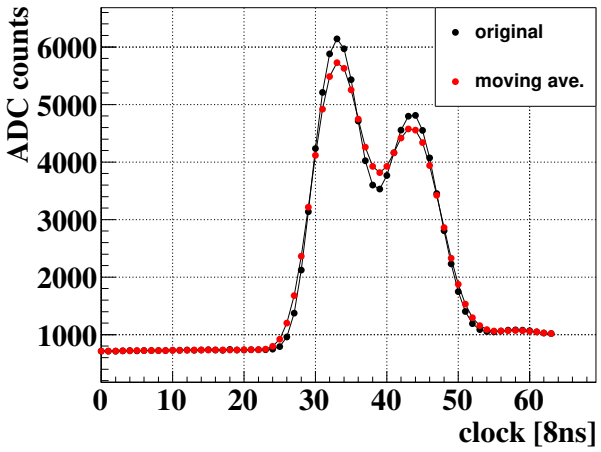

Figure 4.3: Example of the original and smoothed waveforms in HINEMOS. The black (red) dots represent the original (smoothed) waveform. In this waveform, peak candidates exist around 34 and 44 clocks. The nominal timing for HINEMOS is 34.5 clock.

4.1.3 Detectors using 500-MHz Sampling ADCs

4.1.3.1 Pulse Identification

To find pulses in the 256 sampling points of 500-MHz sampling ADCs, we searched for local maximum points and defined them as peaks if their heights exceeded a given threshold. We selected an appropriate peak for vetoing in a later stage in the event reconstruction (Sec. 4.3.2).

4.1.3.2 Energy and Timing

To reconstruct deposited energies and hit timings from waveforms recorded with the 500-MHz sampling ADCs, we calculated the sum of ADC counts after subtracting the baseline in each pulse. The range of the summation was determined for each detector. We finally translated the sum of ADC counts into the energy (the number of photoelectrons) in IB and newBHCV (BHPV and BHGC), based on the energy calibration.

For the timing, we calculated the constant-fraction timings in each pulse. We adjusted each pulse timing based on the timing calibration.

4.2 Event Reconstruction with CSI

Using the energy and timing in each CSI crystal, we sequentially reconstructed clusters, photons, π^0's, and K_L's in each event.

4.2.1 Clustering

An electromagnetic shower spread out to multiple crystals in CSI whose Molière radius is 3.57 cm [5]. We grouped such crystals into a cluster, and this process is referred to as "clustering." We first selected CSI crystals whose deposited energy was larger than 3 MeV and hit timing was within a 150-ns wide window. The crystals within 71 mm of each other were grouped into a cluster. The crystals that do not belong to clusters are referred to as "isolated-hit-crystal." The isolated-hit-crystal was used for a veto cut, as will be described in Sec. 4.3.1.1. The cluster energy ($e_{\rm clus}$), x-y position ($\boldsymbol{r}_{\rm clus}$), and

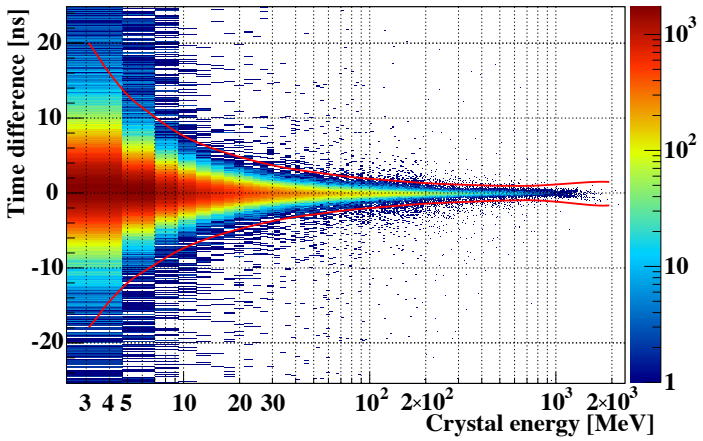

Figure 4.4: Distribution of the hit time of the crystals relative to the cluster time as a function of the energy of the crystals (quoted from Ref. [45]). Color represents the number of events in arbitrary units.

timing ($t_{\rm clus}$) were calculated as

$$e_{\rm clus} = \sum_i^n e_i, \tag{4.1}$$

$$\boldsymbol{r}_{\rm clus} = \frac{\sum_i^n \boldsymbol{r}_i e_i}{\sum_i^n e_i}, \tag{4.2}$$

$$t_{\rm clus} = \frac{\sum_i^n t_i/\sigma_t^2}{\sum_i^n 1/\sigma_t^2}, \tag{4.3}$$

where n is the number of crystals in the cluster and e_i, $\boldsymbol{r}_i$, and t_i represent each crystal's energy, (x,y) position, and hit time, respectively. The $\sigma_t = 5/e_i \oplus 3.63/\sqrt{e_i} \oplus 0.13$ is the timing resolution of each crystal as a function of energy [42], where $\oplus$ represents addition in quadrature, and σ_t and e_i are in the units of ns and MeV, respectively.

Figure 4.4 shows the distribution of hit timing of each constitutive crystal relative to the cluster timing as a function of the crystal energy. The two red lines represent the spline interpolation of the $\pm 5\sigma$ region of the time difference bin. At this stage, a cluster could contain crystals originated from accidental hits. To eliminate such crystals, we first calculated the timing differences between t_i and $t_{\rm clus}$ normalized with the standard deviation as

$$\Delta T_i^{\rm norm} = \frac{|t_i - t_{\rm clus}|}{5\sigma(e_i)}. \tag{4.4}$$

We then eliminated the crystal which had the maximum $\Delta T_i^{\rm norm}$ in the cluster ($\Delta T_{\rm max}^{\rm norm}$) larger than 1. The eliminated crystal was categorized as an isolated crystal hit. After we eliminated the crystal, we again calculated $t_{\rm clus}$ and $\Delta T_{\rm max}^{\rm norm}$. If $\Delta T_{\rm max}^{\rm norm} > 1$, we eliminated the crystal and recalculated $t_{\rm clus}$ and $\Delta T_{\rm max}^{\rm norm}$. We repeated these processes until $\Delta T_{\rm max}^{\rm norm} \leq 1$.

Finally, we calculated the timing differences between the earliest and the latest cluster. We removed the cluster with the largest timing deviation from the average cluster timing until all clusters within 30 ns window.

4.2.2 Reconstruction of π^0

The π^0's were reconstructed from a pair of clusters whose deposited energies were larger than 20 MeV. If we found more than two clusters in an event, we selected the two clusters with the closest timing to each other.

To reconstruct a π^0 from two photons, we first reconstructed $Z_{\rm vtx}$. We then calculated each photon momentum and calculated a π^0 4-momentum. After that, we corrected the photon energies and positions based on the cluster energies and positions and the $Z_{\rm vtx}$ of the π^0. We again reconstructed the π^0 after the correction. Finally, we calculated the timing of $\pi^0 \to 2\gamma$ decay. We explain such procedures of the reconstruction of the π^0 below.

4.2.2.1 Reconstruction of the π^0 Decay Position

The $Z_{\rm vtx}$ is calculated from the opening angle (θ) between two photons. In addition to Eq. 2.3, we can describe θ using cosine theorem as

$$\cos\theta = \frac{|\mathbf{x}_{\gamma_1}|^2 + |\mathbf{x}_{\gamma_2}|^2 - |\mathbf{x}_{\gamma_1} - \mathbf{x}_{\gamma_2}|^2}{2\,|\mathbf{x}_{\gamma_1}||\mathbf{x}_{\gamma_2}|}, \tag{4.5}$$

where $\mathbf{x}_{\gamma_i}$ is a three-vector from $(0,0,Z_{\rm vtx})$ to $(x_{\rm clus}, y_{\rm clus}, Z_{\rm CSI})$ [*1] for the i-th photon. Using Eqs. 2.3 and 4.5, and assuming that the $\pi^0 \to 2\gamma$ decayed on the beam-axis, we calculated the distance between $Z_{\rm vtx}$ and the CSI surface (dZ), defined as $dZ = Z_{\rm CSI} - Z_{\rm vtx}$, from

$$(1-\cos^2\theta)\,dZ^4 + \left\{2\,\boldsymbol{r}_1\cdot\boldsymbol{r}_2 - (r_1^2+r_2^2)\cos^2\theta\right\}dZ^2 + (\boldsymbol{r}_1\cdot\boldsymbol{r}_2)^2 - r_1^2 r_2^2\cos^2\theta = 0, \tag{4.6}$$

where $\boldsymbol{r}_i$ is each photon's $\boldsymbol{r}_{\rm clus}$. There are at most two solutions for dZ^2. If both two solutions of dZ^2 are positive, we discard the event for the two-cluster analysis because we cannot identify the correct dZ.

4.2.2.2 Reconstruction of the π^0 Momentum

The π^0 transverse (P_t) and longitudinal (P_z) momentum were calculated as

$$P_t = \left|\sum_{i=1}^{2} \frac{E_i\,\boldsymbol{r}_i}{\sqrt{r_i^2 + dZ^2}}\right|, \tag{4.7}$$

$$P_z = \sum_{i=1}^{2} \frac{E_i\,dZ}{\sqrt{r_i^2 + dZ^2}}, \tag{4.8}$$

where E_i is energy and $\boldsymbol{r}_i$ is $\boldsymbol{r}_{\rm clus}$ of the i-th photon.

4.2.2.3 Correction for Energy and Position of Clusters

We corrected cluster energies and positions based on the cluster energies and positions and the $Z_{\rm vtx}$ of the π^0.

First, the cluster energy ($e_{\rm clus}$), defined in Eq. 4.1, had to be corrected because the showers leaked out from the cluster and the crystals with energies below 3 MeV threshold were not included in clusters. To correct for such energy losses, we corrected the cluster energy using an energy-dependent correction function prepared with a MC simulation.

Second, the cluster position ($\boldsymbol{r}_{\rm clus}$), defined in Eq. 4.2, had to be corrected because the cluster position was different from the incident photon position due to the shower depth in CSI. Figure 4.5 shows the relationship between the cluster position and the incident photon position. To obtain the incident photon position on the CSI surface, we first calculated a shower depth L_s in mm as

$$L_s \;=\; (p_0 + p_1 \ln(e_{\rm clus}))X_0, \tag{4.9}$$

[*1] $Z_{\rm CSI}$ is 6168 mm.

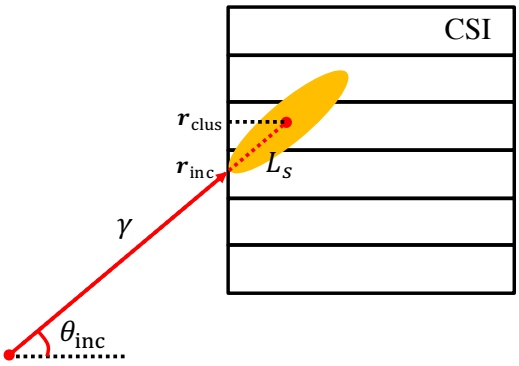

Figure 4.5: Schematic view of the correction of the hit position of photon.

where $X_0 = 18.5$ mm is the radiation length of CsI, e_{clus} is the cluster energy in GeV, and $p_0 = 6.490$ and $p_1 = 0.993$ are the parameters obtained by a MC simulation. The incident photon position on the CSI surface ($\boldsymbol{r}_{inc}$) was calculated as

$$\boldsymbol{r}_{inc} = \boldsymbol{r}_{clus}\left(1 - \frac{L_s \sin\theta_{inc}}{r_{clus}}\right), \tag{4.10}$$

where θ_{inc} is the polar angle of the photon momentum obtained from $\boldsymbol{r}_{clus}$ and the π^0 decay vertex position. The deposited energy was corrected again using a correction map as a function of the deposited energy and the incident angle prepared with a MC simulation.

After we corrected the cluster energies and positions, we again reconstructed the π^0 using the same procedures as in Sections 4.2.2.1 and 4.2.2.2.

4.2.2.4 Reconstruction of the π^0 Decay Timing

We finally calculated the timing of $\pi^0 \to 2\gamma$ decay (event vertex time). To obtain the event vertex time, we first calculated the timing of the photon at the π^0 decay position (vertex time) using the cluster timing and the time of flight between $(0, 0, Z_{vtx})$ and $\boldsymbol{r}_{inc}$.

The vertex time (t_{vtx}) is calculated as

$$t^i_{vtx} = t^i_{clus} - \sqrt{r_i^2 + dZ^2}/c, \tag{4.11}$$

where r_i is r_{inc} of the i-th photon and c is the speed of light.

Using the vertex times of photons, the event vertex time (T_{vtx}) is defined as

$$T_{vtx} = \frac{\sum_{i=1}^{2} t^i_{vtx}/\sigma_t^2(E_i)}{\sum_{i=1}^{2} 1/\sigma_t^2(E_i)}, \tag{4.12}$$

where $\sigma_t(E\,[\mathrm{MeV}]) = (3.8/\sqrt{E\,[\mathrm{MeV}]} \oplus 0.19)$ ns represents the vertex timing resolution as a function of energy.

4.2.3 Reconstruction of the K_L for Normalization Decay Modes

The K_L was reconstructed to study the normalization decay modes, $K_L \to 2\pi^0$, $K_L \to 3\pi^0$, and $K_L \to 2\gamma$. The $K_L \to 2\pi^0$ decays were used to estimate SES, as described in Sec. 2.1.1. The $K_L \to 3\pi^0$ and $K_L \to 2\gamma$ decays were used to cross-check the SES.

For $K_L \to 2\pi^0$ and $K_L \to 3\pi^0$, we reconstructed K_L's from any pair of π^0's, and selected the most likely one from the K_L candidates. For $K_L \to 2\gamma$, we reconstructed K_L's from two photons with the same procedure as for the π^0 reconstruction, but assuming the nominal K_L mass in the calculation of the opening angle of photons. After we reconstructed the K_L from the normalization decay, we reconstructed the decay x and y positions of K_L. We describe such K_L reconstruction procedures below.

4.2.3.1 K_L Reconstruction

Reconstruction of $K_L \to 2\pi^0$ and $K_L \to 3\pi^0$ decays For the $K_L \to 2\pi^0$ and $K_L \to 3\pi^0$ decays, there are 3 and 15 possible photon pairings, respectively. We reconstructed π^0's in all the combinatorics and selected the one with the following procedure. First, for each photon pairing, we calculated the average $Z_{\rm vtx}$ of reconstructed π^0's ($Z_{\rm vtx}^{\rm K_L}$), defined as

$$Z_{\rm vtx}^{\rm K_L} = \frac{\sum_i^{N/2} Z_{\rm vtx}^i/\sigma_i^2}{\sum_i^{N/2} 1/\sigma_i^2}, \tag{4.13}$$

where i denotes each possible photon pairing, N is the number of photons, σ_i represents the resolution of the reconstructed vertex position given as a function of two photon energies, and $Z_{\rm vtx}^i$ represents the z position of each reconstructed π^0. We evaluated the consistency between π^0 vertexes using χ_z^2 and $\Delta Z_{\rm vtx}$, defined as

$$\chi_z^2 = \sum_i^{N/2} \frac{(Z_{\rm vtx}^i - Z_{\rm vtx}^{\rm K_L})^2}{\sigma_i^2}, \tag{4.14}$$

$$\Delta Z_{\rm vtx} = \max(|Z_{\rm vtx}^i - Z_{\rm vtx}^j|). \tag{4.15}$$

We selected the photon pairing with the smallest χ_z^2. In the normalization analysis (Sec. 7.1), we used a cut on $\Delta Z_{\rm vtx}$ to ensure the K_L reconstruction.

Reconstruction of $K_L \to 2\gamma$ decay For $K_L \to 2\gamma$, we reconstructed K_L's from two photons with similar procedures to the π^0 reconstruction. The difference from the π^0 reconstruction was the difference of the assumption of the nominal mass between the π^0 and K_L.

4.2.3.2 Correction for K_L Decay Position with COE

The position of the center of deposited energy (COE) in CSI is approximately the position that the K_L would hit if it had not decayed (see Appendix B). Using the COE position, we corrected the decay x-y vertex position. The COE position on the CSI surface ($\boldsymbol{R}_{\rm COE}$) is defined as

$$\boldsymbol{R}_{\rm COE} = \frac{\sum_i^N \boldsymbol{r}_i E_i}{\sum_i^N Ei}, \tag{4.16}$$

$$\tag{4.17}$$

where $\boldsymbol{r}_i$ and E_i are the incident position ($\boldsymbol{r}_{\rm inc}$) and energy of the i-th photon, respectively. We corrected the decay vertex x-y position ($\boldsymbol{R}_{\rm vtx}^{K_L}$) using $\boldsymbol{R}_{\rm COE}$ and the target position ($Z_{\rm target}$) of -21507 mm as

$$\boldsymbol{R}_{\rm vtx}^{K_L} = \frac{Z_{\rm vtx}^{\rm K_L} - Z_{\rm target}}{Z_{\rm CSI} - Z_{\rm target}} \boldsymbol{R}_{\rm COE}. \tag{4.18}$$

Using the reconstructed $\boldsymbol{R}_{\rm vtx}^{K_L}$ and $Z_{\rm vtx}^{\rm K_L}$, we again reconstructed the π^0's. By summing up the four-momenta of π^0's, we finally reconstructed the K_L.

4.2.3.3 Reconstruction of the K_L Decay Timing

The event vertex time ($T_{\rm vtx}^{\rm K_L}$) was calculated as

$$T_{\rm vtx}^{\rm K_L} = \frac{\sum_i^N t_{\rm vtx}^i/\sigma_t^2(E_i)}{\sum_i^N 1/\sigma_t^2(E_i)}, \tag{4.19}$$

where $\sigma_t(E)$ is the same as in Eq. 4.12.

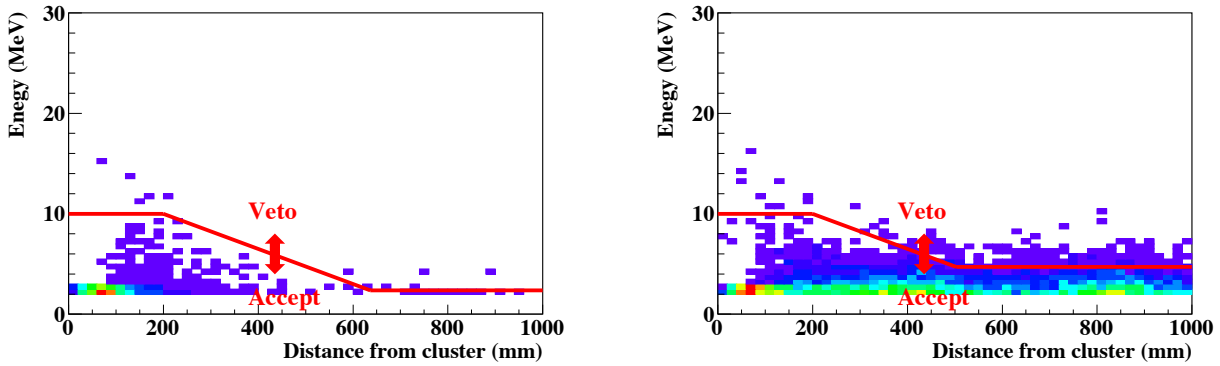

(a) Usual CSI channel (b) Noisy CSI channel

Figure 4.6: Distributions of isolated-hit-crystal energy and distance from the closest cluster of $K_L \to \pi^0\nu\bar{\nu}$ MC events. The left and right figures show the distribution of a usual CSI channel and a noisy CSI channel, respectively. The red line shows the veto threshold.

4.3 Reconstruction of Veto Information

In this section, we explain the reconstruction of veto information from detectors.

4.3.1 CSI

To reduce background events caused by an extra photon hitting CSI but not being identified as a photon cluster due to the photo-nuclear reaction in the shower propagation, the activities in CSI, which were not used in the π^0 reconstruction, were used for vetoing events.

4.3.1.1 Isolated Hit Crystal Veto

The event was vetoed if the hit time of isolated-hit-crystal was within ± 10 ns of the photon timing, and the deposited energy was larger than a given threshold. The energy requirement was determined based on the baseline fluctuation of each CSI channel and the distance from the closest cluster as

$$\begin{array}{ll} E \leq 10 \text{ MeV} & (d \leq 200 \text{ mm}) \\ E \leq (13.5 - 0.0175d\,[\text{mm}]) \text{ MeV} \cup E \leq 3\,\sigma_i^{\text{noise}} \text{ MeV} & (d > 200 \text{ mm}), \end{array} \tag{4.20}$$

where σ_i^{noise} is the baseline fluctuation of each CSI channel obtained by the random trigger data. Examples of the thresholds are also shown in Fig. 4.6. In the small d region, the threshold was set higher to reduce the signal event loss due to a shower shape fluctuation. In the larger d region, the threshold was determined by the noise level in CSI because some CSI channels had a low gain with a larger noise. We optimized the threshold in each CSI channel to reduce the signal event loss due to such a noise fluctuation.

4.3.1.2 Extra-Cluster Veto

The clusters which were not used in the π^0 reconstruction were referred to as extra clusters. We calculated the vertex time for extra clusters using the vertex of the reconstructed π^0 and K_L. If the timing was within ± 10 ns from the event vertex time, we vetoed the event.

4.3.2 Veto Counters

For the veto counters, we reconstructed the veto energy and timing which were used in the decision for vetoing. The veto energy and timing were made based on the deposited energies and timings in each detector reconstructed from waveforms (Sec. 4.1).

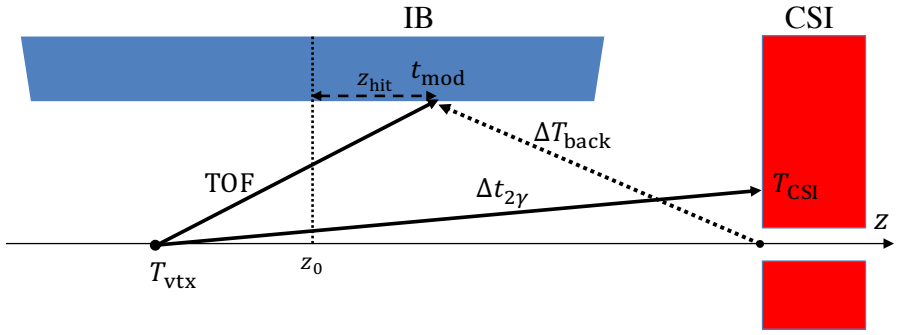

Figure 4.7: Schematic view of the timings used in the module-veto-timing calculation.

For the timings in each module, we first corrected for the time of flight (TOF) from the decay vertex to the hit position in each counter. We then calculated the module-veto-timing ($t^{\mathrm{veto}}_{\mathrm{mod}}$) from the timing in each module (t_{mod}) as

$$t^{\mathrm{veto}}_{\mathrm{mod}} = t_{\mathrm{mod}} - T_{\mathrm{vtx}} - \mathrm{TOF}, \tag{4.21}$$

where TOF is the time-of-flight in each counter. Among modules in each detector, we selected one module to be used for vetoing events. The energy and timing in the selected module are regarded as a veto energy and timing. The selection method is different in each detector. In the following sections, we explain the veto scheme for the veto counters used from 2016 and the special treatment in some veto counters. Details of the veto scheme in other veto counters are available in [31, 35].

4.3.2.1 MB and IB

Figure 4.7 shows a schematic view of timings in IB. For MB and IB, t_{mod} was calculated as

$$t_{\mathrm{mod}} = \frac{t_u + t_d}{2}, \tag{4.22}$$

where t_u and t_d are the measured timings of the upstream and downstream channels, respectively. The hit position of the particle from the center position of MB (IB), z_{hit}, was calculated from

$$z_{\mathrm{hit}} = \frac{v_{\mathrm{prop}}}{2}\,(t_u - t_d), \tag{4.23}$$

where $v_{\mathrm{prop}} = 168.1$ (181.0) mm/ns is the propagation velocity of light in MB (IB).

For MB and IB, to minimize the effect on the wrong TOF calculation due to the wrong Z_{vtx} originated from the mis-combination in the π^0 reconstruction, we defined the module-veto-timing using the t_{mod}, z_{hit}, and photon timings in CSI, but without using Z_{vtx}. We rearrange Eq. 4.21 as

$$\begin{aligned} t^{\mathrm{veto}}_{\mathrm{mod}} &= t_{\mathrm{mod}} - T_{\mathrm{vtx}} - \mathrm{TOF} && (4.24)\\ &= t_{\mathrm{mod}} - (T_{\mathrm{CSI}} - \Delta t_{2\gamma}) - \mathrm{TOF} && (4.25)\\ &= t_{\mathrm{mod}} - T_{\mathrm{CSI}} + (\Delta t_{2\gamma} - \mathrm{TOF}) && (4.26)\\ &\approx t_{\mathrm{mod}} - T_{\mathrm{CSI}} - \Delta T_{\mathrm{back}}, && (4.27) \end{aligned}$$

where T_{CSI} is the average of photon timings in CSI, $\Delta t_{2\gamma} \equiv T_{\mathrm{CSI}} - T_{\mathrm{vtx}}$, and ΔT_{back} is defined as

$$\Delta T_{\mathrm{back}} = \sqrt{(z_{\mathrm{hit}} + z_0 - Z_{\mathrm{CSI}})^2 + R^2}/c, \tag{4.28}$$

where $z_0 = 4105$ (4332.5) mm is the center position of MB (IB), $Z_{\mathrm{CSI}} = 6168$ mm is the position of the CSI surface, and $R = 1018$ (758.6) mm is the inner radius of MB (IB). With Eq. 4.27, we could get $t^{\mathrm{veto}}_{\mathrm{mod}}$ which does not contain the reconstruction information of the π^0.

4.3.2.2 IBCV and MBCV

For IBCV, the calculation of t_{mod} and z_{hit} was the same as in IB. The module-veto-timing was calculated using Eq. 4.21. The TOF was calculated as

$$\mathrm{TOF} = L/c, \tag{4.29}$$

$$= \sqrt{(z_{\mathrm{hit}} + z_0 - Z_{\mathrm{vtx}})^2 + R^2}/c. \tag{4.30}$$

where L is the distance between the decay vertex and particle hit position in IBCV. The propagation velocity of light in IBCV is the same as in IB.

For MBCV, the module-veto-timing was calculated using Eq. 4.21. Because MBCV is a single-end readout counter, the particle hit position is unknown. The TOF was calculated as

$$\mathrm{TOF} = L/c, \tag{4.31}$$

$$= (Z_{\mathrm{CSI}} - Z_{\mathrm{vtx}})/c, \tag{4.32}$$

where L is the distance between the decay vertex position and the z position of the CSI surface.

4.3.2.3 Wide Veto (FB, NCC, and CV)

If pulses overlapped and their peaks are not resolved, the measured time is possibly shifted outside the veto window. In such a case, a detection inefficiency becomes large. To avoid such inefficiency, a pulse-shape discrimination method was introduced by applying a fast Fourier transform (FFT) to the waveforms of FB, NCC, and CV.

In the discrimination method, we prepared templates of single-hit waveforms in the frequency domain. We then calculated a χ^2 value based on the difference between the observed waveform and the template in the frequency domain. When the χ^2 value exceeded a given threshold, the veto window was widened to accommodate possible timing shifts due to overlapping pulses.

To prepare single-hit waveforms, we first selected waveforms in physics run data whose peak timings were close to the nominal peak timing. We categorized the waveforms in energy bins based on the peak height. In each energy bin, we normalized the waveforms to have the equal area and shifted them to have the same peak timing. We calculated the mean of the height for each sampling point in the waveforms. Finally, we selected single-hit waveforms in which deviations from mean values are less than the pedestal fluctuation for all data points.

After we prepared single-hit waveforms, we applied a FFT to the single-hit waveforms. In each sampling frequency of waveforms, we stored the mean of the magnitudes (μ_i^{temp}) and the standard deviation (σ_i^{temp}), and used them as the template.

To discriminate overlapped pulses, we calculated a χ^2 value based on the difference between the observed waveform and the template in the frequency domain. Figures 4.8 and 4.9 show the example of a waveform in time domain and frequency domain. For each observed waveform, we applied a FFT to convert it to a frequency domain and compared it to the template in the same energy bin. We calculated a χ^2_{FFT} value as

$$\chi^2_{\mathrm{FFT}} = \sum_{i=0}^{4} \left(\frac{y_i^{\mathrm{obs}} - \mu_i^{\mathrm{temp}}}{\sigma_i^{\mathrm{temp}}} \right)^2, \tag{4.33}$$

where i denotes each sample point in the frequency domain, y_i^{obs} is the magnitude in the frequency domain for each waveform. In the calculation, we used the five low frequency sampling points because high frequency components were dominated by baseline fluctuations.

Figure 4.10 shows an example of a waveform of NCC. In NCC, we widened the veto window from 40 ns to 100 ns if the χ^2_{FFT} exceeded the given threshold. In the case of Fig. 4.10, we vetoed the event because the χ^2_{FFT} exceeded the given threshold and the peak timing existed within the widened veto window. The thresholds and veto windows used in the 2016–2018 analysis will be described in Sec. 7.1.2.

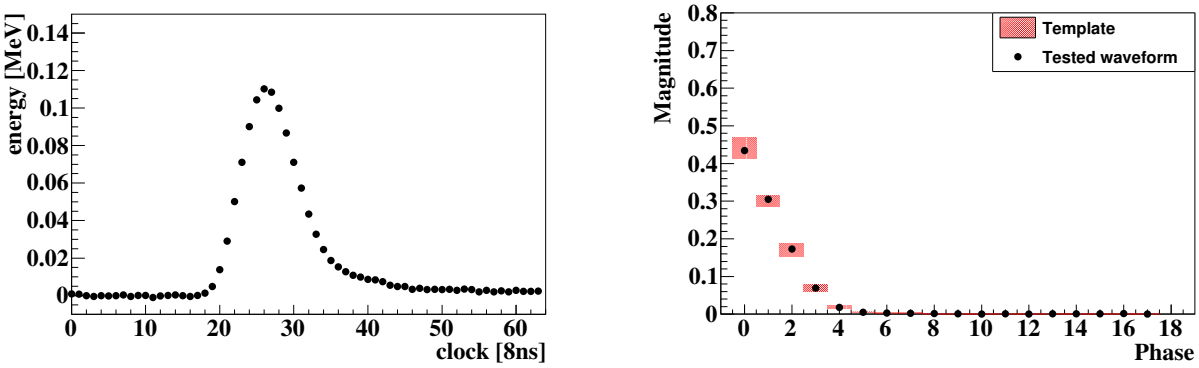

(a) Time domain (b) Frequency domain

Figure 4.8: Example of waveforms of NCC. Black dots in the left plot show a single-pulse-like waveform collected in data in the time domain. The data point in the left figure was normalized so that the energy of the waveform became 1 MeV. Black dots in the right histogram show the single-pulse-like waveform translated into the frequency domain. Red rectangles represent the region within $\mu_i^{\text{temp}} \pm \sigma_i^{\text{temp}}$.

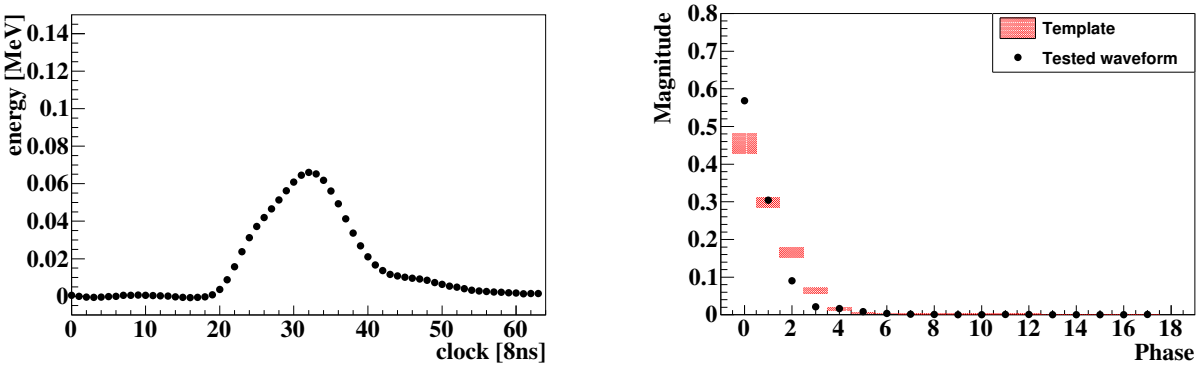

(a) Time domain (b) Frequency domain

Figure 4.9: Example of waveforms of NCC. The meaning of the black dots and red histogram are the same as for Fig. 4.8. Most black dots in the right histogram existed outside the red rectangle region. This indicated that the observed waveform was not a single-pulse-like waveform.

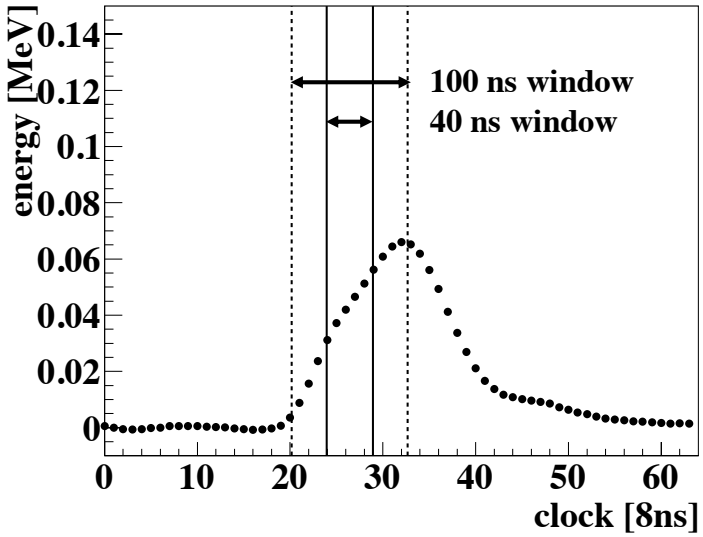

Figure 4.10: Example of a waveform of NCC. The waveform is the same as in Fig. 4.9a. The solid and dotted lines show the veto window for χ^2_{FFT} below and above a given threshold, respectively.

Chapter 5

Monte Carlo Simulation

In this chapter, we describe the Monte Carlo (MC) simulation used for the 2016–2018 data analysis. The procedures of MC simulations in KOTO are as follows.

1. We first prepared a set of parent particles entering the KOTO detector.
2. Using such particles, we simulated decays and interactions with detector components based on GEANT4.
3. We finally converted outputs of the MC simulation into energies and timings considering detector responses.

The following sections explain the set of parent particles, the interactions with detectors, and the detector responses.

5.1 Set of Parent Particles of the KOTO MC Simulation

In the KOTO MC simulation, we first prepared a set of parent particles entering the KOTO detector, hereinafter referred to as "MC seeds." In KOTO, two types of MC seeds were used. One is the beam-core K_L seed used to simulate beam-core K_L's. The other is the beamline seed used to study beam-halo particles.

5.1.1 Beam-Core K_L Seed

5.1.1.1 K_L Momentum Spectrum

Figure 5.1 shows the K_L momentum spectrum at the beam-exit. The K_L momentum was measured by the past study [42] as

$$f(p,\mu,\sigma_0,A,S) = \exp\left\{-\frac{(p-\mu)^2}{2(\sigma_0(1-(A+Sp)(p-\mu)))^2}\right\}, \tag{5.1}$$

where p is momentum in GeV/c, and μ, σ_0, A, and S are fitting parameters [42]. In the past measurement, parameters of $(\mu,\sigma_0,A,S) = (1.420, 0.8102, -0.3014, 0.01709)$ were obtained by fitting the K_L momentum spectrum. We used this K_L spectrum in the beam-core K_L seed.

5.1.1.2 Incident K_L Position and Direction

The incident position and direction of K_L's at the beam-exit were obtained from the position of the secondary particle at the production target and the optics of the collimators which is set 16° away from the proton beam direction. The secondary particle (x, y) position distribution at the target (target-image) was obtained by a simulation resulting from 30-GeV protons hitting the gold production target.

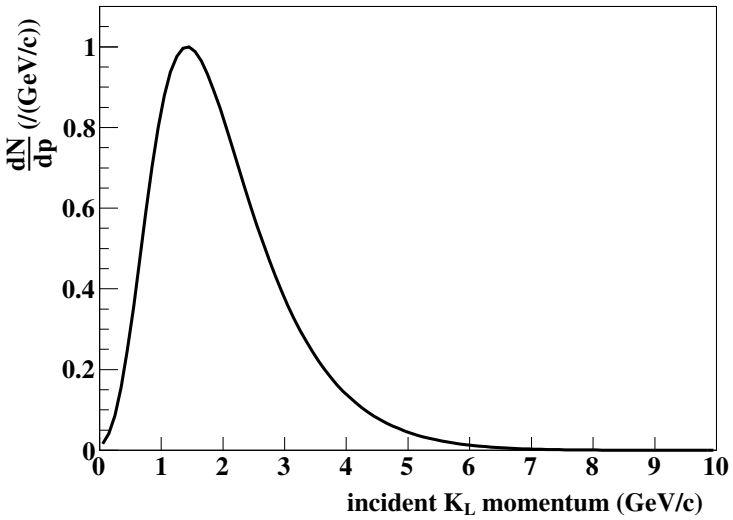

Figure 5.1: K_L momentum spectrum at the beam-exit (quoted from [35]).

Figure 5.2 shows the target-image and the optics of the collimators. To make the beam-core K_L seed, we assumed that the beam edge was determined by the upstream end of the upstream collimator and that the K_L's have a uniform distribution between the collimator walls. In each seed, we randomly selected an incident K_L position based on the target-image, and a position at the upstream end of the upstream collimator. We then drew a line by connecting the two positions and extrapolated it to the beam-exit. Figure 5.3 shows the position distributions of K_L's at the beam-exit (beam profile). In this seed, we did not take into account particles scattered in the beamline components. To study such scattered particles, we prepared another MC seed explained in Sec. 5.1.2.

5.1.2 Beamline Seed

To study beam-halo particles, we prepared incident particles generated by a MC simulation with beamline components (beamline simulation). The simulation process was divided into two steps to run it within a realistic time. In the first step, we simulated 30-GeV protons hitting the gold production target, and collected secondary particles at a plane 1 m away from the target and 16° away from the primary beam line. In the second step, we selected a particle from the collection, let it decay and interact with beamline components, such as a photon-absorber and collimators, and recorded particles at the beam-exit (beamline seed). The time to simulate became short because we only simulated decays and interactions of particles collected in the first step,

The difference between the beam-core K_L seed shows up in the tail region of the beam profile. The beam-core K_L seed has no tail components, as shown in Fig. 5.3 because the beam profile was determined by the optics alone. On the other hand, as shown in Fig. 5.4, the beamline seeds distribute broadly due to scattering with the beamline components. Several spikes in the tail region were caused by reusing the secondary particles for the second step of the beamline simulation.

5.2 Interaction with Detectors

We simulated interactions of particles with detector materials using the GEANT4 toolkit. The QGSP BERT physics list in the Geant4 handled the interactions step by step in the simulation. By tracking particle trajectories, interactions in each step were simulated, and the deposited energy, interaction time, and interaction position were recorded.

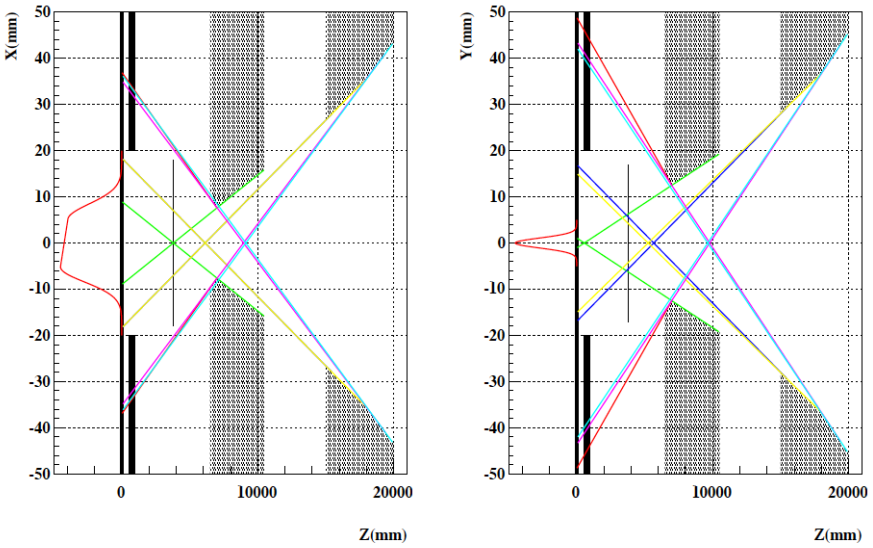

Figure 5.2: Target-image (red lines drawn in the $Z < 0$ region) and collimation lines (colored straight lines) in X-Z (left) and Y-Z (right) planes (quoted from [35]). The black shadows around $6500 < Z < 10500$ mm and $15000 < Z < 20000$ mm represent the upstream and downstream collimators, respectively. In these figures, the origin of Z is the position of the target. The beam-exit corresponds to $Z = 20$ m.

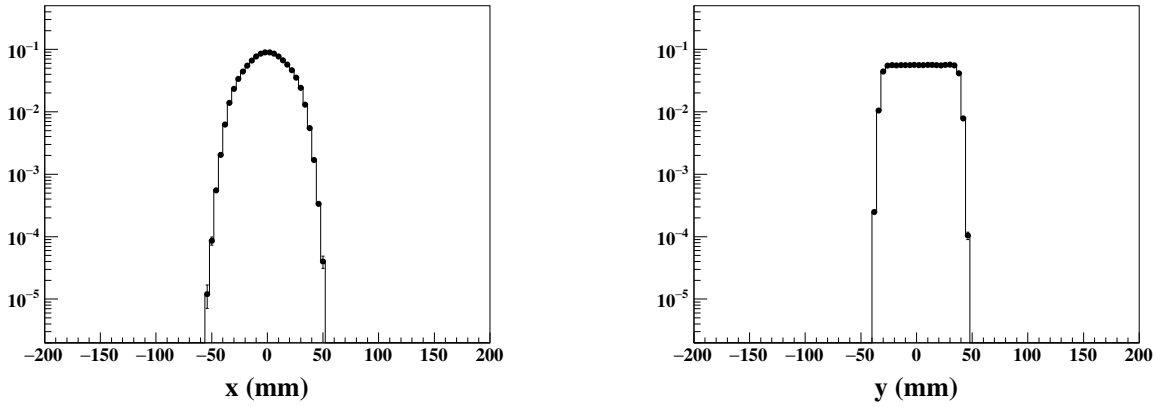

Figure 5.3: Distributions of the K_L incident x (left) and y (right) positions at the beam-exit of the beam-core K_L seeds.

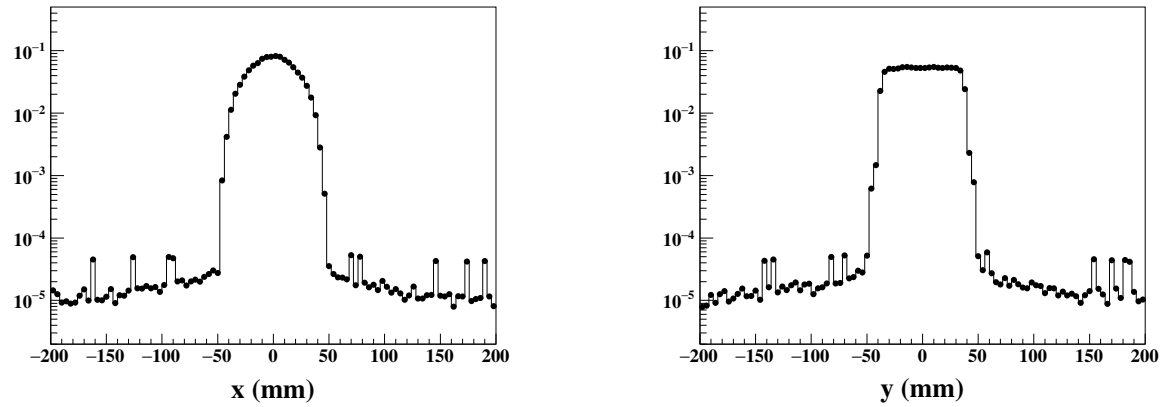

Figure 5.4: Distributions of the incident particle x (left) and y (right) position at the beam-exit of the beamline seeds.

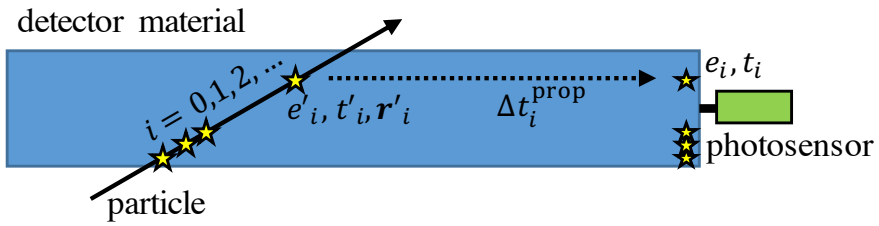

Figure 5.5: Schematic view of simulating energies and timings at the interaction positions and the photosensor positions. Each star marker shows each interaction between a particle and detector material. The i denotes each step of the interaction, e'_i is the deposited energy, t'_i is the interaction time, and $\boldsymbol{r}'_i$ is the interaction position in each step.

5.3 Detector Response

Based on the energies and timings recorded at the interaction positions, we made energies and timings at photosensor positions.

5.3.1 Energy and Timing Conversion

The general procedure to obtain the energy and timing is described in Sec. 5.3.1.1. The procedure for IB is explained in Sec. 5.3.1.2. The procedures for IBCV and MBCV are explained in Sec. 5.3.1.3. Details of procedures for other detectors are available in [35, 31].

5.3.1.1 General Procedures

In each simulation step, we made energies and timings at the photosensor position based on the energies and timings at the interaction position. Figure 5.5 shows the schematic view of energies and timings at the interaction positions and those observed at the photosensor positions. The measured time at the photosensor position was calculated using the effective speed of light in the detector material. For each MC simulation step, we calculated the measured time (t_i) as

$$t_i = t'_i + \Delta t_i^{\mathrm{prop}}, \tag{5.2}$$

where i denotes each step in the simulation, t'_i is the interaction time in the simulation, and $\Delta t_i^{\mathrm{prop}}$ is the propagation time from the interaction point to the sensor position. In some detectors, additional

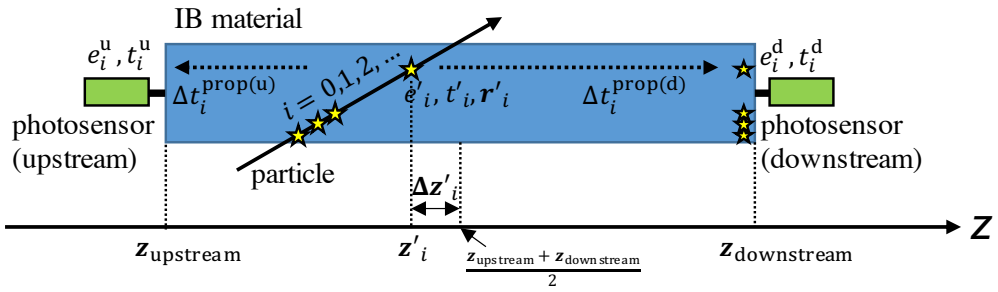

Figure 5.6: Schematic view of IB simulating energies and timings at the interaction positions and the photosensor positions. Each star marker shows each interaction between a particle and detector material. The i denotes each step of the interaction, e'_i is the deposited energy, t'_i is the interaction time, and $\boldsymbol{r}'_i$ is the interaction position in each step. For each simulation step, e'_i and t'_i were converted to energies and timings at the upstream and downstream photosensor positions.

timing smearing was imposed to get a better agreement between data and MC. The energy measured by the photosensor in each simulation step (e_i) was calculated by taking into account the attenuation in the propagation, position dependence of the light yield, and photostatics fluctuation.

5.3.1.2 Procedures in IB

In each IB module, the signal was read by the upstream and downstream photosensors. Figure 5.6 shows the schematic view of IB energies and timings at the interaction positions and those observed at the photosensor positions. In each simulation step, we made energies and timings at the photosensor position based on the energies and timings at the interaction position.

For the energy, we took into account the attenuation of the scintillation light propagating through WLS fibers. The energies measured in upstream photosensor (e_i^{u}) and downstream photosensor (e_i^{d}) from each simulation step were calculated as

$$e_i^{\mathrm{u}} = \frac{e'_i}{2} \exp\left(\frac{-\Delta z'_i}{\Lambda + \alpha \Delta z'_i}\right), \tag{5.3}$$

$$e_i^{\mathrm{d}} = \frac{e'_i}{2} \exp\left(\frac{\Delta z'_i}{\Lambda - \alpha \Delta z'_i}\right), \tag{5.4}$$

where $\Delta z'_i = z'_i - (z_{\mathrm{upstream}} + z_{\mathrm{upstream}})/2$ is the distance between z'_i and the center of IB, and (Λ,α) are the parameters obtained by measurements. The z_{upstream} ($z_{\mathrm{downstream}}$) is the upstream (downstream) end z position of IB, as shown in Fig. 5.6.

For the timings, we considered the propagation time of the scintillation light through WLS fibers, and a timing resolution which is energy dependent. The timings measured in upstream photosensor (t_i^{u}) and downstream photosensor (t_i^{d}) for each i-th simulation step were calculated as

$$t_i^{\mathrm{u}} = t'_i + \Delta t_i^{\mathrm{prop(u)}}, \tag{5.5}$$

$$t_i^{\mathrm{d}} = t'_i + \Delta t_i^{\mathrm{prop(d)}}, \tag{5.6}$$

where $\Delta t_i^{\mathrm{prop(u)}}$ ($\Delta t_i^{\mathrm{prop(d)}}$) is the time of propagation between the interaction position and upstream (downstream) photosensor position. Each propagation time was calculated as

$$\Delta t_i^{\mathrm{prop(u)}} = |z'_i - z_{\mathrm{upstream}}|/v_{\mathrm{prop}} + \mathrm{Gaussian}(\sigma(E_{\mathrm{u}})), \tag{5.7}$$

$$\Delta t_i^{\mathrm{prop(d)}} = |z'_i - z_{\mathrm{downstream}}|/v_{\mathrm{prop}} + \mathrm{Gaussian}(\sigma(E_{\mathrm{d}})), \tag{5.8}$$

where v_{prop} is the effective propagation velocity of light, and $\sigma(E)$ is the timing resolution of IB as a function of the energy. The $\sigma(E) = (19.01/E\,|\mathrm{MeV}|) \oplus 4.534/\sqrt{E\,|\mathrm{MeV}|} \oplus 0.06978$ in ns was used [62], where $E_{\mathrm{u(d)}}$ is the sum of $e_i^{\mathrm{u(d)}}$ in all the simulation step.

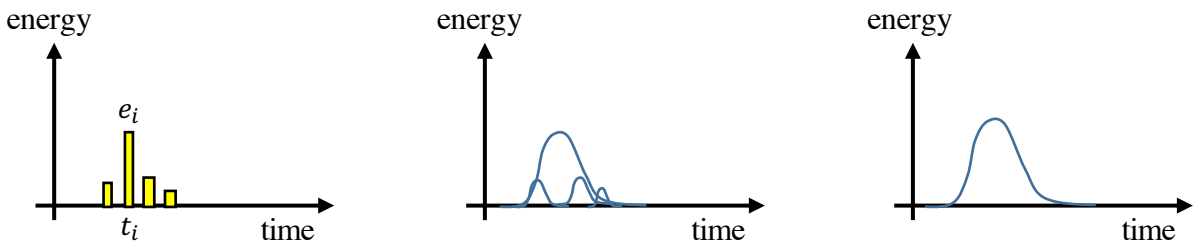

(a) Energies and timings in each step (b) Sub-waveforms in each step (c) Summed up waveform

Figure 5.7: Schematic view of the waveform generation in the MC simulation. From the energies and timings in each simulation step (a), we generated sub-waveforms (b). We finally generated a waveform (c) by summing up sub-waveforms.

5.3.1.3 Procedures in IBCV and MBCV

For IBCV, we used almost the same detector response and parameters as for IB but without smearing the timing by Gaussian. For MBCV, we used energies and timing at the interaction positions.

5.3.2 Generating and Grouping Waveforms

Figure 5.7 shows how the waveforms are generated in the MC simulation. As described in Sec. 4.1, overlapped pulses affect the timing reconstruction in detectors. To reproduce such an effect in MC simulations for each channel, we generated waveforms and overlaid accidental activities. The accidental overlay procedure will be described in Sec. 5.3.3.

We first generated sub-waveforms corresponding to the deposited energy in each simulation step using a "function-based waveform" or "data-based waveform" explained below.

The function-based waveform was implemented in the past analysis. Details of the function-based waveform are available in [31]. For detectors of CC03, CC04, CC05, CSI, IBCV, MBCV, OEV, LCV, and BPCV, each (e_i, t_i) was converted into a waveform with 64 sampling points with the following function,

$$f(t) = A \exp\left(-\frac{(t-t_i)^2}{(\sigma_0 + a(t-t_i))^2}\right), \tag{5.9}$$

where σ_0 and a are parameters given for each detector component, and A is a normalization factor determined by the integration of $f(t)$ to be e_i.

The data-based waveform was implemented and used from this analysis to introduce an overlapped pulse discrimination method (see Sec. 4.3.2.3) in MC simulations. To get a better agreement between data and MC, each (e_i, t_i) was converted into the template of the single-hit waveform in time domain (data-based waveform). We implemented the data-based waveform in FB, NCC, MB, IB, CV, and CC06, whose detector responses with the data-based waveform were studied in this analysis in order to suppress backgrounds originated from overlapped pulses because of their high counting rate.

After we generated sub-waveforms, we summed them in each sampling point to make an output waveform.

5.3.3 Accidental Overlay

To reproduce accidental activities and baseline fluctuations in a MC simulation, accidental activities in detectors were overlaid on the MC events. For accidental activities in detectors, we used waveforms recorded with TMon-trigger during physics data taking because the TMon trigger reflected the instantaneous rate of the beam, as mentioned in Sec. 3.3.1.1

Figure 5.8 shows an example of an accidental overlay in the MC simulation of $K_L \to 2\pi^0$ for a channel in the IB detector.

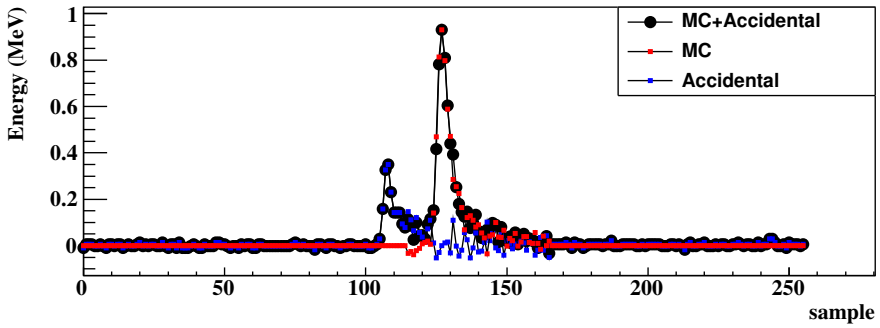

Figure 5.8: Example of an accidental overlay in the MC simulation of $K_L \to 2\pi^0$ in IB. Red rectangles show the waveform generated in the MC simulation (true waveform). Blue rectangles show the accidental activity recorded with TMon-trigger (accidental waveform). Each black dot is the sum of the true and accidental waveform in each sample.

After we generated the waveform overlaid with accidental activities, we reconstructed the energy and timing using the same procedure as for data, as described in Sec. 4.1.

Chapter 6

Outline of 2016–2018 Data Analysis

In this chapter, we describe the outline of the analysis procedures to examine the blind region and the flow of the 2016–2018 data analysis after examining the blind region.

6.1 Outline of Analysis

The outline of the analysis procedures to examine the blind region is shown in Fig. 6.1. For the data sample, we first calibrated detectors and checked the stability of detectors to ensure their performance. After that, we reconstructed π^0's and K_L's with the procedures described in Chapter 4. To avoid human bias in the determination of the selection criteria for $K_L \to \pi^0\nu\overline{\nu}$ (cuts), we did not record the event in the dataset used in the analysis if the number of clusters was two and the π^0 was reconstructed inside the blind region (blinding). For the MC simulation sample, we first generated MC events with the procedures described in Chapter 5 and reconstructed π^0's and K_L's.

We then estimated the number of K_L's at the beam-exit (K_L yield) using $K_L \to 2\pi^0$ samples to estimate the sensitivity for $K_L \to \pi^0\nu\overline{\nu}$ search and normalize background yields. We also analyzed $K_L \to 3\pi^0$ and $K_L \to 2\gamma$ decays to cross-check the results. This analysis was called the normalization mode analysis.

Based on the K_L yield, we estimated the numbers of background events and the sensitivity. The cuts were optimized to maximize the signal acceptance while suppressing the number of background events. After we decided on the cuts, we examined the blind region (unblinding). We never changed the cuts after we examined the blind region.

6.2 After Unblinding

The flow of the 2016–2018 data analysis after unblinding is shown in Fig. 6.2. In the 2016–2018 data analysis, when we determined the cuts, the number of background events was expected to be < 0.1 events. However, we observed four candidate events in the signal region and one extra event in the blind region but outside the signal region [63]. The number of observed events was not consistent with our background estimations, and thus we checked properties of the candidate events and looked for new background sources.

By checking properties of the candidate events, we found an incorrect parameter setting which affected the timing used to veto events with multiple pulses in the veto counters. Figure 6.3 shows the waveform of HINEMOS in one of the candidate events at the time. In this waveform, two peak candidates existed in 33.9 and 47.8 clock, which were determined by the parabola's peak timing as described in Sec. 4.1. Because the nominal timing was incorrectly set to be 41.3 clock, the latter candidate of the peak was selected as the peak, even though the former candidate peak existed inside the veto window. After we corrected the nominal timing parameters, we processed the data again without changing any cuts.

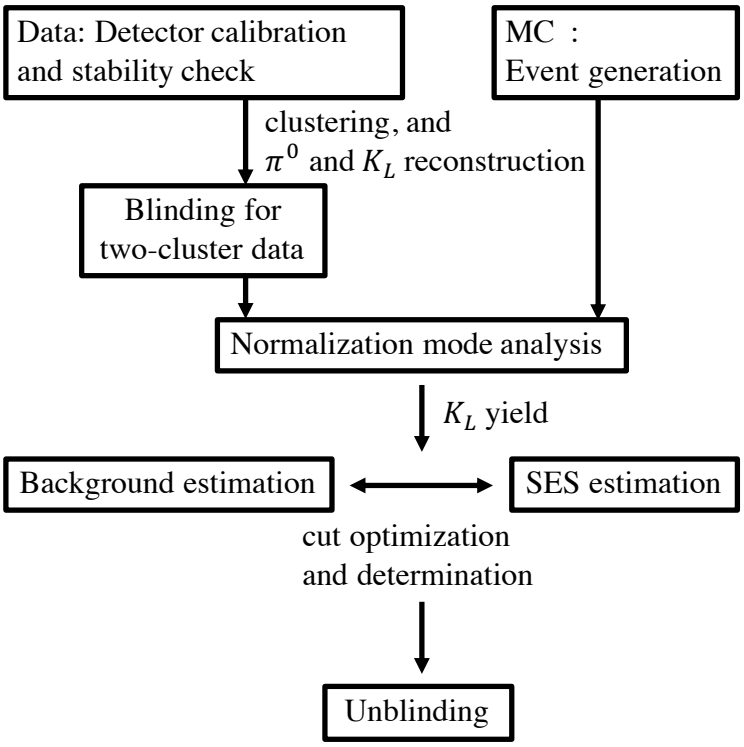

Figure 6.1: Analysis outline to examine the blind region.

Figure 6.4 shows the reconstructed π^0 P_t vs. $Z_{\rm vtx}$ for the events after imposing the $K_L \to \pi^0\nu\overline{\nu}$ selection criteria on the reprocessed data. With the reprocessed data, three of the original four candidate events remained in the signal region. We re-estimated SES for the reprocessed data.

After investigations, we found two new types of backgrounds, one from $K^{\pm}$ decays and one from beam-halo $K_L \to 2\gamma$ decays. We thus updated the expected number of background events with the new background sources.

In this thesis, we describe the results of the 2016–2018 data analysis using the reprocessed data. Details of the normalization mode analysis, sensitivity estimation, and background estimation will be described in the following Chapters.

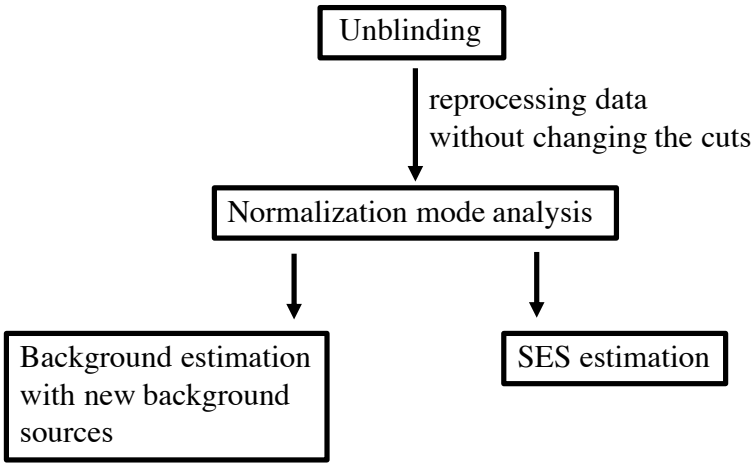

Figure 6.2: Flow of the 2016–2018 data analysis after unblinding.

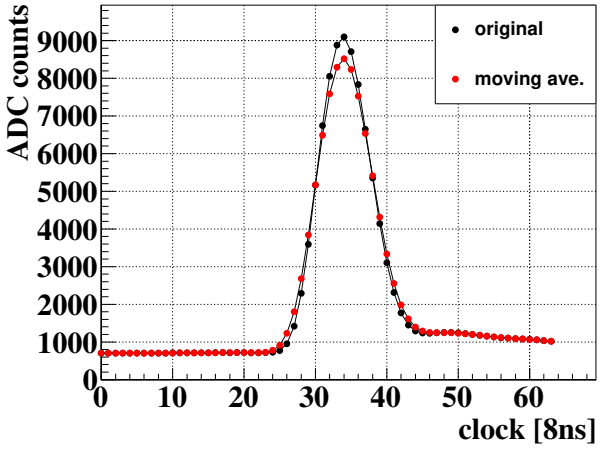

Figure 6.3: Example of the original and smoothed waveform in HINEMOS. The black (red) dots represent the original (smoothed) waveform. In this waveform, peak candidates exist around 34 and 48 clock.

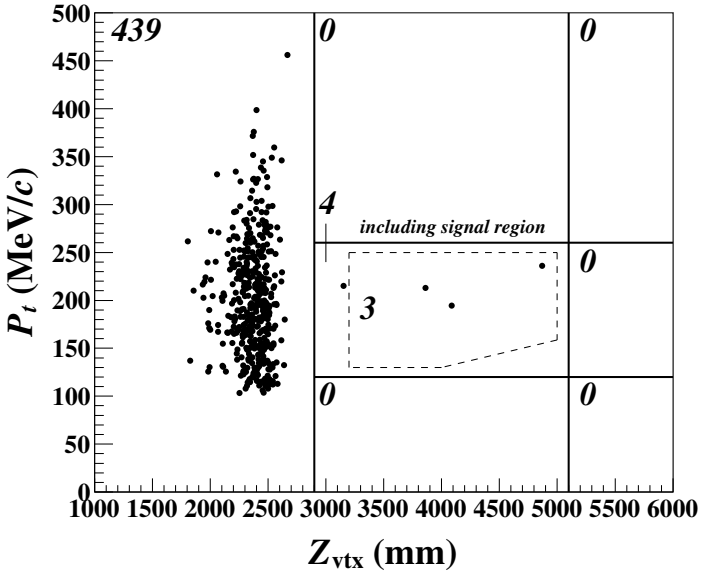

Figure 6.4: Reconstructed π^0 transverse momentum (P_t) vs. π^0 decay vertex position ($Z_{\rm vtx}$) for the events after imposing the $K_L \to \pi^0\nu\overline{\nu}$ selection criteria. The region surrounded by dotted lines is the signal region. The black dots represent observed events, and the numbers indicate the number of observed events in each region.

Chapter 7

Sensitivity for $K_L \to \pi^0 \nu\overline{\nu}$

The sensitivity of the 2016–2018 data for $K_L \to \pi^0 \nu\overline{\nu}$ is described in this chapter. The SES is calculated with Eq. 2.8. As described in Sec. 4, we used a prescale factor p for the normalization trigger. The SES is thus

$$\mathrm{SES} = \frac{1}{A_{\mathrm{sig}}} \frac{A_{\mathrm{norm}}\ \mathcal{B}(K_L \to 2\pi^0)}{p N_{\mathrm{norm}}}, \tag{7.1}$$

where N_{norm} is the number of events after imposing all the $K_L \to 2\pi^0$ selection criteria in the normalization trigger data. To estimate SES, we determined A_{sig}, A_{norm}, and N_{norm}.

We first describe the analysis of the normalization modes to estimate A_{norm}, and N_{norm} in Sec. 7.1. We then describe the signal acceptance and SES in Sec. 7.2. Finally, we describe the uncertainty on SES in Sec. 7.2.

7.1 Normalization Mode Analysis

The purpose of this section is to determine A_{norm}, and N_{norm} in Eq. 7.1 for the $K_L \to 2\pi^0$ decays sample. The other normalization modes, such as $K_L \to 3\pi^0$ and $K_L \to 2\gamma$ decays, were also analyzed to cross-check the results.

7.1.1 Dataset

In this section, data samples and MC simulation samples used in the normalization analysis are described.

Data Sample As the data sample, the dataset taken with the normalization trigger was used in the normalization mode analysis. Because we took the physics and normalization trigger data separately in 2016 as described in Sec. 3.1, the method to estimate the correction factor (p) in Eq. 7.1 for the 2016 data differed from the one for the 2017–2018 data. Note that notations of data taking periods are described in Sec. 3.1.

For the 2016 data, to estimate the number of $K_L \to 2\pi^0$ events in the physics trigger data, the correction factor (p) was calculated as

$$p = \frac{\mathrm{POT}_{\mathrm{phys}}}{\mathrm{POT}_{\mathrm{norm}}/\mathrm{Prescale}_{\mathrm{norm}}}, \tag{7.2}$$

where $\mathrm{POT}_{\mathrm{phys\ (norm)}}$ is the number of protons on target used in the physics (normalization) trigger data after taking into account the DAQ live ratio, and $\mathrm{Prescale}_{\mathrm{norm}}$ is the prescale factor used in the normalization trigger data. The physics trigger was not prescaled. The $\mathrm{Prescale}_{\mathrm{norm}}$, $\mathrm{POT}_{\mathrm{phys\ (norm)}}$, and p are summarized in Table 7.1.

For the 2017–2018 data, $\mathrm{POT}_{\mathrm{norm}} = \mathrm{POT}_{\mathrm{phys}}$ in Eq. 7.2, thus the correction factor (p) is 30, simply the prescale factor used for the normalization trigger.

Table 7.1: Summary of the correction factor p and the number of protons on target used in the physics (normalization) trigger data.

year	period	$\text{Prescale}_{\text{norm}}$	POT_{norm}	POT_{phys}	p
2016	Run69.0	7	0.36×10^{18}	1.78×10^{18}	34.5
	Run69.1	7	0.35×10^{18}	1.34×10^{18}	26.8
2017	Run75.0	30	0.27×10^{18}	0.27×10^{18}	30
	Run75.1	30	0.58×10^{18}	0.58×10^{18}	30
	Run75.2	30	7.31×10^{18}	7.31×10^{18}	30
2018	Run78.0	30	0.51×10^{18}	0.51×10^{18}	30
	Run78.1	30	0.21×10^{18}	0.21×10^{18}	30
	Run78.2	30	7.36×10^{18}	7.36×10^{18}	30
	Run79.0	30	11.14×10^{18}	11.14×10^{18}	30

Table 7.2: Summary of the number of simulated K_L's used for the normalization mode analysis. In this table, the periods of Run75.2, Run78.2, and Run79.0 are categorized as period A, and the other periods are categorized as period B.

decay mode	branching fraction	$N_{K_L}^{\text{sim}}$ for period A	$N_{K_L}^{\text{sim}}$ for period B
$K_L \to 3\pi^0$	19.52%	1×10^9	2×10^8
$K_L \to 2\pi^0$	8.64×10^{-4}	1×10^9	2×10^8
$K_L \to 2\gamma$	5.47×10^{-4}	1×10^9	2×10^8

MC Simulation Sample The K_L's were generated using the beam-core K_L seeds described in Sec. 5.1.1. The MC simulation sample of $K_L \to 2\pi^0$, $K_L \to 3\pi^0$, and $K_L \to 2\gamma$ decays were generated separately. Table 7.2 summarizes the number of simulated K_L's used for the normalization mode analysis. In the normalization mode analysis, a contribution from K_L decays other than the normalization decay modes was negligibly small based on a past study [31].

7.1.2 Selection Criteria

In this section, the selection criteria (cuts) for the normalization mode analysis are described.

To reconstruct decays from the normalization modes, we required all the photons from the normalization modes hitting CSI, and reconstructed K_L's using the procedures described in Chapter 4. To ensure that there are no other detectable particles, we imposed veto cuts on the events. To purify normalization samples, we further imposed the cuts based on information from CSI.

All the cuts on veto counters were the same as the cuts used in the $K_L \to \pi^0\nu\overline{\nu}$ analysis, and they are summarized in Table 7.3. All the cuts on CSI are summarized in Table 7.4, and are explained below. In Table 7.4, the same cuts used for the $K_L \to \pi^0\nu\overline{\nu}$ analysis are noted.

- trigger timing
  Because of the short dead time of the trigger system, timing windows of multiple triggered events possibly overlap, and such event can be recorded twice as different events. To eliminate such events, the average of photon timings (trigger timing) was required to be within ± 15 ns of the nominal trigger timing.

- total energy
  As described in Sec. 3.2.1, we used the CSIEt trigger with the threshold of 550 MeV. However, the effective threshold at the online trigger stage was smeared due to the differences of gains between channels. To remove such bias in the offline analysis, the sum of photon energies (total energy) was required to be larger than 650 MeV.

- photon energy
  To ensure the quality of photon reconstruction, each photon energy was required to be larger than 50 MeV

- photon position
  To reject photons with a large electromagnetic shower leakage, the photon hit position (x, y) on CSI was required to be within the CSI fiducial region defined as $\sqrt{x^2 + y^2} \leq 850$ mm and $\min(|x|, |y|) \geq 150$ mm.

- two-photon distance
  To separate each electromagnetic shower, the distances between photons for all the possible pairs were required to be larger than 150 mm

- $\Delta T_{\rm vtx}^{\rm K_L}$
  To reduce the events caused by photons from accidental activities, the maximum difference between $T_{\rm vtx}^{\rm K_L}$ and vertex time of each photon ($\Delta T_{\rm vtx}^{\rm K_L}$), defined as $\max(|T_{\rm vtx}^{\rm K_L} - t_{\rm vtx}^{i}|)$, was required to be smaller than 3 ns.

- $Z_{\rm vtx}^{\rm K_L}$
  The $Z_{\rm vtx}^{\rm K_L}$ was required to be inside the decay volume of the KOTO detector, $3000 \leq Z_{\rm vtx}^{\rm K_L} \leq 5000$ mm.

- K_L P_t
  Because we use a narrow beam and require that there are no missing particles in the normalization mode analysis, the reconstructed P_t of K_L is expected to be small. We required the reconstructed P_t of K_L to be smaller than 50 MeV/c.

- K_L mass
  The invariant mass of photons in the K_L reconstruction was required to be within ± 15 MeV/c^2 from the nominal K_L mass of 497.614 MeV/c^2 [5]. This requirement was not used in the $K_L \to 2\gamma$ analysis because K_L's were reconstructed by assuming the K_L mass.

- χ_z^2
  To ensure the consistency of π^0 vertexes, the χ_z^2, defined in Eq. 4.15, was required to be less than 20 for the $K_L \to 3\pi^0$ and $K_L \to 2\pi^0$ candidates.

- $\Delta Z_{\rm vtx}$
  To ensure the consistency of π^0 vertexes, the $\Delta Z_{\rm vtx}$, defined in Eq. 4.15, was required to be less than 400 mm for the $K_L \to 3\pi^0$ and $K_L \to 2\pi^0$ candidates.

- $\Delta\pi^0$ mass
  In the K_L reconstruction for $K_L \to 3\pi^0$ and $K_L \to 2\pi^0$ decays, π^0's were re-reconstructed by adjusting the decay vertex x-y position. In such a re-reconstruction, the invariant mass of two photons ($M_{\gamma\gamma}$) was re-calculated. The agreement between $M_{\gamma\gamma}$ and the nominal π^0 mass of 134.9766 MeV/c^2 [5] reflects the consistency of vertexes among the π^0's. We required the $M_{\gamma\gamma}$'s to be within ± 10 (6) MeV/c^2 from the nominal π^0 mass for the $K_L \to 3\pi^0$ ($K_L \to 2\pi^0$) candidates.

- K_L position at the beam-exit
  To reduce events with missing particles in the $K_L \to 2\pi^0$ analysis, we required the (x, y) positions of K_L's at the beam-exit $\boldsymbol{R}_{\rm exit} = (X_{\rm exit}, Y_{\rm exit})$ to be inside the beam core region. The $\boldsymbol{R}_{\rm exit}$ were reconstructed using the positions of the center of deposited energy in CSI as

$$\boldsymbol{R}_{\rm exit} = \frac{Z_{\rm exit} - Z_{\rm target}}{Z_{\rm CSI} - Z_{\rm target}} \boldsymbol{R}_{\rm COE}, \tag{7.3}$$

  where $Z_{\rm exit}$, $Z_{\rm target}$, and $Z_{\rm CSI}$ are the z positions of the beam-exit, the production target, and the upstream surface of CSI, respectively. We required $\max(|X_{\rm exit}|, |Y_{\rm exit}|) \leq 50$ mm.

Table 7.3: Veto window and veto energy threshold of each detector component.

detector component	energy threshold	veto window width	χ^2_{FFT}
FB	1 MeV	51 ns	
FB (wide window)	3.2 MeV	170 ns	20 [a]
NCC	1 MeV	40 ns	
NCC (wide window)	3.2 MeV	100 ns	40 [a]
HINEMOS	1 MeV	60 ns	
IB	1 MeV	50 ns	
MB	1 MeV	40 ns	
IBCV	0.5 MeV	60 ns	
MBCV	0.5 MeV	60 ns	
CV	0.2 MeV	20 ns	
CV (wide window)	0.4 MeV	150 ns	12 [a]
CC03	3 MeV	60 ns	
LCV	0.6 MeV	30 ns	
CSI (isolated hit crystal)		see Sec. 4.3.1.1	
CSI (extra-cluster)		see Sec. 4.3.1.2	
CC04, CC05, CC06 (CsI crystal)	3 MeV	30 ns	
CC04, CC05, CC06 (plastic scintillator)	1 MeV	30 ns	
OEV	1 MeV	20 ns	
BPCV	1 MeV	24 ns	
newBHCV	221 eV	25 ns [b]	
BHPV	2.5 p.e.	15 ns [c]	
BHGC	2.5 p.e.	15 ns [d]	

[a] The wide veto was used when the χ^2_{FFT} exceeded the given threshold. See Sec. 4.3.2.3
[b] The newBHCV adopted the 2-out-of-3 method and the energy threshold here is for the layer-veto-energy.
[c] The BHPV veto was based on the number of consecutive hit modules and if it was three or more, such an event was vetoed.
[d] The BHGC used the number of equivalent photons instead of energy for the veto decision.

Table 7.4: Summary of the selection criteria used in the normalization mode analysis.

selection	$K_L \to 3\pi^0$	$K_L \to 2\pi^0$	$K_L \to 2\gamma$
trigger timing [a]		$\leq \pm 15$ ns	
total energy [a]		$E_{\mathrm{tot}} \geq 650$ MeV	
photon energy		$E_\gamma \geq 50$ MeV	
photon position [a]		$\max(\lvert x\rvert, \lvert y\rvert) \geq 150$ mm	
		$\sqrt{x^2+y^2} \leq 850$ mm	
two-photon distance		$d \geq 150$ mm	
$\Delta T^{\mathrm{K_L}}_{\mathrm{vtx}}$		$\Delta T^{\mathrm{K_L}}_{\mathrm{vtx}} \leq 3$ ns	
$Z^{\mathrm{K_L}}_{\mathrm{vtx}}$		$3000 \leq Z^{\mathrm{K_L}}_{\mathrm{vtx}} \leq 5000$ mm	
K_L P_t		$P_t \leq 50$ MeV/c	
K_L mass	$\leq \pm 15$ MeV/c^2	$\leq \pm 15$ MeV/c^2	–
χ^2_z	$\chi^2_z \leq 20$	$\chi^2_z \leq 20$	–
ΔZ_{vtx}	$\Delta Z_{\mathrm{vtx}} \leq 400$ mm	$\Delta Z_{\mathrm{vtx}} \leq 400$ mm	–
π^0 mass	$\leq \pm 10$ MeV/c^2	$\leq \pm 6$ MeV/c^2	–
K_L pos. at beam exit	–	$\max(\lvert X_{\mathrm{exit}}\rvert, \lvert Y_{\mathrm{exit}}\rvert) \leq 50$ mm	–

[a] The same cut used for the $K_L \to \pi^0\nu\overline{\nu}$ analysis.

7.1.3 Distributions of Kinematics

In this section, distributions of kinematic variables are described for each normalization mode decay.

7.1.3.1 $K_L \to 2\pi^0$ Decays

The $K_L \to 2\pi^0$ decays were used to calculate SES for the $K_L \to \pi^0 \nu\overline{\nu}$ decay. Figures 7.1 and 7.2 show distributions of kinematic variables after imposing $K_L \to 2\pi^0$ cuts except for the cut of interest with the dataset taken in the period of Run79.0. Figure 7.1a shows the reconstructed K_L mass distribution before requiring the nominal K_L mass. Events in the small K_L mass region come from fused clusters made from two or more photons from $K_L \to 3\pi^0$ decays hitting CSI close to each other. Most contaminations due to such fused clusters can be reduced by requiring the nominal K_L mass. Near the nominal K_L mass, the mass peak is slightly shifted, but the cause of this shift has not been understood. Figure 7.1c shows the distribution of the reconstructed $Z_{\rm vtx}$ of the K_L. The cause of the discrepancy in $Z_{\rm vtx} \sim 2800$ mm has not been understood, but the uncertainty on the sensitivity from this discrepancy was found to be small, as will be described in Sec. 7.3.3.6. Figure 7.1f shows the $\Delta T_{\rm vtx}^{\rm K_L}$ distribution. A discrepancy in $\Delta T_{\rm vtx}^{\rm K_L}$ implies that we do not fully understand the timing response of CSI. To avoid the uncertainty from the cut efficiency difference between data and MC, a loose threshold of 3 ns for the $\Delta T_{\rm vtx}^{\rm K_L}$ cut was used. Except for these discrepancies, the data and MC simulations agreed well, and this validates the beam properties and detector responses in MC simulations.

7.1.3.2 $K_L \to 3\pi^0$ and $K_L \to 2\gamma$ Decays

The $K_L \to 3\pi^0$ and $K_L \to 2\gamma$ decay samples were used to cross-check kinematic variables. Figures 7.3 and 7.4 show distributions of kinematic variables after imposing cuts except for the cut of interest with the dataset taken in the period of Run79.0 for $K_L \to 3\pi^0$ and $K_L \to 2\gamma$ samples, respectively.

For the $K_L \to 3\pi^0$ sample, a purity is high because no other K_L decay modes make six photon clusters on CSI. The tail in the K_L mass distribution shown in Fig. 7.3a was caused by the mis-reconstruction of $Z_{\rm vtx}$ due to mis-combinations in the π^0 reconstruction. The requirement on the K_L mass reduces such events. The distributions of K_L mass and $\Delta T_{\rm vtx}^{\rm K_L}$ (Fig. 7.3f) in the allowed region have similar discrepancies as in the $K_L \to 2\pi^0$ decays analysis. Except for these discrepancies of the K_L mass peak and the $\Delta T_{\rm vtx}^{\rm K_L}$, the data and MC simulations agreed well.

For the $K_L \to 2\gamma$ sample, the $Z_{\rm vtx}$ of $K_L \to 2\gamma$ decays was reconstructed using the same strategy as for the π^0 reconstruction; the nominal K_L mass was used instead of the nominal π^0 mass. The x and y vertex positions were calculated in the same way as the $K_L \to 2\pi^0$ and $K_L \to 3\pi^0$ reconstruction. The distribution of $\Delta T_{\rm vtx}^{\rm K_L}$ (Fig. 7.4d) has a similar discrepancy as the $K_L \to 2\pi^0$ decays. Except for the $\Delta T_{\rm vtx}^{\rm K_L}$, the data and MC simulations agreed well. These agreements validate the beam properties and detector responses in MC simulations.

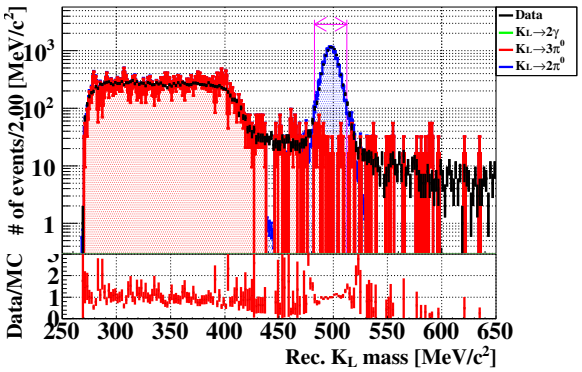

(a) K_L mass

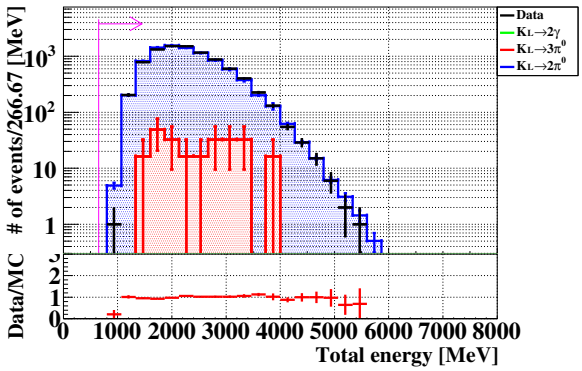

(b) total energy

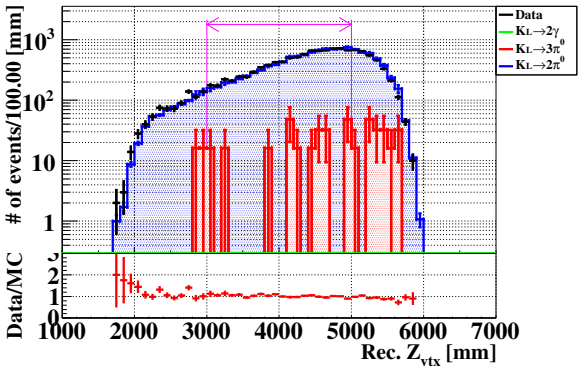

(c) K_L reconstructed $Z_{\rm vtx}$

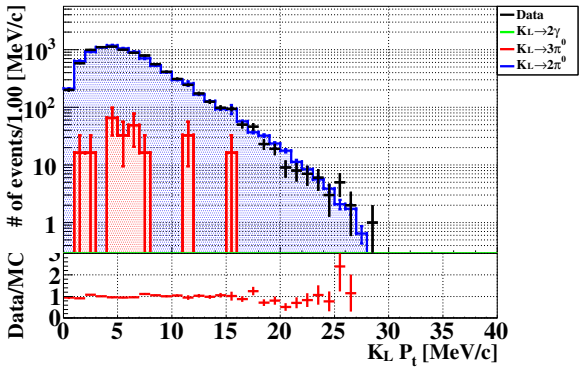

(d) K_L P_t

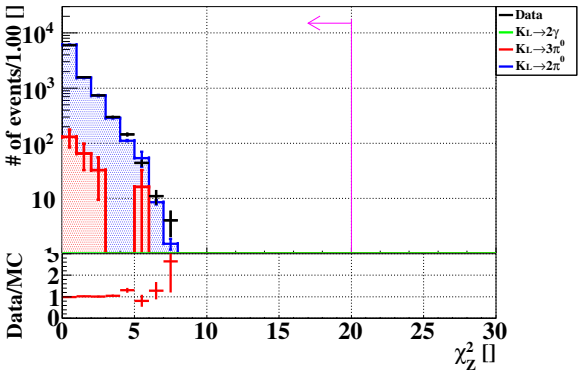

(e) χ^2_z

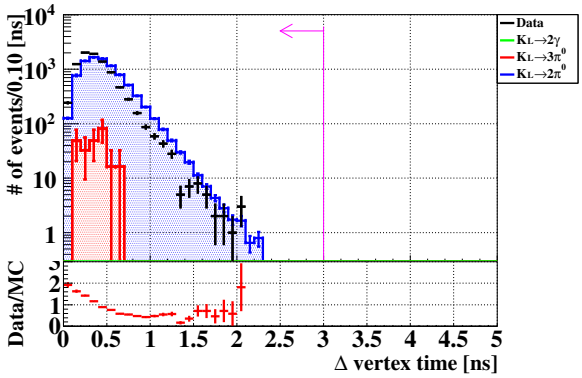

(f) $\Delta T^{\rm K_L}_{\rm vtx}$

Figure 7.1: Distributions of the reconstructed $K_L \to 2\pi^0$ events for K_L mass (a), total energy (b), $Z^{\rm K_L}_{\rm vtx}$ (c), K_L P_t (d), χ^2_z (e), and $\Delta T^{\rm K_L}_{\rm vtx}$ after imposing cuts for $K_L \to 2\pi^0$ except for the cut of interest. Black points represent data. Red, blue, and green histograms represent MC simulations of $K_L \to 3\pi^0$, $K_L \to 2\pi^0$, and $K_L \to 2\gamma$, respectively. The contribution from $K_L \to 2\gamma$ was negligibly small. Magenta lines show the accepted region. The data/MC ratios are shown below each panel. The error bars represent statistical errors.

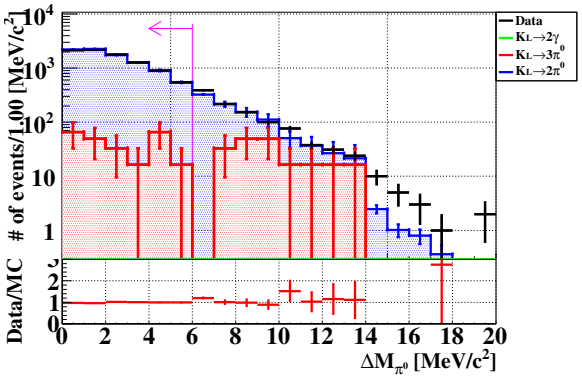

(a) Absolute value of $\Delta\pi^0$ mass

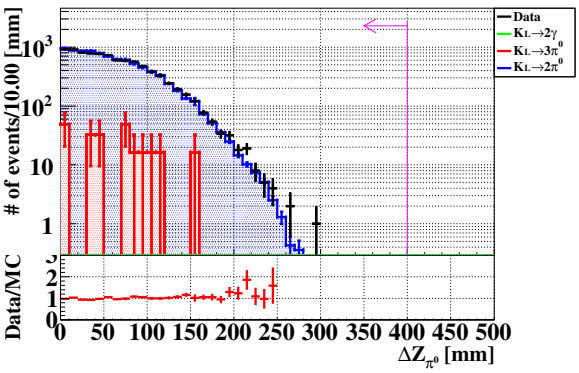

(b) $\Delta Z_{\rm vtx}$

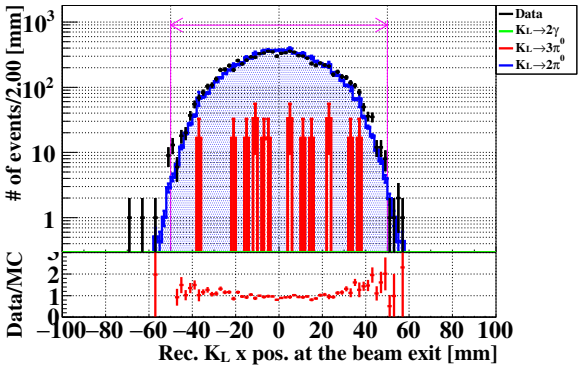

(c) K_L pos. at beam exit (x)

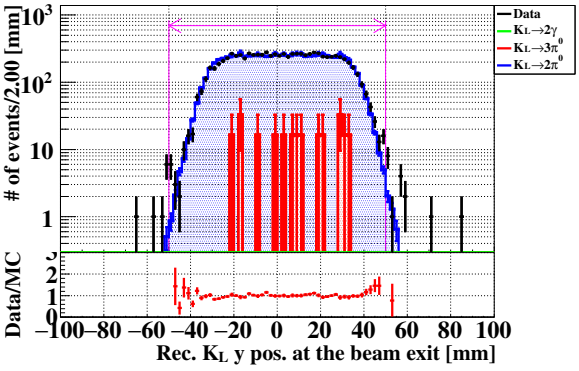

(d) K_L pos. at beam exit (y)

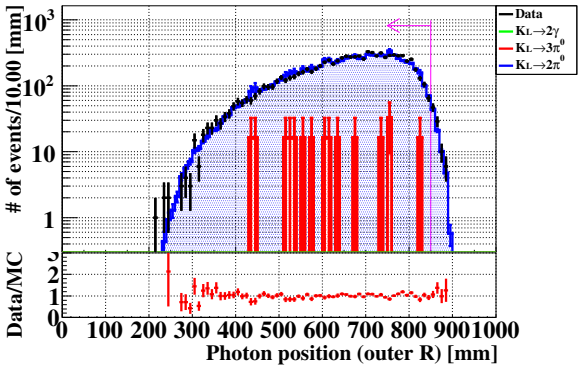

(e) Photon hit position (outer R)

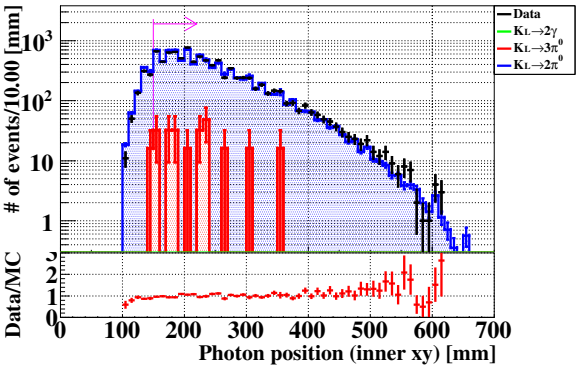

(f) Photon hit position (inner xy)

Figure 7.2: Distributions of reconstructed $K_L \to 2\pi^0$ events for absolute value of $\Delta\pi^0$ mass (a), $\Delta Z_{\rm vtx}$ (b), K_L positions at beam-exit for x (c) and y (d), and outer (e) and inner (f) hit positions of photons after imposing cuts for $K_L \to 2\pi^0$ except for the cut of interest. The meaning of the black points, colors of histograms, lines in magenta, below panel, and error bars are the same as for Fig. 7.1. The contribution from $K_L \to 2\gamma$ was negligibly small.

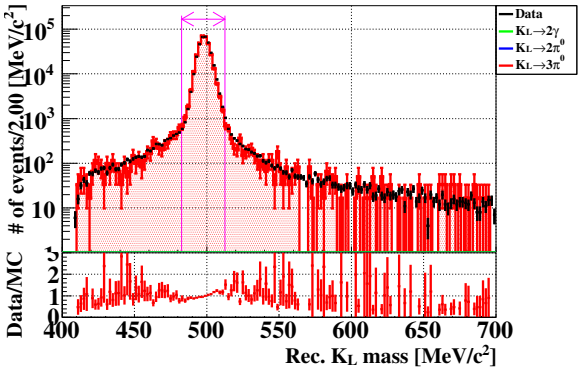

(a) K_L mass

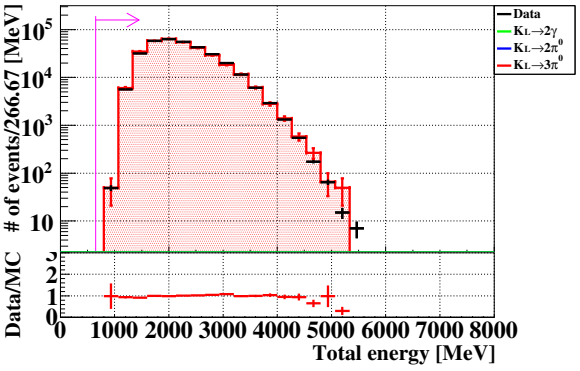

(b) total energy

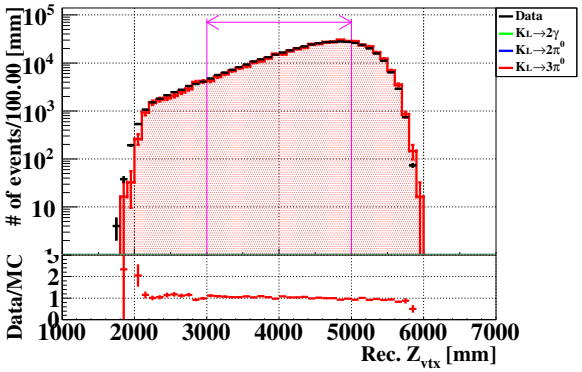

(c) K_L reconstructed $Z_{\rm vtx}$

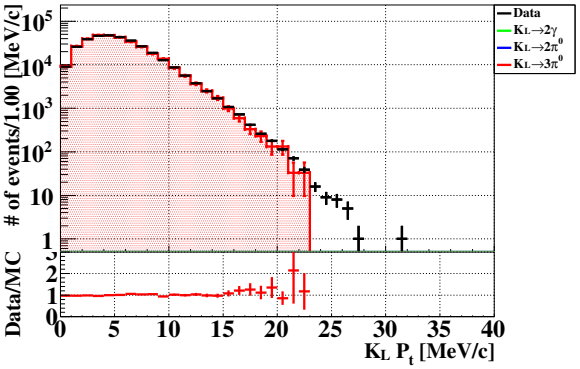

(d) K_L P_t

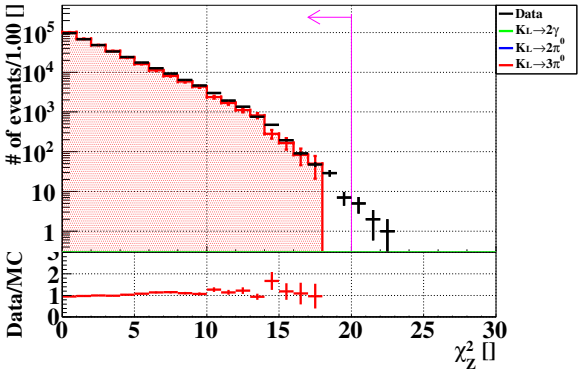

(e) χ^2_z

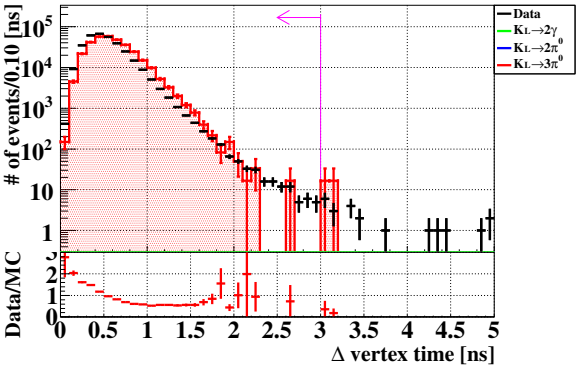

(f) $\Delta T^{\rm K_L}_{\rm vtx}$

Figure 7.3: Distributions of reconstructed $K_L \to 3\pi^0$ events for K_L mass (a), total energy (b), $Z^{\rm K_L}_{\rm vtx}$ (c), K_L P_t (d), χ^2_z (e) and $\Delta T^{\rm K_L}_{\rm vtx}$ (f) after imposing $K_L \to 3\pi^0$ cuts except for the cut of interest. The meaning of the black points, colors of histograms, lines in magenta, below panel, and error bars are the same as for Fig. 7.1. For the $K_L \to 3\pi^0$ sample, a purity is high because no other K_L decay modes make six photon clusters on CSI.

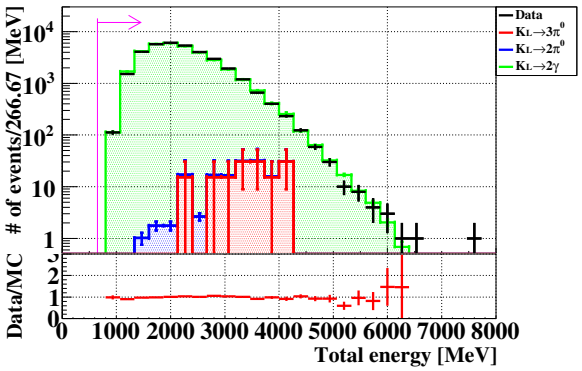

(a) total energy

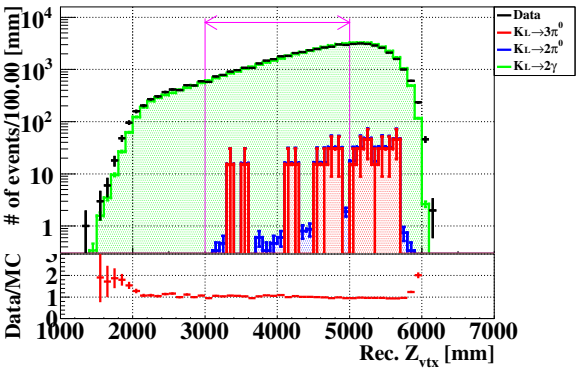

(b) K_L reconstructed $Z_{\rm vtx}$

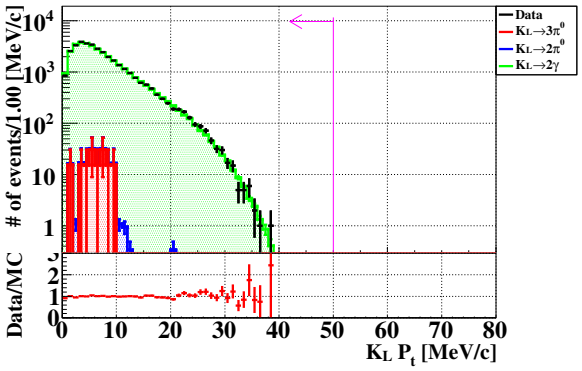

(c) K_L P_t

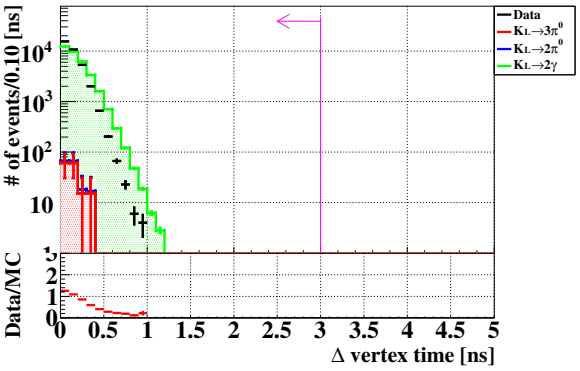

(d) $\Delta T^{\rm K_L}_{\rm vtx}$

Figure 7.4: Distributions of reconstructed $K_L \to 2\gamma$ events for total energy (a), $Z^{\rm K_L}_{\rm vtx}$ (b), K_L P_t (c), and $\Delta T^{\rm K_L}_{\rm vtx}$ (d) after imposing cuts for $K_L \to 2\gamma$ except for the cut of interest. The meaning of the black points, colors of histograms, lines in magenta, below panel, and error bars are the same as for Fig. 7.1.

Table 7.5: Summary of the A_{norm}, p, N_{norm}, K_L yield and K_L flux. $K_L \to 2\pi^0$ decays samples were used.

year	period	A_{norm}	p	N_{norm}	K_L yield	K_L flux [$/2 \times 10^{14}$ POT]
2016	Run69.0	1.49×10^{-4}	34.5	1243	3.40×10^{11}	$(3.82 \pm 0.13) \times 10^7$
	Run69.1	1.45×10^{-4}	26.8	1167	2.57×10^{11}	$(3.85 \pm 0.13) \times 10^7$
2017	Run75.0	1.98×10^{-4}	30	359	6.48×10^{10}	$(4.80 \pm 0.26) \times 10^7$
	Run75.1	1.89×10^{-4}	30	739	1.41×10^{11}	$(4.84 \pm 0.20) \times 10^7$
	Run75.2	1.69×10^{-4}	30	8083	1.71×10^{12}	$(4.68 \pm 0.06) \times 10^7$
2018	Run78.0	1.71×10^{-4}	30	527	1.11×10^{11}	$(4.35 \pm 0.21) \times 10^7$
	Run78.1	1.24×10^{-4}	30	172	4.88×10^{10}	$(4.73 \pm 0.37) \times 10^7$
	Run78.2	1.14×10^{-4}	30	5387	1.67×10^{12}	$(4.53 \pm 0.07) \times 10^7$
	Run79.0	1.27×10^{-4}	30	8846	2.49×10^{12}	$(4.48 \pm 0.06) \times 10^7$
Total		1.39×10^{-4}		26523	6.83×10^{12}	$(4.54 \pm 0.04) \times 10^7$

7.1.4 Results of Normalization Mode Analysis

The A_{norm}, p, N_{norm}, K_L yield, and K_L flux are summarized in Table 7.5. The A_{norm} was calculated by

$$A_{\text{norm}} = \frac{N^{\text{rem}}_{K_L \to 2\pi^0}}{N^{\text{sim}}_{K_L \to 2\pi^0}}, \tag{7.4}$$

where $N^{\text{rem}}_{K_L \to 2\pi^0}$ is the number of remaining events after imposing the $K_L \to 2\pi^0$ selection criteria on the $K_L \to 2\pi^0$ MC simulation, and $N^{\text{sim}}_{K_L \to 2\pi^0}$ is the number of generated $K_L \to 2\pi^0$ events in the $K_L \to 2\pi^0$ MC simulation. Because we defined N_{norm} as the number of remaining events after imposing all the $K_L \to 2\pi^0$ selection criteria, we needed to take into account contaminations from other K_L decays in N_{norm}. We found a contamination of 3% from other K_L decays in the $K_L \to 2\pi^0$ decay analysis, and corrected A_{norm} by 3%. The K_L flux is defined as

$$K_L \text{ flux} = \frac{K_L \text{ yield}}{\text{POT}}. \tag{7.5}$$

Figures 7.5, 7.6, and 7.7 show the K_L flux estimated with decay samples of $K_L \to 2\pi^0$, $K_L \to 3\pi^0$, and $K_L \to 2\gamma$, respectively. The K_L flux estimated from $K_L \to 2\pi^0$ decays fluctuated between the periods by 21% at maximum due to the efficiency difference of veto cuts between data and MC. However, the ratio of K_L flux estimated with $K_L \to 2\pi^0$ to $K_L \to 3\pi^0$ or $K_L \to 2\gamma$, shown in Fig. 7.8, fluctuated within a statistical uncertainty between periods. This indicates that the uncertainty from a part of veto cuts between periods is canceled out by taking the ratio of two decay modes. The estimation of the uncertainty on SES from veto cuts will be described in Sec. 7.3.3.4.

Figure 7.9 shows the K_L flux estimated with normalization decay modes using the whole dataset. The flux estimated with $K_L \to 3\pi^0$ and $K_L \to 2\pi^0$ decay samples agreed within an uncertainty. However, the flux estimated with $K_L \to 2\gamma$ decay samples was 5.2% smaller than the one with $K_L \to 2\pi^0$ decays samples. We have not fully understood the cause of the difference between the normalization decay modes, and thus we took the difference into account as a systematic uncertainty on SES.

With the dataset taken in 2016–2018, the K_L yield was estimated to be 6.83×10^{12}, which corresponds to 1.5 times larger than the previous $K_L \to \pi^0 \nu\overline{\nu}$ search [35].

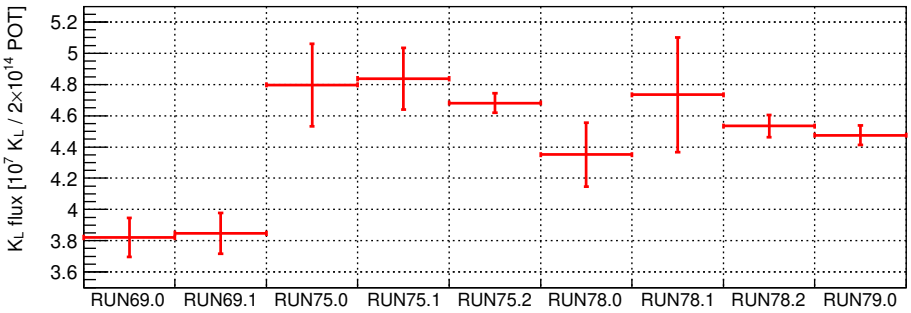

Figure 7.5: K_L flux estimated for each run period with $K_L \to 2\pi^0$ decay samples. The error bars represent statistical errors.

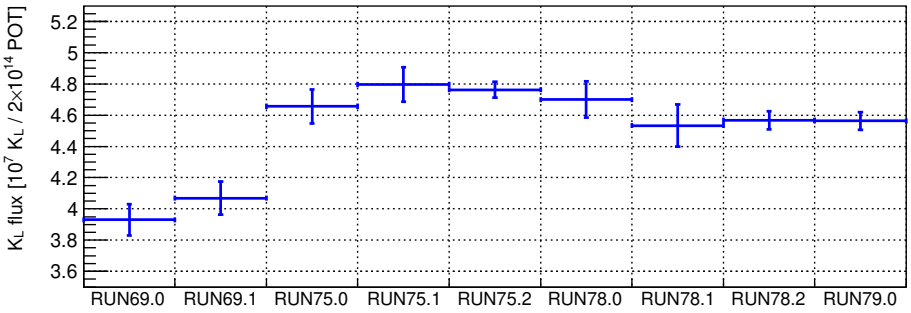

Figure 7.6: K_L flux estimated for each run period with $K_L \to 3\pi^0$ decay samples. The error bars represent statistical errors.

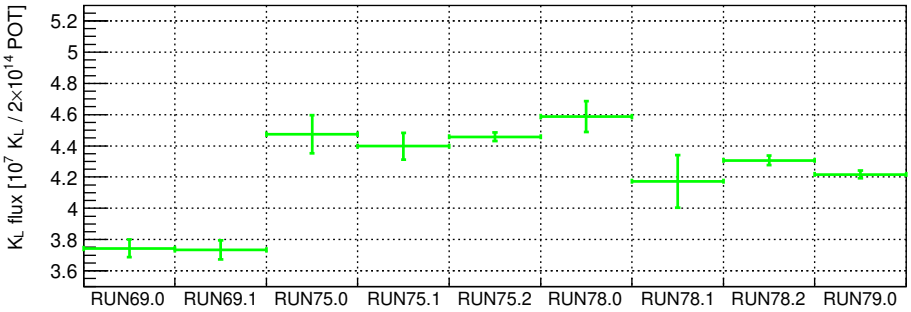

Figure 7.7: K_L flux estimated for each run period with $K_L \to 2\gamma$ decay samples. The error bars represent statistical errors.

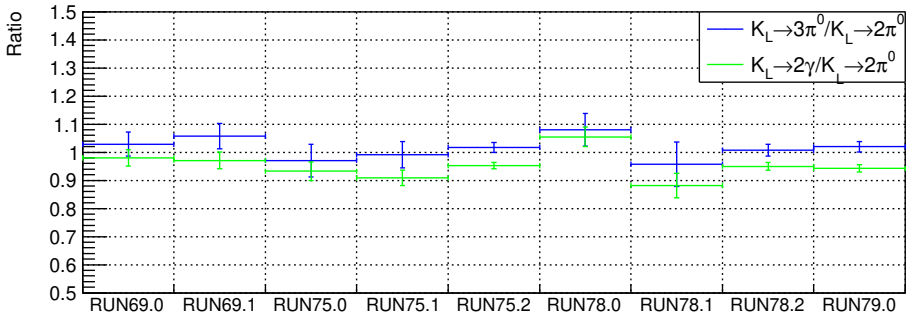

Figure 7.8: Ratio of K_L fluxes estimated with $K_L \to 3\pi^0$ and $K_L \to 2\pi^0$ (blue) and $K_L \to 2\gamma$ and $K_L \to 2\pi^0$ (green). The error bars represent statistical errors.

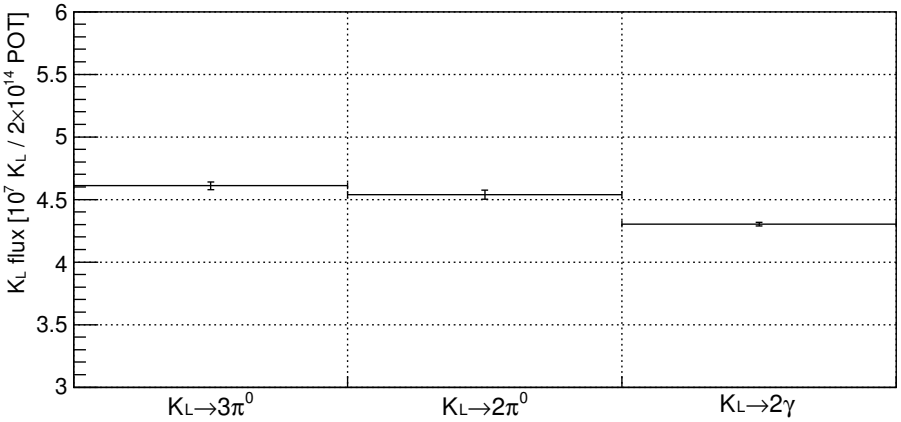

Figure 7.9: K_L flux estimated using the whole periods for each normalization decay mode. The error bars represent the statistical errors.

7.2 Sensitivity for $K_L \to \pi^0\nu\overline{\nu}$

The signal acceptance and the sensitivity for $K_L \to \pi^0\nu\overline{\nu}$ are explained in this section. The signal acceptance ($A_{\rm sig}$) was estimated using $K_L \to \pi^0\nu\overline{\nu}$ MC simulation and calculated as

$$A_{\rm sig} = \frac{N_{\rm sig}^{\rm rem}}{N_{\rm sig}^{\rm sim}}, \tag{7.6}$$

where $N_{\rm sig}^{\rm rem}$ is the number of remaining events after imposing the cuts, and $N_{\rm sig}^{\rm sim}$ is the number of generated $K_L \to \pi^0\nu\overline{\nu}$ events in the $K_L \to \pi^0\nu\overline{\nu}$ MC simulation. Based on the results of $A_{\rm sig}$ and the normalization mode analysis, the SES was calculated with Eq. 7.1

7.2.1 Selection Criteria of $K_L \to \pi^0\nu\overline{\nu}$

The selection criteria for $K_L \to \pi^0\nu\overline{\nu}$ (cuts) are explained here. All the cuts are summarized in Table 7.6, and each cut is explained below.

Trigger-related Cuts

The physics triggers consisted of the Lv1 and Lv2 triggers as described in Sec. 3.3.1. The effective threshold at the online trigger stage was smeared due to the differences of timings and gains between channels. To remove such biases in the offline analysis, we imposed the same cuts used in L1 and L2 trigger but with a tighter thresholds than the online thresholds.

- total energy
  The sum of photon energies (total energy) was required to be larger than 650 MeV due to the same reason as in Sec. 7.1.2. The distribution of total energy is shown in Fig. 7.10a.
  The loss of signal events due to the CSIEt trigger was estimated using the special run whose CSIEt threshold was set lower than 550 MeV. Because the Lv1 trigger system was upgraded between Run78.2 and Run79.0, we evaluated the loss for periods Run69.0–Run78.2 and Run79.0 separately. In both Run69.0–Run78.2, and Run79.0 periods, the signal event losses were less than 0.4%. Details of the signal event losses due to the CSIEt trigger are explained in Appendix C.
- two clusters
  Clusters were identified based on the energies and timings from CSI. For the $K_L \to \pi^0\nu\overline{\nu}$ search, the number of clusters was required to be two.

To select events with two clusters at the online stage, we implemented and used the online clustering trigger system from 2017. The loss of the signal events due to the online clustering trigger was estimated by a MC simulation and a data-driven approach. For the clustering algorithm, we used a different procedure between the online and offline. We thus implemented a system to count the number of clusters using the online clustering procedure ($N_{\rm clus}^{\rm online}$) in the MC simulation. In the online calculation, we masked noisy channels manually during the data taking, depending on the noise level, as mentioned in Sec. 3.2.2. It was not easy to implement such a masking channel situation in the MC simulation because the situation frequently changed within a period. We thus studied the effect of the noise by a data-driven approach. We evaluated the online clustering trigger efficiency ($\epsilon_{\rm clus}$) by a factorization:

$$\epsilon_{\rm clus} = \epsilon_{\rm clus}^{\rm true} \times (1 - L_{\rm clus}^{\rm TMon}), \tag{7.7}$$

where $\epsilon_{\rm clus}^{\rm true}$ is the signal efficiency without contributions from the noise and accidental activities, and $L_{\rm clus}^{\rm TMon}$ is the probability of the signal event loss due to the noise and accidental activities.

The $\epsilon_{\rm clus}^{\rm true}$ and $L_{\rm clus}^{\rm TMon}$ were estimated as follows. The $\epsilon_{\rm clus}^{\rm true}$ was estimated using $K_L \to \pi^0\nu\overline{\nu}$ MC simulations without overlaying accidental activities. Figure 7.11 left shows the distribution of $N_{\rm clus}^{\rm online}$ of the $K_L \to \pi^0\nu\overline{\nu}$ MC events without overlaying accidental activities. The $\epsilon_{\rm clus}^{\rm true}$ was estimated to be 99.8% based on the occupancy of the events with $N_{\rm clus}^{\rm online} = 2$. The $L_{\rm clus}^{\rm TMon}$ was estimated using the data taken with the TMon trigger. Figure 7.11 right shows the distribution of $N_{\rm clus}^{\rm online}$ of the data taken with the TMon trigger, calculated online in the period of Run79.0. We lost signal events when the noise and accidental activities made additional clusters. Based on the probability of $N_{\rm clus}^{\rm online} \geq 1$, we estimated $L_{\rm clus}^{\rm TMon}$ to be 0.1–0.2% in 2017–2018.

Finally, the $\epsilon_{\rm clus}$ was calculated using Eq. 7.7 and estimated to be 99.6–99.8% in 2017–2018. The events in $K_L \to \pi^0\nu\overline{\nu}$ MC simulation were weighted with $\epsilon_{\rm clus}$ in each period. The uncertainty of $\epsilon_{\rm clus}$ on SES will be explained in Sec. 7.3.3.1.

- $R_{\rm COE}$
  In the offline analysis, we required $R_{\rm COE}$ to be larger than 200 mm which was a tighter threshold than the online threshold of 165 mm[*1]. The distribution of $R_{\rm COE}$ is shown in Fig. 7.10b.

  A small loss of the signal efficiency from the trigger was due to the accidental activities in CSI. The offline $R_{\rm COE}$ was calculated using two on-time photons, but the online $R_{\rm COE}$ was calculated using all the hits in CSI crystals, including off-time hits. This difference caused the loss of the signal efficiency [35]. The signal event loss was 3% in the 2016 and a part of 2017 run. Details of the signal event losses due to the online COE trigger are explained in Appendix C.

- trigger timing
  The average of photon timings (trigger timing) was required to be within ±15 ns of the nominal trigger timing due to the same reason as in Sec. 7.1.2.

Photon selection

To ensure the photon reconstruction quality, the following photon selection cuts were used.

- photon energy
  The distributions of photon energies are shown in Fig. 7.10c and 7.10d. The photon energy was required to be larger than 100 MeV to ensure the quality of photon reconstruction.

[*1] Though we did not use the online COE trigger in 2018, we applied the offline COE cut to the whole datasets to simplify the cut sets. The signal loss from the offline COE cut was only 0.1%.

The energy was also required to be smaller than 2000 MeV to avoid unusually energetic photons, and this also helped to reduce $K_L \to 2\gamma$ events, as shown in Fig. 7.14.

- photon position
  The distributions of photon positions are shown in Fig. 7.10e and 7.10f. The photon hit position (x, y) on CSI was required to be within the CSI fiducial region, defined as $\sqrt{x^2+y^2} < 850$ mm and $\min(|x|, |y|) > 150$ mm, to avoid the mis-measurement of the photon energy due to the leakage of electromagnetic shower.

Kinematic Cuts for $K_L \to \pi^0\nu\overline{\nu}$

To ensure the quality of π^0 reconstruction and to reduce background events, the following cuts on the two photons were used.

- P_t-$Z_{\rm vtx}$ (signal region)
  The distributions of P_t and $Z_{\rm vtx}$ are shown in Fig. 7.12a and 7.12b. The region in the P_t and $Z_{\rm vtx}$ plane as the area encompassing $130 < P_t < 250$ MeV/c and $3200 < Z_{\rm vtx} < 5000$ mm was defined as the signal region excluding the area with $P_t < 1/35|\text{mm}| \cdot (Z_{\rm vtx} - 4000\ |\text{mm}|) + 130$ MeV/c for $4000 < Z_{\rm vtx} < 5000$ mm. Details on the signal region will be described in Sec. 7.2.2.
- projection angle
  As shown in Fig. 7.13a, we calculated the opening angle between the photon directions projected on the x-y plane (projection angle). The distributions of the projection angles of data and MC are shown in Fig. 7.12c. Figure 7.15a shows the distribution of the projection angles for $K_L \to \pi^0\nu\overline{\nu}$ and $K_L \to 2\gamma$ MC events under a loose cut condition, in which we did not impose the projection angle cut and P_t related cuts of P_t, $R_{\rm COE}$, and "P_t/P_z-$Z_{\rm vtx}$, E-$Z_{\rm vtx}$," described below. To reduce the $K_L \to 2\gamma$ events, we required the projection angle to be less than 150°. Note that $K_L \to 2\gamma$ events also can be suppressed by the P_t cut well, as shown in Fig. 7.15b.
- cluster distance
  The distance between the two photons on CSI, as shown in Fig. 7.13a, was required to be larger than 300 mm to ensure a clear cluster separation. The distribution of cluster distance is shown in Fig. 7.12d.
- $\Delta T_{\rm vtx}$
  Figure 7.16 shows the vertex timing difference between the two photons ($\Delta T_{\rm vtx}$). The $\Delta T_{\rm vtx}$ was required to be within 1 ns to ensure that the two clusters are originated from the same π^0 decay. This cut reduced hadron-cluster events, as will be described in Sec. 8.3.1.
- $E\theta$
  As shown in Fig. 7.13b, we calculated the product of the photon energy and the photon momentum angle with reference to the beam-axis ($E\theta$). To reduce the $K_L \to 2\pi^0$ background from photon mis-combinations in the π^0 reconstruction, we required the $E\theta$ to be larger than 2500 MeV·deg, as shown in Fig. 7.17a. The distributions of $E\theta$ of data and MC are shown in Fig. 7.12e. Details of the mechanism of the $K_L \to 2\pi^0$ background from photon mis-combinations will be described in Sec. 8.2.2.
- $E_{\rm ratio}$
  Figure 7.12f shows the energy ratio between the two photons: $E_{\rm ratio} = E_{\gamma_2}/E_{\gamma_1}$ ($E_{\gamma_2} > E_{\gamma_1}$). The $E_{\rm ratio}$ was required to be larger than 0.2 to reduce the $K_L \to 2\pi^0$ background from photon mis-combinations in the π^0 reconstruction, as shown in Fig. 7.17b. Details of the mechanism of the $K_L \to 2\pi^0$ background from photon mis-combinations will be described in Sec. 8.2.2.
- P_t/P_z-$Z_{\rm vtx}$, E-$Z_{\rm vtx}$
  To select a π^0 with plausible kinematics, we selected events inside the accepted region defined in the P_t/P_z and $Z_{\rm vtx}$ plane and E and $Z_{\rm vtx}$ plane shown Fig. 7.18.

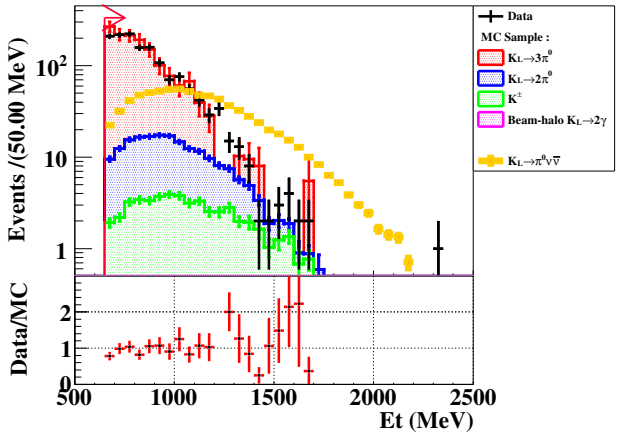

(a) total energy

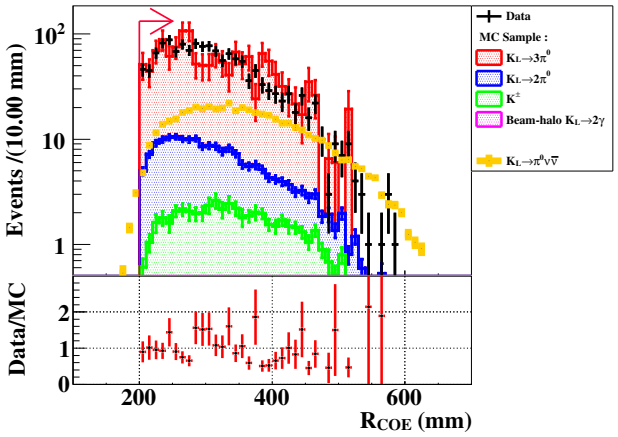

(b) R_{COE}

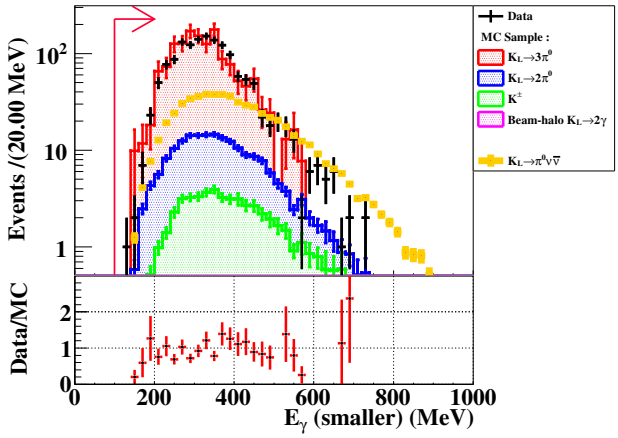

(c) photon energy (smaller)

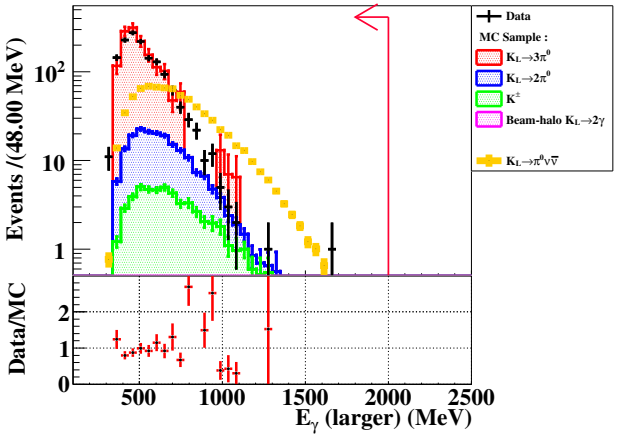

(d) photon energy (larger)

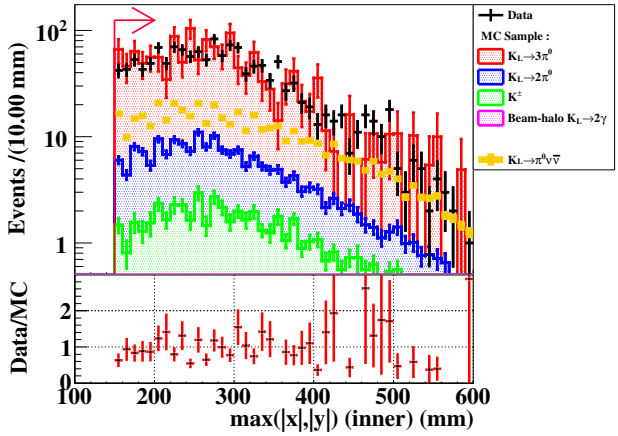

(e) photon position (inner)

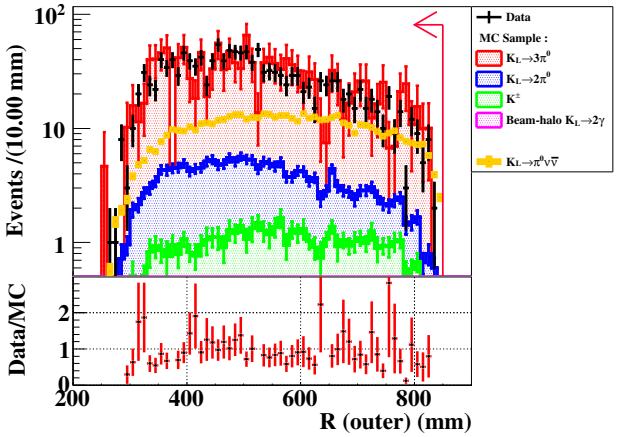

(f) photon position (outer)

Figure 7.10: Distributions of the total energy (a), R_{COE} (b), smaller photon energy (c), larger photon energy (d), inner photon position (e), and outer photon position (f) under a loose cut condition in the blind region. The black histograms represent the data. The red, blue, green, and magenta histograms represent MC simulations of $K_L \to 3\pi^0$, $K_L \to 2\pi^0$, $K^\pm$, and beam-halo $K_L \to 2\gamma$ decays, respectively. The number of events in the MC simulation except for $K_L \to \pi^0\nu\overline{\nu}$ was normalized with K_L yield. The orange histograms represent the $K_L \to \pi^0\nu\overline{\nu}$ MC, whose vertical axis is in arbitrary units. All the trigger-related cuts and photon-selection cuts are applied on the data and the $K_L \to 3\pi^0$ and $K_L \to 2\pi^0$ MC, whereas they are not applied on the $K_L \to \pi^0\nu\overline{\nu}$ MC. Besides, the other kinematic cuts are applied except for the cuts of interest. For the veto cuts, the energy thresholds of IB and MB are loosened to 10 MeV, and veto cuts on IBCV and MBCV are not applied. The pink lines and arrows indicate the region accepted by the cuts.

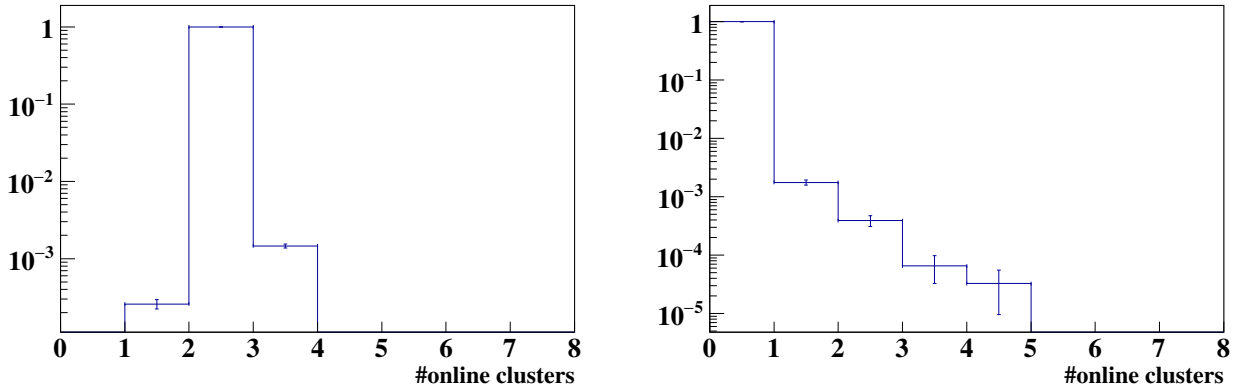

Figure 7.11: Left: the distribution of the number of clusters calculated with the algorithm used in the online clustering trigger for the events of the $K_L \to \pi^0 \nu\overline{\nu}$ MC simulation without overlaying accidental activities. Right: the distribution of the number of clusters recorded in the data taken with the TMon trigger. In both plots, the area of the histogram is scaled to be one.

- dead channels
  The distance between the dead channels and the photon position on CSI was required to be larger than 53 mm to avoid the mis-measurement of photon energies. In 2016–2018, we had two dead channels in CSI.

Veto Cuts

To ensure that there are no other detectable particles other than the π^0 from $K_L \to \pi^0 \nu\overline{\nu}$ decay, we required no coincident hit in veto counters. We used the same veto cuts as in the normalization mode analysis, described in Sec. 7.1.2.

Figure 7.19 shows distributions of IB veto-energy and veto-time under a loose cut condition in the blind region. The agreement of veto-energy distribution between data and MC validates the IB detector response in MC simulations. For the veto-time distribution, the timing shift of 0.2 ns was observed due to the timing offset difference between data and MC, which was corrected in the timing calibration. This time offset was negligible in the analysis because the IB veto window of 50 ns was far wider than the offset.

Figure 7.20 shows the χ^2_{FFT} distribution for NCC and FBAR under a loose cut condition in the blind region. The agreement of the distribution validates the NCC and FBAR detector responses in MC simulations.

Shape-Related Cuts

To reduce background events, shape-related cuts based on each cluster in CSI and waveform of each CSI crystal were used. These shape-related cuts were essential to reduce hadron-cluster background events, as will be described in Sec. 8.3.1.

- cluster size
  Figure 7.21a shows the cluster size distribution of events in the $K_L \to \pi^0 \nu\overline{\nu}$ MC simulation and the Z0Al run. In accordance with the Molière radius of the CsI ($R_M = 3.57$ cm), an electromagnetic shower spread out to multiple crystals for photon clusters[*2]. To select plausible photon clusters, the number of crystals used in each cluster (cluster size) was required to be 5 or more.

[*2] For small crystals (2.5×2.5 cm), a 90% energy of photon is ideally lost by $6.4\,(= \pi R_M^2/2.5^2)$ crystals.

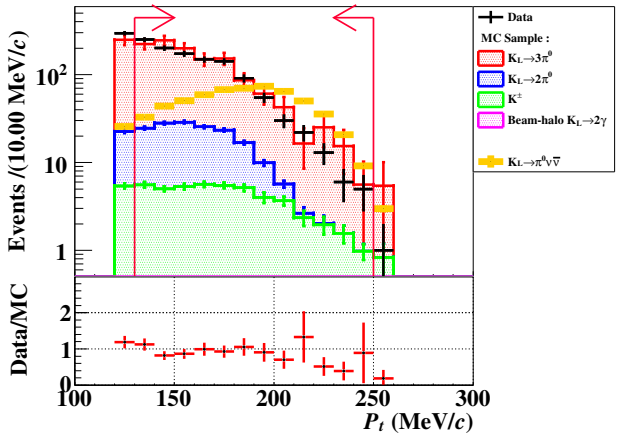

(a) P_t

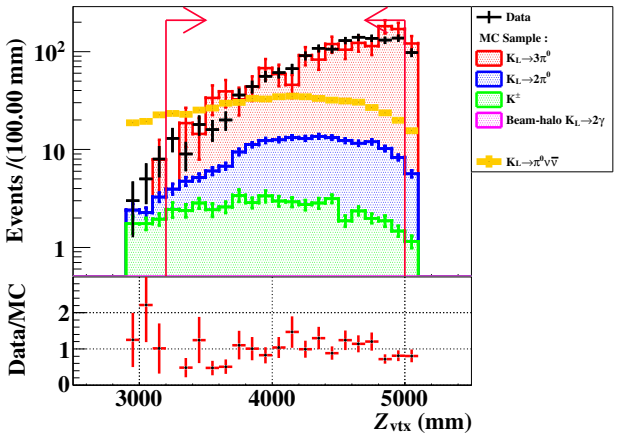

(b) $Z_{\rm vtx}$

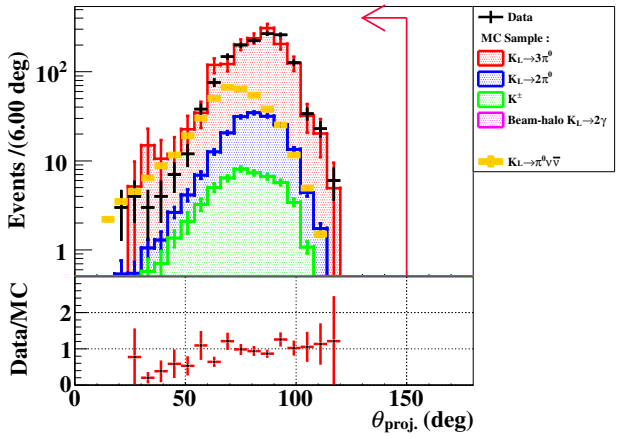

(c) projection angle

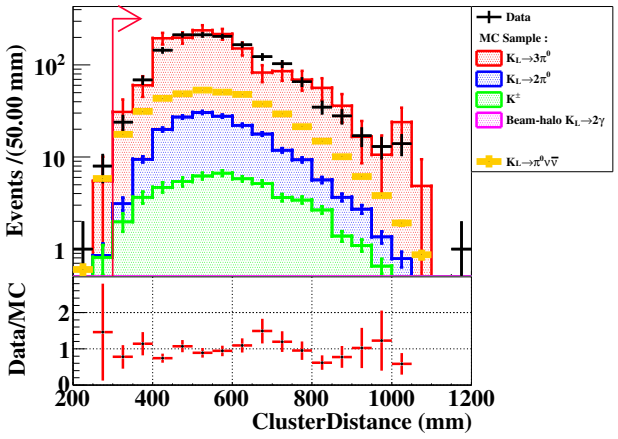

(d) cluster distance

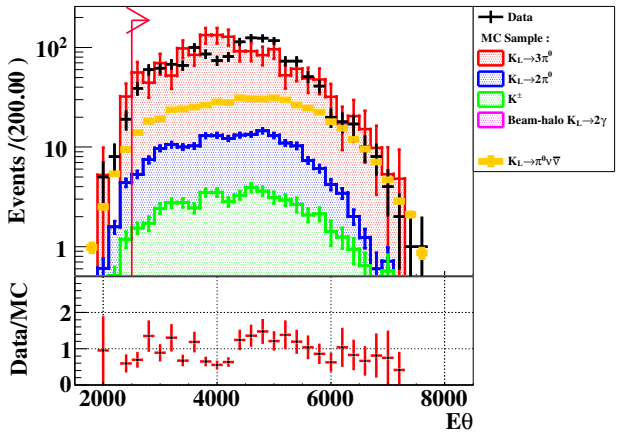

(e) $E\theta$

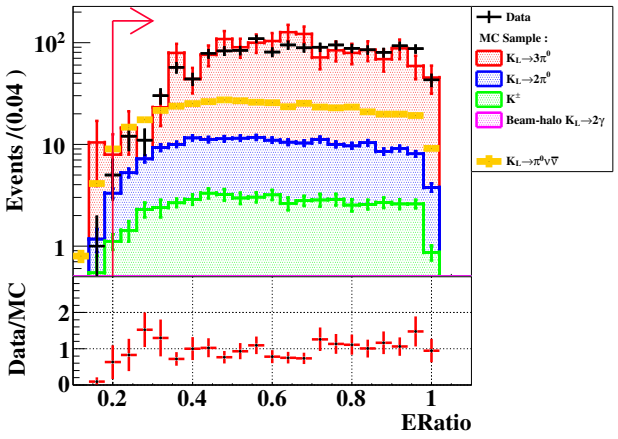

(f) $E_{\rm ratio}$

Figure 7.12: Distributions of the P_t (a), $Z_{\rm vtx}$ (b), projection angle (c), cluster distance (d), smaller $E\theta$ (e), and $E_{\rm ratio}$ (f) under a loose cut condition in the blind region. In the loose cut condition, the kinematic cuts are applied except for the cuts of interest. The veto cut condition and the meaning of the colors of histograms and lines in pink are the same as for Fig. 7.10.

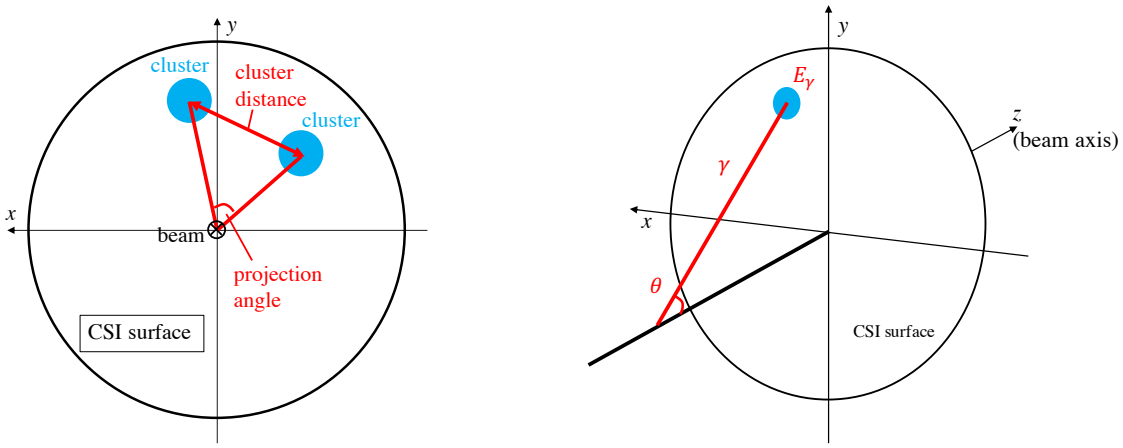

(a) Projection angle and cluster distance (b) $E\theta$

Figure 7.13: Left: the schematic view of the CSI surface to show the relationship between cluster positions, the projection angle, and cluster distance. Right: the schematic view of the photon hitting CSI to show the relationship between the cluster position and the photon momentum angle with reference to the beam-axis (θ) for the variable of $E\theta$.

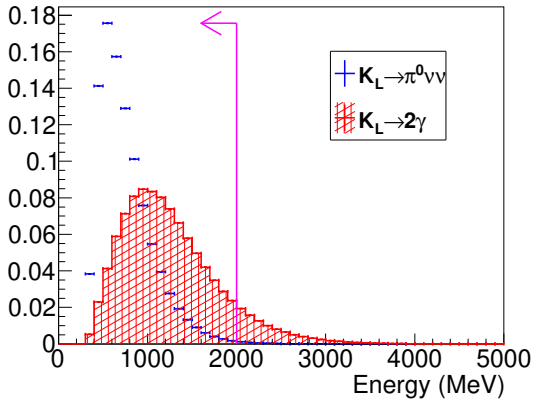

Figure 7.14: Distributions of the larger photon energy in $K_L \to \pi^0 \nu\overline{\nu}$ (blue) and $K_L \to 2\gamma$ (red) MC events. The magenta line and arrow represent the accepted region for the signal. The photon energy from $K_L \to \pi^0 \nu\overline{\nu}$ is smaller than the one from $K_L \to 2\gamma$ due to two neutrinos.

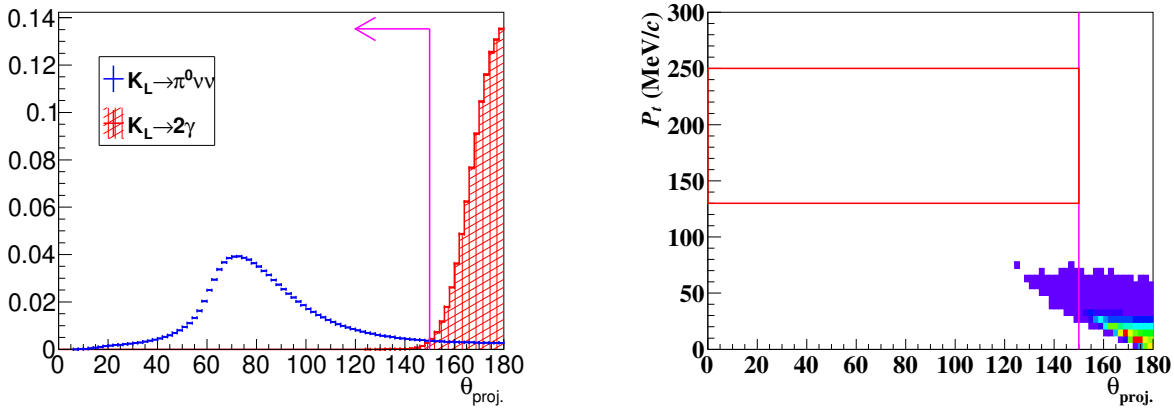

(a) $K_L \to \pi^0 \nu\overline{\nu}$ vs. $K_L \to 2\gamma$ (b) P_t vs. projection angle

Figure 7.15: Left: the distributions of the projection angle of the $K_L \to \pi^0 \nu\overline{\nu}$ (red) and $K_L \to 2\gamma$ (blue) MC events. The magenta line and arrow represent the accepted region for the signal. Right: the distribution of the P_t vs. projection angle of $K_L \to 2\gamma$ MC events. The magenta line represents the threshold for the projection angle. The region inside the red lines represents the accepted region for the signal.

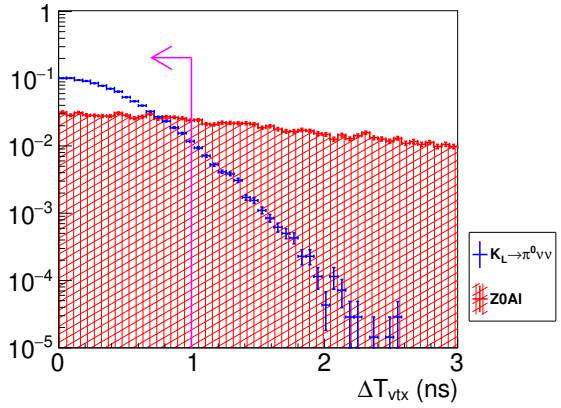

Figure 7.16: Distribution of ΔT_{vtx} for the data taken in Z0Al run (red) and $K_L \to \pi^0 \nu\overline{\nu}$ MC events (blue). The magenta line and arrow represent the accepted region of the signal.

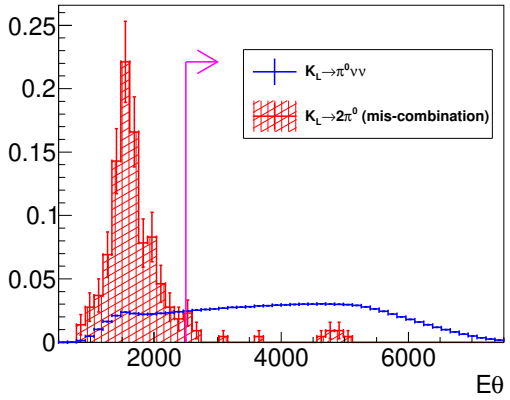

(a) $E\theta$

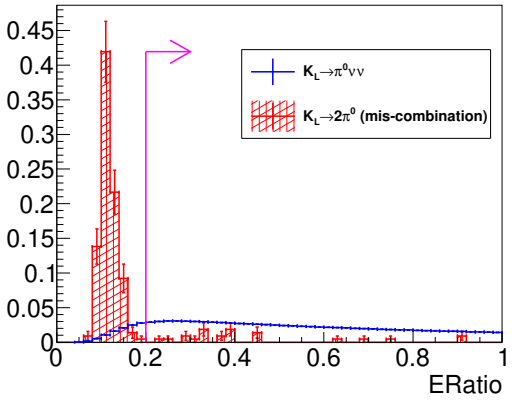

(b) Energy ratio

Figure 7.17: Distributions of a smaller $E\theta$ (left) and E_{ratio} (right) of $K_L \to 2\pi^0$ (red) and $K_L \to \pi^0 \nu\overline{\nu}$ (blue) MC events. For $K_L \to 2\pi^0$ decays, the events from photon mis-combinations in the π^0 reconstruction were enhanced by cuts in which we required the distance between the actual π^0 decay position and the reconstructed π^0 decay position to be larger than 500 mm. The magenta line and arrow represent the accepted region of the signal.

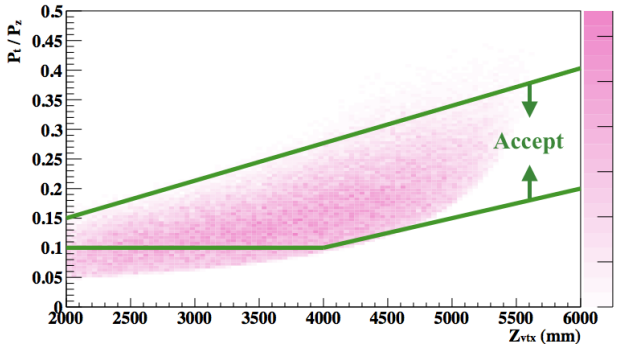

(a) P_t/P_z - Z_{vtx}

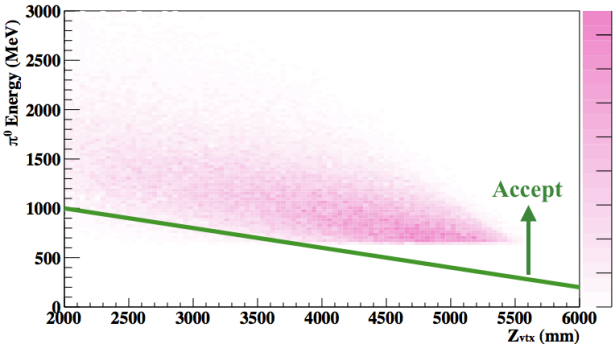

(b) E_{π^0} - Z_{vtx}

Figure 7.18: P_t/P_z-Z_{vtx} (left) and E-Z_{vtx} (right) selection quoted from [35]. Distribution of the $K_L \to \pi^0 \nu\overline{\nu}$ events is shown with the accepted region bounded by green lines.

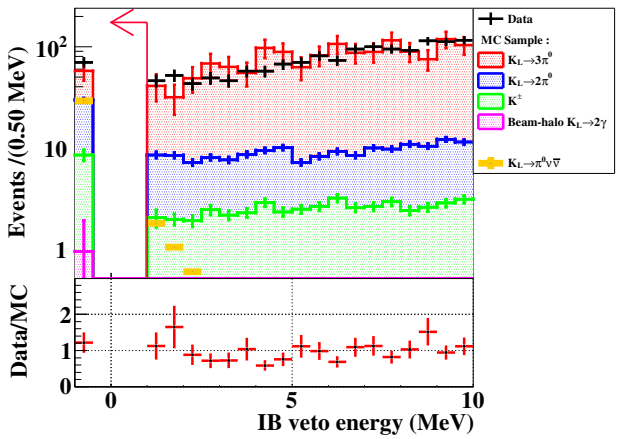

(a) IB veto-energy

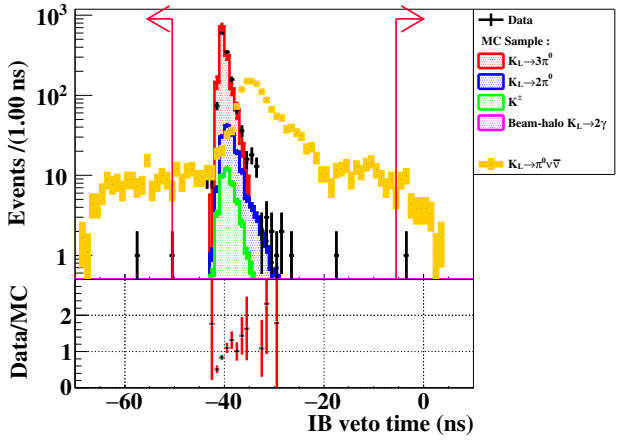

(b) IB veto-time

Figure 7.19: Distributions of IB veto-energy (left) and veto-time (right) under a loose cut condition in the blind region. In the loose cut condition, the energy thresholds of IB and MB are loosened to 10 MeV, and veto cuts on IBCV and MBCV are not applied. Events with the deposited energy lower than 1 MeV were filled as the -1 MeV deposited energy. The meaning of the colors of histograms and lines in pink are the same as for Fig. 7.10.

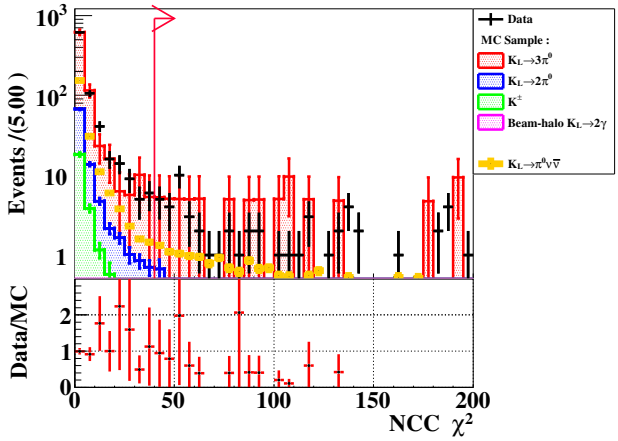

(a) χ^2_{FFT} in NCC

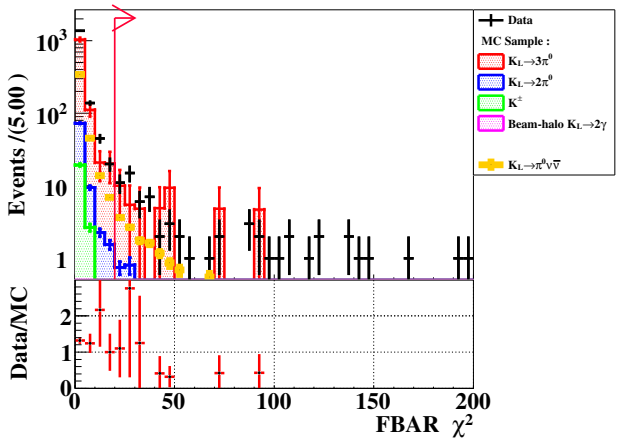

(b) χ^2_{FFT} in FBAR

Figure 7.20: Distributions of χ^2_{FFT} in NCC (left) and FBAR (right) under a loose cut condition in the blind region. In the loose cut condition, the energy thresholds of IB and MB are loosened to 10 MeV, and veto cuts on IBCV and MBCV are not applied. Besides, the energy threshold of NCC (FBAR) is loosened to 10 MeV in the NCC (FBAR) FTT-χ^2 distribution. The meaning of the colors of histograms and lines in pink are the same as for Fig. 7.10.

- cluster RMS
  Cluster RMS is defined as

$$\sqrt{\frac{\Sigma e_i r_i^2}{\Sigma e_i}}, \tag{7.8}$$

  where e_i is the energy in each crystal and r_i is the distance between the crystal position of interest and the center of energy of the cluster. Figure 7.21b shows the cluster RMS distribution of events in the $K_L \to \pi^0\nu\overline{\nu}$ MC simulation and Z0Al run. The cluster RMS was required to be larger than 10 mm to select the electromagnetic shower.

- cluster shape discrimination (CSD)
  The following methods were used to suppress backgrounds in the 2016–2018 dataset, some of which were newly developed using a neural network (NN) method.

  – CSD-Had
    To suppress the hadron cluster background, two types of cuts were used in the 2015 data analysis. One was shape-χ^2 cut[*3], and the other was another cluster shape NN cut [35]. For the 2016–2018 analysis[*4], an algorithm using a Convolution Neural Network, named CSD-Had, was developed. As inputs, it used the shape-χ^2 variable as well as the cluster energy and timing patterns in CSI, and its reconstructed incident angle. As a training sample of photons, the $K_L \to \pi^0\nu\overline{\nu}$ MC simulation was used. As a training sample of neutrons, the data taken in the Z0Al run was used.
    Figure 7.21c shows the distribution of the output of CSD-Had ($o_{\text{CSD-Had}}$) where it varies from 0 to 1. The $o_{\text{CSD-Had}}$ was required to be larger than 0.985. The threshold was determined to give the same signal acceptance (80%) as the two cluster shape cuts of shape-χ^2 and cluster shape NN used in the 2015 analysis. Details of the hadron cluster background with CSD-Had will be described in Sec. 8.3.1.

  – CSD-η
    To suppress the CV-η background, a cut named eta-χ^2 was used [35] in the 2015 data analysis. For the 2016–2018 data analysis[*5], the algorithm using NN, named CSD-η, was developed to achieve a larger reduction. As inputs, it used the cluster energy and timing patterns in CSI, and its reconstructed incident angle. As a training sample of signal, the $K_L \to \pi^0\nu\overline{\nu}$ MC simulation was used. As a training sample of background, the CV-η MC simulation was used.
    Figure 7.21d shows the distribution of the output of CSD-η ($o_{\text{CSD-}\eta}$) where it varies from 0 to 1. The $o_{\text{CSD-}\eta}$ was required to be larger than 0.91. The threshold was determined to give the same signal acceptance (84%) as of the cut of eta-χ^2. Details of the CV-η background with CSD-η will be described in Sec. 8.3.2.

  – CSD-$\pi^+\pi^-\pi^0$
    To suppress the $K_L \to \pi^+\pi^-\pi^0$ background, an algorithm using NN, named CSD-$\pi^+\pi^-\pi^0$, was developed for the 2016–2018 data analysis[*6]. As inputs, it used the photon energies, positions, momenta as well as the reconstructed π^0 energy, Z_{vtx}, and momentum. As a training sample of signal, the $K_L \to \pi^0\nu\overline{\nu}$ MC simulation was used. As a training sample of background, the $K_L \to \pi^+\pi^-\pi^0$ MC simulation was used.
    Figure 7.22a shows the distribution of the output of CSD-$\pi^+\pi^-\pi^0$ ($o_{\text{CSD-}\pi^+\pi^-\pi^0}$) where it varies from 0 to 1. The $o_{\text{CSD-}\pi^+\pi^-\pi^0}$ was required to be larger than 0.922. The threshold was determined to maintain 90% of the signal acceptance. Details of the $K_L \to \pi^+\pi^-\pi^0$ background with CSD-$\pi^+\pi^-\pi^0$ will be described in Sec. 8.2.1.

[*3] This evaluates the consistency of a shower shape with a template made by MC simulations.
[*4] This algorithm was developed by Y.-C. Tung.
[*5] This algorithm was developed by Q. S. Lin.
[*6] This algorithm was developed by J. C. Redeker.

– theta-χ^2
To suppress background events caused by photon mis-combinations in the π^0 reconstruction in the $K_L \to 2\pi^0$ decay, an algorithm using NN, named theta-χ^2, was introduced in the 2015 data analysis [35], and was also used for the 2016–2018 data analysis.
Figure 7.22b shows the distribution of theta-χ^2. We used the same requirement on the theta-χ^2 as in the 2015 analysis [35] and required the output of theta-χ^2 (χ^2_θ) to be less than 4.5 for each photon.

- pulse shape discrimination (PSD)
To suppress the hadron cluster background, we used the difference of the pulse shapes originated from photons and neutrons. For the 2015 data analysis, a discrimination [64] which extracts the pulse shape information by fitting each CSI crystal waveform with the asymmetric Gaussian (Eq. 5.9) was used. Because the waveform was fitted without using the tail region due to an imperfect reproducibility with the asymmetric Gaussian, there was a room to improve the reduction. For the 2016–2018 data analysis[*7], another method using a fast Fourier transform (FFT) applied on each CSI crystal waveform, named PSD-FFT, was developed. With the FFT, a wide range of waveforms can be used to extract pulse shape information.
A discrete Fourier transform is calculated as

$$h_i = \sum_{n=0}^{N-1} t_n \exp(-2\pi i k n/N), \tag{7.9}$$

where N is the number of samples in the waveform, and t_n is the height of each sample of the waveform. Templates of the magnitude of h_i were prepared for both photon and neutron clusters. To make the photon template, photons in the reconstructed $K_L \to 3\pi^0$ events were used. To make the neutron template, the data taken in the Z0Al run was used. We defined a likelihood for each crystal in a cluster:

$$L^{\text{crystal}} = \prod_i \frac{1}{\sigma_i^{\text{temp}}} \exp\left(-\frac{(|h_i^{\text{meas}}| - |h_i^{\text{temp}}|)^2}{2(\sigma_i^{\text{temp}})^2}\right), \tag{7.10}$$

and a likelihood for a cluster:

$$L^{\text{cluster}} = \prod_j L_j^{\text{crystal}}, \tag{7.11}$$

where $|h_i^{\text{meas}}|$ represents the magnitude in the frequency domain of the waveform of each CSI crystal in events, $|h_i^{\text{temp}}|$ and σ_i^{temp} represent the mean and standard deviation of the templates, respectively. A likelihood ratio (R^{cluster}) was calculated as

$$R^{\text{cluster}} = \frac{L_\gamma^{\text{cluster}}}{L_\gamma^{\text{cluster}} + L_n^{\text{cluster}}}, \tag{7.12}$$

where $L_\gamma^{\text{cluster}}$ and L_n^{cluster} are the likelihoods obtained from photon and neutron templates, respectively. Among R^{cluster} of the two clusters in each event, the smaller was defined as $o_{\text{PSD-FFT}}$. We required $o_{\text{PSD-FFT}}$ to be larger than 0.5 to maintain the signal acceptance of 90%. Details of the hadron cluster background with PSD-FFT will be described in Sec. 8.3.1.
In MC simulations, we weighted events with the PSD-FFT cut efficiency factor as a function of each cluster energy and position because we could not reproduce waveforms in CSI. The efficiency factor for each cluster was obtained with photon samples from $K_L \to 3\pi^0$ for lower energy photons and $K_L \to 2\gamma$ for higher energy photons. Figure 7.23 shows the efficiency factor. The product of efficiency factors of two photons was assigned as the event weight.

[*7] This method was developed by J. Li and Y.-C. Tung.

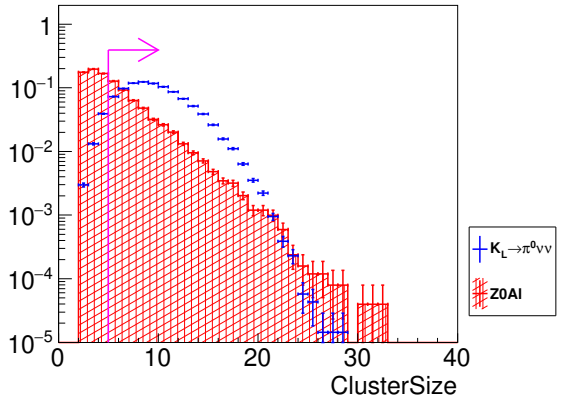

(a) Cluster size

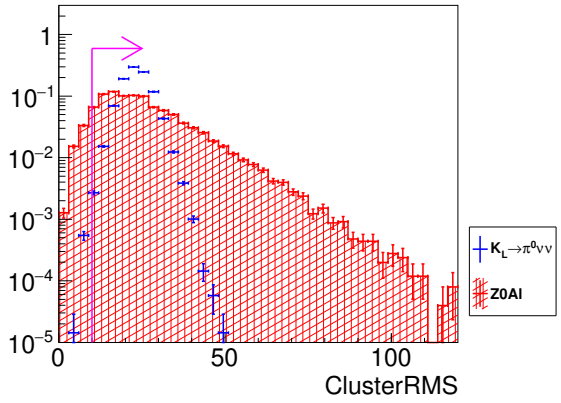

(b) Cluster RMS

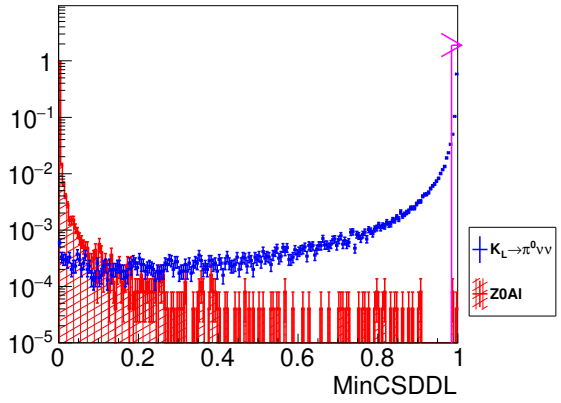

(c) CSD-Had

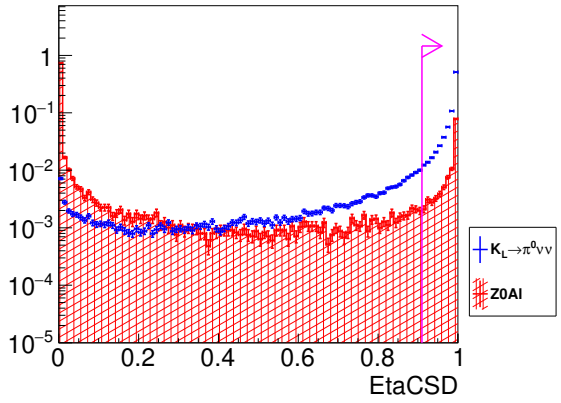

(d) CSD-η

Figure 7.21: Distributions of the cluster size (a), cluster RMS (b), $o_{\text{CSD-Had}}$ (c), and $o_{\text{CSD-}\eta}$ (d) for events in the $K_L \to \pi^0 \nu\overline{\nu}$ MC simulation (blue) and Z0Al run (red). The magenta line and arrow represent the accepted region of the signal.

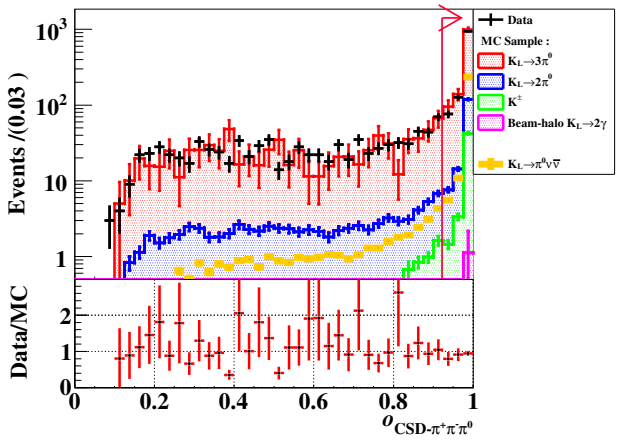

(a) CSD-$\pi^+\pi^-\pi^0$

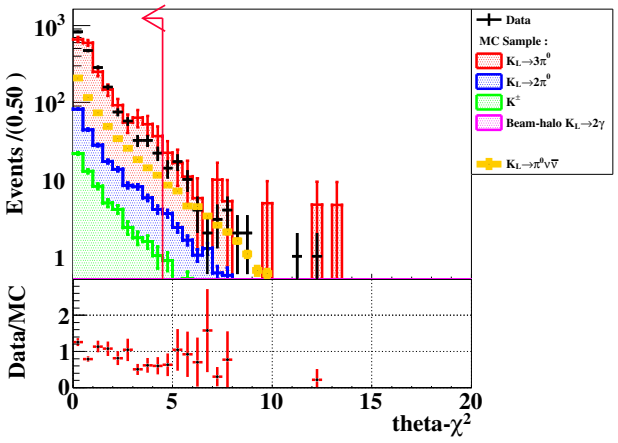

(b) theta-χ^2

Figure 7.22: Distributions of $o_{\text{CSD-}\pi^+\pi^-\pi^0}$ (left) and χ^2_θ (right) under a loose veto cut condition in the blind region. The veto cut condition and the meaning of the colors of histograms and lines in pink are the same as for Fig. 7.10.

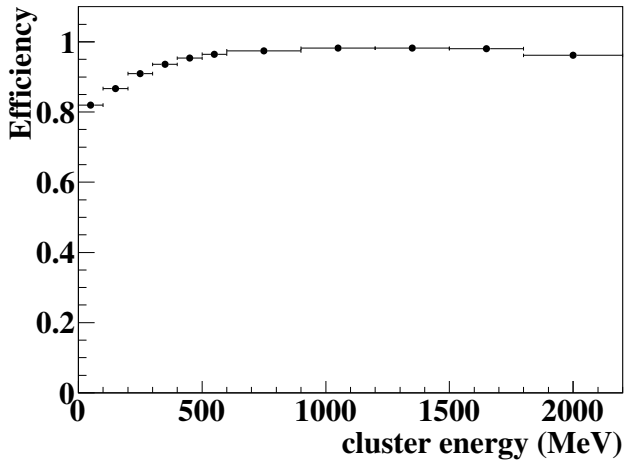

Figure 7.23: PSD-FFT cut efficiency as a function of the energy of the cluster whose position in CSI is within the region of $|x| < 750$ mm and $|y| < 750$ mm.

Table 7.6: Summary of the selection criteria used in the $K_L \to \pi^0 \nu\overline{\nu}$ analysis.

category	selection name	selection criterion
trigger-related cuts	trigger timing	$< \pm 15$ ns
	total energy	$E_{\text{tot}} \geq 650$ MeV
	COE	$R_{\text{COE}} \geq 200$ mm
photon-selection cuts	photon energy	100 MeV $\leq E_\gamma \leq 2000$ MeV
	photon position (inner)	$\max(\lvert x\rvert, \lvert y\rvert) \geq 150$ mm
	photon position (outer)	$R \leq 850$ mm
π^0 selection cuts	signal region	see Sec. 7.2.2
	projection angle	$\theta_{\text{proj.}} \leq 150$
	cluster distance	≥ 300 mm
	ΔT_{vtx}	$\Delta T_{\text{vtx}} \leq 1$ ns
	$E \cdot \theta$	$E \cdot \theta \geq 2500$ MeV $\cdot$ deg
	energy ratio	$E_2/E_1 \geq 0.2$
	P_t/P_z-Z_{vtx}, E-Z_{vtx}	see Fig. 7.18
	dead channel	$d_{\text{dead}} \geq 53$ mm
shape-related cuts	cluster size	$n_{\text{crystal}} \geq 5$
	cluster RMS	$RMS_{\text{cluster}} \geq 10$
	CSD-Had [a]	$o_{\text{CSD-Had}} > 0.985$
	CSD-η [a]	$o_{\text{CSD-}\eta} > 0.91$
	CSD-$\pi^+\pi^-\pi^0$ [a]	$o_{\text{CSD-}\pi^+\pi^-\pi^0} > 0.922$
	theta-χ^2	$\chi^2_\theta < 4.5$
	PSD-FFT [a]	$o_{\text{PSD-FFT}} > 0.5$
veto cuts		see Table 7.3

[a] Cuts introduced for the 2016–2018 data analysis

Table 7.7: The number of events after selection criterion except for the cuts of P_t and $Z_{\rm vtx}$.

Selection criteria	No. events
Triggered events	6.55×10^9
Two clusters	1.57×10^9
Trigger related cuts	3.20×10^9
Photon selection cuts	2.40×10^9
Kinematic cuts	3.04×10^7
Veto cuts	5.64×10^4
Shape-related cuts	443

7.2.2 Signal Region

We defined the signal region in the reconstructed π^0 transverse momentum (P_t) and π^0 decay vertex position ($Z_{\rm vtx}$) plane. Figure 7.24 shows the signal region used in the 2016–2018 data analysis.

The upstream boundary was determined to avoid the upstream-π^0 background events. The region of $Z_{\rm vtx} \leq 3200$ mm is contaminated with the upstream-π^0 background events, as will be described in Sec. 8.3.3. Compared to the boundary used in the 2015 analysis ($Z_{\rm vtx} = 3000$ mm), the signal acceptance decreased by 7%.

The downstream boundary was determined to avoid the hadron-cluster background events. In the 2015 analysis, the downstream boundary was at $Z_{\rm vtx} = 4700$ mm. In the 2016–2018 analysis, we found that the region of $Z_{\rm vtx} < 5000$ mm was not contaminated with the hadron-cluster background events, as will be described in Sec. 8.3.1. To achieve a better sensitivity for $K_L \to \pi^0\nu\overline{\nu}$, the region of $Z_{\rm vtx} < 5000$ mm was used for the signal region. Compared to the boundary used in the 2015 analysis ($Z_{\rm vtx} = 4700$ mm), the signal acceptance increased by 16%.

The requirement on the P_t maximum was determined by the kinematics of $K_L \to \pi^0\nu\overline{\nu}$. In the rest frame, the maximum momentum of π^0 P_t from $K_L \to \pi^0\nu\overline{\nu}$ decay is 230 MeV/c. Due to the finite beam size, and the energy and timing resolutions of CSI, the reconstructed P_t can be slightly larger than the kinematical limit. We thus required the P_t to be smaller than 250 MeV/c. The signal acceptance decreased by only 0.8% due to the requirement on the upper bound of P_t.

The requirement on the P_t minimum was determined to avoid the $K_L \to \pi^+\pi^-\pi^0$ background, as will be described in Sec. 8.2.1. The region of $P_t \leq 130$ MeV/c is contaminated with the $K_L \to \pi^+\pi^-\pi^0$ background events. To avoid such background events, the region of $P_t > 130$ MeV/c was used for the signal region. Besides, the area defined as

$$P_t < \left(\frac{1}{35 \text{ mm}} (Z_{\rm vtx} - 4000 \text{ mm}) + 130 \right) \text{ MeV}/c \quad (4000 < Z_{\rm vtx} < 5000 \text{ mm}), \tag{7.13}$$

was found to be contaminated with $K_L \to \pi^+\pi^-\pi^0$ events. To avoid $K_L \to \pi^+\pi^-\pi^0$ background events, this area was also excluded from the signal region. By excluding this area, the signal acceptance decreased by only 0.8%[*8].

In total, the signal acceptance increased by 6% than for the 2015 data analysis by changing the signal region.

7.2.3 Data Reduction

The data reduction is summarized in Table 7.7. In 2016–2018, the number of events collected with the physics trigger was 6.55×10^9. The reductions by veto cuts and shape-related cuts were larger than the reductions by the others.

[*8] The excluded area is also cut by the CSD-$\pi^+\pi^-\pi^0$. If we included that area and removed the CSD-$\pi^+\pi^-\pi^0$ cut, the signal acceptance is recovered by 12%.

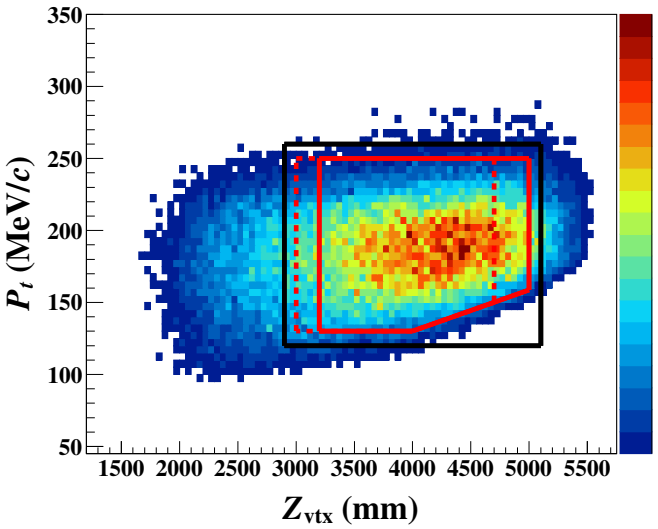

Figure 7.24: Reconstructed π^0 transverse momentum (P_t) vs. π^0 decay vertex position (Z_{vtx}) for the $K_L \to \pi^0\nu\overline{\nu}$ MC events. The region surrounded by red (black) solid lines is the signal (blind) region used in the 2016–2018 data analysis. The region surrounded by red dotted lines is the signal region used in the 2015 data analysis.

7.2.4 Signal Acceptance and Sensitivity

Figure 7.25 shows the breakdown of the signal acceptance. The breakdown of the signal acceptances after cut stages in Run75.2, Run78.2, and Run79.0 are shown in Table 7.8. The difference in signal acceptance between periods mainly came from veto cuts because the different beam conditions made the different accidental hit rates in veto counters, and that caused the different accidental losses. The signal acceptance (A_{sig}) and the single event sensitivity (SES) are summarized in Table 7.9. The A_{sig} was estimated using the $K_L \to \pi^0\nu\overline{\nu}$ MC simulation based on Eq. 7.6. The K_L decay probability of 3.34% in the region of $3200 < Z_{\mathrm{vtx}} < 5000$ mm is included in A_{sig}.

The overall SES of the data taken in 2016–2018 was calculated using Eqs. 2.4 and 2.5 as

$$\mathrm{SES}_{\mathrm{overall}} = \frac{1}{\mu_{\mathrm{overall}}}\,\mathcal{B}(K_L \to \pi^0\nu\overline{\nu}) \tag{7.14}$$

$$= \frac{1}{\sum_i \mu_i}\,\mathcal{B}(K_L \to \pi^0\nu\overline{\nu}) \tag{7.15}$$

$$= \frac{1}{\sum_i A_i^{\mathrm{sig}}\, N_i^{K_L}}, \tag{7.16}$$

where μ_{overall} is the total expected number of $K_L \to \pi^0\nu\overline{\nu}$ events in 2016–2018, and for the data taking period i, μ_i is the expected number of $K_L \to \pi^0\nu\overline{\nu}$ events, A_i^{sig} is the signal acceptance, and $N_i^{K_L}$ is the number of K_L's at the beam-exit (K_L yield). As a result, we estimated SES in 2016–2018 to be $(7.20 \pm 0.05_{\mathrm{stat}}) \times 10^{-10}$ which corresponds to 1.8 times higher sensitivity than the previous $K_L \to \pi^0\nu\overline{\nu}$ search [26]. The statistical uncertainty comes from the number of $K_L \to 2\pi^0$ events used for the normalization.

7.3 Systematic Uncertainties on the Sensitivity

The systematic uncertainties on SES are described in this section. As shown in Eq. 7.1, the uncertainty on A_{sig}, A_{norm}, and $\mathcal{B}(K_L \to 2\pi^0)$ contributes to the uncertainty on the SES[*9]. The uncertainty on

[*9]The uncertainty on N_{norm} was taken into account as the statistical uncertainty

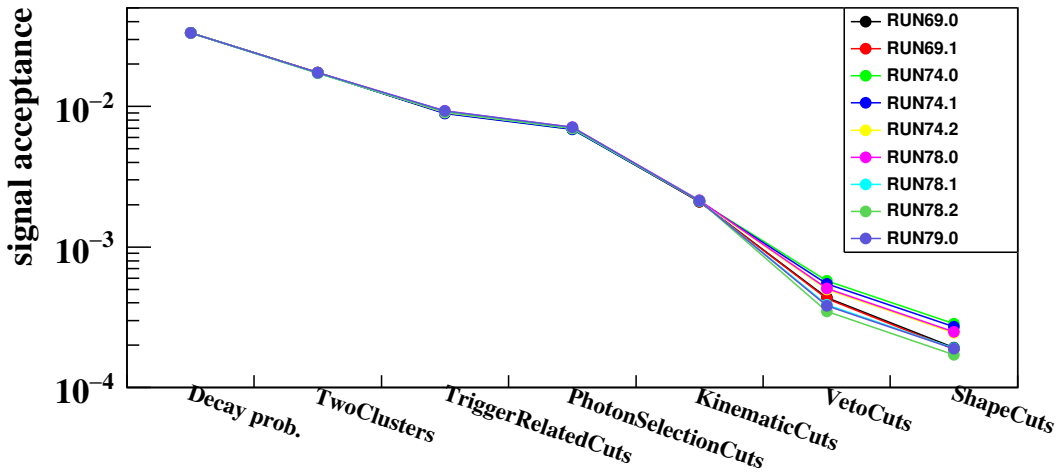

Figure 7.25: Breakdown of the signal acceptance. Acceptances in each run-period are shown in different lines.

Table 7.8: Breakdown of the signal acceptance after applying cuts in the periods of Run75.2, Run78.2, and Run79.0.

	Run75.2	Run78.2	Run79.0
Decay Prob.	3.34×10^{-2}	3.34×10^{-2}	3.34×10^{-2}
Two clusters	1.73×10^{-2}	1.73×10^{-2}	1.73×10^{-2}
Trigger-related cuts	9.09×10^{-3}	9.12×10^{-3}	9.27×10^{-3}
Photon selection	6.99×10^{-3}	6.99×10^{-3}	7.11×10^{-3}
Kinematic cuts	2.14×10^{-3}	2.13×10^{-3}	2.13×10^{-3}
Veto cuts	4.98×10^{-4}	3.49×10^{-4}	3.83×10^{-4}
Shape-related cuts	2.46×10^{-4}	1.72×10^{-4}	1.90×10^{-4}

$\mathcal{B}(K_L \to 2\pi^0)$, 0.69% [5], was taken into account as the uncertainty on the SES. In the following sections, the uncertainties on the $A_{\rm sig}$ and $A_{\rm norm}$ are described.

7.3.1 Overview

Two keys exist to estimate uncertainties on the $A_{\rm sig}$ and $A_{\rm norm}$; the acceptances are calculated using MC simulations, and the ratio between the two acceptances is used in the SES calculation.

The $A_{\rm sig}$ and $A_{\rm norm}$ are calculated with Eqs. 7.6 and 7.4, respectively. Because $A_{\rm sig}$ and $A_{\rm norm}$ were evaluated using MC simulations, the discrepancies between data and MC should be taken into account as systematic uncertainties.

In the SES calculation, we took the ratio of $A_{\rm sig}$ to $A_{\rm norm}$, as in Eq. 7.1. We expect that the uncertainty originated from accidental activities in veto cuts is canceled out by taking the ratio because accidental activities contribute to events in any K_L decays randomly. To consider such a cancellation, we factorized $A_{\rm sig}$ and $A_{\rm norm}$ as

$$A_{\rm norm} = A^{\rm norm}_{\rm geom} \times A^{\rm norm}_{\rm trigger} \times A^{\rm norm}_{\rm photon} \times A^{\rm norm}_{\rm kine} \times A^{\rm norm}_{\rm veto}, \tag{7.17}$$

$$A_{\rm sig} = A^{\rm sig}_{\rm geom} \times A^{\rm sig}_{\rm trigger} \times A^{\rm sig}_{\rm photon} \times A^{\rm sig}_{\rm kine} \times A^{\rm sig}_{\rm veto} \times A^{\rm sig}_{\rm shape}, \tag{7.18}$$

where $A_{\rm geom}$ is the geometrical acceptance, and $A_{\rm trigger}$, $A_{\rm photon}$, $A_{\rm kine}$, $A_{\rm veto}$, and $A_{\rm shape}$ are acceptances of the trigger related cuts, photon selection, kinematic cuts, veto cuts, and shape-related cuts,

Table 7.9: Summary of the signal acceptance (A_{sig}) and the single event sensitivity (SES). The A_{sig} was estimated by analyzing $K_L \to \pi^0\nu\overline{\nu}$ MC events. The K_L decay probability of 3.34% is included in A_{sig}.

year	period	A_{sig}	K_L yield	SES
2016	Run69.0	1.92×10^{-4}	3.40×10^{11}	1.53×10^{-8}
	Run69.1	1.88×10^{-4}	2.57×10^{11}	2.07×10^{-8}
2017	Run75.0	2.85×10^{-4}	6.48×10^{10}	5.41×10^{-8}
	Run75.1	2.71×10^{-4}	1.41×10^{11}	2.62×10^{-8}
	Run75.2	2.46×10^{-4}	1.71×10^{12}	2.37×10^{-9}
2018	Run78.0	2.49×10^{-4}	1.11×10^{11}	3.63×10^{-8}
	Run78.1	1.91×10^{-4}	4.88×10^{10}	1.07×10^{-7}
	Run78.2	1.72×10^{-4}	1.67×10^{12}	3.49×10^{-9}
	Run79.0	1.90×10^{-4}	2.49×10^{12}	2.11×10^{-9}
Total			6.83×10^{12}	7.20×10^{-10}

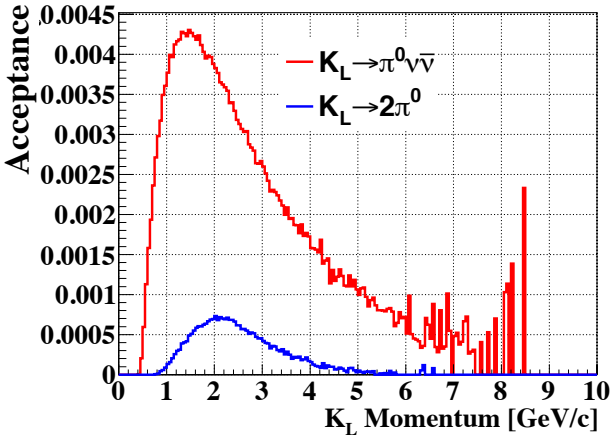

Figure 7.26: Geometrical acceptance as a function of initial K_L momentum. The red (blue) histograms represent the geometrical acceptance for $K_L \to \pi^0\nu\overline{\nu}$ ($K_L \to 2\pi^0$).

respectively. The acceptances of A_{trigger}, A_{photon}, A_{kine}, A_{veto}, and A_{shape} are referred to as the cut related acceptances. Details of the uncertainties in each subdivided acceptance are explained in the following sections.

7.3.2 Geometrical Acceptance

We defined the geometrical acceptance as the probability that all the photons from the K_L decay occurring in the region of $3200 < z < 5000$ mm hit CSI. Figure 7.26 shows the geometrical acceptance for $K_L \to \pi^0\nu\overline{\nu}$ and $K_L \to 2\pi^0$. If the momentum spectrum is different between data and MC, the geometrical acceptance difference between data and MC becomes a source of the systematic uncertainty on the SES.

To estimate the uncertainty, we varied the initial K_L momentum spectrum in the MC simulation and evaluated the effect on the geometrical acceptance. We varied the parameter vector of $\boldsymbol{a}_0$ in Eq. 5.1 with Gaussian considering the correlation between parameters using the variance-covariance matrix given in [31], where the variance-covariance matrix was obtained when we determined the parameter vector of $\boldsymbol{a}_0$ by fitting for the K_L momentum spectrum in the past study. For each variation, the relative acceptance, $A^{\text{rel}}_{\text{geom}}(\boldsymbol{a}) = A^{\text{norm}}_{\text{geom}}(\boldsymbol{a})/A^{\text{sig}}_{\text{geom}}(\boldsymbol{a})$, was calculated. We then calculated the relative deviation of the acceptance ratio, $1 - A^{\text{rel}}_{\text{geom}}(\boldsymbol{a})/A^{\text{rel}}_{\text{geom}}(\boldsymbol{a}_0)$, with 10^6 trials with various $\boldsymbol{a}$. Figure 7.27 shows the histogram in which we filled a relative deviation of acceptance ratio with 10^6 trials. The

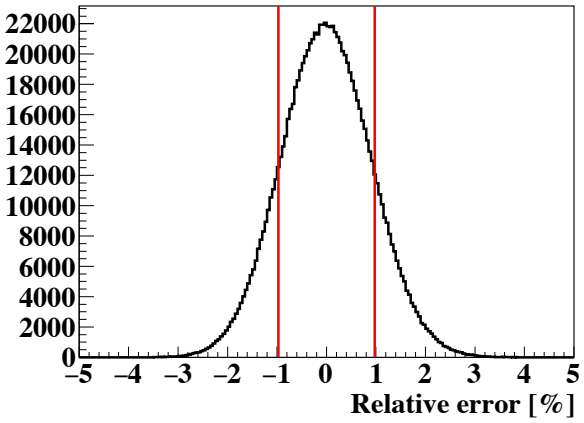

Figure 7.27: Deviation of the relative acceptance from the one using the initial parameter vector of $\boldsymbol{a}_0$. The region within the red lines represents the 68.27% region.

68.27% region was used for the estimation of the systematic uncertainty. Finally, the uncertainty on the geometrical acceptance was found to be 0.98%.

7.3.3 Cut Related Acceptances

In this section, we explain the cut related acceptance of $A_{\rm trigger}$, $A_{\rm photon}$, $A_{\rm kine}$, $A_{\rm veto}$, and $A_{\rm shape}$. To evaluate the acceptance value of each cut, we used a variable of "partial acceptance (PA)" defined as

$$PA^i_{\rm data\,(MC)} = \frac{N^{\rm all}_{\rm data\,(MC)}}{N^{\rm all-}_{\rm data\,(MC)}}, \tag{7.19}$$

where i is the index of each cut, $N^{\rm all}_{\rm data\,(MC)}$ is the number of events after imposing all the cuts for data (MC), and $N^{\rm all-}_{\rm data\,(MC)}$ is the number of events after imposing all the cuts except the i-th cut for data (MC). The PA^i denotes the acceptance value of the i-th cut.

To estimate uncertainties of the cut related acceptance, we used two different methods according to the type of the cut.

- For the cut related acceptance in which we did not expect the cancellation by taking the ratio between $A_{\rm sig}$ and $A_{\rm norm}$, the difference of the partial acceptance between data and MC,

$$\Delta^{SR}_i = \left| \frac{PA^i_{\rm MC}}{PA^i_{\rm data}} - 1 \right|, \tag{7.20}$$

  was regarded as an uncertainty, where i is the index of each cut. The total uncertainty for all the cuts in which we did not expect the error cancellation was calculated from the sum in quadrature as

$$\sigma_{SR} = \sqrt{\sum_i (\Delta^{SR}_i)^2}. \tag{7.21}$$

- For the estimation of the uncertainty of the cut related acceptance in which we expected the cancellation by taking the ratio between $A_{\rm sig}$ and $A_{\rm norm}$, we used the $K_L \to 2\gamma$ decay to emulate $K_L \to \pi^0 \nu\overline{\nu}$ decay because both decay modes do not have extra photons hitting veto counters in the final state. First, the double ratio of partial acceptances between data and MC, and between

$K_L \to 2\pi^0$ and $K_L \to 2\gamma$ was calculated as

$$DR_i = \left(\frac{PA^{\mathrm{MC}}_{K_L\to 2\pi^0}}{PA^{\mathrm{data}}_{K_L\to 2\pi^0}} \right) / \left(\frac{PA^{\mathrm{MC}}_{K_L\to 2\gamma}}{PA^{\mathrm{data}}_{K_L\to 2\gamma}} \right), \tag{7.22}$$

$$\tag{7.23}$$

where i is the index of each cut. The deviation of the double ratio was regarded as an uncertainty Δ_{DR} and calculated as

$$\Delta_i^{DR} = |DR_i - 1|, \tag{7.24}$$

where i is the index of each cut. The total uncertainty for all the cuts in which we expected the error cancellation was calculated as

$$\sigma_{DR} = \sqrt{\sum_i (\Delta_i^{DR})^2}. \tag{7.25}$$

After we calculated the σ_{SR} and σ_{DR} in each period (σ_{period}), the total uncertainty for all the cuts in the 2016–2018 dataset σ_{all} was calculated by taking the average of σ_{period} weighted by the corresponding statistics in each period as

$$\sigma_{\mathrm{all}} = \frac{\sum_i (\sigma^i_{\mathrm{period}} N^i_{\mathrm{norm}})}{N_{\mathrm{norm}}}, \tag{7.26}$$

where i represents the i-th period, and N^i_{norm} and N_{norm} are the number of collected $K_L \to 2\pi^0$ events in the i-th period and in 2016–2018, respectively. Details of uncertainties in each cut related acceptance are explained below.

7.3.3.1 Trigger Related

The uncertainties originating from trigger related cuts are described in this section. The uncertainties on the offline CSIEt cut and offline COE cut were categorized into the uncertainty on the kinematic cut (Sec. 7.3.3.3) due to technical reasons. The uncertainty originating from the efficiency correction for the online CSIEt trigger was found to be negligibly small. The uncertainties originating from the trigger timing cut, the online COE trigger efficiency, and the online clustering trigger efficiency were taken into account as the uncertainty on the trigger related cuts. For the trigger timing cut, we expect an error cancellation between $K_L \to \pi^0\nu\overline{\nu}$ and $K_L \to 2\pi^0$ because timings of triggers are not related to decay modes. Because the online COE trigger and online clustering trigger were used to collect $K_L \to \pi^0\nu\overline{\nu}$ samples but not for $K_L \to 2\pi^0$, and we do not expect error cancellations.

The discrepancy between data and MC from the trigger timing cut was studied using Eqs. 7.22–7.25. The uncertainty was estimated to be 0.18%. Because the acceptance of the trigger timing cut was almost 100%, the estimated uncertainty was small.

As in Sec. 7.2.1, the signal event loss due to the online COE trigger was evaluated by weighting the MC events using the efficiency map. We took into account the reproducibility of this weighting method as an uncertainty on SES. Using a validation sample in which we selected events in the normalization trigger data after applying loose selection cuts, we calculated PA as

$$PA_{\mathrm{data}} = \frac{N_{\mathrm{w/COE\,decision}}}{N_{\mathrm{w/o\,COE\,decision}}}, \tag{7.27}$$

$$PA_{\mathrm{MC}} = \sum_i^N \epsilon_i, \tag{7.28}$$

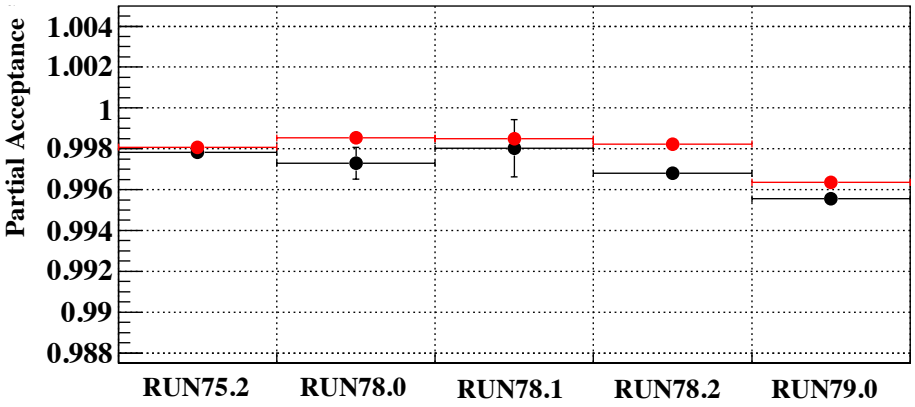

Figure 7.28: Partial Acceptance of the online clustering trigger in each period estimated using control samples. The trigger was used from the period of Run75.2. Each black (red) dot shows the acceptance of data (MC), respectively.

where $N_{\text{w/COE decision}}$ and $N_{\text{w/o COE decision}}$ are the number of events after and before imposing the online COE trigger decision, and ϵ_i is the COE trigger efficiency, described in Sec. 7.2, for the i-th event. In the loose cut set, the energy thresholds of FB, NCC, IB, MB, OEV, and CC03 were loosened to 5 MeV, and events outside the blind region were selected. The discrepancy between data and MC was evaluated using Eqs. 7.24 and 7.25, and the uncertainty was estimated to be 0.18% in 2016–2018. Because the dataset using online COE trigger was not dominant in the 2016–2018 data, the estimated uncertainty was smaller than in the 2015 data of 1.9% [35].

As in Sec. 7.2.1, the signal event loss due to the online clustering trigger was evaluated by weighting the MC events using the trigger efficiency of Eq. 7.7. We evaluated the uncertainty originating from the online clustering trigger using the same validation sample and the same manner as the ones used for evaluating the uncertainty originating from the online COE trigger. Figure 7.28 shows the PA for data and MC in each period. The PA_{MC} agreed with PA_{data}, and this validates the understanding of the online clustering trigger system. The uncertainty originating from the online clustering efficiency was estimated to be 0.07%.

7.3.3.2 Photon Selection

The discrepancy between data and MC caused by photon selection cuts was studied using Eqs. 7.20 and 7.21. Although some cancellations are expected between $K_L \to \pi^0 \nu\overline{\nu}$ and $K_L \to 2\pi^0$, we considered the uncertainty due to photon selection cuts conservatively. As a validation sample, we used π^0's which were selected from a reconstructed $K_L \to 2\pi^0$ sample without imposing the photon selection cuts. Figure 7.29 shows the PA for photon selection cuts in the period of Run79.0. Using Eq. 7.26, we estimated the photon selection cut uncertainty to be 0.57% in the 2016–2018 data.

7.3.3.3 Kinematic Cuts for $K_L \to \pi^0 \nu\overline{\nu}$

The discrepancy between data and MC from kinematic cuts for $K_L \to \pi^0 \nu\overline{\nu}$ was studied using Eqs. 7.20 and 7.21 because those cuts were used for only $K_L \to \pi^0 \nu\overline{\nu}$ samples. As a validation sample, we used π^0's from the reconstructed $K_L \to 2\pi^0$ sample. Using each pair of photons from a π^0, we re-reconstructed a π^0 assuming the decay vertex to be on the beam-axis as the same manner in the $K_L \to \pi^0 \nu\overline{\nu}$ analysis. Figure 7.30 shows the PA in the period of Run79.0. The largest discrepancy was in the T_{vtx} cut in which we also observed the discrepancy for the normalization mode analysis as described in Sec. 7.1. Using Eq. 7.26, we estimated the photon selection cut uncertainty to be 2.9% in the 2016–2018 data.

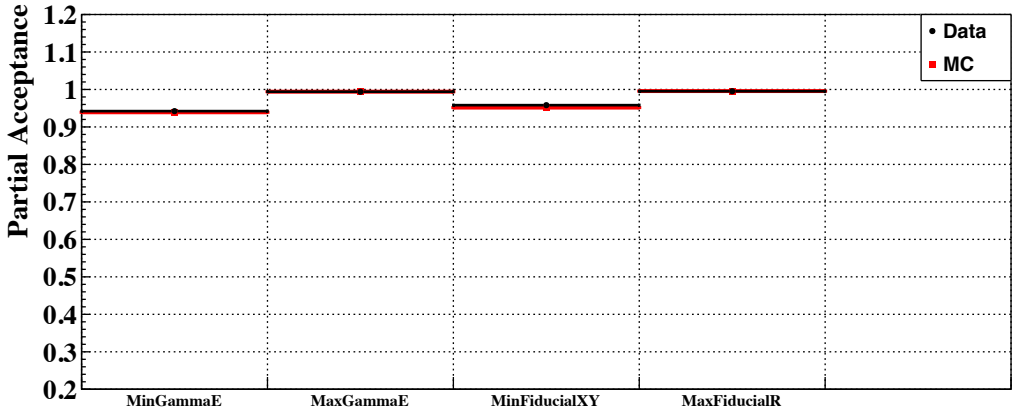

Figure 7.29: Partial Acceptances of the photon selection cuts in the control sample based on the period of Run79.0. The black and red points represent data and MC, respectively.

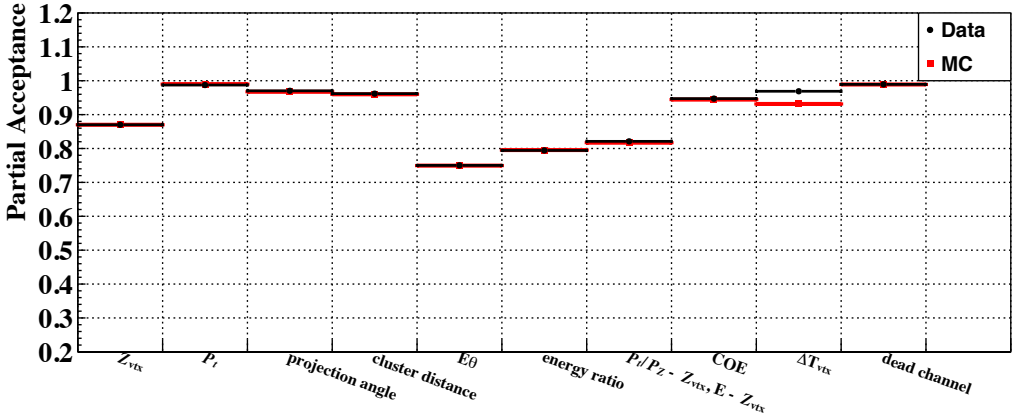

Figure 7.30: Partial Acceptances of the kinematic cuts for $K_L \to \pi^0 \nu\overline{\nu}$ in the control sample based on the period of Run79.0. The black and red points represent data and MC, respectively.

Table 7.10: Summary of relative systematic uncertainties on the single event sensitivity.

source	A_{category}	uncertainty [%]
geometrical	A_{geom}	0.98
trigger related	A_{trigger}	0.26
photon selection cuts	A_{photon}	0.57
kinematic cuts for $K_L \to \pi^0\nu\overline{\nu}$	$A^{\text{sig}}_{\text{kine}}$	2.9
veto cuts	A_{veto}	3.2
shape-related cuts	A_{shape}	5.2
kinematic cuts for $K_L \to 2\pi^0$	$A^{\text{norm}}_{\text{kine}}$	3.2
$K_L \to 2\pi^0$ branching fraction		0.69
inconsistency between normalization modes		5.2
total		9.2

7.3.3.4 Veto Cuts

For the veto cuts, we expect error cancellations between $K_L \to \pi^0\nu\overline{\nu}$ and $K_L \to 2\pi^0$ because all photons in the final state hit CSI for both decays, and thus accidental hits contribute to veto counters randomly. The discrepancy between data and MC caused by veto cuts was studied using Eqs. 7.22–7.25. Figure 7.31 shows the PA of veto cuts for $K_L \to 2\pi^0$ and $K_L \to 2\gamma$, and $DR - 1$ in the period of Run79.0. Using Eq. 7.26, the uncertainty was estimated to be 3.2%.

7.3.3.5 Shape-related Cuts

The discrepancy between data and MC caused by shape-related cuts was studied using Eqs. 7.20 and 7.21 because those cuts were used for only $K_L \to \pi^0\nu\overline{\nu}$ samples. We used the same validation sample as in the kinematic cuts for $K_L \to \pi^0\nu\overline{\nu}$. Figure 7.32 shows the PA in the period of Run79.0. Using Eq. 7.26, we estimated the photon selection cut uncertainty to be 5.2% in the 2016–2018 data.

7.3.3.6 Kinematic Cuts for $K_L \to 2\pi^0$

The discrepancy between data and MC caused by kinematic cuts for $K_L \to 2\pi^0$ except for the trigger timing, total energy, photon energy and photon position cuts (see Sec. 7.1.2) was studied using Eqs. 7.20 and 7.21 because those cuts were used for only $K_L \to 2\pi^0$ samples. Figure 7.33 shows the PA in the period of Run79.0. Using Eq. 7.26, we estimated the photon selection cut uncertainty to be 3.2% in the 2016–2018 data.

7.3.4 Summary of the Sensitivity for $K_L \to \pi^0\nu\overline{\nu}$

Table 7.10 summarizes the systematic uncertainties on SES. The maximum difference between the K_L flux calculated using $K_L \to 2\pi^0$, $K_L \to 3\pi^0$, and $K_L \to 2\gamma$, was 5.2%, and it was taken into account as a source of uncertainty, as mentioned in Sec. 7.1.4. In total, the uncertainty was estimated to be 9.2% by summing all the uncertainties in quadrature.

Based on the result in Sec. 7.2.4 and of the systematic uncertainty, SES for the 2016–2018 dataset was estimated to be

$$\text{SES} = (7.20 \pm 0.05_{\text{stat}} \pm 0.66_{\text{syst}}) \times 10^{-10}.$$

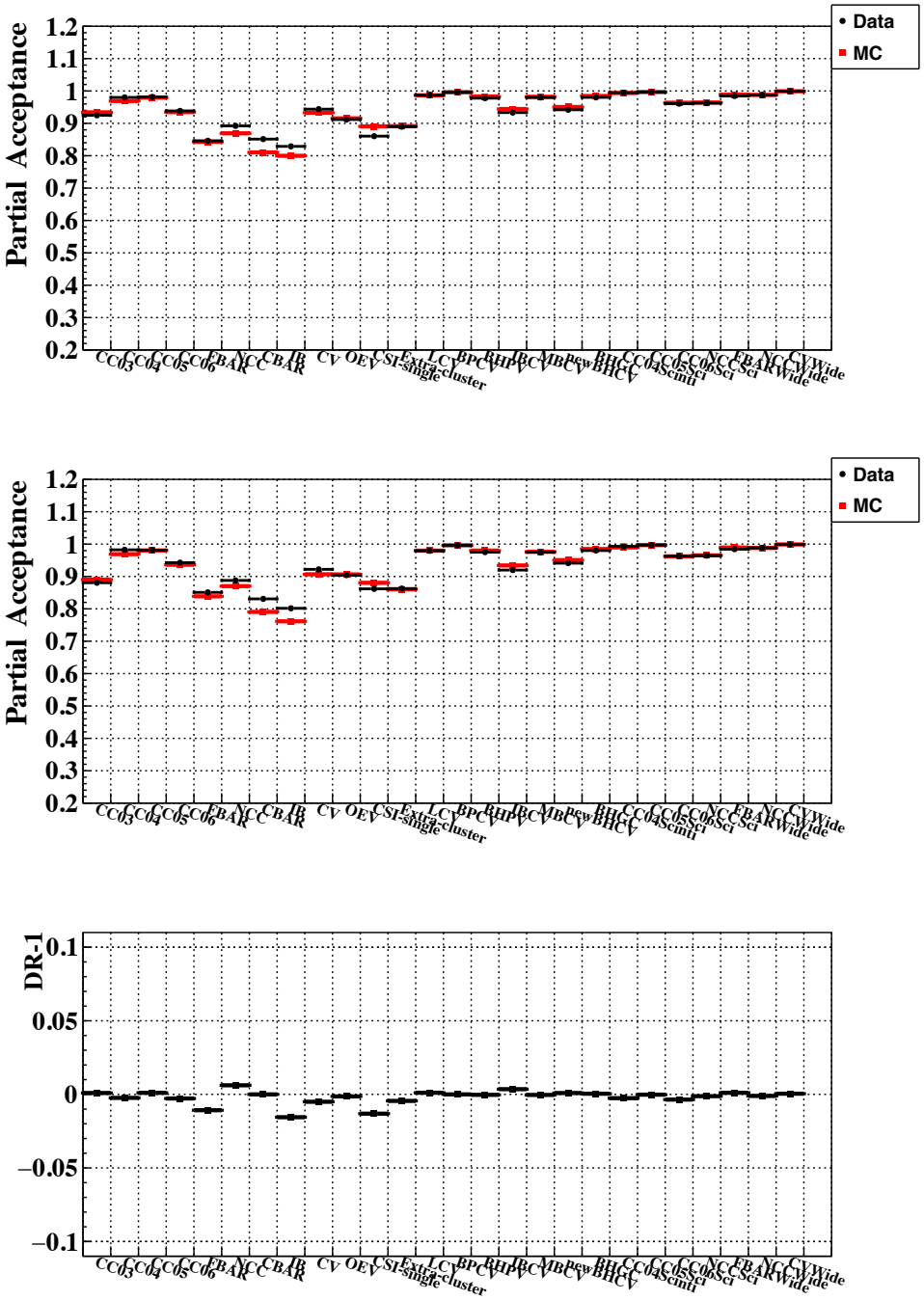

Figure 7.31: Partial Acceptances of the veto cuts in the control sample based on the period of Run79.0 for $K_L \to 2\pi^0$ (top) and $K_L \to 2\gamma$ (center). The black and red points represent data and MC, respectively. The bottom figure shows the $DR-1$ based on the period of Run79.0.

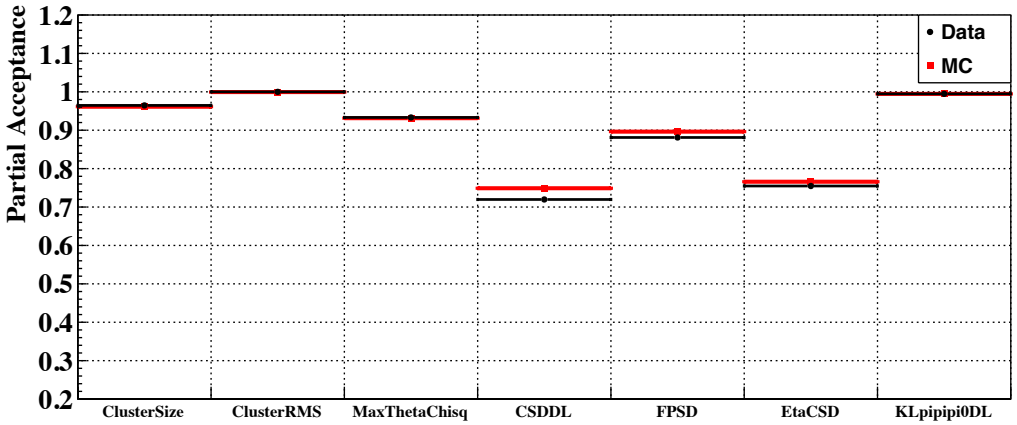

Figure 7.32: Partial Acceptances of the shape-related cuts in the control sample based on the period of Run79.0. The black and red points represent data and MC, respectively.

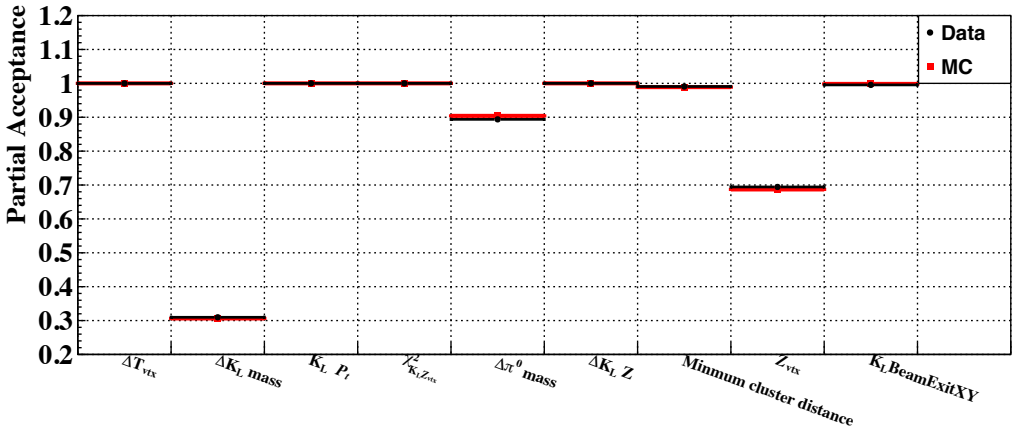

Figure 7.33: Partial Acceptances of the kinematic cuts for $K_L \to 2\pi^0$ in the control sample based on the period of Run79.0. The black and red points represent data and MC, respectively.

Chapter 8

Background Estimations

8.1 Overview

Background estimations for the $K_L \to \pi^0\nu\overline{\nu}$ analysis are described in this chapter. The number of background events from each source was normalized to the corresponding SES of 7.20×10^{-10}. Table 8.1 summarizes our background estimations. Background sources were categorized into three groups: K_L decay background, neutron-induced background, and $K^{\pm}$ decay background. As described in Sec. 6.1, we observed candidate events in the signal region and studied some background sources after looking inside the blind region. In particular, we found and studied two new background sources, one from $K^{\pm}$ decays, and one from beam-halo $K_L \to 2\gamma$ decays.

In the following sections, we first explain K_L decay backgrounds except for the beam-halo $K_L \to 2\gamma$ background. We then explain neutron-induced backgrounds. We finally explain new backgrounds from the $K^{\pm}$ decay and the beam-halo $K_L \to 2\gamma$ decay.

8.2 K_L Decay Background

In this section, K_L decay backgrounds except for the beam-halo $K_L \to 2\gamma$ are explained. The number of background events from K_L decays were estimated using MC simulations. K_L's were generated as in Sec. 5.1.1.

8.2.1 $K_L \to \pi^+\pi^-\pi^0$ Background

The mechanism of $K_L \to \pi^+\pi^-\pi^0$ background was the following: two charged-pions passing through the CSI beam hole were not detected by downstream veto counters, and a π^0 that decayed near the CSI surface was reconstructed with a P_t larger than the kinematical constraint due to the finite beam size. Figure 8.1 shows the P_t vs. $Z_{\rm vtx}$ of the events after imposing the cuts except for the CSD-$\pi^+\pi^-\pi^0$ cut. In the MC simulation study, the events inside the blind region had two charged-pions absorbed in a 0.5-mm-thick G10 pipe shown in Fig. 8.2 without being detected by veto counters. The background events had a correlation between P_t and $Z_{\rm vtx}$ due to the finite beam size. Figure 8.3 shows the schematic view of the π^0 direction and decay position. The correlation between the reconstructed $P_t^{\rm rec}$ and $Z_{\rm vtx}$ can be described as

$$P_t^{\rm rec} = P_{\pi^0}^{\rm rec} \sin\theta_{\rm rec}, \tag{8.1}$$

$$\simeq P_{\pi^0}^{\rm rec} \tan\theta_{\rm rec} = P_{\pi^0}^{\rm rec} \frac{r_{\pi^0} + d_{\rm beam}}{dZ}, \tag{8.2}$$

$$= P_{\pi^0}^{\rm rec} \frac{r_{\pi^0}}{dZ} + P_{\pi^0}^{\rm rec} \frac{d_{\rm beam}}{dZ}, \tag{8.3}$$

$$\simeq P_t^{\rm true} + P_{\pi^0}^{\rm rec} \frac{d_{\rm beam}}{Z_{\rm CSI} - Z_{\rm vtx}}, \tag{8.4}$$

Table 8.1: Summary of background estimation.

source		Number of events
K_L	$K_L \to \pi^+\pi^-\pi^0$	< 0.02 †
	$K_L \to 2\pi^0$	< 0.08 †
	$K_L \to 2\gamma$ (beam-core)	0.005 ± 0.005
	$K_L \to 3\pi^0$	0.01 ± 0.01
	$K_L \to \pi^\pm e^\mp \nu$	< 0.08 †
	$K_L \to 2\gamma$ (beam-halo)	0.26 ± 0.07 *
	$K_L \to \pi^+\pi^-$	< 0.03 *, †
	$K_L \to \pi^\pm e^\mp \gamma\nu$	< 0.05 *, †
	$K_L \to \pi^0\pi^\pm e^\mp \nu$	< 0.04 *, †
	$K_L \to e^+e^-\gamma$	< 0.09 *, †
	$K_L \to K^\pm e^\mp \nu$	< 0.04 *, †
Neutron	Hadron-cluster	0.017 ± 0.002
	Upstream-π^0	0.03 ± 0.03
	CV-η	0.03 ± 0.01
	CV-π^0	< 0.10 †
$K^\pm$		0.87 ± 0.25 *
total		1.22 ± 0.26

* Background sources studied after looking inside the blind region.
† At the 90% confidence level.

where $P^{\rm rec}_{\pi^0}$ is the reconstructed π^0 absolute momentum, $\theta_{\rm rec}$ is the reconstructed polar angle, $d_{\rm beam}$ is the distance of the π^0 decay position from the beam center, r_{π^0} is the distance between the π^0 decay position projected on the CSI surface and the position that the π^0 would hit CSI if it had not decayed, dZ is $Z_{\rm CSI} - Z_{\rm vtx}$, and $P_t^{\rm true}$ is the actual π^0 transverse momentum perpendicular to the beam-axis. In the 2015 data analysis [35], this correlation was studied, and the signal region was optimized by excluding the area with $P_t < \left(\frac{1}{35\ \rm mm}\left(Z_{\rm vtx} - 4000\ \rm mm\right) + 130\right)$ MeV/c for $Z_{\rm vtx} > 4000$ mm. In the 2016–2018 analysis, we used the same exclusion because the downstream detector configuration and the π^0 reconstructed method for the 2016–2018 data were the same as for the 2015 data.

An additional background suppression was obtained by applying a cut using the neural net method described in Sec. 7.2.1 in the 2016–2018 analysis. Figure 8.4 shows the P_t vs. $Z_{\rm vtx}$ of the events after applying CSD-$\pi^+\pi^-\pi^0$ cut to events in Fig. 8.1. While keeping the 90% signal acceptance, the $K_L \to \pi^+\pi^-\pi^0$ background was reduced by a factor of > 1.8 (68% C.L.), where the upper limit was due to no remaining events after applying the cut. We finally estimated the number of $K_L \to \pi^+\pi^-\pi^0$ background events to be < 0.02 (90% C.L.).

8.2.2 $K_L \to 2\pi^0$ Background

The neutral final state of $K_L \to 2\pi^0$ decays consists of four photons. There are three mechanisms to make two clusters on CSI from such photons. The first is a so-called even-pairing, in which CSI is hit by two photons decayed from the same π^0. The second is a so-called odd-pairing, as shown in Fig. 8.5 left, in which CSI is hit by two photons decayed from different π^0's. The third is a fusion, as shown in Fig. 8.5 right, in which three or four photons hit CSI, and two of them fuse into a single cluster when photon (x, y) positions on CSI are close to each other. For even-pairing background events, the kinematics of the π^0 from $K_L \to 2\pi^0$ decay is similar to the one from $K_L \to \pi^0\nu\overline{\nu}$ decay, and thus veto cuts are essential. For odd-pairing background events, not only the photon detection inefficiency in veto counters but also the kinematic variables are essential. In the case of odd-pairing background, we cannot reconstruct the π^0 correctly due to the miscombination of photons. The π^0

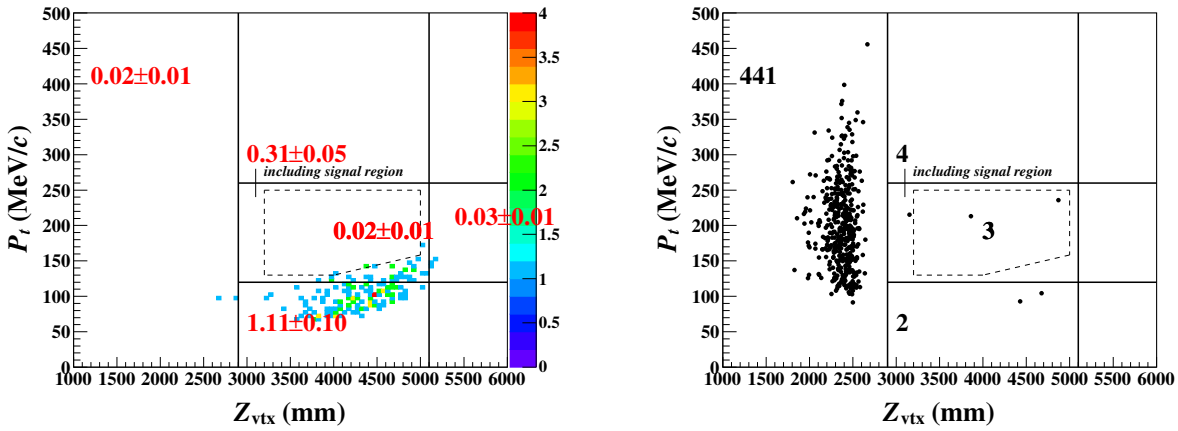

(a) $K_L \to \pi^+\pi^-\pi^0$ MC simulation (b) Data

Figure 8.1: P_t vs. $Z_{\rm vtx}$ of the events after imposing the $K_L \to \pi^0\nu\overline{\nu}$ selection criteria except for CSD-$\pi^+\pi^-\pi^0$ on the $K_L \to \pi^+\pi^-\pi^0$ MC events (a) and data (b). The numbers indicate the number of background events in each different region. Although the actual P_t from $K_L \to \pi^+\pi^-\pi^0$ decay is lower than 132 MeV/c due to the kinematical limit, the reconstructed P_t can be large when $K_L \to \pi^+\pi^-\pi^0$ decays occur off the beam-axis near CSI. For the $K_L \to \pi^+\pi^-\pi^0$ MC simulation, we simulated 8.0×10^{13} $K_L \to \pi^+\pi^-\pi^0$ events, which correspond to 9×10^1 times higher statistics than data. In this cut set, contributions from other background sources were expected to be 0.79 ± 0.20 events in the region of $2900 < Z_{\rm vtx} < 5100$ mm and $P_t < 120$ MeV/c.

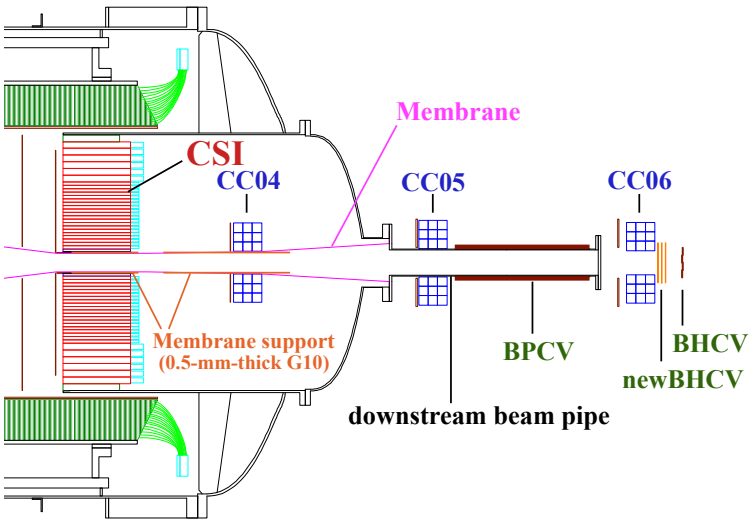

Figure 8.2: Downstream part of the KOTO detectors (quoted from [35] and modified).

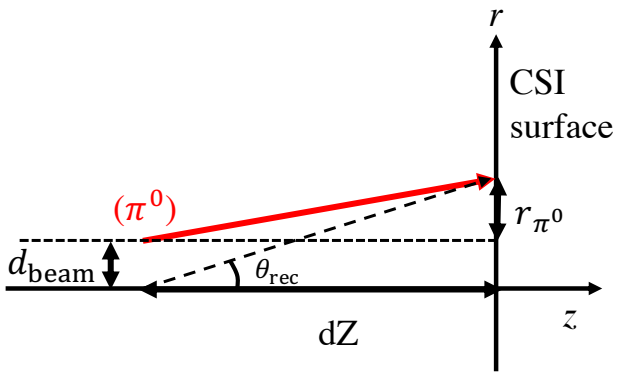

Figure 8.3: Effect on the finite beam size. The red arrow represents the π^0 trajectory if it had not decayed.

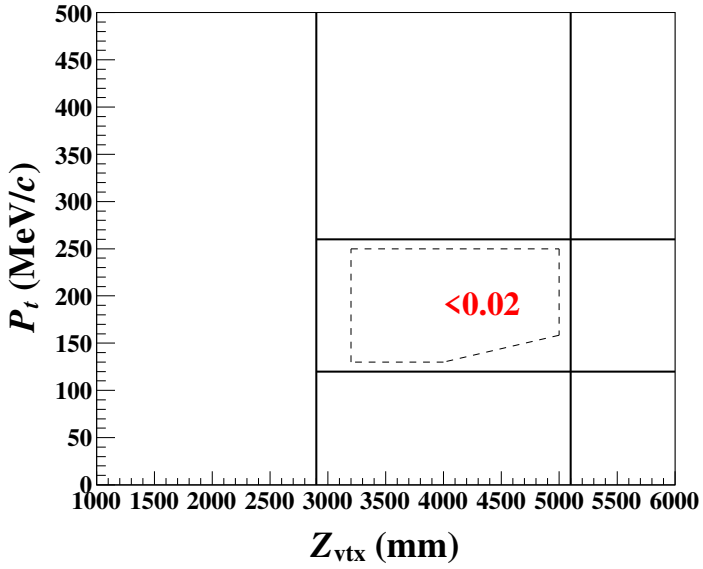

Figure 8.4: P_t vs. Z_{vtx} of the events after imposing the $K_L \to \pi^0\nu\overline{\nu}$ selection criteria on the $K_L \to \pi^+\pi^-\pi^0$ MC events. The upper limit on the number of events is at the 90% confidence level.

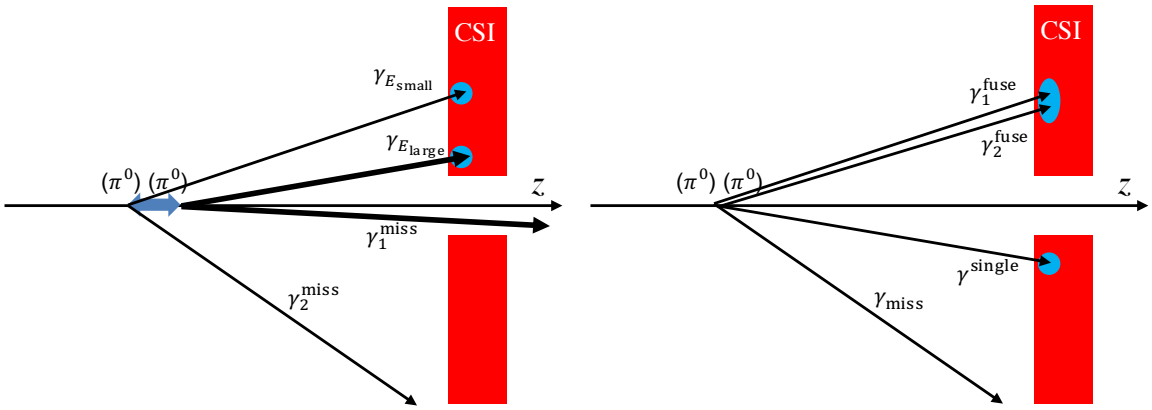

Figure 8.5: Left: the schematic view of an odd-pairing event. The blue arrow indicates the π^0 directions of the $K_L \to 2\pi^0$ decay at the rest frame. Right: the schematic view of a fusion event. Two photons ($\gamma_1^{\rm fuse}$, $\gamma_2^{\rm fuse}$) fuse into a cluster.

could be reconstructed in the decay region though the actual $K_L \to 2\pi^0$ decays occurred upstream. In such a case, energies of photons hitting CSI tend to be unbalanced, as shown in Fig. 8.5 left, due to the following reasons.

1. If the actual P_t of π^0 is large, photons from such π^0's tends to have a large P_t and to hit NCC before reaching CSI. Therefore, the actual P_t of π^0 tends to be small.

2. In case of the odd-pairing events, one photon from a π^0 whose direction is forward and the other from a π^0 whose direction is backward at rest hit CSI. Therefore, photon energies do not balance due to the Lorentz boost.

The kinematic cuts on $E_{\rm ratio}$ and $E\,\theta$ are sensitiveness to the energy balance of photons and reduce odd-pairing $K_L \to 2\pi^0$ background events. For fusion background events, the shape-related cut of CSD-Had reduces the events which contain clusters which are not like single-photon-like clusters.

To estimate this background, we simulated 1.6×10^{11} $K_L \to 2\pi^0$ events, which corresponds to 27 times higher statistics than the data. Figure 8.6 shows the P_t vs. $Z_{\rm vtx}$ of the $K_L \to 2\pi^0$ MC events after imposing the $K_L \to \pi^0\nu\overline{\nu}$ selection criteria. Because there were no remaining events after imposing the cuts, the number of background events was set to be < 0.08 (90% C.L.).

The validity of the $K_L \to 2\pi^0$ background estimation was studied by applying loose cuts to increase statistics. For the loose cuts, we applied the $K_L \to \pi^0\nu\overline{\nu}$ selection criteria but without applying veto cuts of CSI isolated hit crystal, BHPV, and BHGC, as well as without using the CSD-$\pi^+\pi^-\pi^0$ cut to increase statistics in the region of $P_t < 130{\rm MeV}/c$. Figure 8.7 shows the P_t vs. $Z_{\rm vtx}$ of the data and MC simulations with the loose cuts. The numbers of observed events in data are consistent with the numbers of estimated background events in the regions of $Z_{\rm vtx} > 2900$ mm. This agreement shows that we understand the detector responses in MC simulations.

8.2.3 $K_L \to 2\gamma$ (beam-core) Background

The $K_L \to 2\gamma$ background from beam-core K_L's is suppressed by requiring the reconstructed π^0 P_t to be large, as described in Sec. 2.1.3.1. However, if a K_L decays into two photons away from the beam-axis, the reconstructed P_t can be large due to almost the same mechanism as in Eq. 8.4. In the case of $K_L \to 2\gamma$ decay, the reconstructed decay z position is shifted upstream because of the nominal mass difference between K_L and π^0. The $P_t^{\rm rec}$ is described as

$$P_t^{\rm rec} \simeq P_t^{\rm true}\frac{m_{\pi^0}}{m_{K_L}} + P_{\pi^0}^{\rm rec}\frac{d_{\rm beam}}{dZ_{\rm rec}}, \tag{8.5}$$

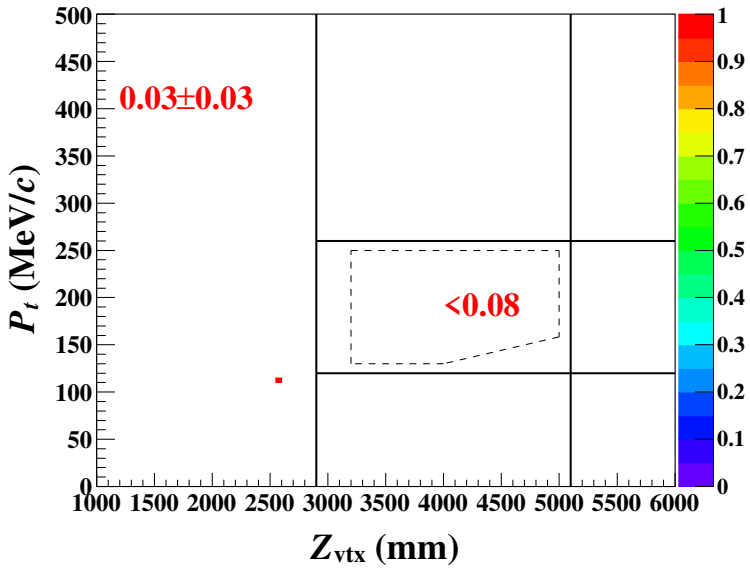

Figure 8.6: P_t vs. $Z_{\rm vtx}$ of the events after imposing the $K_L \to \pi^0\nu\overline{\nu}$ selection criteria on the $K_L \to 2\pi^0$ MC events. The upper limit on the number is at the 90% confidence level.

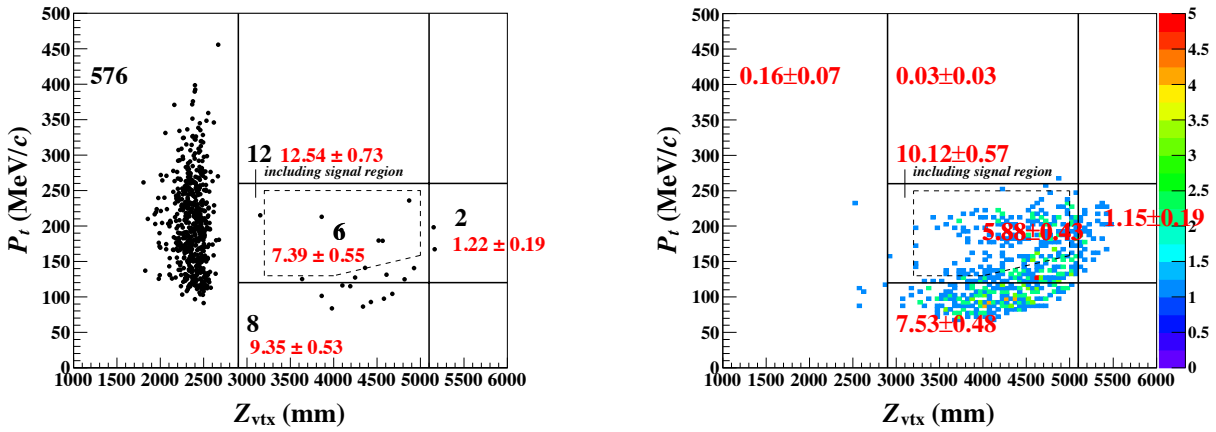

(a) Data (b) $K_L \to 2\pi^0$ MC simulation

Figure 8.7: P_t vs. $Z_{\rm vtx}$ of the events after imposing the loose selection criteria on the data (a) and $K_L \to 2\pi^0$ MC (b) events. The black and red numbers show the number of events in each region for data and MC simulation, respectively. The red numbers in the left figure contain the contributions from $K_L \to \pi^+\pi^-\pi^0$, $K^\pm$, and beam-halo $K_L \to 2\gamma$ decays MC simulations.

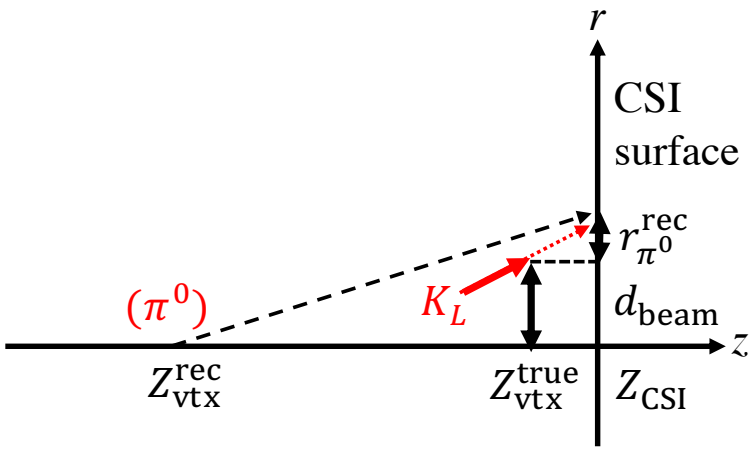

Figure 8.8: K_L decays away from the beam-axis. The solid red arrow represents the K_L trajectory, and the dotted red arrow represents the K_L trajectory if it had not decayed.

where $P_t^{\rm true}$ is the actual transverse momentum of K_L along the beam-axis, m_{π^0} and m_{K_L} are the mass of π^0 and K_L, respectively, $P_{\pi^0}^{\rm rec}$ is the reconstructed absolute momentum assuming $\pi^0 \to 2\gamma$ decays, and $dZ_{\rm rec}$ is the distance between the reconstructed decay z position assuming $\pi^0 \to 2\gamma$ decays ($Z_{\rm vtx}^{\rm rec}$) and $Z_{\rm CSI}$, as shown in Fig. 8.8.

For the beam-core K_L's, a 12.5-μm-thick polyamide film located at $Z = -500$ mm (vacuum window) is a source of scattering K_L's. The scattered K_L's which are scattered at the vacuum window can decay into two photons away from the beam-axis, which we refer it to as beam-core $K_L \to 2\gamma$ background. We simulated 7.4×10^{11} beam-core $K_L \to 2\gamma$ events, which corresponds to 1.9×10^2 times higher statistics than data. Figure 8.9 shows the P_t vs. $Z_{\rm vtx}$ for the $K_L \to 2\gamma$ MC events after imposing the $K_L \to \pi^0\nu\overline{\nu}$ selection criteria. The number of beam-core $K_L \to 2\gamma$ background events was estimated to be 0.005 ± 0.005.

8.2.4 $K_L \to 3\pi^0$ Background

In the $K_L \to 3\pi^0$ decay, four extra photons are available for vetoing the event, and thus the $K_L \to 3\pi^0$ background is highly suppressed by the veto cuts. For example, the detection inefficiency of IB for a 100 MeV photon is designed to be $O(10^{-4})$–$O(10^{-6})$[*1]. [62]. However, the photon detection inefficiency due to accidental activities were not fully studied at the time, and thus we studied the $K_L \to 3\pi^0$ background that arose from the photon detection inefficiencies in veto counters due to accidental hits overlapping a photon pulse and shifting its measured time outside the veto window.

To suppress the background due to the pulse overlapping, a pulse-shape discrimination method was introduced by applying a fast Fourier transform (FFT) to the waveform recorded by the veto counters, as described in Sec. 7.2.1. The veto window was widened to accommodate possible timing shifts due to overlapping pulses when the χ^2 value calculated from this method exceeded a given threshold. The veto windows and thresholds of $\chi^2_{\rm FFT}$ used in the 2016–2018 analysis are summarized in Table 7.3.

The detection inefficiency due to overlapped pulses was estimated by overlaying the accidental activity on the MC events. It was not easy to simulate $K_L \to 3\pi^0$ events with large enough statistics for the background estimation in a realistic amount of time due to the large branching ratio of this decay. To estimate the accidental effect on the detection efficiency, we divided the simulation process into two as follows:

1. The $K_L \to 3\pi^0$ events were simulated without overlaying accidental activities, and events remaining after applying kinematic cuts to select $K_L \to \pi^0\nu\overline{\nu}$ were recorded (collected seeds).

[*1] The detection efficiency is dependent on the incident angle of photons.

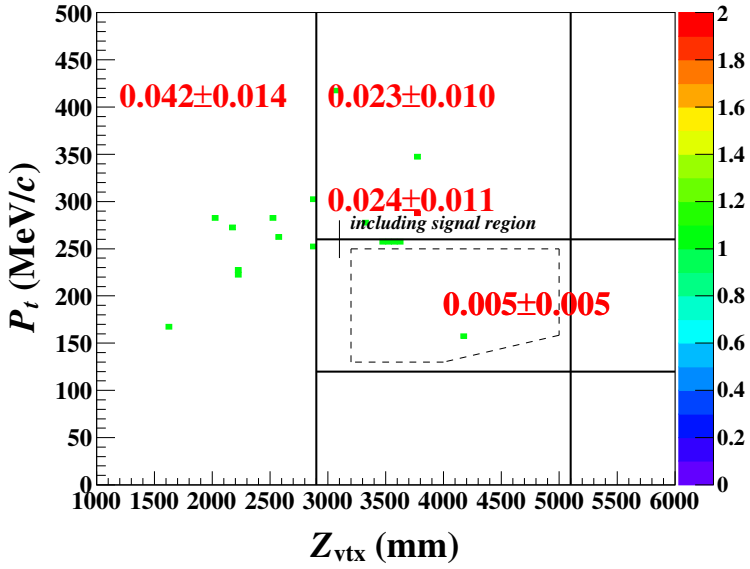

Figure 8.9: P_t vs. Z_{vtx} of the events after imposing the $K_L \to \pi^0\nu\overline{\nu}$ selection criteria on the beam-core $K_L \to 2\gamma$ MC events.

2. Different accidental activities were overlaid on each collected seed.

Because the $K_L \to 3\pi^0$ events have a small probability to satisfy the kinematic cuts, it is efficient to apply the cuts first and then overlay accidental activities, than to overlay accidental activities first and then apply the cuts.

By overlaying 5000 different accidental activities on the collected seed, 1×10^{14} $K_L \to 3\pi^0$ MC events were simulated, which corresponds to 0.7×10^2 times higher statistics than data. The number of background events from $K_L \to 3\pi^0$ was estimated to be 0.01 ± 0.01 as shown in Fig. 8.10.

The validity of the estimation of the $K_L \to 3\pi^0$ background due to overlapped-pulses was studied by applying loose cuts to increase the statistics. In the loose cuts, we loosened the energy threshold of NCC to 20 MeV, and we selected events with $\chi^2_{\text{FFT}} > 40$ in NCC. Figure 8.11 shows the P_t vs. Z_{vtx} of the events after applying the loose cuts for data and MC. In this loose cuts, the events in Fig. 8.11a had overlapped-like-pulses in waveforms. Figure 8.12 shows waveforms in NCC in the right-most event in Fig. 8.11a. As explained in Sec. 2.4.2.2, typical NCC modules have one Common readout used for the veto decision and three individual readouts. The on-time (off-time) pulse in the rear (front) part of the Individual readout implied that different particles hit each individual module, and the overlapped pulse was observed in the Common readout. The number of observed data events which had overlapped-like-pulses in waveforms is consistent with the number of events expected by the MC simulation. This agreement shows that we understand the detector responses in the MC simulation.

8.2.5 $K_L \to \pi^{\pm}e^{\mp}\nu$ Background

The mechanism of the $K_L \to \pi^{\pm}e^{\mp}\nu$ background is categorized into two. For the first mechanism, the background is caused by two charged-particles hitting CSI but not being detected by CV. For the second mechanism, the background is caused by charged-particles hitting detector components and producing π^0.

Events by the first mechanism are highly suppressed by the CV veto cut, whose detection inefficiency against a charged-particle that penetrated CV per layer was estimated to be less than 1.5×10^{-5} in the past study [48]. Because the condition of accidental activities in the past study was not the same as in 2016–2018, we studied the background that arose from a charged-particle detection inefficiency in CV due to accidental hits overlapping a charged-particle pulse and shifting its measured time outside the veto window. Due to the large branching ratio of $K_L \to \pi^{\pm}e^{\mp}\nu$ decay, it was not easy to simulate

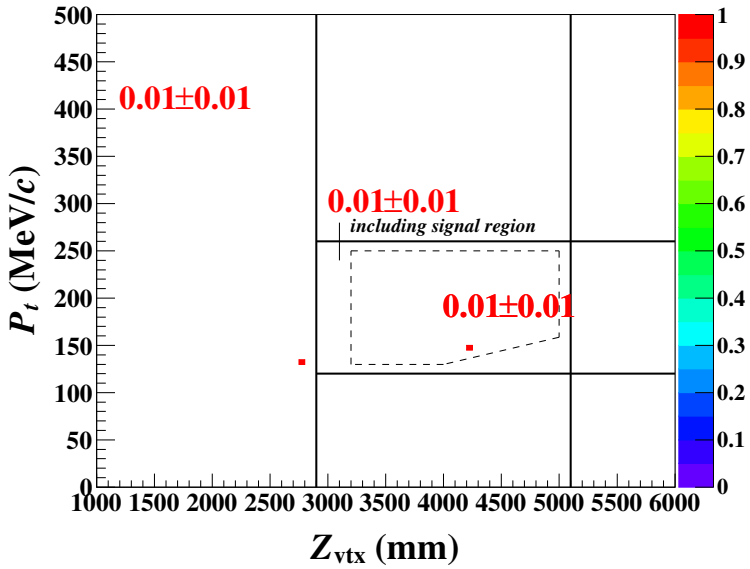

Figure 8.10: P_t vs. $Z_{\rm vtx}$ of the events after imposing the $K_L \to \pi^0\nu\overline{\nu}$ selection criteria on the $K_L \to 3\pi^0$ MC events.

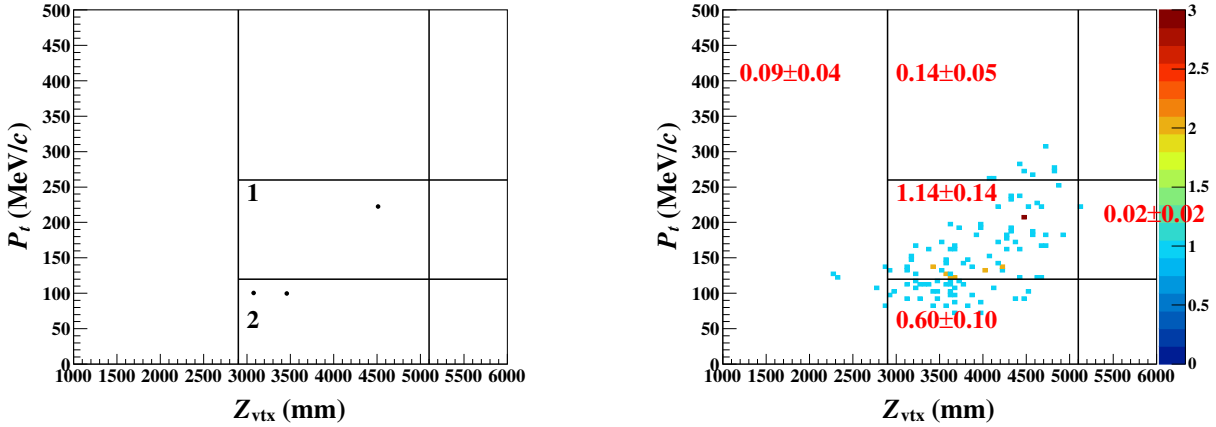

(a) Data (b) $K_L \to 3\pi^0$ MC simulation

Figure 8.11: P_t vs. $Z_{\rm vtx}$ of the events after imposing the loose selection criteria on the (a) data and (b) $K_L \to 3\pi^0$ MC events. The numbers indicate the number of background events in each region.

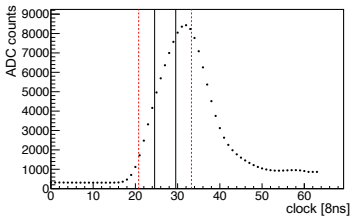

(a) NCC-Common

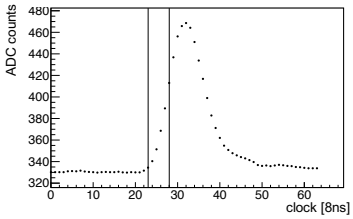

(b) NCC-Individual (front)

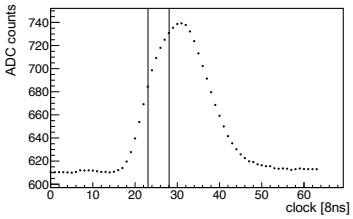

(c) NCC-Individual (middle)

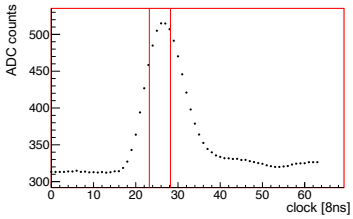

(d) NCC-Individual (rear)

Figure 8.12: Observed overlapping pulses in NCC in the right-most event in Fig. 8.11a. The NCC-Common signal was used for the veto decision. The region inside the vertical solid (dotted) lines is the veto window (widened veto window).

$K_L \to \pi^\pm e^\mp \nu$ MC events with large enough statistics for background estimation. We thus simulated this event with a similar strategy as in the $K_L \to 3\pi^0$ background estimation. We first prepared seeds by applying kinematic cuts, and then overlaid 30000 different accidental activities on each collected seed. With this method, we simulated 8×10^{13} $K_L \to \pi^\pm e^\mp \nu$ MC events, which corresponds to 0.7×10^2 times higher statistics than data. The number of background events due to the first mechanism was estimated to be < 0.08 (90% C.L.).

To estimate the background by the second mechanism, we separated the simulation process into two to increase MC statistics efficiently. We first prepared a sample by selecting events that have π^0's produced by charged-particles hitting detector components. We then simulated π^0's and accompanying particles 100 times with different seeds. As a result, we did not observe any remaining events in the MC simulation and estimated the number of background events due to the second mechanism to be < 0.04 (90% C.L.).

8.2.6 Backgrounds from Other K_L Decays

We studied backgrounds from the $K_L \to \pi^+\pi^-$, $K_L \to \pi^\pm e^\mp \gamma\nu$, $K_L \to \pi^0\pi^\pm e^\mp \nu$, $K_L \to e^+e^-\gamma$, and $K_L \to K^\pm e^\mp \nu$ decays (referred to as minor K_L decays). The branching fractions of the decays except for $K_L \to K^\pm e^\mp \nu$ are summarized in Table 2.1. The $K_L \to K^\pm e^\mp \nu$ decay has not been observed but the branching fraction is predicted to be $(0.5071 \pm 0.0199) \times 10^{-8}$ [65]. In the 2016–2018 background study, we assumed that the branching fraction of the $K_L \to K^\pm e^\mp \nu$ decay is 1×10^{-8} conservatively.

The numbers of background events from minor K_L decays were studied by N. Shimizu [66] and estimated using MC simulations. Because no events remained after imposing the $K_L \to \pi^0\nu\overline{\nu}$ selection criteria on each minor K_L decay MC simulation, we set upper limits on the numbers of background events at the 90% C.L. as < 0.03 for $K_L \to \pi^+\pi^-$, < 0.05 for $K_L \to \pi^\pm e^\mp \gamma\nu$, < 0.04 for $K_L \to \pi^0\pi^\pm e^\mp \nu$, < 0.09 for $K_L \to e^+e^-\gamma$, and < 0.04 for $K_L \to K^\pm e^\mp \nu$.

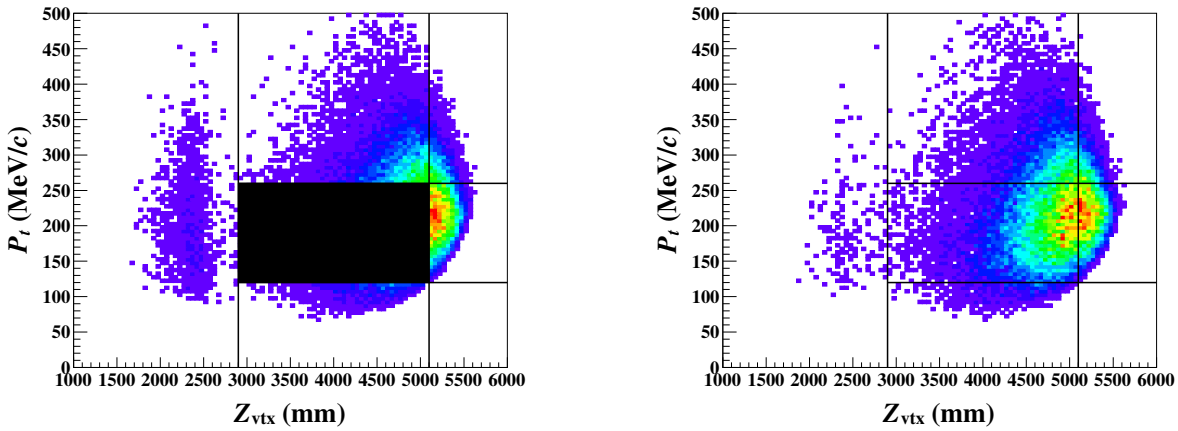

(a) Physics data sample (b) Control sample

Figure 8.13: P_t vs. $Z_{\rm vtx}$ of the events after imposing a loose selection criteria on the (a) physics data sample and (b) control sample.

8.3 Neutron-Induced Background

8.3.1 Hadron-Cluster Background

8.3.1.1 Mechanism

When a beam-halo neutron hits CSI and produces a cluster, another neutron from the hadronic interaction can produce an additional cluster. If we misidentify two hadronic clusters as photon clusters, the event can be a background. To suppress the hadron-cluster background, we used the energy and timing information in CSI.

8.3.1.2 Control Sample

To study this background, we used a control sample taken in the Z0Al run described in Sec. 3.3.3.1. In this sample, neutrons scattered at the aluminum plate hit CSI and produce the hadron-cluster background. Using this control sample, two new cuts, CSD-Had and PSD-FFT (see Sec. 7.2.1), were developed to suppress the hadron-cluster background. Figure 8.13 shows the P_t vs. $Z_{\rm vtx}$ of the physics data sample and control sample. For these samples, trigger-related cuts, photon-selection cuts, kinematic cuts for $K_L \to \pi^0\nu\overline{\nu}$, shape-related cuts of cluster size and cluster RMS, and the veto cuts were imposed, while $\Delta T_{\rm vtx}$ and some of the veto cuts were loosened to increase the statistics. Figures 8.14 and 8.15 show the agreement between the physics data sample and control sample in the region of $120 < P_t < 500$ MeV/c and $2900 < Z_{\rm vtx} < 6000$ mm excluding the blind region.

8.3.1.3 Contamination in the Control Sample

The photon contamination in the control sample is explained in this section. The beam-core K_L can scatter at the aluminum plate. If such a K_L decays into two photons away from the beam-axis, the event can contaminate the hadron-cluster control sample. To confirm such contamination, the $R_{\rm COE}$ distribution was studied because $R_{\rm COE}$ of $K_L \to 3\pi^0$ events represents the extrapolated K_L positions at CSI (see Sec. 4.2.3). As shown in Fig 8.16, the $K_L \to 3\pi^0$ decays with large $R_{\rm COE}$ increased when the aluminum plate was inserted, and its amount in the region of $R_{\rm COE} > 200$ mm is consistent with the MC simulation, where the $R_{\rm COE} > 200$ mm is the requirement on the $K_L \to \pi^0\nu\overline{\nu}$ analysis.

Figure 8.17 shows the P_t vs. $Z_{\rm vtx}$ after imposing CSD-Had, CSD-η, and PSD-FFT cuts on the events shown in Fig. 8.13b and events in the scattering $K_L \to 2\gamma$ MC simulation. The fraction of the contamination was estimated to be 3×10^{-5} by comparing the number of events in Fig. 8.17b

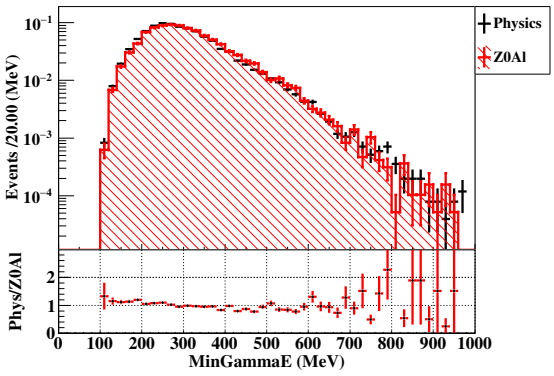

(a) Cluster energy (smaller)

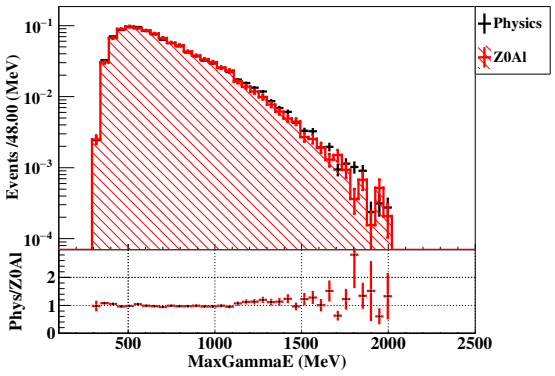

(b) Cluster energy (larger)

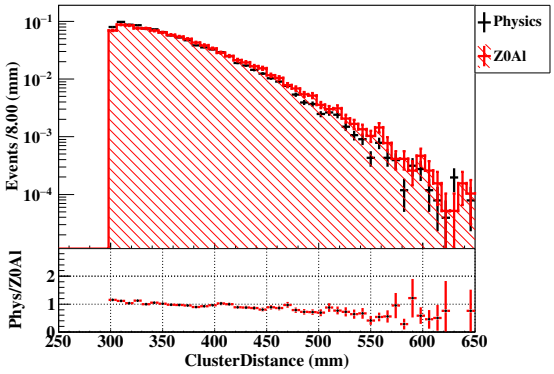

(c) Cluster distance

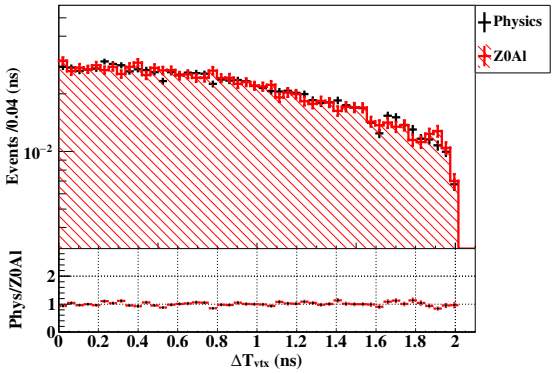

(d) ΔT_{vtx}

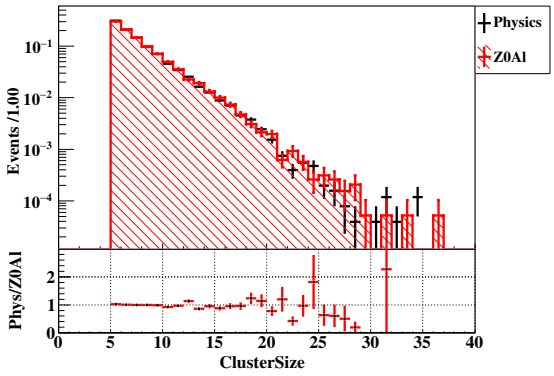

(e) Cluster size (smaller)

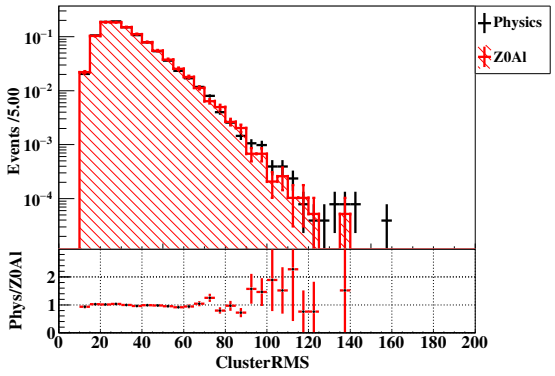

(f) ClusterRMS (smaller)

Figure 8.14: Distributions of smaller cluster energy (a), larger cluster energy (b), cluster distance (c), ΔT_{vtx} (d), smaller cluster size (e), and smaller cluster RMS (f) for events in the physics run and the Z0Al run. The histogram in black and red shows the physics and Z0Al run data, respectively. Each histogram is normalized to have the same area. The ratios of histograms between the physics and Z0Al run are shown below each panel. The error bars represent statistical errors.

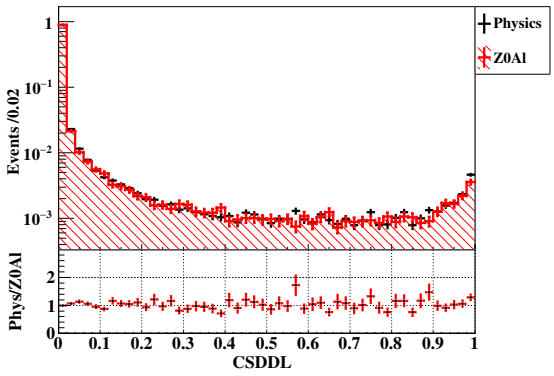

(a) CSD-Had (each cluster)

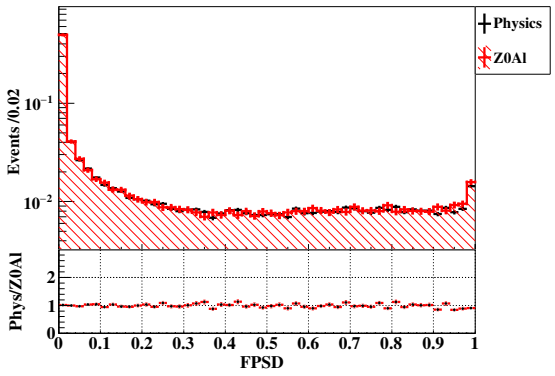

(b) PSD-FFT (each cluster)

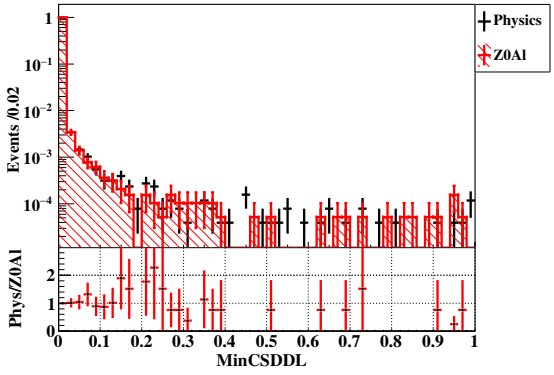

(c) CSD-Had (smaller)

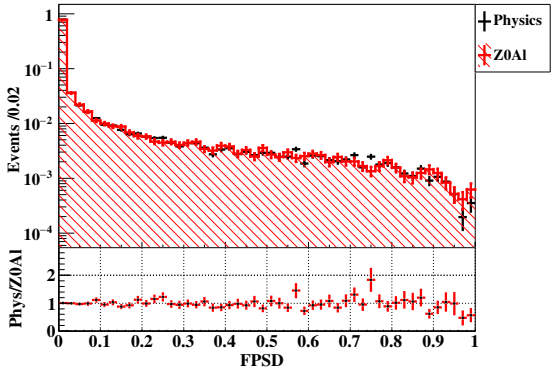

(d) PSD-FFT (smaller)

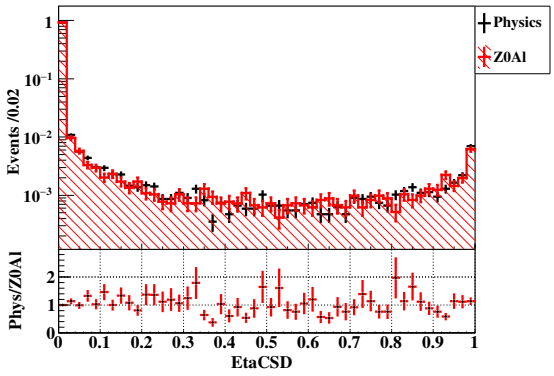

(e) CSD-η

Figure 8.15: Distributions of $o_{\text{CSD-Had}}$ of two clusters (a), $o_{\text{PSD-FFT}}$ of two clusters (b), smaller $o_{\text{CSD-Had}}$ between two clusters, smaller $o_{\text{PSD-FFT}}$ between two clusters, and $o_{\text{CSD-}\eta}$ (e) in the physics and Z0Al run data. The meanings of the colors of histograms, below panels, and error bars are the same as for Fig. 8.14.

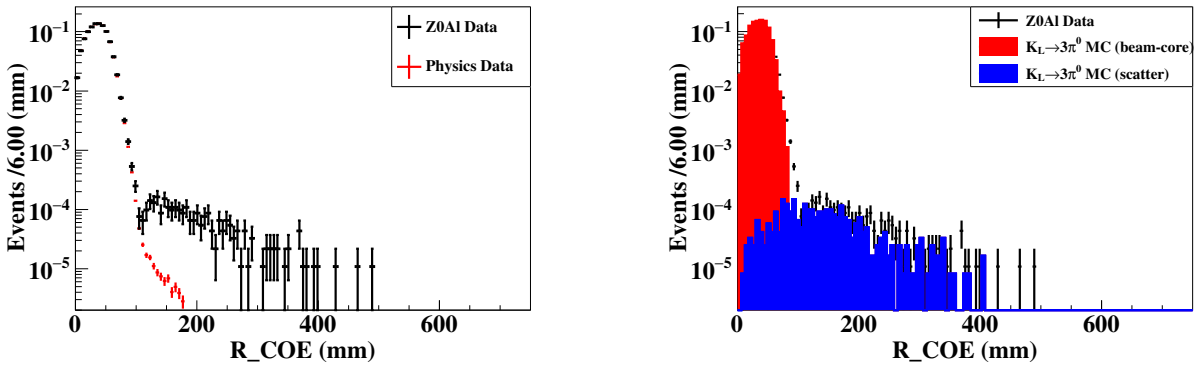

Figure 8.16: R_{COE} distribution of $K_L \to 3\pi^0$ decay samples. Left: a comparison between the Z0Al run (black) and physics run (red). Right: a comparison between data and MC for the Z0Al run. The black histogram represents the data. The red histogram represents the beam-core $K_L \to 3\pi^0$ MC simulation. The blue histogram represents the MC simulation of K_L's scattered at the aluminum plate decaying into six photons. The histograms of MC simulations are normalized with the number of collected K_L's in the Z0Al run.

and Fig. 8.13b in the region of $120 < P_t < 500$ MeV/c and $2900 < Z_{\mathrm{vtx}} < 6000$ mm (control region). Figure 8.17 indicates that the contribution from scattering $K_L \to 2\gamma$ decays existed in the hadron-cluster control sample, although the fraction of the contamination is small.

8.3.1.4 Rejection Factor of the Shape-related Cuts

The rejection factor of the shape-related cuts against hadron-cluster background events could be calculated by comparing the number of events before (Fig. 8.13b) and after (Fig. 8.17) imposing the cuts. However, it was difficult to subtract the contribution from scattering $K_L \to 2\gamma$ decays since the number of remaining events in the control sample after imposing the cuts was small.

To estimate the rejection factor of shape-related cuts of CSD-Had and PSD-FFT, a weighting method was adopted to avoid photon contaminations. We first collected hadron-cluster background events with the cuts used to obtain Fig. 8.13b, though more looser veto cuts were imposed. We treated each cluster of those hadron-cluster events as a single hadron-cluster. For every cluster, we imposed cuts of both CSD-Had and PSD-FFT, and calculated a survival probability given as a function of the energy and incident angle. Figure 8.18 shows the survival probability map. The rejection factor for each hadron-cluster is $O(10^{-3})$, which indicates the effect of the contamination from scattering $K_L \to 2\gamma$ decays, which was estimated to be 3×10^{-5}, is small. Finally, we obtained the number of expected remaining events after applying CSD-η, CSD-Had, and PSD-FFT as follows:

1. We collected events after applying CSD-η cut on events in Fig. 8.13b.

2. Next, we estimated the number of expected remaining events after applying CSD-Had and PSD-FFT as $N_{\mathrm{exp}} = \sum_i (w_1^i \times w_2^i)$. Here, $w_{1(2)}^i$ is the survival probability after applying CSD-Had and PSD-FFT for each cluster in the i-th event given as a function of the energy and incident angle.

The validity of the weighting method was studied by loosening the cut of CSD-Had to increase the statistics. Figure 8.19 shows comparisons between the cut-base and weighting method analyses as a function of the threshold of CSD-Had. The numbers of remaining events after imposing CSD-η, CSD-Had, and PSD-FFT (cut-base) were consistent with the sum of number of events expected from the weighing method and scattering $K_L \to 2\gamma$ MC simulation. Based on the number of expected events after imposing shape-related cuts using the weighting method, the rejection factor of shape-related

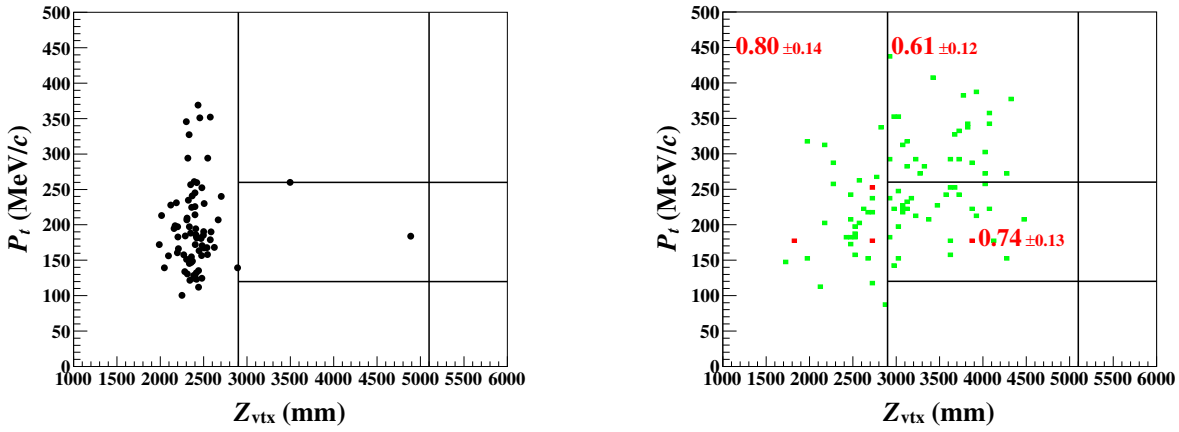

(a) Control sample.

(b) Scatter $K_L \to 2\gamma$ MC.

Figure 8.17: P_t vs. Z_{vtx} after imposing CSD-Had, CSD-η, and PSD-FFT cuts on the events in Fig. 8.13b (left) and events in the scattering $K_L \to 2\gamma$ MC simulation (right). The numbers in red indicate the number of events in each region bounded by lines. The number of events in the MC simulation is normalized with the number of collected K_L's in the Z0Al run.

cuts was estimated to be $(1.8 \pm 0.2) \times 10^{-6}$. Compared to the cut-base analysis, which was not taken the contamination from scattering $K_L \to 2\gamma$ decays into account, the rejection factor was improved by 27 ± 19, where most of the uncertainty came from the statistical uncertainty in the cut-base analysis.

8.3.1.5 The Number of Background Events

The number of hadron-cluster background events was estimated by the product of the background yield and rejection factor of shape-related cuts. The background yield was obtained as $\alpha \times N_{\text{Al}}$, where α is the ratio of the number of events in the physics and Z0Al run in the control region excluding the blind region before imposing CSD-η, CSD-Had, and PSD-FFT cuts. The N_{Al} is the number of events in the Z0Al run in the signal region before imposing CSD-η, CSD-Had, and PSD-FFT cuts.

In the 2015 analysis, the downstream boundary of the signal region was set at $Z_{\text{vtx}} = 4700$ mm to avoid the hadron-cluster background. In the 2016–2018 analysis, the rejection factor of the shape-related cuts of $O(10^{-6})$ was achieved by introducing new cuts and taking the photon contaminations into account. Because the hadron-cluster background was suppressed sufficiently, we extended the downstream boundary of the signal region to $Z_{\text{vtx}} = 5000$ mm. Compared to the 2015 analysis, the signal acceptance increased by 16%. Based on the rejection factor of 1.8×10^{-6}, $\alpha = 3.0$ and $N_{\text{Al}} = 3089$, the number of hadron-cluster background was estimated to be 0.017 ± 0.002, as shown in Fig. 8.20.

8.3.2 CV-π^0 and CV-η Backgrounds

The CV-η and CV-π^0 backgrounds are caused by beam-halo neutrons hitting CV and producing η and π^0, respectively. These backgrounds were studied with MC simulations. The yields were normalized with the ratio between data and MC for events in the region of $Z_{\text{vtx}} > 5100$ mm with the loose selection criteria.

Figure 8.21a shows P_t vs. Z_{vtx} of the events after imposing the $K_L \to \pi^0\nu\overline{\nu}$ selection criteria on the CV-π^0 MC simulation. No events remained in the signal region, and the number of CV-π^0 background events was estimated to be < 0.10 (90% C.L.).

Figure 8.21b shows P_t vs. Z_{vtx} of the events after imposing the $K_L \to \pi^0\nu\overline{\nu}$ selection criteria on the CV-η MC simulation. Compared to the cut used in the 2015 analysis to suppress the CV-η background, the new shape-related cut improved the rejection against CV-η background by 50%, while

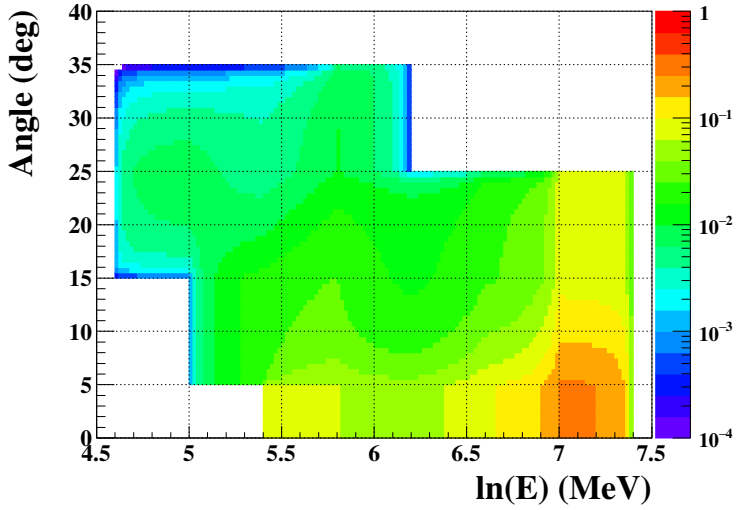

Figure 8.18: Map of survival probability after applying both CSD-Had and PSD-FFT for each hadron-cluster as a function of cluster energy and incident angle.

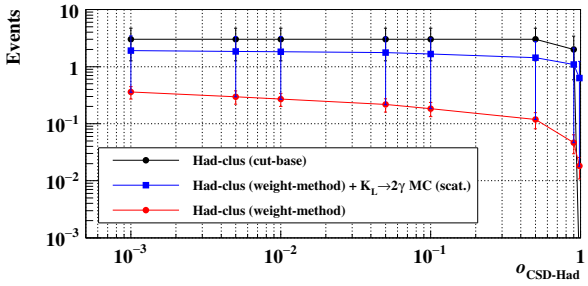

(a) Region above the blind region
($260 < P_t < 500$ MeV/c and $2900 < Z_{\rm vtx} < 5100$ mm).

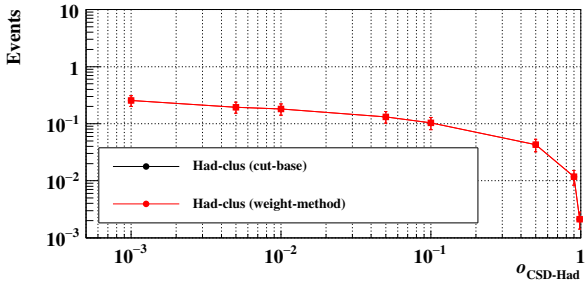

(b) Region above right of the blind region
($260 < P_t < 500$ MeV/c and $5100 < Z_{\rm vtx} < 6000$ mm).

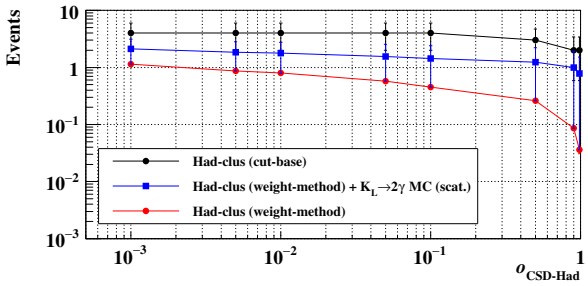

(c) Blind region
($120 < P_t < 260$ MeV/c and $2900 < Z_{\rm vtx} < 5100$ mm).

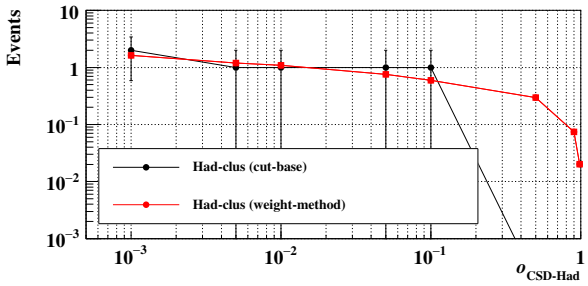

(d) Right-side of the blind region
($120 < P_t < 260$ MeV/c and $5100 < Z_{\rm vtx} < 6000$ mm).

Figure 8.19: Comparisons between the cut-base and weighting method analyses. Each plot shows events in $260 < P_t < 500$ MeV/c and $2900 < Z_{\rm vtx} < 5100$ mm (a), $260 < P_t < 500$ MeV/c and $5100 < Z_{\rm vtx} < 6000$ mm (b), $120 < P_t < 260$ MeV/c and $2900 < Z_{\rm vtx} < 5100$ mm (c), and $120 < P_t < 260$ MeV/c and $5100 < Z_{\rm vtx} < 6000$ mm (d). Black dots represent the number of remaining events after imposing CSD-η, CSD-Had, and PSD-FFT but changing the threshold of CSD-Had (cut-base). Red dots represent the number of hadron-cluster events expected using the weighting method in each CSD-Had threshold. Blue dots represent the number of events after summing up the hadron-cluster events expected from the weighting-method and scattering $K_L \to 2\gamma$ events expected from MC simulation in each CSD-Had threshold. In the downstream regions of (b) and (d), there are no contributions from scattering $K_L \to 2\gamma$ events, as shown in Fig. 8.17b.

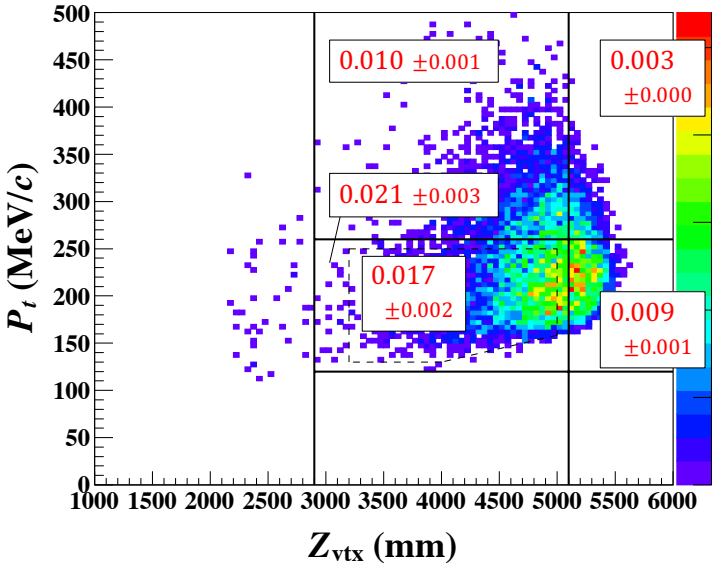

Figure 8.20: P_t vs. $Z_{\rm vtx}$ of the hadron-cluster background events. The numbers in red indicate the number of events in each region bounded by lines.

the signal acceptance was kept the same. The number of CV-η background events was estimated to be 0.03 ± 0.01.

8.3.3 Upstream-π^0 Background

The upstream-π^0 background is caused by beam-halo neutrons hitting NCC. After the neutrons interacted with NCC, the event can be a background with the following two mechanisms.

1. A π^0 can be produced at NCC by hadronic interactions, and two photons from the π^0 can hit CSI. Most of the π^0's produced at NCC are reconstructed in the position of NCC ($Z_{\rm vtx} < 2900$ mm), but some can be reconstructed in the signal region if photon energies are mis-measured due to the photo-nuclear effect in CSI. In this case, the event can be a background (referred to as "γ-γ" events).

2. After the beam-halo neutrons interacted with NCC, one neutron and one photon produced at NCC can hit CSI. The event can be a background if the hadronic cluster is misidentified as a photon cluster, and a π^0 is reconstructed in the signal region (referred to as "n-γ" events).

The shape-related cuts can suppress the background produced by the latter mechanism, but it is not the case for the background produced by the former mechanism.

The upstream-π^0 background was studied with MC simulations. The background yield was normalized with the ratio between data and MC for events in the region of $Z_{\rm vtx} < 2900$ mm selected with loose selection criteria. The survival probability map obtained in the hadron-cluster analysis was used to estimate the number of events of the n-γ type.

Figure 8.22 shows P_t vs. $Z_{\rm vtx}$ of the upstream-π^0 MC events after imposing the $K_L \to \pi^0\nu\overline{\nu}$ selection criteria. The remaining events in the blind region were found to be concentrated near the upstream end around of $Z_{\rm vtx} < 3200$ mm. To avoid this background, the upstream boundary of the signal region was moved to $Z_{\rm vtx} = 3200$ mm from $Z_{\rm vtx} = 3000$ mm which was used in the 2015 analysis. Compared to the signal acceptance estimated using the previous $Z_{\rm vtx}$ cut, the signal acceptance decreased by 7%, but the number of background events decreased by 80%. In Fig. 8.22, the rightmost event is a n-γ event and the second event from the right is a γ-γ event. The number of upstream-π^0 background events was estimated to be 0.03 ± 0.03.

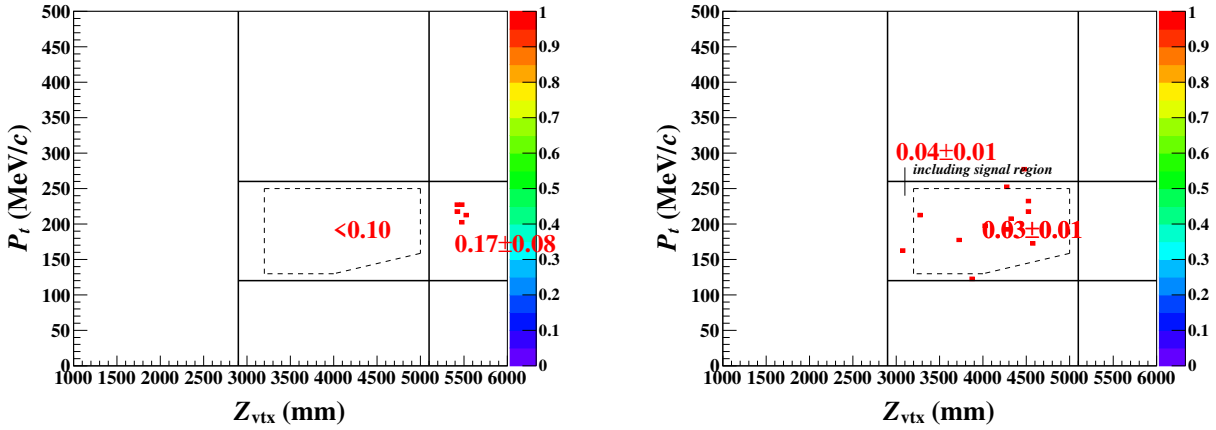

(a) CV-π^0 (b) CV-η

Figure 8.21: P_t vs. $Z_{\rm vtx}$ of the events after imposing the $K_L \to \pi^0\nu\overline{\nu}$ selection criteria on the CV-π^0 (left) and CV-η (right) MC simulation. The background yield was estimated using a data-driven approach. The upper limit on the number is at the 90% confidence level.

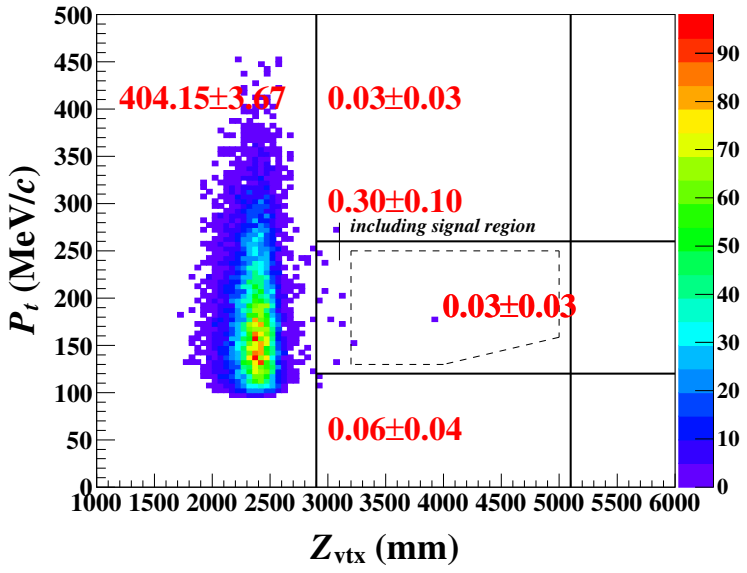

Figure 8.22: P_t vs. $Z_{\rm vtx}$ of the events after imposing the $K_L \to \pi^0\nu\overline{\nu}$ selection criteria on the upstream-π^0 MC simulation. The background yield was estimated using a data-driven approach. The numbers indicate the number of background events in each region.

8.4 $K^{\pm}$ Background

The $K^{\pm}$ decay was found to be a significant source of background in the 2016–2018 analysis. The background mechanism, the $K^{\pm}$ flux measurement, and the number of $K^{\pm}$ background events are explained in the following sections.

8.4.1 Mechanism

As mentioned in Sec. 2.1.3.2, if a $K^{\pm}$ is generated at the downstream collimator, the $K^{\pm}$ can enter the KOTO detector. One mechanism of the $K^{\pm}$ generation is that K_L's scattered at the γ-absorber hit the downstream collimator, and generated $K^{\pm}$'s by a charge-exchange process. Another mechanism is that $\pi^{\pm}$'s decayed from K_L's hit the downstream collimator, and generated $K^{\pm}$'s by a hadronic interaction.

Among $K^{\pm}$ decays, $K^{\pm} \to \pi^0 e^{\pm} \nu$ is the most likely source of background. This is because the kinematics of the π^0 is similar to that of the $K_L \to \pi^0 \nu\overline{\nu}$ decay due to the small mass of $e^{\pm}$ compared to the mass of K_L. In addition, the detection efficiency for the $e^{\pm}$ is low if a low energy $e^{\pm}$ is emitted in the backward direction and hits non-active materials, such as lead-plates in FB.

8.4.2 $K^{\pm}$ Flux

The events from $K^{\pm}$ decays had not been studied before the 2016–2018 analysis. We explain how we measured $K^{\pm}$'s flux in our beam. The $K^{\pm}$ flux was measured mainly by N. Shimizu.

8.4.2.1 $K^{\pm}$ Identification

To measure the $K^{\pm}$ flux, we identified $K^{\pm}$'s using the $K^{\pm} \to \pi^{\pm}\pi^0$ decay because of the following reasons:

1. As shown in Table 8.2, the branching fraction of the $K^{\pm} \to \pi^{\pm}\pi^0$ decay is large (20.67% [5]).

2. The $K^{\pm} \to \pi^{\pm}\pi^0$ decay can be reconstructed from events with three clusters in CSI as described next.

The $K^{\pm} \to \pi^{\pm}\pi^0$ decay was reconstructed using the feature of two-body decay. Figure 8.23 shows the schematic view of the $K^{\pm} \to \pi^{\pm}\pi^0$ decay. The π^0 transverse momentum ($P_t^{\pi^0}$) and decay vertex position (Z_{vtx}) was reconstructed from two neutral clusters assuming the $\pi^0 \to 2\gamma$ decay on the beam-axis. We treated the π^0 decay vertex position as the $K^{\pm}$ decay vertex position. The relationship between the $\pi^{\pm}$ transverse momentum ($P_t^{\pi^{\pm}}$) and longitudinal momentum ($P_z^{\pi^{\pm}}$) is

$$P_z^{\pi^{\pm}} = P_t^{\pi^{\pm}} \frac{dZ}{r_{\pi^{\pm}}}, \tag{8.6}$$

where dZ is the distance between the CSI z position and Z_{vtx}, and $r_{\pi^{\pm}}$ is the distance between the center of CSI and the charged cluster position in CSI. Since this decay is a two-body decay, we assumed

$$P_x^{\pi^{\pm}} + P_x^{\pi^0} = 0, \tag{8.7}$$

$$P_y^{\pi^{\pm}} + P_y^{\pi^0} = 0, \tag{8.8}$$

where $P_i^{\pi^{\pm}\,(\pi^0)}$ is i's component of the $\pi^{\pm}$ (π^0) momentum. Finally, the $K^{\pm}$ is reconstructed using the $\boldsymbol{P}^{\pi^0}$ and $\boldsymbol{P}^{\pi^{\pm}}$.

Table 8.2: Main decay modes of $K^{\pm}$ and their branching fractions [5].

decay mode	branching fraction
$K^{\pm} \to \mu^{\pm}\nu$	$(63.56 \pm 0.11)\%$
$K^{\pm} \to \pi^{\pm}\pi^{0}$	$(20.67 \pm 0.08)\%$
$K^{\pm} \to \pi^{\pm}\pi^{\pm}\pi^{\mp}$	$(5.583 \pm 0.024)\%$
$K^{\pm} \to \pi^{0}e^{\pm}\nu$	$(5.07 \pm 0.04)\%$
$K^{\pm} \to \pi^{0}\mu^{\pm}\nu$	$(3.352 \pm 0.033)\%$
$K^{\pm} \to \pi^{0}\pi^{0}\pi^{\pm}$	$(1.760 \pm 0.023)\%$

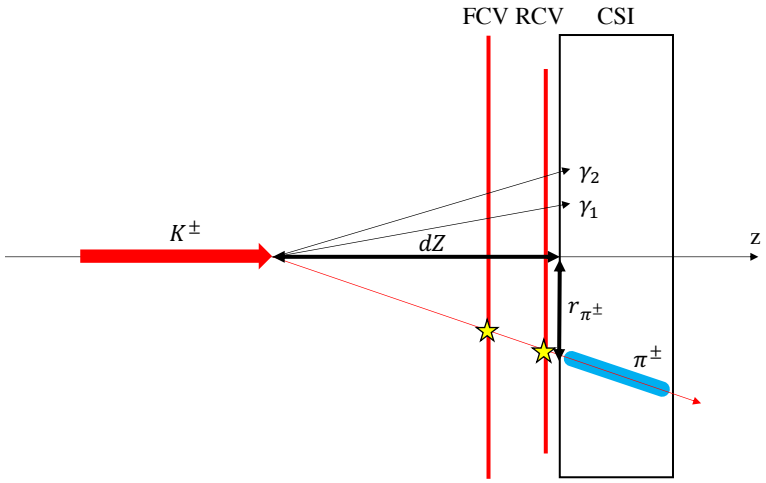

Figure 8.23: Schematic view of the $K^{\pm} \to \pi^{\pm}\pi^{0}$ decay. Both FCV and RCV are required to have one hit each, and their hit positions are required to be consistent with the position of the $\pi^{\pm}$ cluster.

Table 8.3: Selection criteria using the CSI information in the $K^{\pm}\to\pi^{\pm}\pi^0$ analysis.

category	selection name	selection criterion
photon-selection	photon timing	$\Delta T_{\rm vtx} \leq 1.5$ ns
	cluster size	$n_{E_{\gamma_1}} \geq 5$, $n_{E_{\gamma_2}} \geq 4$
	shape-χ^2	$\chi^2_{\rm shape} \leq 10$
	cluster shape NN	$o_{\rm SNN} > 0.8$
$\pi^{\pm}$-selection	MIP-like selection	$200 \leq E_{\pi^{\pm}} \leq 400$ MeV
$K^{\pm}\to\pi^{\pm}\pi^0$-selection	$\pi^{\pm}$-π^0 timing	$-3 \leq \delta T^{\rm vtx}_{\pi^{\pm}\pi^0} \leq 2$ ns
	$\pi^{\pm}$-π^0 angle	$\theta_{\pi^{\pm}\pi^0} \geq 140^{\circ}$
	P_t	$P_t \geq 80$ MeV/c
	$Z_{\rm vtx}$	$2000 < Z_{\rm vtx} < 5250$ mm
	$M_{\pi^0\pi^{\pm}}$	$440 < M_{\pi^{\pm}\pi^0} < 600$ MeV/c^2

8.4.2.2 Event Selection

As mentioned in Sec. 3.3.3.2, we collected the $K^{\pm}\to\pi^{\pm}\pi^0$ sample with the $\pi^{\pm}\pi^0$ trigger in 2020. This trigger selected events with three clusters in CSI, one coincident hit in FCV and RCV each, and no coincident hits in other veto counters. Among three possible cluster pairs to form a π^0, we selected one with the smallest sum of the shape-χ^2 outputs, which were calculated for clusters in a π^0 candidate. The two clusters used for a π^0 are referred to as photon clusters, and the other is referred to as a $\pi^{\pm}$ cluster. The x-y position of a $\pi^{\pm}$ cluster in CSI was required to be consistent with the hit position of CV (CV matching).

To have $K^{\pm}\to\pi^{\pm}\pi^0$ decays with enough statistics, we applied kinematic cuts looser than the $K_L\to\pi^0\nu\overline{\nu}$ analysis. The used kinematic cuts are summarized in Table 8.3, and distributions of variables used in the kinematic cuts are shown in Figs. 8.24 and 8.25. To select events with photons from a π^0, the selected events were required to have the vertex time difference between two photons ($\Delta T_{\rm vtx}$) within 1.5 ns. The cluster sizes of γ_1 and γ_2 ($E_{\gamma_1} > E_{\gamma_2}$) were required to be ≥ 5 and ≥ 4, respectively. To select electromagnetic showers, the shape-χ^2 and cluster shape NN were required to be $\chi^2_{\rm shape} \leq 10$ and $o_{\rm SNN} > 0.8$, respectively. The energy of the $\pi^{\pm}$ cluster ($E_{\pi^{\pm}}$) was required to be $200 < E_{\pi^{\pm}} < 400$ MeV to select a minimum-ionizing particle. The vertex time difference between π^0 and $\pi^{\pm}$, defined as $\delta T^{\rm vtx}_{\pi^{\pm}\pi^0} = (T^{\rm vtx}_{\gamma_1} + T^{\rm vtx}_{\gamma_2})/2 - T^{\rm vtx}_{\pi^{\pm}}$, was required to be $-3 \leq \delta T^{\rm vtx}_{\pi^{\pm}\pi^0} \leq 2$ ns. The opening angle between the π^0 and $\pi^{\pm}$ directions projected on the x-y plane ($\theta_{\pi^{\pm}\pi^0}$) was required to be larger than 140° to select two-body decay events. The P_t was required to be larger than 80 MeV/c to reduce $K_L\to\pi^+\pi^-\pi^0$ contamination because the $K_L\to\pi^+\pi^-\pi^0$ decay is characterized by the small Q-value. The reconstructed vertex position of $Z_{\rm vtx}$ was required to be $2000 < Z_{\rm vtx} < 5250$ mm, and the reconstructed $K^{\pm}$ invariant mass ($M_{K^{\pm}}$) was required to be $440 < M_{K^{\pm}} < 600$ MeV/c^2. The similar veto cuts as the ones used in the $K_L\to\pi^0\nu\overline{\nu}$ analysis were imposed on the $K^{\pm}\to\pi^{\pm}\pi^0$ events. In the veto cuts, we used a new charged-particle veto counter named "Downstream Charged Veto (DCV)" instead of using BPCV. Details of DCV are available in Appendix D. As shown in Fig. 8.24 and Fig. 8.25, we obtained good agreements between data and MC, which revealed the existence of $K^{\pm}$'s.

8.4.2.3 Results of $K^{\pm}$ Flux Measurement

To estimate $K^{\pm}$ flux from the measurement, we calculated the ratio of the $K^{\pm}$ to K_L flux at the beam-exit in the run to cancel out a part of uncertainties. First, the K_L flux was estimated using $K_L\to\pi^+\pi^-\pi^0$ decays with the same $K^{\pm}\to\pi^{\pm}\pi^0$ selection criteria except for the $M_{\pi^0\pi^{\pm}}$ requirement and veto cuts of downstream veto counters (CC04, CC05, DCV[*2], BHPV, and BHGC) to enhance $K_L\to\pi^+\pi^-\pi^0$ events. The K_L flux was measured as 5.9×10^7 K_L /2×10^{14} POT. We then estimated

[*2] See Appendix D.

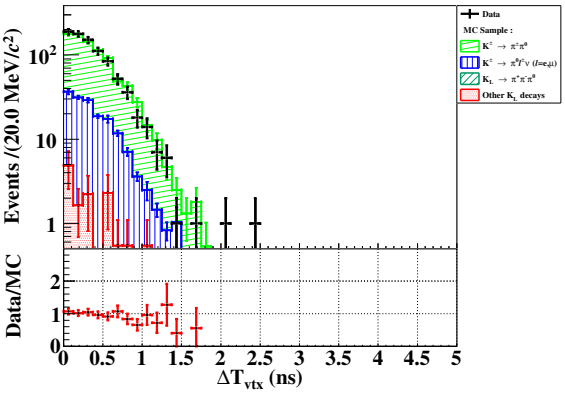

(a) $\Delta T_{\rm vtx}$

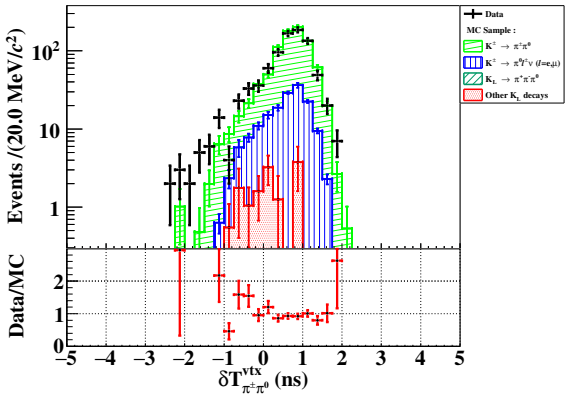

(b) $\delta T^{\rm vtx}_{\pi^{\pm}\pi^0}$

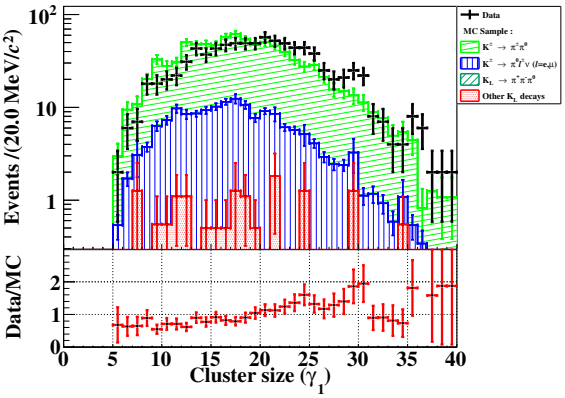

(c) Cluster size (E_{γ_1})

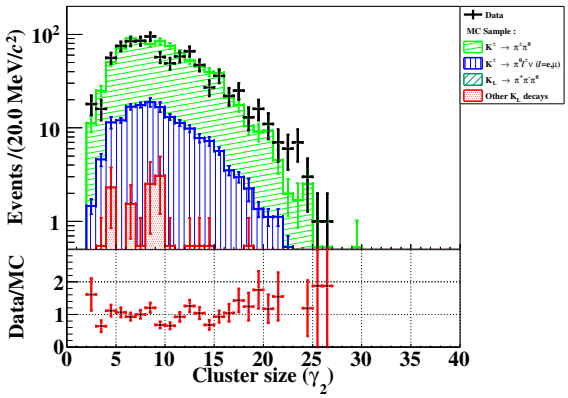

(d) Cluster size (E_{γ_2})

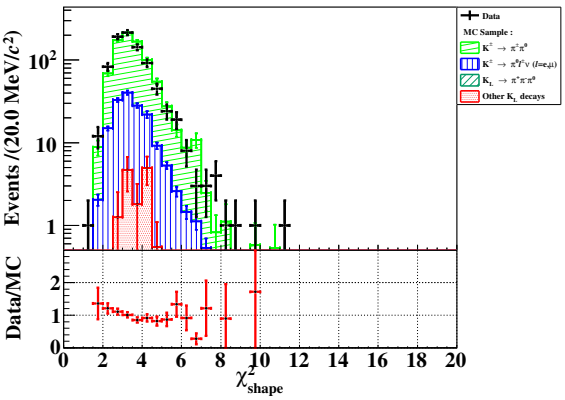

(e) $\chi^2_{\rm shape}$

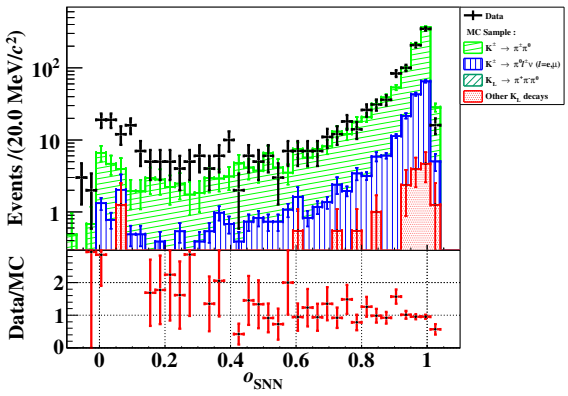

(f) $o_{\rm SNN}$

Figure 8.24: Distributions of $\Delta T_{\rm vtx}$ (a), $\delta T^{\rm vtx}_{\pi^{\pm}\pi^0}$ (b), Cluster size (E_{γ_1}) (c), Cluster size (E_{γ_2}) (d), larger $\chi^2_{\rm shape}$ between photon clusters (e), and smaller $o_{\rm SNN}$ between photon clusters (f) for $K^{\pm}\to\pi^{\pm}\pi^0$ events after imposing cuts except for the one of interest. Black points represent data. The colored histograms represent MC events (stacked). Light-green, blue, and green histograms represent $K^{\pm}\to\pi^{\pm}\pi^0$, $K^{\pm}\to\pi^0\ell^{\pm}\nu$ ($\ell=e,\mu$) and $K_L\to\pi^+\pi^-\pi^0$ MC, respectively. Red histograms represent MC simulations of other K_L decays ($K_L\to\pi^{\pm}e^{\mp}\nu, K_L\to\pi^{\pm}\mu^{\mp}\nu, K_L\to 2\pi^0, K_L\to\pi^{\pm}e^{\mp}\nu_e\gamma, K_L\to\pi^0\pi^{\pm}e^{\mp}\nu_e$). The data/MC ratios are shown below each panel. The error bars represent statistical errors.

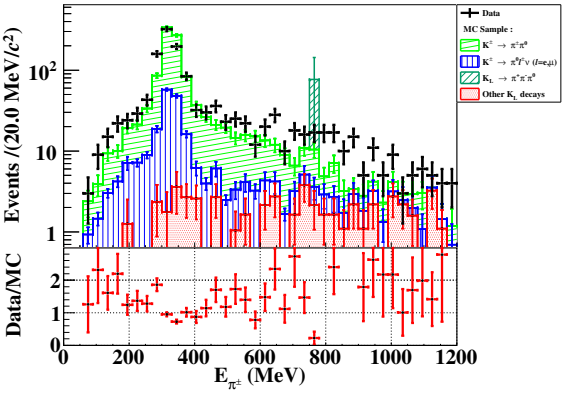

(a) $E_{\pi^\pm}$

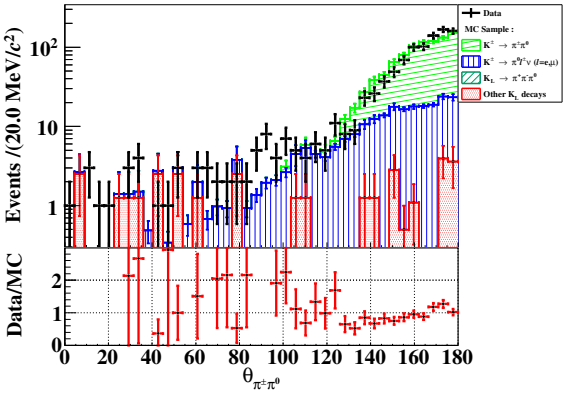

(b) $\theta_{\pi^\pm\pi^0}$

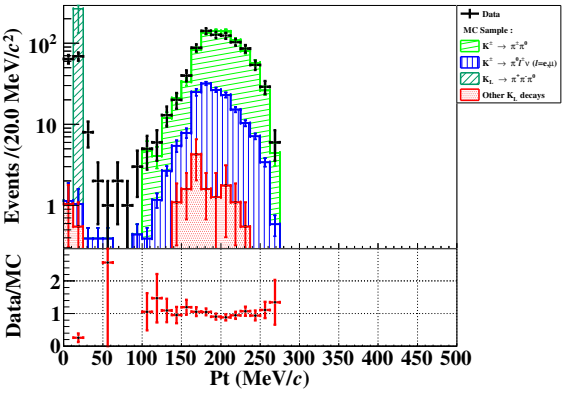

(c) P_t

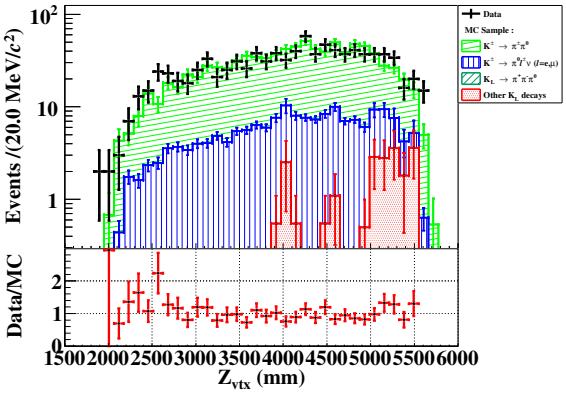

(d) $Z_{\rm vtx}$

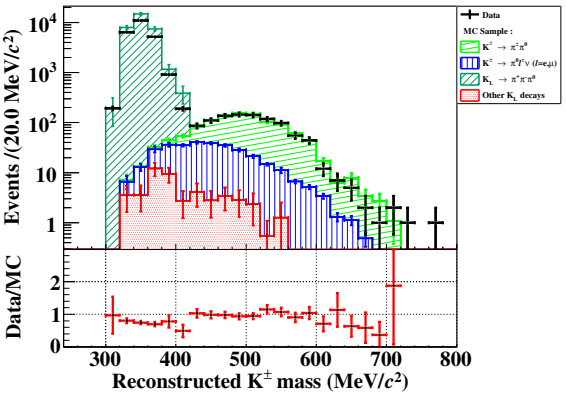

(e) Reconstructed $\pi^\pm\pi^0$ mass

Figure 8.25: Distributions of $E_{\pi^\pm}$ (a), $\theta_{\pi^\pm\pi^0}$ (b), P_t (c), $Z_{\rm vtx}$ (d), and Reconstructed $\pi^\pm\pi^0$ mass (e) for $K^\pm \to \pi^\pm\pi^0$ events after imposing cuts except for the one of interest. The meaning of the black points, colors of histograms, below panels, and error bars are the same as for Fig. 8.24.

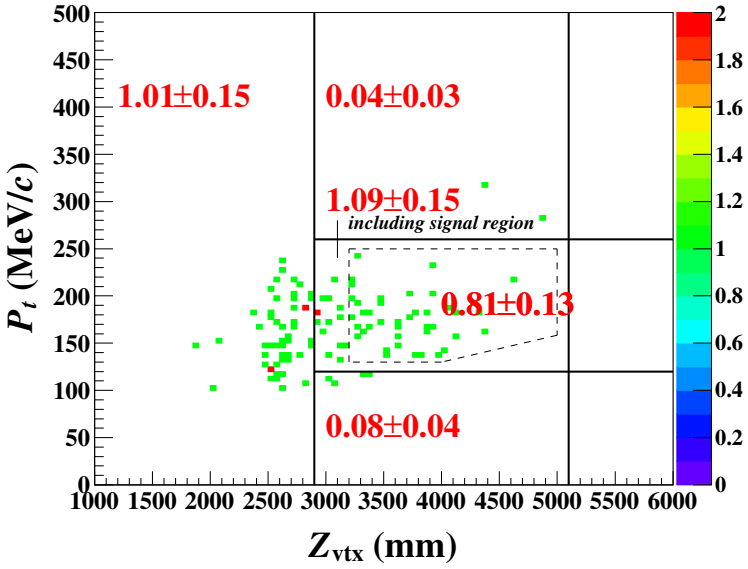

Figure 8.26: P_t vs. $Z_{\rm vtx}$ of the events after imposing the $K_L \to \pi^0\nu\overline{\nu}$ selection criteria on the $K^\pm \to \pi^0 e^\pm \nu$ MC simulation. The background yield was normalized using the measured $K^\pm$ flux. The numbers indicate the number of background events in each region.

the ratio of the $K^\pm$ to K_L flux at the beam-exit to be $(2.6 \pm 0.1) \times 10^{-5}$ based on the 847 observed events in the $K^\pm \to \pi^\pm\pi^0$ sample after applying all the $K^\pm \to \pi^\pm\pi^0$ selections and the acceptance of $K^\pm$ decays estimated using MC simulations.

8.4.3 The Number of $K^\pm$ Background Events

Figures 8.26, 8.27, and 8.28 show the P_t vs. $Z_{\rm vtx}$ of the events after imposing all the $K_L \to \pi^0\nu\overline{\nu}$ cuts on the $K^\pm \to \pi^0 e^\pm \nu$, $K^\pm \to \pi^0 \mu^\pm \nu$, and $K^\pm \to \pi^\pm\pi^0$ MC events, respectively. The background yield was normalized using the measured $K^\pm$ to K_L flux ratio. The estimated number of $K^\pm \to \pi^0 e^\pm \nu$, $K^\pm \to \pi^0 \mu^\pm \nu$, and $K^\pm \to \pi^\pm\pi^0$ background events were 0.813, 0.019, and 0.004, respectively. The number of background events from $K^\pm$ decays ($N_{\rm BG}^{K^\pm}$) was estimated to be 0.84 ± 0.13.

The systematic uncertainty on the number of background events originating from the cuts used in the $K_L \to \pi^0\nu\overline{\nu}$ analysis against $K^\pm$ decays was studied using the control sample collected in 2020. In this control sample as mentioned in Sec. 3.3.3.2, we took data with the physics trigger with the sweeping magnet turned off to enhance the $K^\pm$ flux at the beam-exit. We simultaneously collected data with the $\pi^\pm\pi^0$ trigger to measure the $K^\pm$ yield. As shown in Fig. 8.29, 27 events remained in the signal region after imposing the cuts on the control sample. This number agreed with 26.0 ± 3.2 events expected from the $K^\pm$ decay MC simulation (Fig. 8.29). The ratio of these two numbers ($R_{A_{K^\pm}}$) was calculated to be $1.04 \pm 0.24_{\rm stat} \pm 0.10_{p_{K^\pm}}$, where the uncertainty of 0.24 comes from the statistics of data and MC, and the uncertainty of 0.10 comes from the cut acceptance difference between the configurations of the magnet on and off to take into account the $K^\pm$ spectrum difference between them. We corrected $N_{\rm BG}^{K^\pm}$ with $R_{A_{K^\pm}}$ and estimated $N_{\rm BG}^{K^\pm}$ to be $0.87 \pm 0.13_{\rm stat} \pm 0.21_{\rm syst}$.

8.5 Beam-Halo $K_L \to 2\gamma$ Background

Beam-halo K_L's decaying into two photons away from the beam-axis can be a background source due to the same mechanism as the beam-core $K_L \to 2\gamma$ background (Sec. 8.2.3). In the following sections, we first estimate the beam-halo K_L flux using $K_L \to 3\pi^0$ decays. Based on the flux, we estimated the number of background events. The flux and its uncertainty were evaluated by Y. Noichi.

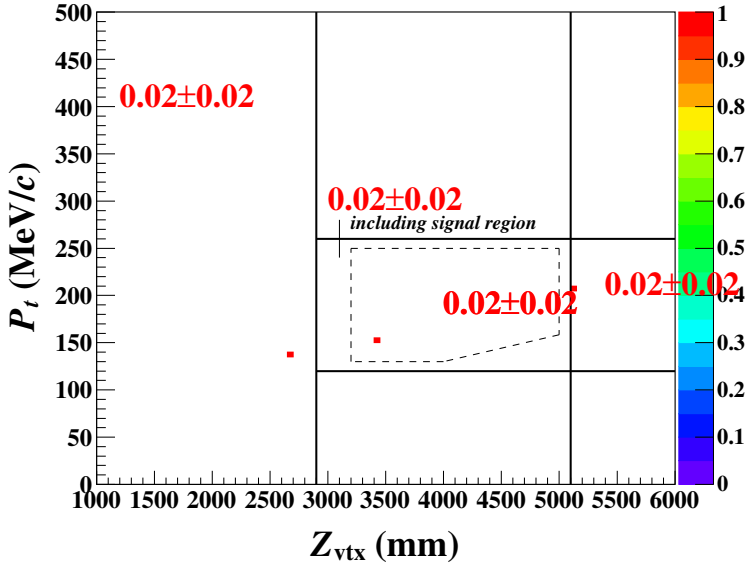

Figure 8.27: P_t vs. $Z_{\rm vtx}$ of the events after imposing the $K_L \to \pi^0\nu\overline{\nu}$ selection criteria on the $K^\pm \to \pi^0\mu^\pm\nu$ MC simulation. The background yield was normalized using the measured $K^\pm$ flux. The numbers indicate the number of background events in each region.

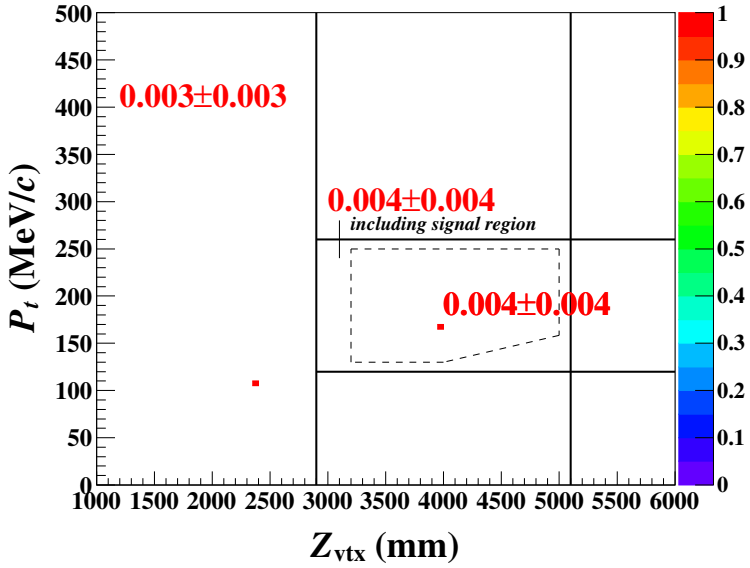

Figure 8.28: P_t vs. $Z_{\rm vtx}$ of the events after imposing the $K_L \to \pi^0\nu\overline{\nu}$ selection criteria on the $K^\pm \to \pi^\pm\pi^0$ MC simulation. The background yield was normalized using the measured $K^\pm$ flux. The numbers indicate the number of background events in each region.

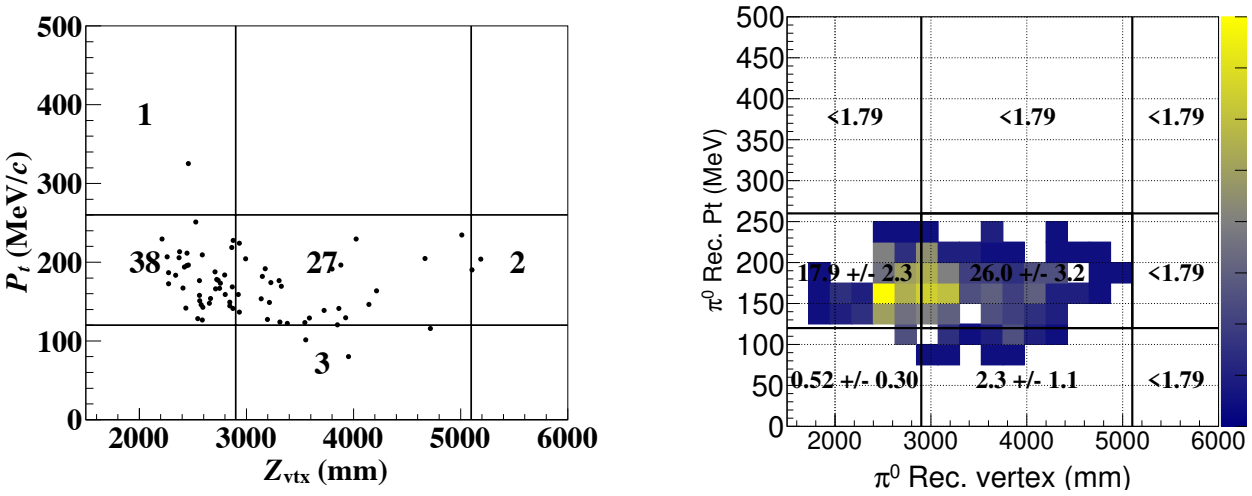

(a) Data (b) MC

Figure 8.29: P_t vs. Z_{vtx} of the events in the data collected with the sweeping magnet turned off, after imposing the $K_L \to \pi^0\nu\overline{\nu}$ selection criteria on data (a) and $K^{\pm}$ decays MC events (b). The plot of the MC simulation was provided by N. Shimizu. The numbers indicate the number of background events in each region.

8.5.1 Beam-Halo K_L Flux

The beam-halo K_L was studied using the position of COE of the $K_L \to 3\pi^0$ decays because the position of COE is approximately the position that the K_L hit if it had not decayed (see Appendix B).

Figure 8.30a shows the R_{COE} distribution of events in the data and beam-halo $K_L \to 3\pi^0$ MC simulation. We collected events with $R_{\text{COE}} > 200$ mm as the sample of beam-halo K_L's, where the threshold of R_{COE} comes from the offline requirement of the $K_L \to \pi^0\nu\overline{\nu}$ analysis. The disagreement between data and MC shows that we did not fully understand the properties of beam-halo K_L's in the MC simulation. To correct the beam-halo K_L flux in the MC simulation, we weighted each beam-halo K_L event. Figure 8.30b shows the weight factor calculated by the ratio between data and MC as a function of R_{COE}.

Figure 8.31 shows the distributions of the reconstructed K_L Z_{vtx} and energy of $K_L \to 3\pi^0$ events with $R_{\text{COE}} > 200$ mm. The weighting factors were applied to events in the MC simulation. After the weighting, the beam-halo K_L MC simulation reproduces data well.

8.5.2 Results of Beam-Halo $K_L \to 2\gamma$ Background

Figure 8.32 shows the P_t vs. Z_{vtx} of the beam-halo $K_L \to 2\gamma$ background MC events after imposing all the $K_L \to \pi^0\nu\overline{\nu}$ cuts. By weighting according to the R_{COE}, the number of background events was estimated to be $0.26 \pm 0.06_{\text{stat}} \pm 0.02_{\text{syst}}$, where the uncertainty of 0.06 comes from the statistics of beam-halo $K_L \to 2\gamma$ MC, and the uncertainty of 0.02 comes from the uncertainties of weighting factors.

8.6 Summary of Backgrounds

In the 2016–2018 analysis, the number of hadron-cluster background events was found to be negligibly small, but the two new backgrounds for $K^{\pm}$ and beam-halo $K_L \to 2\gamma$ decays were found to be significantly large. With the SES of $(7.20 \pm 0.05_{\text{stat}} \pm 0.66_{\text{syst}}) \times 10^{-10}$, we estimated the total number of background events to be 1.22 ± 0.26.

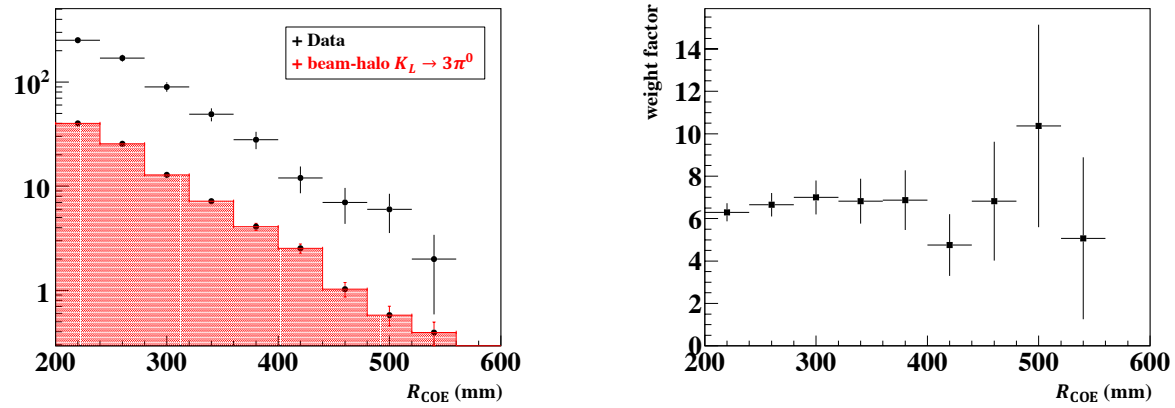

(a) R_{COE} (wide range) (b) R_{COE} (> 200 mm)

Figure 8.30: Left: distributions of R_{COE} between data and MC using $K_L \to 3\pi^0$ decays. Black points represent data and red histograms represent the beam-halo K_L MC events. Right: the weight factor as a function of R_{COE}.

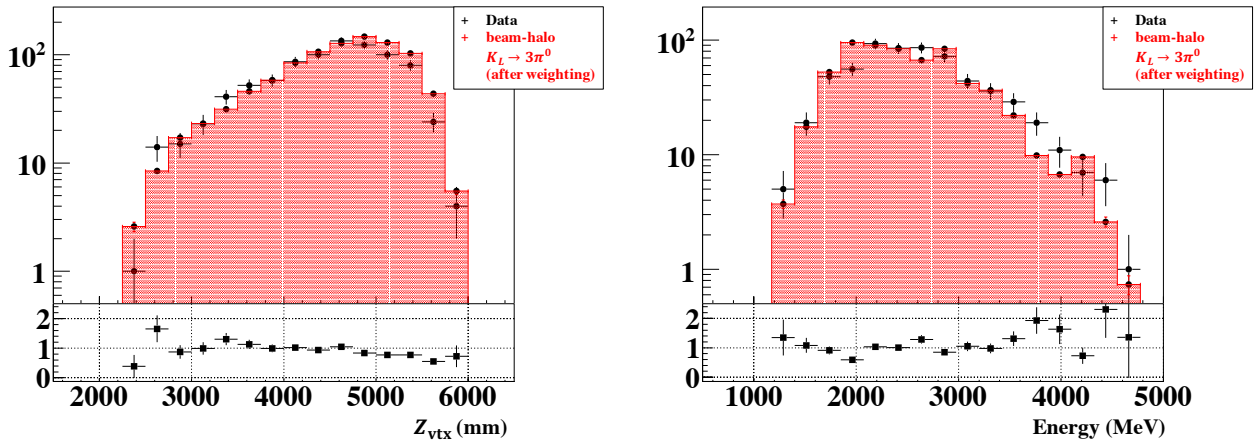

(a) Z_{vtx} (b) K_L energy

Figure 8.31: Distributions of the reconstructed K_L Z_{vtx} (a) and energy (b) for the $K_L \to 3\pi^0$ events with $R_{\mathrm{COE}} > 200$ mm. Black points represent data and red histograms represent beam-halo $K_L \to 3\pi^0$ MC after weighting.

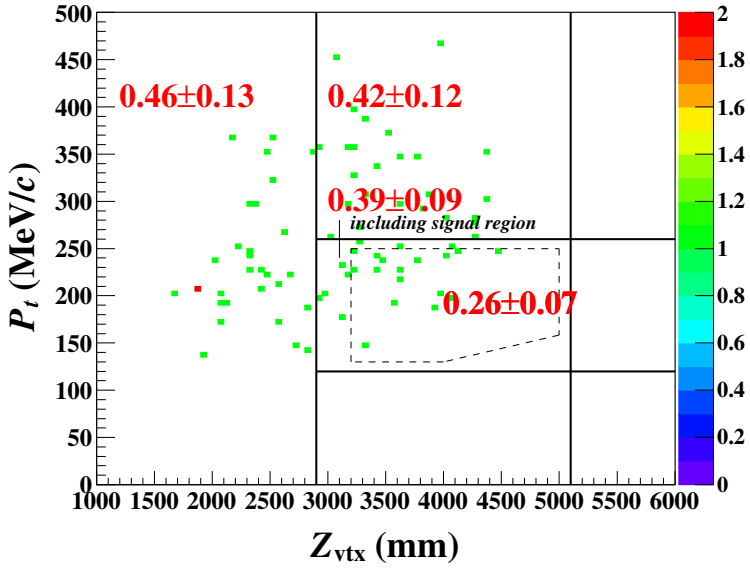

Figure 8.32: P_t vs. $Z_{\rm vtx}$ of the events after imposing the $K_L \to \pi^0\nu\overline{\nu}$ selection criteria on the beam-halo $K_L \to 2\gamma$ MC simulation. The background yield was estimated using a data-driven approach. The numbers indicate the number of background events in each region.

Chapter 9

Results of $K_L \to \pi^0 \nu\overline{\nu}$ search

9.1 Event Properties

Figure 9.1 shows the reconstructed P_t vs. $Z_{\rm vtx}$ of the events after imposing the $K_L \to \pi^0 \nu\overline{\nu}$ selection criteria. We observed three events in the signal region and one extra event outside the signal region but inside blind region. The second event from the right in Fig. 9.1 has overlapping pulses in NCC. Observed waveforms in an NCC module are shown in Fig. 9.2. The probability of observing such an event is 2.2%. The number of expected background events is 1.22 ± 0.26. The probability of observing three or more background events is 13% according to Poisson statistics. Figures 9.3–9.5 show kinematic distributions of observed events and expected signal and background events in the signal region. We did not find any significant features to identify the signal or background event in the observed events. Based on these results, we concluded that the numbers of observed events are statistically consistent with the background expectations in all regions.

9.2 Results

With the 2016–2018 dataset, we obtained a SES of $(7.20 \pm 0.05_{\rm stat} \pm 0.66_{\rm syst}) \times 10^{-10}$, and observed three events in the signal region. Assuming Poisson statistics and considering uncertainties [68], we set an upper limit on the branching fraction of the $K_L \to \pi^0 \nu\overline{\nu}$ decay in the 2016–2018 dataset to be 4.9×10^{-9} at the 90% C.L.

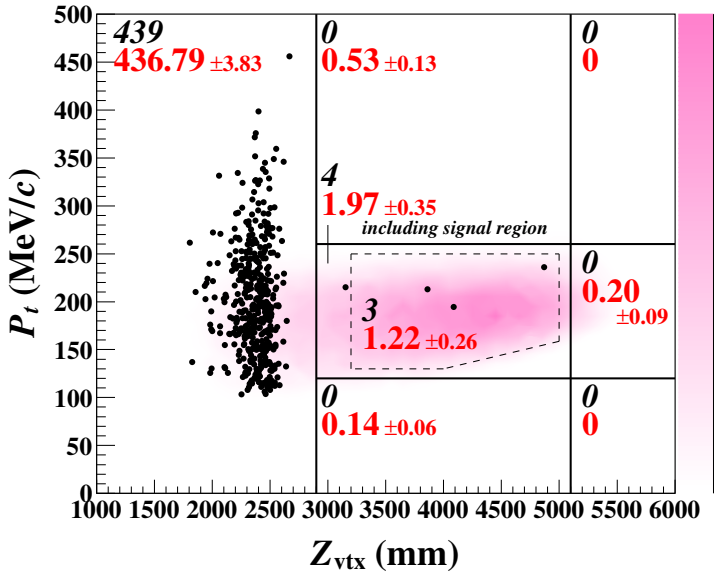

Figure 9.1: P_t vs. $Z_{\rm vtx}$ of the events after imposing the $K_L \to \pi^0\nu\overline{\nu}$ selection criteria. The region surrounded by dotted lines is the signal region. The black dots represent observed events, and the shaded contour indicates the $K_L \to \pi^0\nu\overline{\nu}$ distribution from the MC simulation. The black italic (red regular) numbers indicate the number of observed (background) events in each region [67].

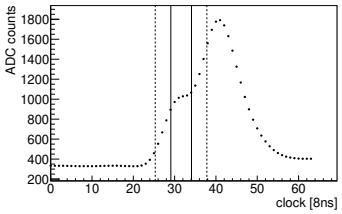

(a) NCC-Common

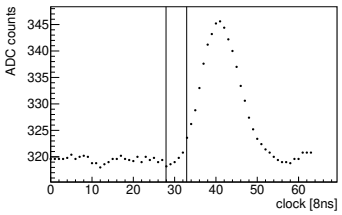

(b) NCC-Individual (front)

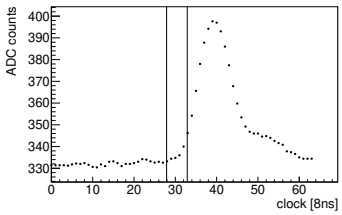

(c) NCC-Individual (middle)

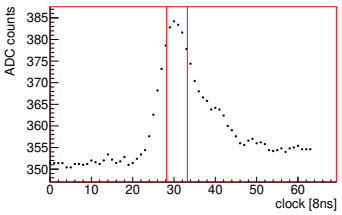

(d) NCC-Individual (rear)

Figure 9.2: Observed overlapped-like-pulses in NCC of the second event from the right in Fig. 9.1. The NCC-Common signal was used for the veto decision. The region inside the vertical solid (dotted) lines is the veto window (widened veto window). The peak in the NCC-Common existed outside of the widened veto window. The on-time (off-time) pulse in the rear (front) part of the Individual readout implied occurring pulse overlapping in the Common readout.

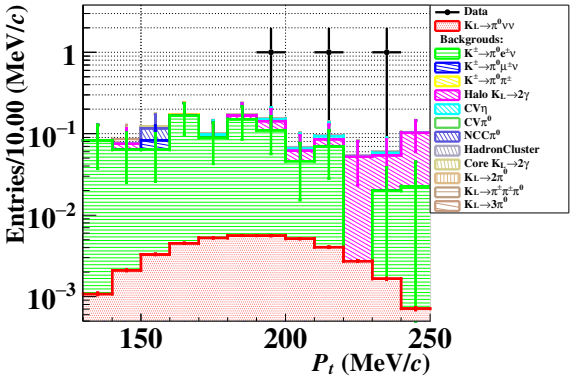

(a) P_t

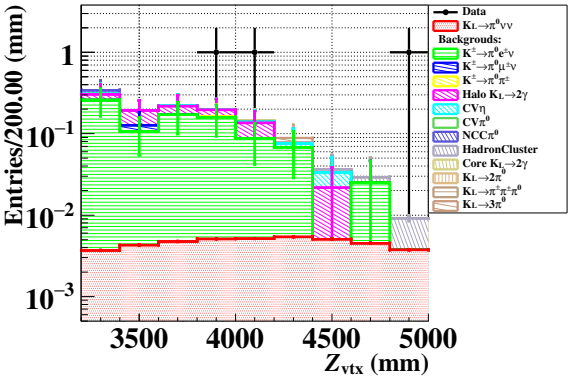

(b) Z_{vtx}

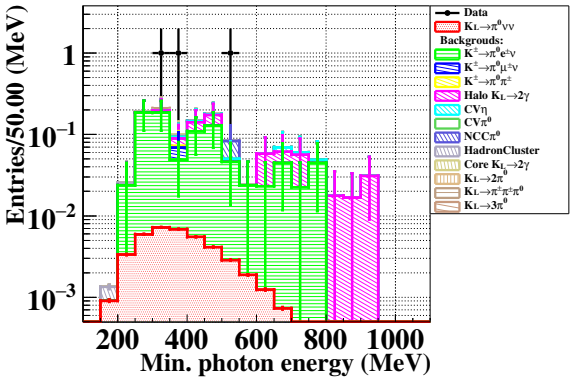

(c) Cluster energy (smaller)

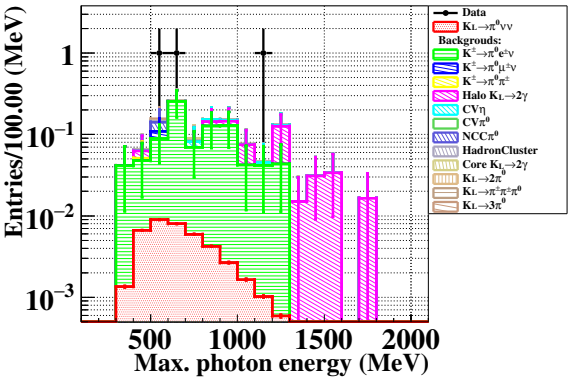

(d) Cluster energy (larger)

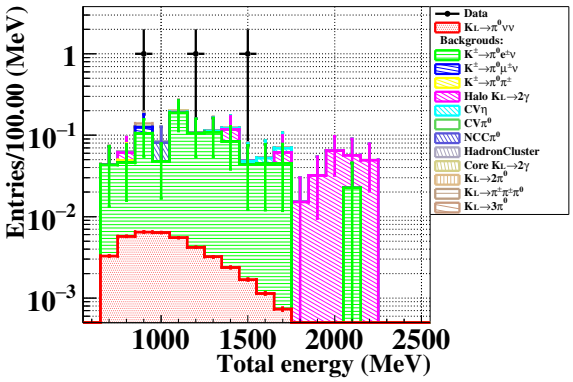

(e) Total energy

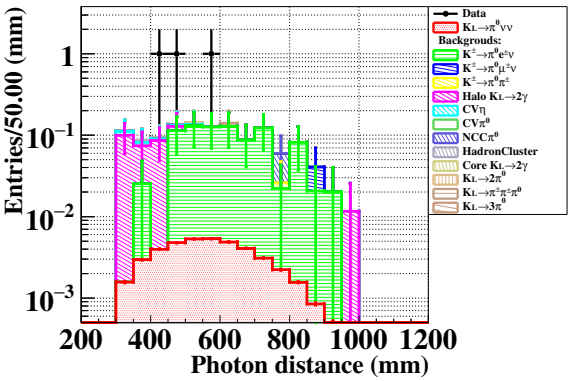

(f) Cluster distance

Figure 9.3: Distributions of P_t (a), Z_{vtx} (b), smaller cluster energy (c), larger cluster energy (d), total energy (e), and cluster distance (f) for events in the signal region. Black points represent data, and colored histograms represent signal and expected background events. The signal events were normalized using the branching fraction of $K_L \to \pi^0 \nu\overline{\nu}$ predicted in the SM, which corresponds to 0.04 events.

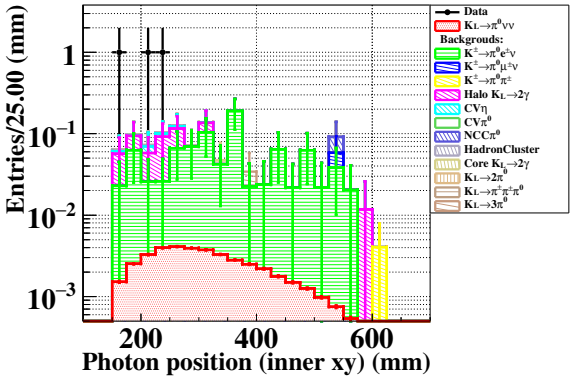

(a) Cluster position (inner)

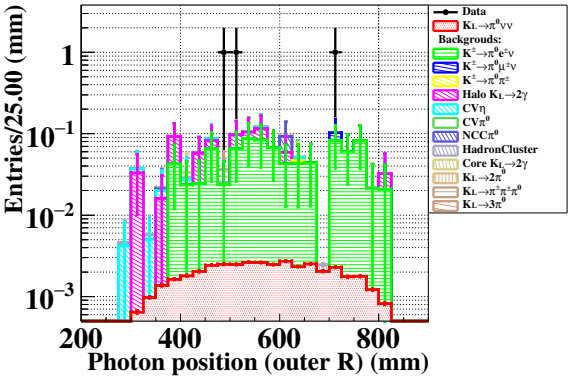

(b) Cluster position (outer)

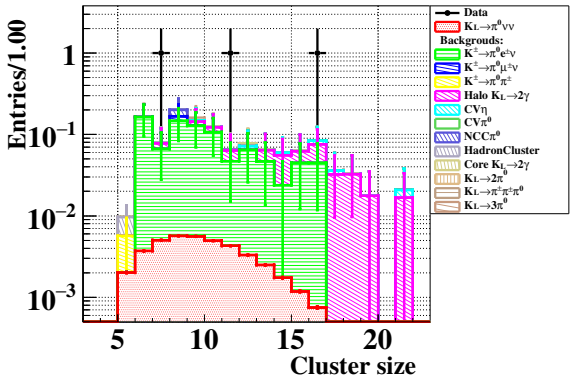

(c) Cluster size (smaller)

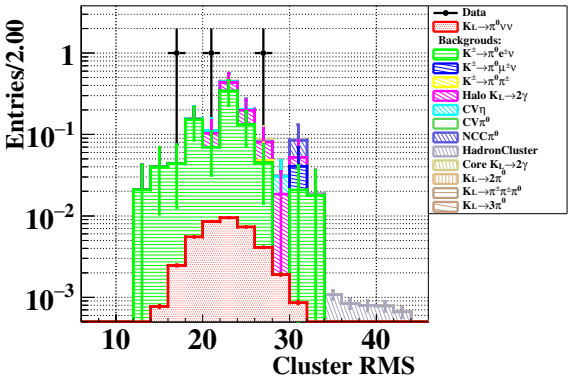

(d) Cluster RMS (smaller)

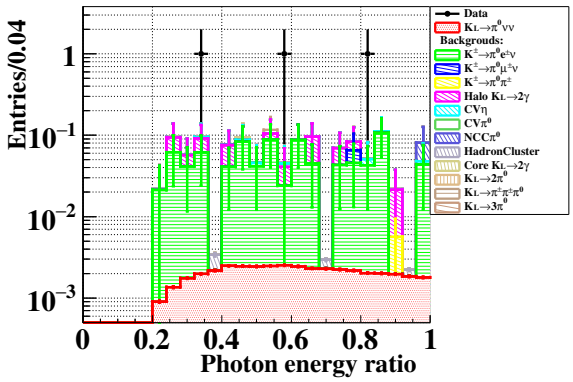

(e) Energy ratio

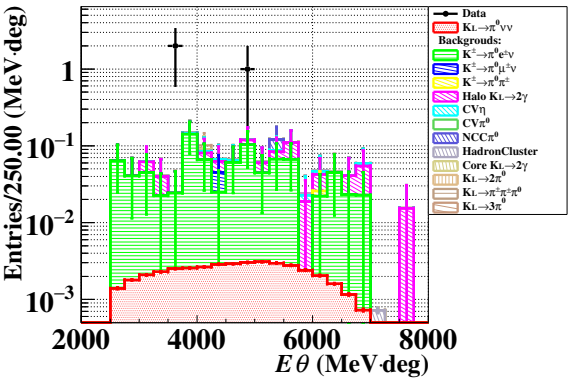

(f) Eθ

Figure 9.4: Distributions of inner cluster position (a), outer cluster position (b), smaller cluster size (c), smaller cluster RMS (d), E_{ratio} (e), and $E\theta$ (f) for events in the signal region. Black points represent data, and colored histograms represent signal and expected background events. The signal events were normalized using the branching fraction of $K_L \to \pi^0 \nu\overline{\nu}$ predicted in the SM, which corresponds to 0.04 events.

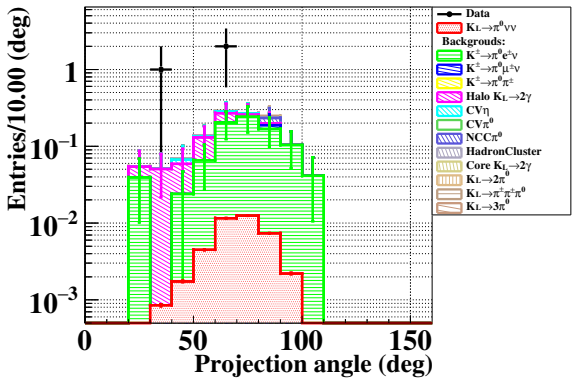

(a) Projection angle

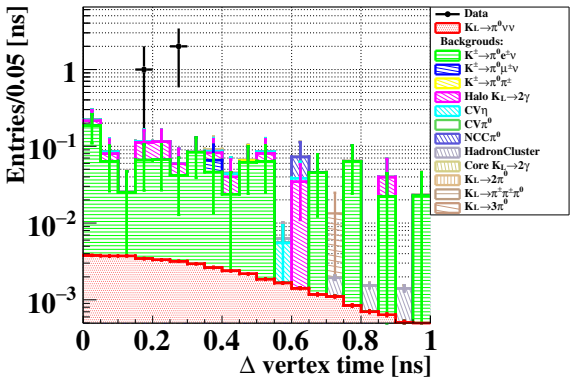

(b) $\Delta T_{\rm vtx}$

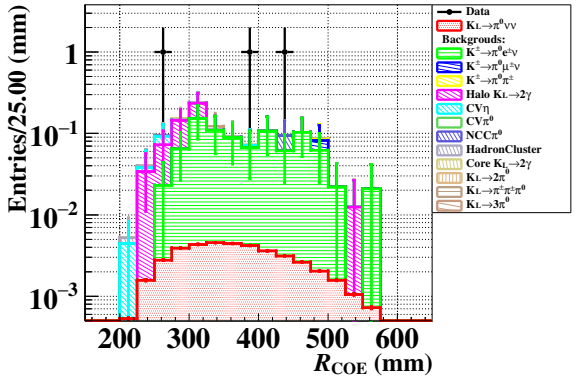

(c) $R_{\rm COE}$

Figure 9.5: Distributions of projection angle (a), $\Delta T_{\rm vtx}$ (b), and $R_{\rm COE}$ (c) for events in the signal region. Black points represent data, and colored histograms represent signal and expected background events. The signal events were normalized using the branching fraction of $K_L \to \pi^0 \nu\overline{\nu}$ predicted in the SM, which corresponds to 0.04 events.

Chapter 10

Discussion

10.1 Impacts of the Results of the 2016–2018 Data Analysis

The important results of the 2016–2018 data analysis are as follows.

1. We achieved the highest sensitivity for $K_L \to \pi^0\nu\overline{\nu}$ search of 7.2×10^{-10}, which corresponds to 1.8 times higher than the 2015 data analysis.
2. We suppressed the hadron-cluster background which was the dominant background in the 2015 data analysis.
3. We revealed that backgrounds from $K^{\pm}$ and beam-halo $K_L \to 2\gamma$ were dominant in our measurement, which were not found and thus were not considered in the 2015 data analysis. We estimated the total number of background events to be 1.22 ± 0.26.
4. We observed three candidate events in the signal region. We concluded that the number of observed events is statistically consistent with the background expectation.

Based on these results, in the 2016–2018 dataset, we set an upper limit on the branching fraction of the $K_L \to \pi^0\nu\overline{\nu}$ decay to be 4.9×10^{-9} (90% C.L.). The result of the 2016–2018 data analysis is consistent with that of the 2015 data analysis [26] because of the following reason. In the 2015 data analysis, no candidate event was observed. In that case, assuming Poisson statistics[*1], the upper limit of the number of the signal events is < 2.3 at the 90% C.L. If we collect 1.8 times higher statistics than in 2015, the upper limit of the number of the signal events extrapolated from the result of the 2015 data analysis is $< 4.1 (= 1.8 \times 2.3)$ at the 90% C.L. In the 2016–2018 data analysis, we observed three candidate events with the 1.8 times higher sensitivity than in 2015. Because three events are smaller than 4.1 events, the result of the 2016–2018 data analysis is consistent with that of the 2015 data analysis.

10.2 Comparison to the Analysis of the Data Taken in 2015

In this section, we discuss the comparison between the 2016–2018 data analysis and the 2015 data analysis. The numbers in the 2015 data analysis are referred from [35].

10.2.1 Detector

Table 10.1 summarizes the barrel photon veto counters in middle section. After the 2015 physics run, we installed a new cylindrical photon veto counter IB (see Sec. 2.4.3.2). We accordingly removed Barrel Charged Veto (BCV) [35] which was charged-particle veto counter attached on the inner surface of MB, and installed new charged-particle veto counters IBCV and MBCV (see Sec. 2.4.3.3). During the

[*1] In this discussion, we did not take the uncertainty on the SES into account because the effect was small.

detector upgrade period, we also replaced PMTs in some detectors to recover the detector performance.

Table 10.1: Barrel photon veto counters in middle section.

year	detectors	radiation length (X_0)
2015	MB	14
2016–2018	MB, IB	14+5

Signal Acceptance Related to IB For the effect on the sensitivity, we estimated the uncertainty from all the veto cuts to be only 3.2%. This uncertainty is comparable to the uncertainty from veto cuts of 3.7% in the 2015 data analysis [35].

Background Reduction Related to IB For the effect on the background, IB was designed to suppress $K_L \to 2\pi^0$ backgrounds by a factor of three. In the 2015 data analysis, the number of $K_L \to 2\pi^0$ background events was estimated to be 0.02 ± 0.02 [35], which corresponds to 0.04 ± 0.04 events if we extrapolated to the 2016–2018 sensitivity. In the 2016–2018 analysis, we estimated the number of $K_L \to 2\pi^0$ background to be < 0.08 (90% C.L.). In this work, we could set only the upper limit due to the limited statistics of simulated events passing all of the selection cuts in MC samples that were able to be generated in a realistic amount of time. We thus studied with loose cuts and showed that the MC agreed with the data. From this agreement, we expect that IB works with the designed performance. For further discussion with all the cuts applied, we need an appropriate amount of data and MC samples in the following years.

10.2.2 Data Taking

DAQ performance Table 10.2 summarizes DAQ performance and trigger conditions in 2015 and 2016–2018. As in Sec. 3.3.1.2, we increased the buffer size in the Lv2 trigger system, which improved a DAQ live ratio by ∼10%, and the Lv1 trigger system upgrade just before Run79.0 reduced the number of events sent to the Lv2 trigger system, which improved a DAQ live ratio by ∼5%.

Table 10.2: DAQ performance and trigger condition.

year	live ratio	Lv1 trigger	Lv2 trigger
2015	80%	CSIEt + veto	COE
2016–2018	90–99%	CSIEt + veto	COE / cluster counting

POT and K_L yield Table 10.3 summarizes the accumulated number of POT and K_L yield, and SES in 2015 and 2016–2018. The POT is provided by the accelerator group, and the K_L yield is obtained from the $K_L \to 2\pi^0$ sample in our measurement. The uncertainty on the sensitivity originated from the number of POT canceled out because the sensitivity was normalized with the $K_L \to 2\pi^0$ decay sample. Of a factor of 1.8 times difference in SES, a 1.5 times difference is due to increased statistics.

Table 10.3: POT, K_L yield, and SES.

year	POT	K_L yield	SES
2015	2.19×10^{19}	4.68×10^{12}	1.30×10^{-9}
2016–2018	3.05×10^{19}	6.83×10^{12}	7.20×10^{-10}

Beam Conditions Table 10.4 summarizes the beam conditions and the signal acceptance in 2015 and 2016–2018. As explained in Sec. 2.3.1, the primary proton beam had a spiky time structure in spills, and that caused the instantaneous rate higher than the mean rate. The $R_{\text{ins.}}$ in the table shows the ratio between the instantaneous rate and the mean rate. The relationship between the signal event loss and the counting rate is mentioned in Sec. 2.1.5. Because the beam conditions varied largely, and the detector components and cut sets were also changed largely, it is not easy to compare the effect on only the beam conditions to the signal acceptance between the 2015 and 2016–2018 data analysis. We thus studied only the effect on the change of the analysis methods using only the 2016–2018 data in the next subsection.

Table 10.4: Beam conditions.

year	beam-power	$R_{\text{ins.}}$	A_{sig}
2015	24–42 kW	2	$(1.31\text{–}2.80)\times10^{-4}$
2016–2018	31–51 kW	1.5–2	$(1.72\text{–}2.85)\times10^{-4}$

10.2.3 Analysis Method

In the 2016–2018 analysis, we introduced some new methods to recover the signal acceptance and suppress backgrounds.

Signal acceptance Table 10.5 shows the signal acceptance differences originated from the change of the analysis methods. Due to the beam and detector condition differences between 2015 and 2016–2018, we only used 2016–2018 MC samples and studied differences of the signal acceptance by applying the cuts used in the 2015 data analysis.

For the trigger related cuts, we removed the online COE trigger and introduced the online clustering trigger in 2017. The signal event loss due to the online COE trigger disappeared after 2017, and that recovered the signal acceptance by 2.2%. The signal event loss due to the online clustering trigger is 0.2–0.4%. For the kinematic cuts except for the P_t and Z_{vtx} cuts (signal region), we used the same selection criteria as in the 2015 data analysis. Compared to the signal region used in the 2015 data analysis, we expanded the downstream boundary but shrank the upstream boundary, and that recovered the signal acceptance by 6%. For the veto cuts, we introduced new methods to detect overlapped pulse events efficiently by using a fast Fourier transform. Compared to the veto methods used in the 2015 data analysis, the signal acceptance was recovered by 10%. For the shape-related cuts, we introduced new cuts to suppress $K_L \to \pi^+\pi^-\pi^0$, hadron-cluster, and CV-η backgrounds. The thresholds of the new cuts to suppress hadron-cluster and CV-η backgrounds were determined to give the same signal acceptance as the cuts used in the 2015 data analysis. The thresholds of the new cut to suppress the $K_L \to \pi^+\pi^-\pi^0$ background was determined to maintain 90% of the signal acceptance. In total, the signal acceptance was recovered by 8% due to the change of the analysis methods.

Table 10.5: Signal acceptance difference originated from the cuts.

Cuts	Difference of A_{sig}
Trigger-related	+2%
Photon selection	-
Kinematic cuts	+6%
Veto cuts	+10%
Shape-related cuts	−10%

Background Table 10.6 shows the improvements of the rejection power ($R_{\text{improvement}}$) by updating cuts or revising analysis methods. The $R_{\text{improvement}}$ is defined as $r_{\text{2016-18}}/r_{\text{2015}}$, where $r_{\text{2016-18}}$ and r_{2015} are the rejection powers of the cuts used in the analysis of the 2016–2018 and 2015 data, respectively. Here we studied improvements of the rejection power for important background sources in the 2016–2018 data analysis.

For the $K_L \to \pi^+\pi^-\pi^0$ background, we introduced the new shape-related cut named CSD-$\pi^+\pi^-\pi^0$. By applying the CSD-$\pi^+\pi^-\pi^0$ cut, no event remained, and $R_{\text{improvement}}$ was estimated to be > 1.8 (68% C.L.). For the hadron-cluster background, we revised the analysis method to avoid the effect on the contamination from the scattering $K_L \to 2\gamma$. The $R_{\text{improvement}}$ was estimated to be 27 ± 19 due to revising the analysis method. The uncertainty mostly came from the statistical uncertainty in the 2015 data analysis method. For the upstream-π^0 background, we shrank the upstream boundary from 3000 mm to 3200 mm. The $R_{\text{improvement}}$ was estimated to be 5.8 ± 5.6 due to changing the signal region. The uncertainty mostly came from the statistical uncertainty of the γ-γ event in the second from the right in Fig. 8.17a. For the CV-η background, the rejection power improved by 1.5 ± 0.7 compared to the cut used in the 2015 data analysis. The uncertainty came from the statistical uncertainty of the remaining events in CV-η MC samples.

Table 10.6: Improvements of the rejection power.

Background	$R_{\text{improvement}}$
$K_L \to \pi^+\pi^-\pi^0$	> 1.8 (68% C.L.)
Hadron-cluster	27 ± 19
Upstream-π^0	5.8 ± 5.6
CV-η	1.5 ± 0.7

10.2.4 New Knowledge of the Background Sources

In the 2016–2018 data analysis, we studied backgrounds from $K^\pm$, beam-halo $K_L \to 2\gamma$, $K_L \to \pi^+\pi^-$, $K_L \to \pi^\pm e^\mp \gamma\nu$, $K_L \to \pi^0\pi^\pm e^\mp \nu$, $K_L \to e^+e^-\gamma$, and $K_L \to K^\pm e^\mp \nu$ decays that were not studied in the 2015 data analysis. Among those, we found that $K^\pm$ and beam-halo $K_L \to 2\gamma$ decays were dominant background sources in our measurement. We estimated the number of background events from $K^\pm$ decays to be 0.87 ± 0.25 and the beam-halo $K_L \to 2\gamma$ decay to be 0.26 ± 0.07. To test the existence of new physics processes at the KOTO experiment, it is essential to suppress such backgrounds in future datasets. In the later section, we discuss new methods to suppress backgrounds from $K^\pm$ and beam-halo $K_L \to 2\gamma$ decays.

10.2.5 Summary of the Comparisons

For the new barrel photon veto counter IB, we show the good agreement between data and MC under the loose cut condition and thus expect that IB suppresses the $K_L \to 2\pi^0$ background as designed. To discuss the detector performance with all of the cuts, we need an appropriate amount of data and MC samples in future datasets. For the sensitivity for $K_L \to \pi^0\nu\overline{\nu}$ search, we achieved 1.8 times higher sensitivity than in 2015. Of a factor of 1.8 times improvement, a 1.5 times is due to increased statistics, thanks to the successful data acquisition over three years. By introducing new analysis methods, we achieved an acceptance recovery of 8%. For the backgrounds, we suppressed the hadron-cluster background, which was the dominant background in the 2015 data analysis, and found that $K^\pm$ and beam-halo $K_L \to 2\gamma$ decays were dominant backgrounds in our measurement. The methods to suppress $K^\pm$ and beam-halo $K_L \to 2\gamma$ backgrounds will be discussed in the next section.

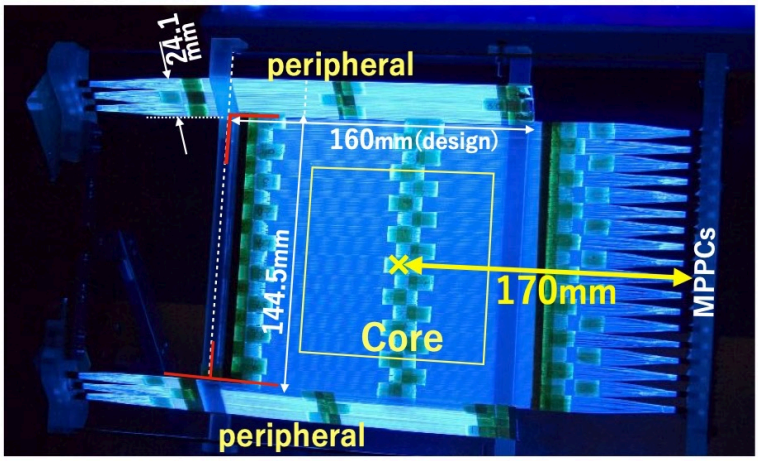

Figure 10.1: Picture of UCV (provided by K.Kotera.)

10.3 Further Background Suppression

In this work, we focused on the $K_L \to \pi^0\nu\overline{\nu}$ search with the data collected in 2016–2018 because the dominant backgrounds from $K^\pm$ and beam-halo $K_L \to 2\gamma$ were newly found and studied in this analysis. In future datasets, it is important to suppress such backgrounds to test the existence of new physics processes at the KOTO experiment. In this section, we discuss new methods to suppress backgrounds, especially $K^\pm$ and beam-halo $K_L \to 2\gamma$ backgrounds.

10.3.1 $K^\pm$ decays

As described in 8.4, $K^\pm \to \pi^0 e^\pm \nu$ is the most likely source of background. In particular, the kinematics of the π^0 is similar to that of the $K_L \to \pi^0\nu\overline{\nu}$ decay due to the small nominal mass of $e^\pm$. Because of this, it is not easy to suppress the $K^\pm$ background by a software effort. We thus installed a new charged-particle veto counter in the beam, located at the upstream edge of the KOTO detector. The new veto counter is called "Upstream Charged Veto (UCV)."

The important requirements on UCV are as follows.

1. Sufficient detection efficiency for charged particles.

2. Small material budget to reduce particles scattered by UCV and reduce the counting rate of UCV.

To achieve these requirements, we have developed UCV consisting of 0.5×0.5 mm scintillation fibers, as shown in Fig. 10.1. Each fiber acts as a scintillation light radiator and a light guide to MPPCs attached to the fiber. The used scintillation fibers have a small material budget. Before installing UCV, we checked the inefficiency with electrons and confirmed the inefficiency to be $\sim 5\%$ [69]. The irradiation of MPPCs by the beam particles increases the rate of noise and thus increases the probability of accidental loss. However, because the MPPCs are designed to be replaceable, we expect that the probability of accidental loss from UCV can be kept low. We installed UCV in the end of 2020 and are checking its performance in the actual environment.

For future (2022–), we are considering to install new UCV consisting of a 0.2-mm-thick scintillation film with a 1% detection inefficiency for charged particles [70]. We are also considering to install a new sweeping magnet at the beam-exit to reduce the number of $K^\pm$'s entering the KOTO detector by a factor of ten. In total, we expect to reduce the $K^\pm$ background events by a factor of 1000 compared to the ones in the 2016–2018 data analysis.

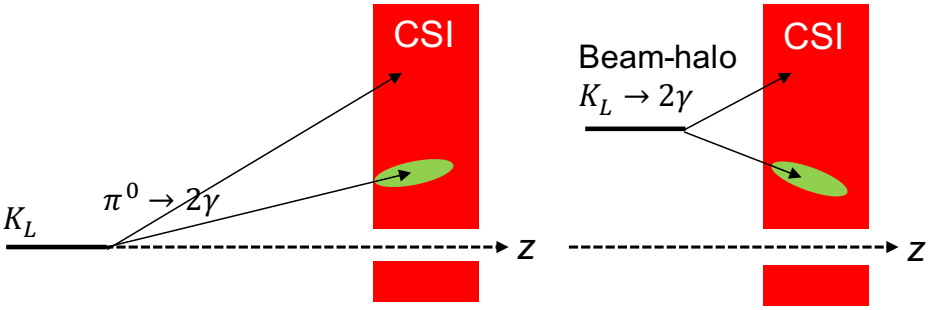

Figure 10.2: Schematic view of the shower development difference in CSI between the photon from the beam-axis and from the off-axis.

10.3.2 Beam-halo $K_L \to 2\gamma$

The background from beam-halo $K_L \to 2\gamma$ decays was the second largest background in the 2016–2018 analysis, which was estimated to be 0.26 ± 0.07 events. In addition, if we install UCV consisting of 0.2-mm-thick scintillation film, the beam-halo K_L flux is expected to increase by a factor of 1.5 than the case without UCV [71]. To suppress the background from beam-halo $K_L \to 2\gamma$ decays in future datasets, we are developing new cuts to extract the shower shape differences and kinematic variable differences in CSI. The new cuts were studied by Y. Noichi.

For the shower shape differences, Fig. 10.2 shows the schematic view of the shower development in CSI for photons from the beam-axis and the off-axis. We expect that the shower development from such photons is different. Y. Noichi developed an algorithm [71] using the shape-χ^2 variable (see. 7.2.1), which evaluates the consistency of a shower shape with a template made by MC simulations. In the algorithm, we reconstruct the event with two different assumptions that the event comes from $K_L \to \pi^0\nu\overline{\nu}$ and beam-halo $K_L \to 2\gamma$. For the $K_L \to \pi^0\nu\overline{\nu}$ assumption, we reconstruct the π^0 assuming the $\pi^0 \to 2\gamma$ decay on the beam-axis. For the beam-halo $K_L \to 2\gamma$ assumption, we reconstructed the K_L assuming $K_L \to 2\gamma$ decay on the COE-axis, where the origin of the COE-axis of (x, y) is defined by the position of COE in CSI. In both cases, we calculated the shape-χ^2 using the reconstructed decay vertex position, and calculated the likelihood ratio. Figure 10.3 shows that the likelihood ratio distribution [71]. With this algorithm, 89% of the background events were expected to be reduced, while 90% of the signal efficiency was kept.

For the kinematic variable differences, as shown in Sec. 9.1, some kinematic variables in beam-halo $K_L \to 2\gamma$ decays have features, such as cluster energies. Because $K_L \to 2\gamma$ decays do not have missing particles in the background event, cluster energies from beam-halo $K_L \to 2\gamma$ tend to be higher than the ones from $K_L \to \pi^0\nu\overline{\nu}$. To extract such features, Y. Noichi developed an algorithm [71] using the Toolkit for MutiVariate data Analysis (TMVA). As the inputs, we used cluster energies, cluster distance, projection angle, total energy, P_t, Z_{vtx}, R_{COE}, and incident angles. With this algorithm, 72% of the background events were expected to be reduced, while 90% of the signal acceptance was kept [71].

By combining the above two algorithms and optimizing thresholds of those cuts, we expect to reduce the beam-halo $K_L \to 2\gamma$ background by 94%, while keeping 90% of the signal efficiency [71].

10.3.3 Hadron-Cluster Backgrounds

In this thesis, we revealed the contribution from the hadron-cluster background was small. In future datasets, one concern is that the hadron-cluster background is expected to increase by installing UCV. In 2019, when we inserted a prototype UCV consisting of 1-mm-thick scintillation fibers, the hadron-cluster background events increase by a factor of 3–4 [72]. Based on this measurement, if we install UCV consisting of 0.2-mm-thick scintillation film in the future, the hadron-cluster background events will increase by a factor of 1.4–1.6.

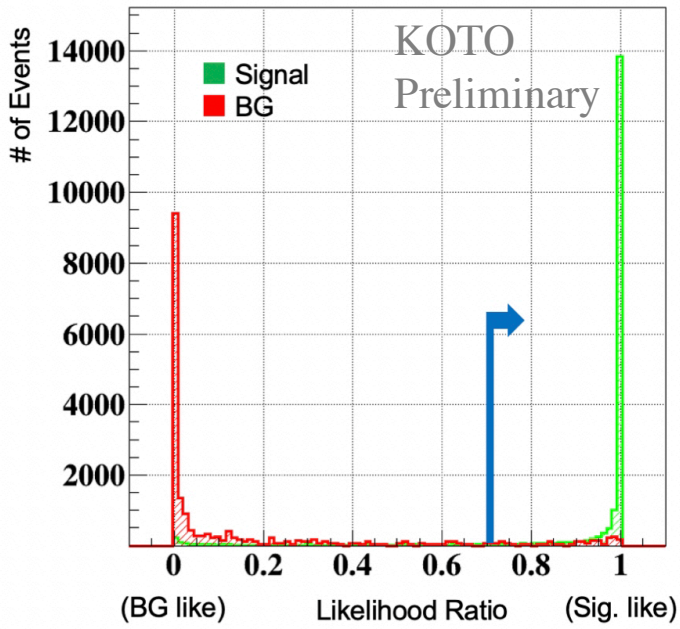

Figure 10.3: Likelihood ratio distributions. The green and red histograms show the $K_L \to \pi^0\nu\overline{\nu}$ and beam-halo $K_L \to 2\gamma$ MC events, respectively. The blue arrow shows the threshold to maintain the signal acceptance of 90%. This figure is quoted from Ref. [71].

Besides, we upgraded the CsI calorimeter after the 2018 physics run to suppress the hadron-cluster background. The key in this upgrade is to use the difference between the interaction length for neutrons[*2] and radiation length for photons[*3]. By attaching MPPCs on the upstream edges on the CsI crystals, we could calculate timing differences between MPPCs attached upstream and PMTs attached downstream on the CsI crystals. The timing difference can be interpreted as the depth of the interaction position in the CsI crystal, which is sensitiveness to the kind of incident particles. Using the data taken after 2019, M. Osugi studied the performance of the new system. Figure 10.4 shows the difference of the cluster timing measured by MPPCs and PMTs. In each cluster, we reconstructed the cluster timing using MPPCs and PMTs, and calculated the timing difference between them (ΔT). We then selected the larger timing difference between two clusters (ΔT^{larger}). Based on this measurement, we expect to reduce the hadron-cluster background events by a factor of 2×10^{-2}, while the acceptance for photon events was kept to 90% [73].

10.3.4 Upstream-π^0 Backgrounds

In the upstream-π^0 background events, there were two types of mechanisms (See Sec. 8.3.3). One is the n–γ events which were already suppressed by shape-related cuts. In addition, by applying a cut using MPPCs in CSI, installed after the 2018 physics run, we expect to reduce the n–γ background events. The other is the γ–γ events which were concentrated near the upstream end around of $Z_{\text{vtx}} = 3200$ mm. We expect to reduce the γ–γ background events by applying a tighter cut on Z_{vtx}. Although we need to simulate more upstream-π^0 MC events, the background can be suppressed to be 0.001 events by requiring $Z_{\text{vtx}} > 3300$ mm.

[*2] The interaction length of CsI for neutrons is $\sim$ 40 cm.
[*3] The radiation length of CsI is $\sim$ 2 cm.

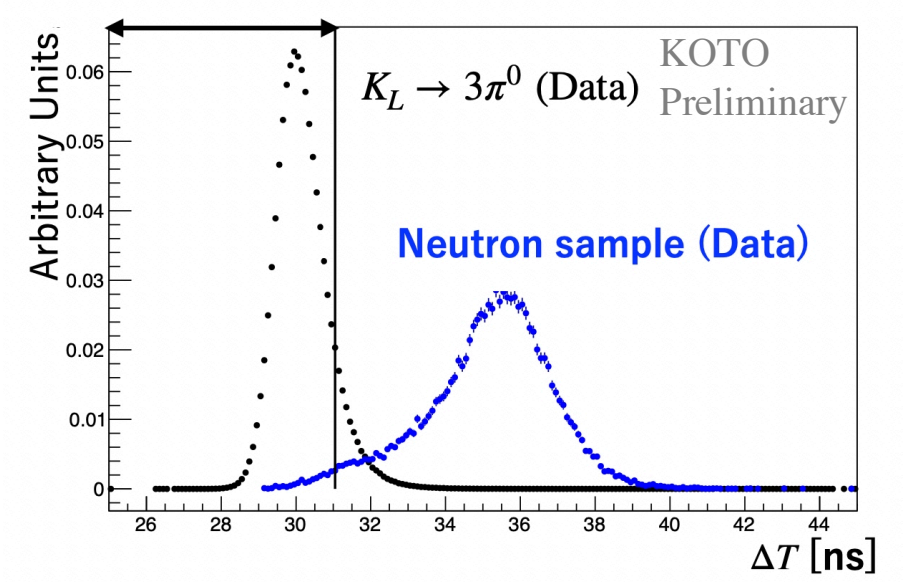

Figure 10.4: Distribution of ΔT^{larger}. The black and blue dots represent the π^0 and hadron-cluster events, respectively. The π^0 sample was selected from the $K_L \to 3\pi^0$ sample. The black vertical line shows the threshold to maintain a 90% acceptance for the π^0 sample. The figure is quoted from Ref. [73].

10.4 Discovery Potential in Future Datasets

Although the number of observed events of three is statistically consistent with the background expectation, some BSM models [15, 16] predicted the branching fraction of $K_L \to \pi^0\nu\overline{\nu}$ higher than the Grossman-Nir bound and pointed out that their models could explain observed events. In this section, we discuss a potential to discover a BSM physics in future datasets with the new methods described above.

Table 10.7 shows the background expectation in the 2016–2018 data and future datasets. In the calculation of the number of background events in future datasets, we assume that

- $K^{\pm}$ background
  - The new sweeping magnet reduces the $K^{\pm}$ background by a factor of 10.
  - The UCV consisting of 0.2-mm-thick scintillation film is installed, whose detection inefficiency for charged particles is 1%.
- Beam-halo $K_L \to 2\gamma$ background
  - The scattering K_L's at UCV increases the beam-halo K_L flux by a factor of 1.5.
  - The 94% of beam-core and beam-halo K_L backgrounds are suppressed by the new cuts.
- Hadron-cluster background
  - The background events increase by a factor of 1.5 due to the installation of UCV.
  - An additional rejection factor of 2×10^{-2} is obtained from the upgrade of the CsI calorimeter.
- The upstream-π^0 background is suppressed to be 0.001 events by requiring a tighter cut on Z_{vtx}.
- The backgrounds for which we calculated central values in the 2016–2018 data analysis are taken into account.

Table 10.7: Background estimation in 2016–2018 and in future datasets.

	2016–2018	Future 1	Future 2
SES	7.2×10^{-10}	7.2×10^{-10}	1.0×10^{-10}
BG	1.22	0.07	0.49

In the case of Future 1 in Table 10.7, we assume SES of 7.2×10^{-10}, which is the same SES as in 2016–2018. In the case of Future 2 in Table 10.7, we assume SES of 1.0×10^{-10}, which is the boundary to achieve SES of $O(10^{-11})$.

Though the number of observed events is statistically consistent with the background expectation of 1.22 events in the 2016–2018 data analysis, let us assume, for example, that observed two out of three events come from BSM contributions. In this case, we expect to observe two events from BSM contributions in the Future 1 data. With the new methods to suppress backgrounds, we expect that the number of background events is 0.07 in the Future 1 data. Assuming Poisson statistics, the probability of observing two or more background events is only 0.2%, which is sufficiently significant. A potential to discover new physics thus exists before achieving the target SES of KOTO in the near future.

If one observed event comes from BSM contributions, a discovery potential exists in the Future 2 data. With the new methods to suppress backgrounds, we expect that the number of background events is 0.49 in the Future 2 data. We expect to observe seven events from BSM contributions in the Future 2 data, and the probability of observing seven or more background events is only 1×10^{-6}.

Chapter 11

Conclusion

This thesis describes the study of the $K_L \to \pi^0\nu\overline{\nu}$ decay with the KOTO 2016–2018 data.

To take $K_L \to \pi^0\nu\overline{\nu}$ data samples in 2016–2018, I managed trigger conditions and run-types during runs. After I confirmed that the DAQ system worked well, I showed that the data taken in 2016–2018 corresponded to 3.05×10^{19} POT, which corresponded to 1.4 times higher statistics than the 2015 data [26].

To estimate the sensitivity for $K_L \to \pi^0\nu\overline{\nu}$ decay, I first confirmed that the data reproduced MC events by checking distributions of kinematic variables and energy and timing in veto counters. After that, I estimated the sensitivity to be 7.20×10^{-10}, which corresponded to 1.8 times higher sensitivity than the previous $K_L \to \pi^0\nu\overline{\nu}$ search with the 2015 data [26]. I established a new method for estimating the systematic uncertainty of the new trigger system, which counted the number of clusters in CSI, and I showed that the uncertainty was 0.07%.

To estimate the hadron-cluster background caused by neutrons hitting the KOTO calorimeter, we took the control sample with the insertion of the aluminum plate in the beam. I revealed that the contamination of scattered $K_L \to 2\gamma$ events in the control sample was not negligible. Using the weighting method, I estimated the number of the hadron-cluster background to be 0.017 events. After I summarized all the background studies, I estimated the number of background events in the 2016–2018 data analysis to be 1.22 ± 0.26.

After fixing the cuts for $K_L \to \pi^0\nu\overline{\nu}$, we examined the blind region and found three events inside the signal region. I calculated the probability to observe three or more events to be 13% based on the background estimation. We conclude that the number of observed events is statistically consistent with the background expectation. Because dominant backgrounds from $K^\pm$ and beam-halo $K_L \to 2\gamma$ decays were newly found and studied in the 2016–2018 data analysis, I focused on the analysis of the 2016–2018 dataset, and calculated an upper limit on the branching fraction of the $K_L \to \pi^0\nu\overline{\nu}$ decay in the 2016–2018 dataset to be 4.9×10^{-9} (90% C.L.). I showed that the result of the 2016–2018 data analysis was consistent with the result of the 2015 data analysis.

For prospects, I discussed further background suppression. By installing a new charged-particle veto counter in the beam, located at the upstream edge of the KOTO detector, and new sweeping magnet, we can suppress the background from $K^\pm$ sufficiently. We also can suppress the beam-halo $K_L \to 2\gamma$ background by applying new shape-related cuts. With such updates, we expect to search for a new physics via $K_L \to \pi^0\nu\overline{\nu}$ decays with the sensitivity of $O(10^{-10})$–$O(10^{-11})$ in KOTO.

In conclusion, this analysis achieved the highest sensitivity to search for $K_L \to \pi^0\nu\overline{\nu}$, gave the conclusion for the candidate events, and provided essential keys to search for $K_L \to \pi^0\nu\overline{\nu}$ in our future measurements.

Appendix A

Calibration Runs

Cosmic Ray Run The cosmic ray data was taken to calibrate the detectors: FB, NCC, HINEMOS, MB, IB, MBCV, IBCV, OEV, CSI, LCV, CC03, CC04, CC05, and CC06. The data was collected before and after beam periods and during weekly accelerator-maintenance periods. Events were triggered based on the deposited energies in CSI, NCC, MB, CC04, CC05, CC06, and OEV.

Beam Plug Closed Run With the beam plug in the beamline closed, particles penetrating the plug, such as muons, can be selected. Using the data, the timings of CV, CC04, CC05, CC06, BHPV, and BHGC were calibrated. For CC04, CC05, and CC06 calibration, the coincident signals of NCC and CC04, NCC and CC05, and NCC and CC06 were used, respectively. The timings of the front and rear parts of CV were calibrated using either coincident signals of NCC and CC04, NCC and CC05, or NCC and CC06. For BHPV and BHGC calibration, events triggered by newBHCV were used.

BPCV Calibration Run To calibrate BPCV, we collected events from $K_L \to \pi^+\pi^-\pi^0$ decays by requiring hits in CC06.

Aluminum Target Run To calibrate energies in CSI, we inserted a 5-mm-thick aluminum plate in the beam at the end of FB, and collected π^0's generated in the plate. Because we know the location of the target, we can calibrate energies in CSI by comparing the reconstructed π^0 $Z_{\rm vtx}$ position and the aluminum plate position. We collected the data using the physics trigger.

Appendix B

R_{COE}

The position of the center of deposited energy (COE) position on the CSI surface ($\boldsymbol{R}_{\mathrm{COE}}$) is defined as

$$\boldsymbol{R}_{\mathrm{COE}} = \frac{\sum E_i \boldsymbol{r}_i^{xy}}{\sum Ei}, \tag{B.1}$$

where E_i is the energy and $\boldsymbol{r}_i^{xy}$ is the position in CSI on the x-y plane of each photon, respectively. Here we describe the relationship between the position of COE in CSI and the position of the decay vertex of K_L's.

From the momentum of photons, we get

$$\sum \boldsymbol{p}_i^t = \boldsymbol{p}_{K_L}^t, \tag{B.2}$$

where $\boldsymbol{p}_i^t$ and $\boldsymbol{p}_{K_L}^t$ represent momentum of each photon and K_L on the x-y plane. We then get

$$\sum E_i \frac{(\boldsymbol{r}_i^{xy} - \boldsymbol{r}_{\mathrm{vtx}}^{xy})}{|\boldsymbol{r}_i - \boldsymbol{r}_{\mathrm{vtx}}|} = \boldsymbol{p}_{K_L}^t \tag{B.3}$$

$$\sum \frac{E_i \boldsymbol{r}_i^{xy}}{|\boldsymbol{r}_i - \boldsymbol{r}_{\mathrm{vtx}}|} - \sum \frac{E_i \boldsymbol{r}_{\mathrm{vtx}}^{xy}}{|\boldsymbol{r}_i - \boldsymbol{r}_{\mathrm{vtx}}|} = \boldsymbol{p}_{K_L}^t \tag{B.4}$$

$$\sum \frac{E_i \boldsymbol{r}_i^{xy}}{|\boldsymbol{r}_i - \boldsymbol{r}_{\mathrm{vtx}}|} - \boldsymbol{r}_{\mathrm{vtx}}^{xy} \sum \frac{E_i}{|\boldsymbol{r}_i - \boldsymbol{r}_{\mathrm{vtx}}|} = \boldsymbol{p}_{K_L}^t \tag{B.5}$$

where $\boldsymbol{r}_i$ is the position of photons in CSI, $\boldsymbol{r}_{\mathrm{vtx}}$ is the position of the decay vertex of K_L, and $\boldsymbol{r}_{\mathrm{vtx}}^{xy}$ is the position of decay vertex of K_L projected on the x-y plane. By using w_i, defined as $w_i \equiv \frac{E_i}{|\boldsymbol{r}_i - \boldsymbol{r}_{\mathrm{vtx}}|}$, we get

$$\boldsymbol{r}_{\mathrm{vtx}}^{xy} = \frac{\sum (w_i \boldsymbol{r}_i^{xy}) - \boldsymbol{p}_{K_L}^t}{\sum w_i}. \tag{B.6}$$

If the decay vertex position is not close to the CSI surface, all the photons have similar $|\boldsymbol{r}_i - \boldsymbol{r}_{\mathrm{vtx}}|$. In this case, from Eq. B.6, we get

$$\boldsymbol{r}_{\mathrm{vtx}}^{xy} \simeq \frac{\sum E_i \boldsymbol{r}_i^{xy}}{\sum E_i} - \frac{\boldsymbol{p}_{K_L}^t}{\sum w_i} \tag{B.7}$$

$$= \boldsymbol{R}_{\mathrm{COE}} - \frac{\boldsymbol{p}_{K_L}^t}{\sum w_i} \tag{B.8}$$

If P_t of K_L, such as beam-core K_L's, is small, $\boldsymbol{r}_{\mathrm{vtx}}^{xy} \simeq \boldsymbol{R}_{\mathrm{COE}}$. For beam-halo K_L's, the actual P_t of K_L is not large because the scattering source of K_L's is far from CSI, and thus we can assume $\boldsymbol{r}_{\mathrm{vtx}}^{xy} \simeq \boldsymbol{R}_{\mathrm{COE}}$.

Appendix C

Signal Loss due to the Online Trigger

CSIEt trigger The loss of signal events due to the CSIEt trigger was estimated using the special run whose CSIEt threshold was set lower than 550 MeV. Figure C.1 shows the CSIEt trigger efficiency as a function of the energy sum of two photons ($E_{\rm tot}$). The efficiency was fitted with the following function:

$$\epsilon_{\rm Et}(E_{\rm tot}) = \frac{1}{1+\exp\{-(E_{\rm tot}+p_0)/p_1\}}, \tag{C.1}$$

where p_0 and p_1 are fitting parameters. The events in the $K_L \to \pi^0\nu\overline{\nu}$ MC simulation were weighted with the efficiency function. In both Run69.0–Run78.2, and Run79.0 periods, the signal event losses were less than 0.4%.

Online COE trigger The offline $R_{\rm COE}$ was calculated using two on-time photons, but the online $R_{\rm COE}$ was calculated using all the hits in CSI crystals, including off-time hits. This difference caused the loss of the signal efficiency. To study such loss, we prepared a map of the trigger efficiency as a function of offline $R_{\rm COE}$ and $E_{2\gamma}/E_{\rm CSItot}$, where $E_{2\gamma}$ is the energy sum of two photons and $E_{\rm CSItot}$ is the energy sum of all the channels in CSI. Figure C.2 shows the COE trigger efficiency map as a function of an offline $R_{\rm COE}$ and $E_{2\gamma}/E_{\rm CSItot}$. The events in the $K_L \to \pi^0\nu\overline{\nu}$ MC simulation were weighted with the efficiency map. The signal event loss was 3% in the 2016 and a part of 2017 run.

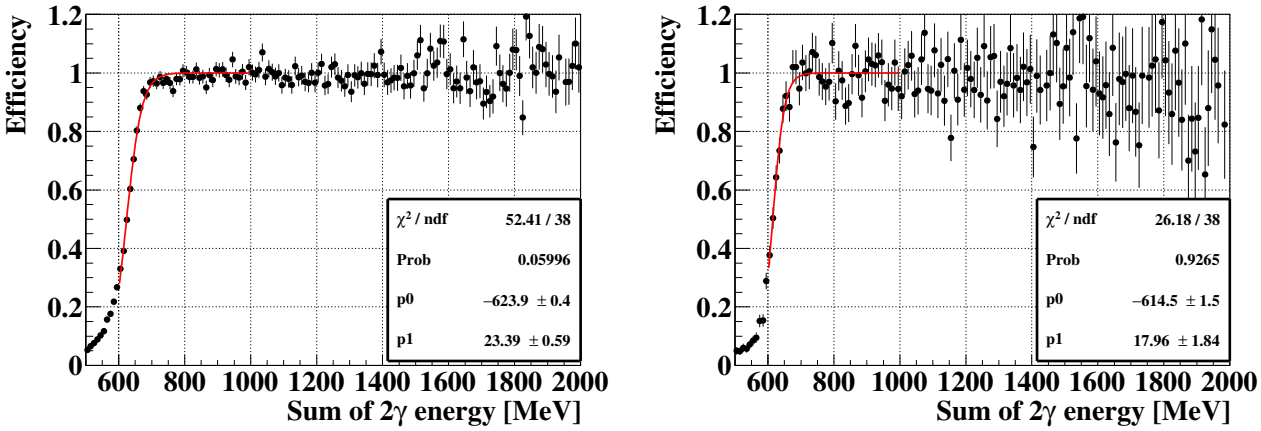

(a) Run69.0–Run78.2 (b) Run79.0

Figure C.1: CSIEt trigger efficiency as a function of the energy sum of two photons in the period of (a) Run69.0–Run78.2 and (b) Run79.0. The p_0 and p_1 are fitting parameters in Eq. C.1.

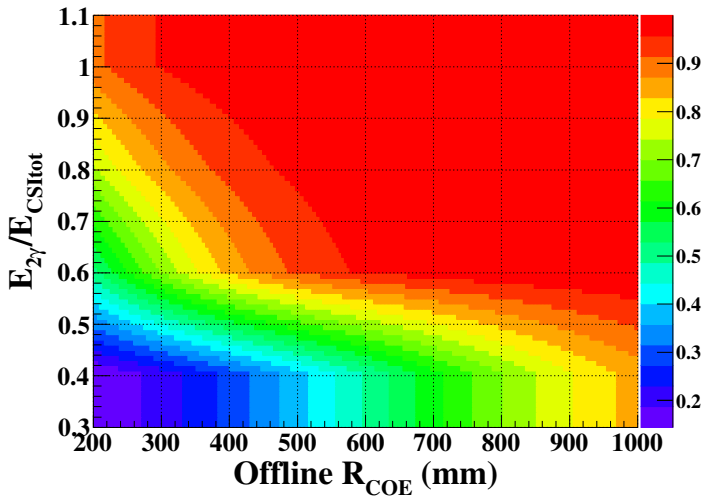

Figure C.2: COE trigger efficiency map as a function of an offline R_{COE} and $E_{2\gamma}/E_{\mathrm{CSItot}}$.

Appendix D

Downstream Charged Veto (DCV)

The DCV is a charged-particle veto counters installed after the 2018 physics run. The purpose of DCV is to suppress the $K_L \to \pi^+\pi^-\pi^0$ background.

As described in Sec. 8.2.1, we suppressed the $K_L \to \pi^+\pi^-\pi^0$ background by applying the CSD-$\pi^+\pi^-\pi^0$ cut and excluding the area of $P_t < \left(\frac{1}{35\ \mathrm{mm}}\ (Z_{\mathrm{vtx}} - 4000\ \mathrm{mm}) + 130\right)$ MeV/c for $Z_{\mathrm{vtx}} > 4000$ mm. However, the signal acceptance decreased 12% due to these selection criterion. To recover the signal acceptance, it is worth not to use these selection criterion.

As described in Sec. 8.2.1, two charged-pions from $K_L \to \pi^+\pi^-\pi^0$ were absorbed in the beam pipe of the KOTO detector. To detect such pions before absorbing, we installed a new charged-particle veto counter named "Downstream Charged Veto (DCV)" after the 2018 physics run. Figure D.1 shows the configuration of DCV and Fig. D.2 shows the pictures of DCV's. The DCV consists of two parts (DCV1 and DCV2) to cover the beam-pipe along z-axis. Both DCV1 and DCV2 consist of 5-mm-thick plastic scintillators. The scintillation lights are read by MPPC's via wavelength shifting fibers embedded in the scintillator plate. Because DCV was installed inside BPCV, we uninstalled BPCV from the KOTO detector system.

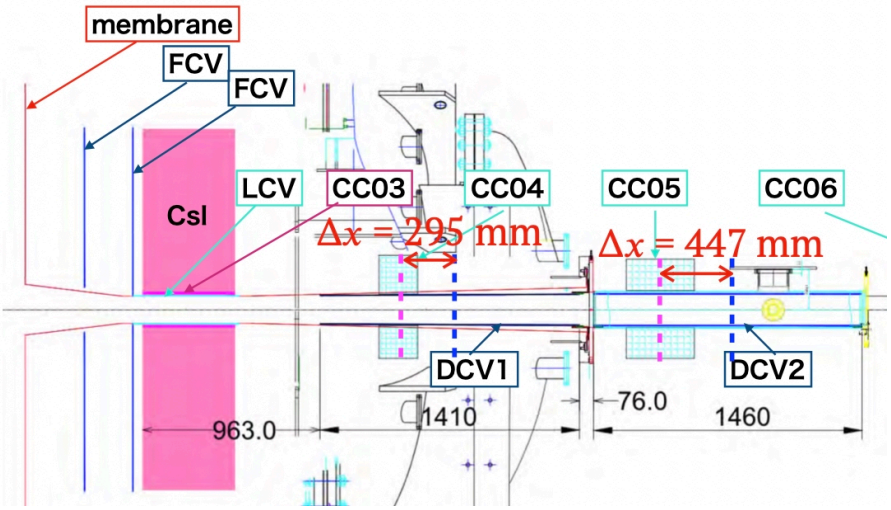

Figure D.1: Configuration of DCV. The DCV1 is located around CC04, and DCV2 is located around CC05. The figure is quoted from Ref. [74].

(a) DCV1 (b) DCV2

Figure D.2: Pictures of DCV1 (a) and DCV2 (b). These figures are quoted from Ref. [74].

References

[1] P. Huet, E. Sather, Phys. Rev. D 51 (1995) 379–394. doi:10.1103/PhysRevD.51.379, [link].
URL https://link.aps.org/doi/10.1103/PhysRevD.51.379

[2] N. Cabibbo, Phys. Rev. Lett. 10 (1963) 531–533. doi:10.1103/PhysRevLett.10.531, [link].
URL https://link.aps.org/doi/10.1103/PhysRevLett.10.531

[3] M. Kobayashi, T. Maskawa, Prog. Theor. Phys. 49 (2) (1973) 652–657. doi:10.1143/PTP.49.652, [link].
URL http://dx.doi.org/10.1143/PTP.49.652

[4] L. Wolfenstein, Phys. Rev. Lett. 51 (1983) 1945–1947. doi:10.1103/PhysRevLett.51.1945, [link].
URL https://link.aps.org/doi/10.1103/PhysRevLett.51.1945

[5] P. D. Group *et al.*, Prog. Theor. Exp. Phys. 2020 (8), 083C01. doi:10.1093/ptep/ptaa104, [link].
URL https://doi.org/10.1093/ptep/ptaa104

[6] S. L. Glashow, J. Iliopoulos, L. Maiani, Phys. Rev. D 2 (1970) 1285–1292. doi:10.1103/PhysRevD.2.1285, [link].
URL https://link.aps.org/doi/10.1103/PhysRevD.2.1285

[7] V. Cirigliano *et al.*, Rev. Mod. Phys. 84 (2012) 399–447, and references therein. doi:10.1103/RevModPhys.84.399, [link].
URL https://link.aps.org/doi/10.1103/RevModPhys.84.399

[8] A. J. Buras *et al.*, J. High Energy Phys. 2015 (11) (2015) 33. doi:10.1007/JHEP11(2015)033, [link].
URL https://doi.org/10.1007/JHEP11(2015)033

[9] F. Mescia, C. Smith, Phys. Rev. D 76 (2007) 034017. doi:10.1103/PhysRevD.76.034017, [link].
URL https://link.aps.org/doi/10.1103/PhysRevD.76.034017

[10] K. Shiomi, Measurement of K_L^0 flux at the J-PARC neutral-kaon beam line for the $K_L^0 \to \pi^0\nu\bar{\nu}$ experiment, Ph.D. thesis, Kyoto University, data last accessed May 12th, 2021 (https://www-he.scphys.kyoto-u.ac.jp/theses/doctor/dt_shiomi.pdf) (2012).

[11] Y. Grossman, Y. Nir, Phys. Lett. B 398 (1) (1997) 163 – 168. doi:10.1016/S0370-2693(97)00210-4, [link].
URL http://www.sciencedirect.com/science/article/pii/S0370269397002104

[12] W. J. Marciano, Z. Parsa, Phys. Rev. D 53 (1996) R1–R5. doi:10.1103/PhysRevD.53.R1, [link].
URL https://link.aps.org/doi/10.1103/PhysRevD.53.R1

[13] E. Cortina Gil et al., J. High Energy Phys. 11 (2020) 042 (2020). doi:10.1007/JHEP11(2020)042.

[14] J. Aebischer, A. J. Buras, J. Kumar, J. High Energy Phys. 2020 (12) (2020) 97. doi:10.1007/JHEP12(2020)097, [link].
URL https://doi.org/10.1007/JHEP12(2020)097

[15] X.-G. He *et al.*, J. High Energy Phys. 2020 (4) (2020) 57. doi:10.1007/JHEP04(2020)057, [link].
URL https://doi.org/10.1007/JHEP04(2020)057

[16] X.-G. He *et al.*, J. High Energy Phys. 2020 (8) (2020) 34. doi:10.1007/JHEP08(2020)034, [link].
URL https://doi.org/10.1007/JHEP08(2020)034

[17] L. S. Littenberg, Phys. Rev. D 39 (1989) 3322–3324. doi:10.1103/PhysRevD.39.3322, [link].
URL https://link.aps.org/doi/10.1103/PhysRevD.39.3322

[18] G. Graham *et al.*, Phys. Lett. B 295 (1) (1992) 169 – 173. doi:10.1016/0370-2693(92)90107-F, [link].
URL http://www.sciencedirect.com/science/article/pii/037026939290107F

[19] M. Weaver *et al.*, Phys. Rev. Lett. 72 (1994) 3758–3761. doi:10.1103/PhysRevLett.72.3758, [link].
URL https://link.aps.org/doi/10.1103/PhysRevLett.72.3758

[20] J. Adams *et al.*, Phys. Lett. B 447 (3) (1999) 240 – 245. doi:10.1016/S0370-2693(98)01593-7, [link].
URL http://www.sciencedirect.com/science/article/pii/S0370269398015937

[21] A. Alavi-Harati *et al.*, Phys. Rev. D 61 (2000) 072006. doi:10.1103/PhysRevD.61.072006, [link].
URL https://link.aps.org/doi/10.1103/PhysRevD.61.072006

[22] J. K. Ahn *et al.*, Phys. Rev. D 74 (2006) 051105. doi:10.1103/PhysRevD.74.051105, [link].
URL https://link.aps.org/doi/10.1103/PhysRevD.74.051105

[23] J. K. Ahn *et al.*, Phys. Rev. Lett. 100 (2008) 201802. doi:10.1103/PhysRevLett.100.201802, [link].
URL https://link.aps.org/doi/10.1103/PhysRevLett.100.201802

[24] J. K. Ahn *et al.*, Phys. Rev. D 81 (2010) 072004. doi:10.1103/PhysRevD.81.072004, [link].
URL https://link.aps.org/doi/10.1103/PhysRevD.81.072004

[25] J. K. Ahn et al., Prog. Theor. Exp. Phys. 2017 (2) (2017) 021C01. doi:10.1093/ptep/ptx001.

[26] J. K. Ahn *et al.*, Phys. Rev. Lett. 122 (2019) 021802. doi:10.1103/PhysRevLett.122.021802, [link].
URL https://link.aps.org/doi/10.1103/PhysRevLett.122.021802

[27] S. Nagamiya, Prog. Theor. Exp. Phys. 2012 (1) (2012) 02B001. doi:10.1093/ptep/pts025, [link].
URL http://dx.doi.org/10.1093/ptep/pts025

[28] T. Koseki *et al.*, Prog. Theor. Exp. Phys. 2012 (1) (2012) 02B004. doi:10.1093/ptep/pts071, [link].
URL http://dx.doi.org/10.1093/ptep/pts071

[29] J. Comfort et al., "Proposal for $K_L \to \pi^0\nu\bar{\nu}$ Experiment at J-Parc" (2016), data last accessed May 12th, 2021 (https://j-parc.jp/researcher/Hadron/en/pac_0606/pdf/p14-Yamanaka.pdf).

[30] T. Yamanaka, Prog. Theor. Exp. Phys. 2012 (1) (2012) 02B006. doi:10.1093/ptep/pts057, [link].
URL http://dx.doi.org/10.1093/ptep/pts057

[31] Y. Maeda, Search for the Decay $K_L \to \pi^0\nu\bar{\nu}$ with a Neutron-Insensitive GeV-Energy Photon Detector, Ph.D. thesis, Kyoto University, data last accessed May 12th, 2021 (https://www-he.scphys.kyoto-u.ac.jp/theses/doctor/dt_maeda.pdf) (2016).

[32] S. Agostinelli et al., Nucl. Instrum. Methods Phys. Res., Sect. A 506 (3) (2003) 250 – 303. doi:10.1016/S0168-9002(03)01368-8, [link].
URL http://www.sciencedirect.com/science/article/pii/S0168900203013688

[33] J. Allison et al., IEEE Trans. Nucl. Sci. 53 (1) (2006) 270–278. doi:10.1109/TNS.2006.869826.

[34] J. Allison et al., Nucl. Instrum. Methods Phys. Res., Sect. A 835 (2016) 186 – 225. doi:10.1016/j.nima.2016.06.125, [link].
URL http://www.sciencedirect.com/science/article/pii/S0168900216306957

[35] K. Nakagiri, Search for the Decay $K_L \to \pi^0\nu\bar{\nu}$ at the J-PARC KOTO Experiment, Ph.D. thesis, Kyoto University, 2019, data last accessed May 12th, 2021 (https://www-he.scphys.kyoto-u.ac.jp/theses/doctor/nakagiri_dt.pdf) (2019).

[36] M. Ikegami, Prog. Theor. Exp. Phys. 2012 (1) (2012) 02B002. doi:10.1093/ptep/pts019, [link].
URL http://dx.doi.org/10.1093/ptep/pts019

[37] K. Hasegawa, Comissioning of energy upgraded linac of J-PARC, in: Proceedings, 27th Linear Accelerator Conference, LINAC2014, no. TUIOB03, 2014, p. 417.
URL https://accelconf.web.cern.ch/accelconf/SRF2011/papers/tuiob03.pdf

[38] H. Hotchi *et al.*, Prog. Theor. Exp. Phys. 2012 (1) (2012) 02B003. doi:10.1093/ptep/pts021, [link].
URL http://dx.doi.org/10.1093/ptep/pts021

[39] K. Agari *et al.*, Prog. Theor. Exp. Phys. 2012 (1) (2012) 02B008. doi:10.1093/ptep/pts034, [link].
URL http://dx.doi.org/10.1093/ptep/pts034

[40] H. Takahashi *et al.*, J. Radioanal. Nucl. Chem. 305 (3) (2015) 803 – 809. doi:10.1007/s10967-015-3940-9.

[41] T. Shimogawa, Nucl. Instrum. Methods Phys. Res., Sect. A 623 (1) (2010) 585 – 587. doi:10.1016/j.nima.2010.03.078, [link].
URL http://www.sciencedirect.com/science/article/pii/S016890021000642X

[42] K. Sato, Measurement of the CsI calorimeter performance and K_L momentum spectrum for the J-PARC KOTO experiment, Ph.D. thesis, Osaka University, data last accessed May 12th, 2021 (http://osksn2.hep.sci.osaka-u.ac.jp/theses/doctor/2015/dt_sato.pdf) (2015).

[43] A. Alavi-Harati *et al.*, Phys. Rev. D 67 (2003) 012005, see in Sec.C.2 *The CsI calorimeter*. doi:10.1103/PhysRevD.67.012005, [link].
URL https://link.aps.org/doi/10.1103/PhysRevD.67.012005

[44] K. Sato *et al.*, Nucl. Instrum. Methods Phys. Res., Sect. A 982 (2020) 164527. doi:https://doi.org/10.1016/j.nima.2020.164527, [link].
URL https://www.sciencedirect.com/science/article/pii/S0168900220309244

[45] T. Masuda, Development and Experimental Study of the KOTO Detector System using Three K_L Neutral Decay Modes, Ph.D. thesis, Kyoto University, data last accessed May 12th, 2021 (https://www-he.scphys.kyoto-u.ac.jp/theses/doctor/taka_dt.pdf) (2014).

[46] Y. Tajima *et al.*, Nucl. Instrum. Methods Phys. Res., Sect. A 592 (3) (2008) 261 – 272. doi:10.1016/j.nima.2008.04.080, [link].
URL http://www.sciencedirect.com/science/article/pii/S0168900208006505

[47] R. Murayama *et al.*, Nucl. Instrum. Methods Phys. Res., Sect. A 953 (2020) 163255. doi:https://doi.org/10.1016/j.nima.2019.163255, [link].
URL https://www.sciencedirect.com/science/article/pii/S0168900219315268

[48] D. Naito *et al.*, Prog. Theor. Exp. Phys. 2016 (2) (2016) 023C01. doi:10.1093/ptep/ptv191, [link].
URL http://dx.doi.org/10.1093/ptep/ptv191

[49] D. Naito, Development of a low-mass and high-efficient charged particle detector for $K_L \to \pi^0\nu\bar{\nu}$ search, Ph.D. thesis, Kyoto University, data last accessed May 12th, 2021 (https://www-he.scphys.kyoto-u.ac.jp/theses/doctor/dt_naito.pdf) (2014).

[50] T. Matsumura *et al.*, Nucl. Instrum. Methods Phys. Res., Sect. A 795 (2015) 19 – 31. doi:10.1016/j.nima.2015.05.036, [link].
URL http://www.sciencedirect.com/science/article/pii/S0168900215006762

[51] Y. Sugiyama, Pulse shape discrimination method to suppress neutron-induced background in the J-PARC KOTO experiment, Ph.D. thesis, Osaka University, data last accessed May 12th, 2021 (http://osksn2.hep.sci.osaka-u.ac.jp/theses/doctor/2016/dt_sugiyama.pdf) (2016).

[52] Y. Maeda *et al.*, Prog. Theor. Exp. Phys. 2015 (6) (2015) 063H01. doi:10.1093/ptep/ptv074, [link].
URL http://dx.doi.org/10.1093/ptep/ptv074

[53] S. Shinohara, PoS FPCP2015 (2015) 079. doi:10.22323/1.248.0079.

[54] S. Shinohara, J. Phys. Conf. Ser. 800 (1) (2017) 012044. doi:10.1088/1742-6596/800/1/012044, [link].
URL http://stacks.iop.org/1742-6596/800/i=1/a=012044

[55] Y. Sugiyama *et al.*, IEEE Trans. Nucl. Sci. 62 (3) (2015) 1115–1121. doi:10.1109/TNS.2015.2417312.

[56] S. Su *et al.*, IEEE Trans. Nucl. Sci. 64 (6) (2017) 1338–1345. doi:10.1109/TNS.2017.2694040.

[57] M. Bogdan, J.-F. Genat, Y. Wah, Custom DAQ Module for timing and energy measurements for J-Parc E14, in: 2009 16th IEEE-NPSS Real Time Conference, 2009, pp. 443–445. doi:10.1109/RTC.2009.5321611.

[58] M. Bogdan, J.-F. Genat, Y. Wah, Custom 12-Bit, 500MHZ ADC/Data Processing Module for the KOTO Experiment at J-Parc, in: 2010 17th IEEE-NPSS Real Time Conference, 2010, pp. 1–2. doi:10.1109/RTC.2010.5750452.

[59] E. Iwai, CsI calorimeter for the J-PARC KOTO experiment, Ph.D. thesis, Osaka University, data last accessed May 12th, 2021 (http://osksn2.hep.sci.osaka-u.ac.jp/theses/doctor/2012/dt_iwai.pdf) (2012).

[60] C. Lin *et al.*, J. Phys. Conf. Ser. 1526 (2020) 012034. doi:10.1088/1742-6596/1526/1/012034.

[61] C. L. on behalf of the KOTO Collaboration, JPS Conf. Proc. 33 (2021) 011105. doi:https://doi.org/10.7566/JPSCP.33.011105.

[62] R. Murayama, New cylindrical gamma-veto detector for the J-PARC KOTO experiment, Ph.D. thesis, Osaka University, data last accessed May 12th, 2021 (http://osksn2.hep.sci.osaka-u.ac.jp/theses/doctor/2017/dt_murayama.pdf) (2017).

[63] S. Shinohara, J. Phys. Conf. Ser. 1526 (1) (2020) 012002. doi:10.1088/1742-6596/1526/1/012002.

[64] Y. Sugiyama *et al.*, Nucl. Instrum. Methods Phys. Res., Sect. A 987 (2021) 164825. doi:https://doi.org/10.1016/j.nima.2020.164825, [link].
URL http://www.sciencedirect.com/science/article/pii/S0168900220312225

[65] A. Pullia, PoS KAON (2008) 026. doi:10.22323/1.046.0026.

[66] N. Shimizu, presentation in KOTO weekly meeting (2020).

[67] J. K. Ahn *et al.*, Phys. Rev. Lett. 126 (2021) 121801. doi:10.1103/PhysRevLett.126.121801, [link].
URL https://link.aps.org/doi/10.1103/PhysRevLett.126.121801

[68] R. D. Cousins, V. L. Highland, Nucl. Instrum. Methods Phys. Res., Sect. A 320 (1) (1992) 331 – 335. doi:10.1016/0168-9002(92)90794-5, [link].
URL http://www.sciencedirect.com/science/article/pii/0168900292907945

[69] T. Nunes, Development and Performance Evaluation of a Low Mass In-Beam Charged Particle Detector (UCV) for the KOTO experiment at J-PARC, presentation in the JPS on Mar. 12th, 2021.
URL https://kds.kek.jp/event/36559/contributions/185036/attachments/142592/176173/12pT2-03.pdf

[70] H. Nanjo, presentation in the JPS on Sep. 16th, 2020. [link].
URL https://kds.kek.jp/event/35569/contributions/174563/attachments/136379/165799/JPS2020.pdf

[71] Y. Noichi, master thesis, Osaka University, 2020, data last accessed May 12th, 2021. [link].
URL http://osksn2.hep.sci.osaka-u.ac.jp/theses/master/2020/MasterThesis2020_Noichi.pdf

[72] N. Shimizu, presentation in the KOTO collaboration meeting on Jul. 3rd, 2020.

[73] M. Osugi, master thesis, Osaka University, 2019, data last accessed May 12th, 2021. [link].
URL http://osksn2.hep.sci.osaka-u.ac.jp/theses/master/2019/MasterThesis2019_Osugi.pdf

[74] H. Kim, presentation in the KOTO collaboration meeting on Jun. 28th, 2019.